DOCTORAL THESIS

Transport properties of ultrathin superconducting niobium films

Author:
Sameh M. A. Altanany

Supervisor:
Prof. Marta Z. Cieplak

Auxiliary Supervisor:
Dr. Irina Zajcewa

Doctoral dissertation submitted in fulfillment of the requirements for the degree of Doctor of Physical Sciences

prepared in the

Institute of Physics of the Polish Academy of Sciences

May 22, 2025

Declaration of Authorship

I, Sameh M. A. Altanany, declare that this thesis titled, "Transport properties of ultrathin superconducting niobium films" and the work presented has not been submitted for consideration in any other academic awards and has been completed in accord with the rules and guidelines of the Institute of Physics, Polish Academy of Science (IFPAN) and the Code of Practice for Research Degree Programs. I also confirm that:

- The Nb films used for this study have been grown in the laboratory of Prof. C. L. Chien at The Johns Hopkins University, USA, by my thesis adviser Prof. Marta Cieplak, with the help of PhD student, Leyi Y. Zhu. I was not involved in any modification of any experimental techniques used for this study. The initial basic film characterization, using X-ray apparatus, have been performed by Dr Roman Minikayev (SL 1.3 group) at the Institute of Physics PAS.
- My main experimental tasks included the following: preparation of the films (photolithography, etching and contact soldering) for the transport experiments: $R(T)$ and $I-V$ measurements, which are of central importance in this study. Most of transport measurements were performed in the laboratory of ON2.4 group at the Institute of Physics of the Polish Academy of Sciences. Dr. Irina Zajcewa, my auxiliary adviser, helped me at the start of my research through familiarizing me with the experimental setups available in the laboratory; she also provided some films prepared for experiment. Dr. Artur Malinowski, a member of research group, supervised technical aspects of the use of PPMS apparatus. Due to technical problems some of the measurements I have conducted in the laboratory of ON-3 group, where Dr. Tatiana Zajarniuk, under the direction of Prof. Andrzej Szewczyk (head of ON-3) supervised technical aspects of the PPMS equipment. Finally, experiments in milikelwin temperature range on thinner films have been performed by our collaborator, Dr. Maciej Chrobak in the AGH University of Science and Technology in Kraków. Myself, under supervision of Dr Zajcewa, participated in person in the initial phase of these measurements, and, together with my thesis adviser, directed Dr. Chrobak in performing the remaining data taking.
- I have been responsible for collecting and analyzing all the experimental data and comparing results to theories, in close consultation and help from my advisor Prof. Marta Cieplak.

Signed:

Date:

Abstract

In this work we investigate the influence of the structural disorder induced by the decrease of the thickness (d) of thin films of niobium (Nb) on the superconducting properties of the films. In the first part of the study the evolution of Berezinskii-Kosterlitz-Thouless (BKT) phase transition is examined in films with d decreasing from 44 nm down to 3.4 nm, using resistance $R(T)$ and current- voltage (I-V) characteristics measurements. Previous study of similar Nb films reveals that decreasing d induces structural transformation from polycrystalline (d >5 nm) into amorphous structure (d <3 nm). From the analysis of $R(T)$ and I-V data using distinct statistical models describing superconducting fluctuations we find the transition temperatures to the superconducting phase: the mean field transition temperature and the BKT transition temperature. We show that as d decreases the superconducting phase transition is influenced by the vortex core energy and film inhomogeneity, leading to gradual smearing of the sharp features of BKT transition predicted by theory. In the I-V characteristics of $d = 8.5$ nm film we observe intermediate resistive states at high currents and temperatures below the mean field-temperature, with features characteristic of phase slip lines (PSLs), predicted to occur in films of large width. Most interestingly, ultrathin Nb films, with d below 5 nm, behave as Josephson junctions arrays (JJA), with many Josephson junctions of diverse lengths. We observe the diode effect at low temperature, accompanied by hysteretic and stochastic behaviors of the first switching current to the next voltage state. With increasing current, before final switching to the normal state, additional intermediate switching current is observed, and we propose to explain this intermediate switching current by phenomenon of multiple Andreev reflection. Qualitative comparison is made to existing theories, but quantitative comparison is hampered by the lack of theories for the JJA with diverse junction lengths.

In the second part of this work, we study the evolution of the vortex glass (VG) phase transition and vortex thermal creep in polycrystalline Nb films with d decreasing from 44 nm down to 7.4 nm, with the use of I-V characteristics measurements in perpendicular magnetic field. Analysis using the VG scaling laws allows to identify VG transition in the thickest film, while in case of thinner films vortex creep produces large uncertainty in the putative VG transition temperature and scaling exponents. Using recent strong pinning theory we perform analysis of the creep, and extract the dependence of the activation energy for vortex pinning on temperature, magnetic field, and film thickness. This analysis provides more insights into vortex dynamics than the standard evaluation of critical current density. The results reveal two distinct regimes of pinning, which we propose to identify with δl or δT_c-types of pinning (due to spacial fluctuations, of mean free path l or of superconducting transition temperature T_c, respectively). In the thickest film δl pinning

is observed, but with the decrease of film thickness the second pinning regime appears, and becomes dominant in the thinnest film. We link these pinning regimes with the structural disorder due to grain boundaries, which produce charge carrier scattering in the thickest film, but with decreasing film thickness gradually evolve into amorphous inclusions, producing fluctuations in the T_c.

Streszczenie

W niniejszej pracy badany jest wpływ nieporządku strukturalnego wywołanego zmniejszeniem grubości (d) cienkich warstw niobu (Nb), na własności nadprzewodzące warstw. W pierwszej części badamy wpływ zmniejszania d, od 44 nm do 3.4 nm, na przejście fazowe Berezinskiego-Kosterlitza-Thoulessa (BKT), wykorzystując pomiary oporu $R(T)$ i charakterystyk prądowo-napięciowych (I-V). Poprzednie badania podobnych warstw Nb ujawniło, że wraz ze zmniejszeniem d zachodzi przejście strukturalne od struktury polikrystalicznej ($d >$5 nm) do amorficznej ($d <$ 3 nm). Analizując dane $R(T)$ oraz I-V przy użyciu kilku modeli statystycznych opisujących fluktuacje nadprzewodnictwa, wyznaczamy temperatury przejścia fazowego do stanu nadprzewodzącego: temperaturę pola średniego oraz temperaturę przejścia BKT. Pokazujemy, że wraz ze zmniejszaniem d energia rdzenia wirowego i nieporządek strukturalny w warstwie mają wpływ na przejście do stanu nadprzewodzącego, prowadząc do stopniowego rozmywania ostrego przejścia BKT przewidzianego przez teorię. W charakterystykach I-V warstwy $d = 8.5$ nm obserwujemy pośrednie stany oporowe przy wysokich prądach i temperaturach poniżej temperatury pola średniego, charakterystyczne dla linii poślizgu fazowego (PSL), przewidywanego w przypadku szerokich warstw. Co najciekawsze, najcieńsze warstwy Nb, o grubościach d poniżej 5 nm, zachowują się jak sieci złącz Josephsona (JJA) z wieloma złączami o zróżnicowanej długości. Obserwujemy efekt diody w niskiej temperaturze, wraz z histerezą i stochastycznym zachowaniem pierwszego prądu przełączającego do następnego stanu napięcia. Przy dalszym wzroście prądu, jeszcze poniżej prądu przełączającego system do stanu normalnego, pojawia się dodatkowy pośredni prąd przełączający, który proponujemy wyjaśnić zjawiskiem wielokrotnego odbicia Andreeva. Przeprowadzone są jakościowe porównania z istniejącymi teoriami, ale ilościowe porównanie nie jest możliwe, bo brak dotychczas teorii dla sieci JJA z wieloma złączami o różnych długościach.

W drugiej części tej pracy badamy wpływ zmniejszania d polikrystalicznych warstw Nb w zakresie od 44 nm do 7.4 nm na przejście fazowe do fazy szkła wirowego (VG) i na termiczne pełzanie wirów, przy użyciu pomiarów charakterystyk I-V w prostopadłym polu magnetycznym. Analizując prawa skalowania przy przejściu VG pokazujemy, że przejście zachodzi w najgrubszej warstwie, podczas gdy w przypadku cieńszych warstw pełzanie wirów uniemożliwia dokładne wyznaczenie temperatury przejścia VG i wykładników skalowania. Wykorzystując najnowszą teorię silnego kotwiczenia wirów, przeprowadzamy analizę pełzania wirów i wyznaczamy zależność energii aktywacji dla kotwiczenia wirów od temperatury, pola magnetycznego i grubości warstwy. Analiza ta dostarcza więcej informacji na temat dynamiki wirowej niż standardowa ocena krytycznej gęstości prądu. Wyniki ujawniają dwa odrębne typy kotwiczenia, które proponujemy identyfikować z typami kotwiczenia δl lub δT_c (typy wynikające z przestrzennych fluktuacji, odpowiednio,

średniej drogi swobodnej l lub temperatury przejścia nadprzewodzącego T_c). W najgrubszej warstwie występuje kotwiczenie δl, ale wraz ze zmniejszaniem się grubości warstwy pojawia się drugi typ kotwiczenia, który staje się dominujący w najcieńszej warstwie. Te dwa typy kotwiczenia proponujemy wyjaśnić nieporządkiem strukturalnym spowodowanym granicami ziaren. Podczas gdy w najgrubszej warstwie granice ziaren powodują rozpraszanie nośników ładunku, wraz ze zmniejszaniem grubości warstwy granice te ewoluują stopniowo w wytrącenia fazy amorficznej, powodując fluktuacje temperatury krytycznej T_c.

Acknowledgements

I sincerely thank my supervisor Prof. Marta Z. Cieplak for her supervison and continuous support throughout my PhD. I am thankful to other people who helped me to achieve the work presented in this thesis; special thanks go to my auxiliary adviser Dr. Irina Zajcewa, Dr. Maciej Chrobak (from the AGH univeristy of Science and Technology in Kraków) and Prof. Andrzej Szewczyk (head of ON-3 group at our institute). My thanks go also to my beloved family for their heartfelt support.

Contents

List of Figures

List of Tables

Chapter 1

Introduction

1.1 Motivation

In conventional superconductors, at the microscopic level, the superconducting (SC) phase is comprised of two key elements. With decreasing temperature, a weak attractive interaction occuring between normal electrons with opposite momenta and spins results in a zero-spin pairs. These pairs are called Cooper pairs and they condense into a macroscopic coherent quantum-state where the quantum mechanical phase is characterized by a single electronic wave-function. A superconductor is thus identified by two of its most characteristic properties, zero resistance and perfect diamagnetism. Two types of excitations can devastate the ground state of superconductivity; quasiparticle excitations generated by Cooper pairs breaking and phase fluctuations which may annihilate the globally coherent phase. The energy scale associated with the first class of excitations is the well-known temperature-dependent superconducting energy gap, $\Delta(T)$, whereas the class associated with the second one is the temperature-dependent superfluid stiffness, $J_s(T)$. The latter is the energy scale that is a measure of the resilience of a superconductor to phase fluctuations. The superfluid stiffness depends on the superfluid density (n_s) and the effective mass of the super-carriers (m^*) as, $J_s \sim n_s/m^*$ [1–4]. In thin films, both the disorder and low dimensionality contribute the enhanced role of phase fluctuations and thus J_s becomes modified [5].

According to the Bardeen-Cooper-Schrieffer (BSC) theory [6, 7], in most conventional superconductors [2], thermal phase fluctuations are negligible what implies that the energy scale $J_s(T) \gg \Delta(T)$ (Cooper pairing energy scale) and the superconducting-to-normal phase transition temperature, T_c, is almost governed by Δ. This explains the stunning success of the BCS theory and therefore the role of J_s has received much less attention. In contrary, Ginzburg-Landau (GL) theory [8] accounts for the phase fluctuations so that $J_s \geq \Delta$, and hence phase fluctuations cause a distortion of the SC phase in the vicinity of the T_c. On the other hand, J_s can also be smaller than Δ, due to increased inhomogeneity effects and the reduction of n_s through strong disorder scattering. Thus, phase fluctuations may significantly contribute to destroying superconductivity although the pairing gap may remain finite [2, 9, 10]. For example, this occurs in strongly-correlated unconventional superconductors, such as organics superconductors or underdoped high-T_c cuprates [11, 12]. Moreover, several recent studies have reported on the role of phase fluctuations in thin films of many strongly disordered conventional s-wave superconductors. For instance, studies on NbN, TiN, InO_x, a-MoGe, $SrTiO_3/LaAlO_3$ interfacial superconductors [13–17] reveal the emergence of pseudogap (PG) state; it is characterized by a gap in electronic spectrum which persist at temperature well above T_c, which accordingly suggests the existence of Cooper pairs, but without global superconductivity. Furthermore, a multitude of information has been generated on these systems using techniques such as low temperature scanning tunneling spectroscopy (STS) [14, 18, 19], scanning squid microscopy [20] as well as low and high-frequency electrodynamic response measurements [15, 16, 21, 22] which enable a direct access to the phase of the order parameter. All these phenomena have renewed the interest about the exploring of the nature of superconductivity, particularly in a two dimensional (2D) or quasi-2D superconductor (also in 3D superconductors with strong disorder).

In 2D or quasi-2D superconductors, there exist bound excitations at low temperature in the form of spin vortices and anti-vortices (with opposite vorticity) which become dissociated by the increase of temperature. Thermal dissociation of bound vortices marks the occurrence of a second order phase transition what leads to a finite resistance below the mean field-transition temperature. The transition, known under the name Berezenskii-kosterlitz-Thoulsess (BKT) for researchers who first studied it, has been theoretically described within the 2D-XY model. It is of distinct topological nature; it does not show any sponteneously broken symmetry upon transition from quasi-long range ordered state to a more disordered state [23–26]. Ever since its discovery, the BKT transition has been the key tool for the understanding of a wide spectrum of physical phenomena, especially in the condensed matter physics: superfluid [1] and superconducting (SC) transitions in 2D systems belong in fact to the same class of universality. In 2016, Kosterlitz, Thouless and (Haldane) received the Nobel Prize for the BKT phase transition and other studies on the topological phases of condensed matter.

For typical BKT scenario, on increasing temperature, the 2D superfluid stiffness $J_s(T)$ abruptly drops to zero at the characteristic BKT transition temperature (T_{BKT}) [25], while the cooper pairing could survive up to the mean field temperature. Additional complicacies in real superconductors such as disorder or intrinsic inhomogeneity effects tend to smear the sharp features characterizing the transition. This complicates the interpretation of experimental results. In the dirty limit of superconductivity, when the mean free path becomes smaller than the BCS-coherence length ($l \ll \xi_0$), inhomogeneity plays an increasing role and phase fluctuations become important. This leads to a modification [17, 27–29] in the ratio of vortex-core energy (μ) to superfluid stiffness J_s predicted within the 2D XY model originally investigated by Kosterlitz and Thouless [23]. The relevance of μ for the BKT transition has been addressed in numerous studies, ranging from the case of layered high-T_c superconductors[30–32] to the superconducting interfaces in artificial heterostructures [33–36]. Furthermore, for granular thin films, the BKT transition has been addressed in the context of Josephson junction arrays (JJA) in which superconducting grains are connected through Josephson proximity coupling effect [37–39]. The properties of JJA vary depending on the junction type [40] which may range from diffusive SNS (superconductor-normal metal-superconductor) junction to tunneling SIS (superconductor-insulator-superconductor) junction; in addition the properties are affected by junction dimensions [38, 41, 42]. Arrays with negligible charging effects in which the Josephson coupling energy, E_J is much larger than the Coloumb energy E_c, $E_J \gg E_c$ ($E_c \sim 1/C$; C is the junction capacitance), are regarded as classical arrays, often discussed within the RCSJ (Resistively and capacitively shunted junctions) model [37, 40, 43]. Moreover, the crossover from the classical behavior of JJA into quantum tunneling behavior has been discussed in [43, 44] where the mechanism of escape to a finite voltage state with increasing measuring current changes from thermal activation (TA) into macroscopic quantum tunneling (MQT). It is not that obvious from the literature how such transport mechanisms, as temperature decreases, may affect the BKT transition. Overall, BKT transition in a wide variety of systems, and from different perspectives is under persistent research, mainly due to the various possible effects of inhomogeneity on the quasi-long range coherence characterizing the transition.

Another appealing subject is vortex matter in the mixed superconducting phase (where magnetic field-induced vortices form) of type-II superconductors. It provides a ground for testing of new concepts and theories, such as various ordered phases and phase transitions between them, with the primary example of melting of ordered Abrikosov vortex lattice in clean superconductors, or melting of vortex glass (VG) in SC systems with quenched disorder [45]. On the other hand, understanding of the effect of vortex pinning by defects on vortex thermodynamics in the presence of flowing currents is very much important for applications, because flowing currents and thermal fluctuations contribute to creep-type vortex motion, which annhiliates dissipation-free transport [46].

In the past, both the VG phase and flux creep phenomenon have been intensively studied, mostly in high T_c superconductors where thermal fluctuations play a significant role. Evaluation of these matters is also important in case of conventional SC ultrathin films, which are frequently employed in nanoscale devices. Of particular interest is the role of intrinsic disorder, which developes in the films with decreasing thickness, giving rise to fragmented superconductivity[13, 47–49]. Some of the SC properties in thin films with enhanced inhomogeneity have been evaluated, e.g., the BKT transition in zero magnetic field, recently discussed in [33, 36, 50], or thermal fluctuations (creep) effects in the presence of magnetic field [51]. However, while studying the VG transition and critical currents for variety of conventional SC films have been reported [27, 52–56], studing the evolution of these properties with the decrease of film thickness is scarce. Few exceptions include studying VG transition in 100 nm Nb film and Nb/Cu superlattices[52], and 3D-to-2D dimensional crossover of creep in Nb films with different thickness (all thicknesses above 100 nm), studied by magnetization measurements [51].

In general, depending on the strength of vortex-defect interactions, two different pinning schemes are considered, weak collective pinning, caused by many atomic size, weak point defects, which collectively give rise to an average pinning force [57], and strong pinning, by relatively sparse but large defects, of the size comparable to the coherence length ξ [58, 59]. As ξ exceeds atomic-size point defects, like in our highly disordered films, strong pinning is expected to dominate. Indeed, as it we will demonstrated in Chapter 4 (Results and discussion), the measured data of the current-voltage (I-V) characteristics of our films follow so-called excess current characteristics [60, 61], which is a feature commonly observed in materials with strong pinning scenario [62–66].

Another classification of pinning depends on the mechanism of vortex-defect interaction, which may originate either from the spatial variations of the SC transition temperature, T_c (δT_c pinning), or from variation in the mean free path l of carriers, caused by scattering near lattice defects (δl pinning); these mechanisms result in distinct behaviors of the critical current density, J_c, with the change of temperature, magnetic field, or film thickness [67, 68]. Therefore, the commonly followed method in order to differentiate between these mechanisms is to evaluate the dependence of J_c on magnetic field, temperature, and film thickness. In our study we go beyond these types of evaluations. We use recently developed strong pinning theory in the presence of thermal fluctuations [69–71] in order to extract most important creep parameter, activation energy for vortex pinning, U_c. We will show that the analysis of dependence of the U_c on temperature and magnetic field provides more insights into vortex dynamics in comparison with the simple analysis of the J_c.

Eventually, the formalisms of the theories addressing the BKT transition, VG transition, vortex pinning and thermal creep phenomena have their own assumptions based on which the phase transitions in superconductors are predicted. Usually, these distinct phenomena are investigated separately, which in some cases may limit the comprehensive understanding of the experimental findings to a certain degree. In literature, many studies have reported on the BKT transition in 2D systems, some of which have recently focused on the role of inhomogeneity on observing the transition. On the other hand, plenty of studies have reported on the VG transition in various systems (both 2D and 3D systems), ranging from high T_c superconductors [72–74] to low T_c superconductors [53, 75–77], using the well-known scaling laws of the standard VG theory. A broad range of discrepancy among experimental studies have been found, explicitly, in the form of clear deviations from the theoretical predictions for the dynamic and static exponents characterizing the critical behavior of VG phase transition [72, 75, 78–80]. Moreover, the problem on VG transition is very often treated separately from theories on vortex pinning and creep phenomena. This in turns raises concerns about the prevailing understanding of the vortex behavior, particularly, in systems with additional complicacies compared to clean ones. In general, the vortex behavior is governed by the intrinsic nature of the dirty superconductor what calls for a more precise evaluation of the problem.

1.2 Subject and aim of this thesis

The main goal of this thesis is to provide a systematic experimental study of the vortex physics in Nb ultrathin films of various thickness, and comparing experimental results with existing theories. Some of ultrathin Nb films have been studied by my co-researchers before, and growing disorder with decreasing film thickness has been documented by structural studies, leading eventually to structural transition, from polycrystalline films with thickness of larger than about 4 nm to purely amorphous structure for thickness below about 3.3 nm [81]. In the films of this study, the disorder generated by this structural transformation is responsible for the vortex behavior in zero and finite external magnetic fields.

The main motivation of this work was the wish to gain a better and a more comprehensive understanding of the aforementioned vortex phenomena. Therefore, we set a goal to observe evolution of the BKT transition, VG phase and vortex pinning properties with decreasing film thickness and enhancing disorder. For studying an individual film with specific thickness (d), the nature of structural disorder is constant whereas the external influential parameters in experiment such as the current (I), the magnetic field (B), and the temperature (T) are variable. Therefore, we will present broad-range investigations on the role of phase fluctuations triggered by film disorder through measuring the resistance and the current-voltage characteristics in zero and external magnetic fields. In the vicinity of the superconducting transition temperature, T_c, our study elucidates the impact of inhomogeneity in the superconducting state ($T < T_c$) on the vortex critical behavior. For thinner samples of this study, we extend our zero-field investigations down to milliKelvin range since inhomogeneity plays an increasing role and careful understanding is required. Overall, our study can be very useful for further understanding the vortex behavior in the SC state of many systems, ranging from weakly to strongly disordered superconductors.

1.3 Thesis Organization

In Chapter II, a brief review on the history of superconductivity is presented followed by discussions that focus on most fundamental phenomenological theories of superconductivity, namely, the London model and the Ginzburg–Landau theory. We discuss concepts and basic equations which are crucial for understanding of the basis of superconductivity and helps differentiate between type-I and type –II superconductivity. Finally, we briefly go over the Bardeen–Cooper–Schrieffer (BCS) theory (the first microscopic theory of superconductivity), followed by introducing the Josephson Effect.

Chapter 3 explains the fundamentals of theories describing different phase transitions that are ubiquitous in superconducting systems. We first start with introducing the BKT phase transition, theorized within the 2D-XY model. Besides, we discuss the most common ways of approaching the transition in experiment. Of particular interest in our study is the temperature-dependence of resistance, $R(T)$, and the nonlinearity of the current-voltage characteristics (IVCs). We also refer to inhomogenity effects on smearing the sharp features of BKT transition; we leave further discussions on the inhomogeneity role for Chapter 5. Then we move our discussion to another distinct class of phase transitions; the vortex glass (VG) phase transition which is widely investigated in type-II superconductor in the presence of external magnetic field. We review the well-known standard scaling laws of vortex glass theory which may be directly compared to experimentally measured data for transport properties; the $R(T)$ and the IVCs data. Finally, we review the existing theories on vortex pinning and thermal creep phenomena; we discuss the general frameworks of weak collective pinning (WCP) theory and strong pinning (SP) theory but with a more extended discussion on recent strong pinning theory (2019), a key theory in our study. The theory allows for a direct evaluation of vortex pinning problem using one of the major parameters, the critical current density (J_c) which can be obtained from the IVCs measurements.

Chapter 4 explains the experimental equipment and procedure used. It starts with demonstrating the technique used for the synthesis of Nb films of this study; the magnetron sputtering technique. Then we briefly discuss the concepts of the X-rays reflectivity technique which has been used for the crystallographic characterization and thickness measurements of the films. Furthermore, we briefly discuss the procedure of sample preparation for transport measurements. Then, we turn discussion to the experimental setup and technical procedures used for the transport properties measurements; the most were performed using a Quantum Design physical property measurement system (PPMS). We first provide an overview of the measurements setup (PPMS) and its major integrated components. We continue discussion with focusing on the AC Transport Measurement System (ACT) option which supports various types of electrical transport current measurements; four-terminal AC current resistance, $R(T)$, measurements and those which require using a DC current such as for the current-voltage (I-V) characteristics measurements which are of central importance in our study. Resistance measurements are used to study the BKT phase transition (in abscence of magnetic fields) and VG phase transition (in external magnetic fields) in our films. I-V measurements are used to further study the BKT transition, VG transition and to extend evaluation of vortex phenomena using vortex pinning theories. We close this chapter with discussing the dilution refrigerator technique, necessary to achieve the milliKelvin -range measurements for thinner films of this study.

In chapter 5, we systematically show our experimental results and discuss the main findings of this study. Firstly, we start with the results obtained in zero magnetic fields on the observation of BKT transition in our Nb thin films. A specific attention is paid for discussing the effect of structural disorder present in the films and induced-inhomogeneity in the superconducting state which smears out the sharp features of the transition. As film thickness decreases, inhomogeneity effects become more interesting what led us to study the temperature dependence of the critical current (over a wide range of temperature) and address the most relevant theories of superconductivity. Secondly, we continue with discussing the results obtained from the data analysis for VG transition in perpendicularly applied magnetic fields by means of the standard scaling laws according to VG theory. Finally, we extend our discussion in magnetic field to the results describing the nature of vortex pinning and thermal excitations in the presence of disorder in our films. Disorder in our films is believed to pin vortices and the critical "de-pinning" current density, obtained from the IVC measurements, plays a major role in defining the nature and the strength of vortex pinning. More insights into vortex physics are provided through exploring the dependence of the energy scale describing vortex thermal creep, U_c, on the temperature, magnetic field and film thickness using recent strong pinning theory. According to theory, U_c is one of the main parameters essential to understanding the nature of vortex pinning and dynamic behavior.

At the end of this thesis, in Chapter 6, the main findings of the measurements conducted for this thesis are summarized and conclusions, which have been drawn from the experimental evidence, are reviewed. Future studies to clarify some points or to further enhance the understanding of various vortex phenomena are proposed.

Chapter 2

Theories of Superconductivity

In this chapter we review briefly the history of superconductivity (Sec.2.1) followed by discussions on the basic phenomenological theories of superconductivity. In particular, we discuss the London equations (Sec.2.2.1) and Ginzburg-Landau (G-L) theory (Sec.2.2.2); we highlight the difference between the two types (Type–I and type-II) of superconductivity. Finally, we close the chapter with brief discussion on the basis of the BCS theory of superconductivity (Sec. 2.3), followed with discussing the Josephson effect (Sec.2.4) and the Jospehson junction behavior in a circuit (The RCSJ model).

2.1 Brief historical overview

Discovery of superconductivity began with the Dutch physicist Heike Kamerlingh Onnes in 1911 who measured the temperature dependence of the dc resistance of mercury (Hg) sample. It has been found that when the mercury is cooled below a critical temperature, T_c= 4.2 K (the boiling point of liquid helium) the resistance decays rapidly to zero ohms indicating the occurrence of phase transition (Fig. 2.1). He named the new phenomenon "superconductivity", indicating an infinite conductivity (i.e., zero resistivity) of the mercury sample.

In 1913, superconductivity was discovered in lead at T_c =7.2 K. In 1930, superconductivity was discovered in bulk niobium (Nb) which showed the highest T_c (=9.2 K) among all pure metals.

In 1933, W. Meissner and R. Ochsenfeld discovered another unique property of superconductors, the perfect diamagnetism (see Fig. 2.2). This is the second property of the superconductivity (below T_c) which point to the complete exclusion of weak magnetic field (B) from the interior of a superconductor via introducing surface currents. Further strengthening of the magnetic field may result in destroying the superconducting state. In most elemental superconductors the state of perfect diamagnetism is destroyed rapidly at a magnetic field termed as the critical field, B_c. With $B > B_c$ which the superconductor turns into normal conductor.

One year later, a simple two-fluid model was proposed by brothers F. and L. London for the sake of interpreting the Meissner Effect. They have also introduced

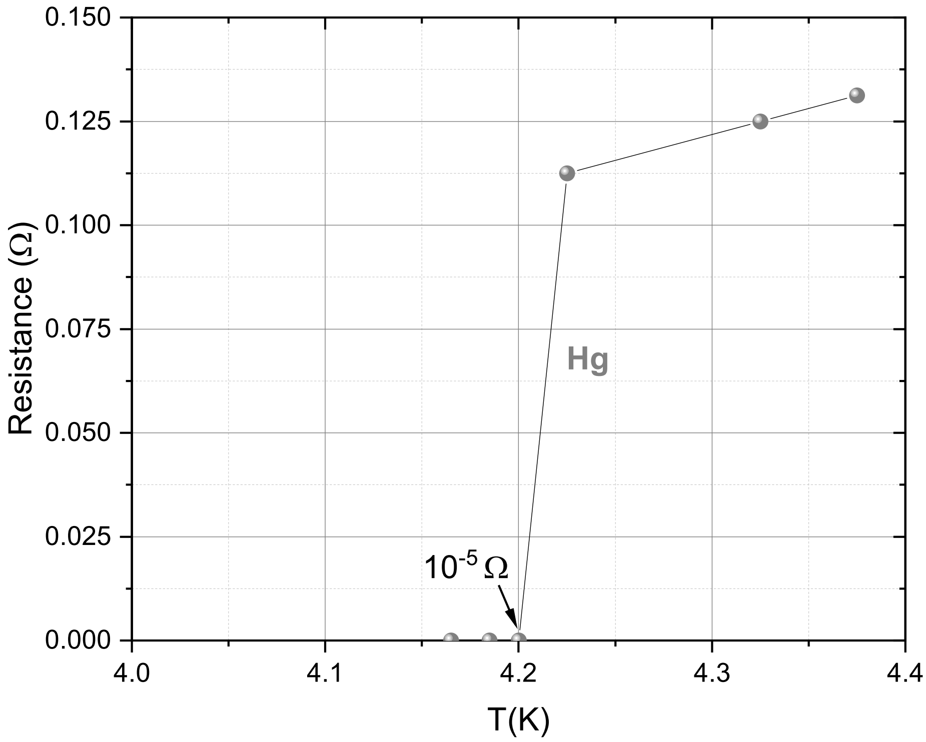

FIGURE 2.1: Resistance versus temperature for mercury demonstrating normal-to-SC phase transition (schematic figure drawn based on Ref.[82]

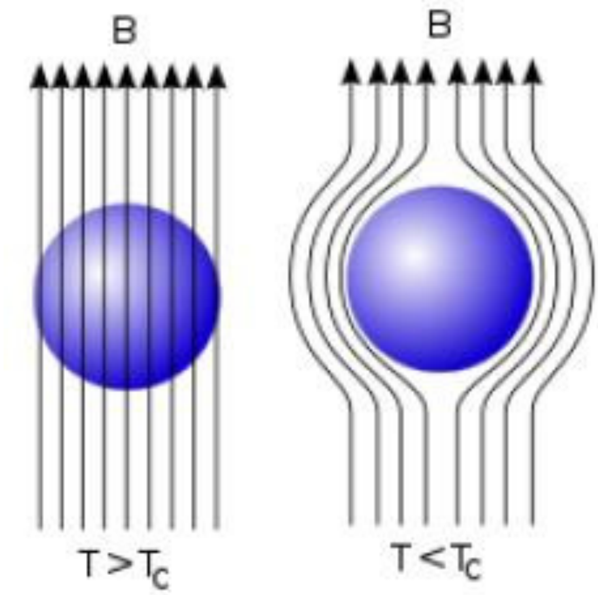

FIGURE 2.2: The Meissner Effect: Expulsion of weak magnetic field ($B < B_c$) from inside the superconductor ($T < T_c$) (the figure is adapted from Wikipedia).

the penetration length; the characteristic length of penetration of the static magnetic flux into a superconductor.

In 1950, V. Ginzburg and L. Landau proposed a novel phenomenological theory (often called “macroscopic theory”) of superconductivity near T_c through which further insights into the distinctive properties of superconductors can be obtained. A profound success of this theory was predicting the existence of type-II superconductors. In 1957, A. Abrikosov studied the behavior of superconducting materials in an external magnetic field and showed that one can differentiate between two types (termed as type-I and type-II) of superconductivity (discussed in Sec.2.2.2).

In the same year, J. Bardeen, L. Cooper and R. Schrieffer proposed a complete microscopic theory of superconductivity for which they won the Nobel Prize in Physics in 1972. The theory is well-known as the BCS theory; the basis of this fundamental theory is the interaction of a kinematic gas of random conduction electrons with phonons in the crystal lattice at low temperatures below the T_c. In normal phase, electrons repel each other by the Coulomb force, but in the superconducting phase a net attraction occurs between two quasiparticles "electrons", leading eventually to the formation of bound pairs (Cooper pairs). Each pair is made of two coupled electrons of anti-parallel spins and momenta and the pairs obey Bose-Einstein statistics. Subsequently, the “condensed phase” of highly correlated “super-electrons” pairs is established. In the condense phase, Cooper pairs move together in a single coherent motion so that a local perturbation,e.g., an impurity in the crystal lattice, cannot scatter an individual pair. The BCS theory still lays the foundations for up-to-date understanding of superconductivity in conventional superconductors. Furthermore, BCS theory , to some extent, may extend and pave the way for the continuous investigation in high-T_c superconductors such as curpate oxides. A further discussion on the BCS theory can be found in Sec. 2.3.

In 1962, a fascinating quantum tunneling effects known as Josephson effects were postulated by B. Josephson. He predicted that these effects occur when a supercurrent tunnels through a weak contact (very thin non-superconducting layer) connecting superconducting electrodes (banks). His predictions were confirmed within a year. The Josephson effect-based technology lays the ground for the promising superconducting electronics.

In 1986, G. Bednorz and K. Alex Muller discovered superconductivity in LaBaCuO near 30 K. The year after, a research group coordinated by K. Wu and Paul Chu discovered superconductivity in $Y_1Ba_2Cu_3O_7$ ceramics with high T_c=92 K. This has garnered a great attention as it was the very first time to find an evidence for superconductivity with T_c exceeding 77 K, the liquid nitrogen boiling temperature. Liquid nitrogen is much more economic than liquid helium for cooling purposes. Only a year after, Bi- and Tl-curpate oxides were discovered with T_c=110 K and 125 K respectively. Subsequently, many research groups have announced their discoveries of even higher T_c -superconductors. Up to this time, high T_c superconductors are under persistent research due to their practical importance. This also holds true for many low T_c superconductors. Here, we point out that it is never that fermions (electrons) alone contribute to superconductivity in the condensate but bosons may also play an siginificant role leading to unconventional superconductivity such as in high T_c-curpates and other complex systems [83–86].

2.2 Phenomenological theories of Superconductivity

2.2.1 London's Equations

Brothers F. and L. London [87] interpreted the Meissner effect on the basis of a two-fluid model in attempts to modify the usual thermodynamic equations; in particular, modifying Ohm's law with preserving Maxwell's equations. They introduced a relationship between magnetic field B, electric field E and current density j in superconductors. Their postulate was that in an applied electric field, Cooper pairs experience no scattering by either impurities or phonons, and therefore they do not contribute to the sample resistance, so the equation of motion for an electron in an electric field has the form:

$$m_e \partial \nu / \partial t = -eE \tag{2.1}$$

and the super-current density

$$j = e n_s \nu \tag{2.2}$$

Here, e is the elementary charge of the electron ($\approx 1.6X10^{-19}C$), m_e is the electron mass, ν is an electron velocity, and n_s is superconducting electron density. By taking the time derivative of j and substituting it in Eq.2.1, one can get to the first equation proposed by London brothers:

$$\partial j / \partial t = n_s e^2 E / m_e \tag{2.3}$$

This equation tells that the supercurrent in a superconductor varies with time due to acceleration of electrons by the electric field. The magnitude of the electric field E is given by:

$$E = \mu_0 \lambda_L^2 \partial j / \partial t \tag{2.4}$$

where

$$\lambda_L = \sqrt{m_e / \mu_0 n_s e^2} \tag{2.5}$$

is the London magnetic penetration depth.

λ_L is the distance in which the magnetic field penetrates into a superconductor and becomes e^{-1} times that of the magnetic field at the surface of the superconductor. λ_L is one of the two fundamental lengths (the other is the coherence length), which define the behavior of a superconductor in the presence of an external magnetic field. λ_L is a significant, meaningful parameter due to its coupling to the superfluid density. In order to have completely excluded magnetic field from the interior of a superconductor ($B = 0$), this requires surface current that induces a magnetic field with magnitude and opposing direction so the penetrating field is cancelled out.

From the Maxwell–Faraday version of Faraday's law of induction $\bigtriangledown \times E = -\partial B/\partial t$ and by taking the curl of Eq. 2.4, one obtains:

$$\partial(m_e/n_s e^2 \bigtriangledown \times j + B)/\partial t = 0 \tag{2.6}$$

This implies that quantity in parenthesis must be a constant value. The London model assumes that the constant value is equal to zero. Therefore,

$$\bigtriangledown \times j = -n_s e^2 B/m_e \tag{2.7}$$

which gives the second equation of London brothers:

$$B = -\mu_0 \lambda_L^2 \bigtriangledown \times j \tag{2.8}$$

Here, μ_0 is a constant, the magnetic permeability of vacuum. Eq. 2.8 can be manipulated by Maxwell's equation $\bigtriangledown \times B = \mu_0 j$ in the form

$$\bigtriangledown^2 B = B/\lambda_L^2 \tag{2.9}$$

Assuming B varies just along the y direction, the solution to Eq. 2.9 will be $B = B_0 e^{-y/\lambda_L}$. This explains the Meissner effect, as it tells that the magnetic field does not penetrate into the superconductor except for a distance in the order of λ_L. It shows that the magnitude of the magnetic flux decays exponentially towards the core of the superconductor. In addition, it shows that the nature of decay depends on the carrier density (n_s) according to Eq. 2.5. λ_L is usually of the order of 10^{-6} m and is depending on the temperature near T_c. Experiment reveals that the temperature-dependence of λ_L close to T_c takes the following form:

$$\lambda_L^{-1}(T) \approx \lambda_L^{-1}(T = 0)\sqrt{1 - t^4} \tag{2.10}$$

where t denotes the reduced temperature T/T_c.

2.2.2 The Ginzburg-Landau (G-L)Theory

The formulas proposed by London model assume that the superfluid density (n_s) is constant in the superconductor. However, it does not link the number of super-electrons with the external parameters such as the applied magnetic field, current or temperature. As a consequence, this limits the applicability of the model to real superconductors where n_s is a function that strictly depends on the spatial variation. In 1950, Ginzburg and Landau proposed an a novel theory which provides a more generalized framework that enables studying superconductivity near T_c where n_s can be linked to external parameters.

Landau has described the second order phase transition in a system from the spontaneous magnetization state (ferromagnetic phase) below the transition critical temperature (T_{CM}) to a vanishing magnetization state (paramagnetic phase) above T_{CM}. The magnetization is continuous at the transition and is small close to T_{CM}; the thermodynamics of such a system is described by expanding the Helmholtz free energy in powers of magnetization M close to the critical transition point.

Landau considered that any second order phase transition may be described in a similar fashion by replacing the magnetization, M, by another quantity (termed as the order parameter) which becomes finite below the transition temperature and zero above it. This has motivated Ginzburg and Landau to develop a simple and exact description of the superconducting properties near T_c.

The novelty of Ginzburg-Landaue (G-L) theory [8] compared to the London theory resides in introducing a complex scalar wave function called the order parameter $\psi(r) = |\psi(r)|e^{i\Phi(r)}$, whose square modulus is the density $n_s(r)$; r is a spatial variable.

$$|\psi(\overrightarrow{r})|^2 = n_s(\overrightarrow{r}) \tag{2.11}$$

$\Phi(r)$ is the phase, related to the supercurrent flowing through the superconductor below T_c. The order parameter $\psi(r)$ is finite below T_c and becomes zero above T_c (i.e., in the normal phase).

According to the (G-L) theory, the Helmholtz free energy is expanded in powers of $\psi(r)$ in the following form:

$$F_s(r,T) = F_n(r,T) + \alpha|\psi|^2 + (\beta/2)|\psi|^4 + (1/m^*)|(-i\hbar\bigtriangledown - e^*A)\psi|^2 + \mu_0 h^2/2 \tag{2.12}$$

where,

$$F_s(T) = \int_V F_s(r,T)d^3r \tag{2.13}$$

The superscripts s and n in Eq. 2.12 denotes the superconducting and the normal phase correspondingly, $\hbar$ is the Planck constant ($h/2\pi$) and V is the volume of the sample. m^* and e^* denotes the mass ($m^* = 2m_e$; e is the electron charge) and the electric charge ($e^* = 2e$) of paired super-electrons. $A(r)$ is the magnetic vector-potential at a point r and h is the microscopic local field at the same point ($\mu_0 h = \bigtriangledown \times A$). The Helmholtz energy is the integral over the total volume of the material, of energy density that is spatially dependent. The temperature dependence is assumed to enter through the phenomenological parameter $\alpha = a(T - T_c)$; it is negative for $T < T_c$ whereas β is a positive constant that is T-independent. The meaning of the phenomenolgical parameters α and β stems from their relation to the measurable characteristic parameters of the superconductor as will be demonstrated below through the consequences of the G-L equations.

For the determination of the order parameter $\psi(r)$ and the vector potential $A(r)$, the Helmholtz energy has to be minimized with respect to ψ and A. The minimization leads to the so-called (G-L) equations given by:

$$\alpha\psi + \beta|\psi|^2\psi + (1/2m_e)(i\hbar \bigtriangledown - e^* A)^2\psi = 0 \tag{2.14}$$

and

$$j = \bigtriangledown \times h = (e/m_e)[\psi(-i\hbar \bigtriangledown - e^* A)\psi + c.c.] \tag{2.15}$$

The above two equations are inherently connected what implies solving them simultaneously. In the following, we summarize the main consequences which arise form solving the G-L equations:

1. The thermodynamic critical field (H_c) relates to the parameters α and β through the simple form:

$$\mu_0 H_c^2 = \alpha^2/\beta \tag{2.16}$$

2. The coherence length, which indicates the distance over which the order parameter $\psi(r)$ varies when a perturbation is introduced at some point, is proportional to the absolute value of α according to:

$$\alpha(T) = \hbar/2m_e\xi^2(T) \tag{2.17}$$

Hence, $\xi(T)$ diverges as temperature approaches T_c as α approaches zero. ξ is temperature-dependent according to the empirical form:

$$\xi(T)/\xi(0) = 1/\sqrt{1 - T/T_c} \tag{2.18}$$

Here, $\xi(0) = 0.855\sqrt{\xi_0 l}$ where ξ_0 denotes the BCS cohrence length l denotes mean free path.

3. The magnetic penetration depth λ_L is linked to the magnetic field H via the form:

$$\mu_0 \bigtriangledown \times H = -(1/\lambda_L^2)A \tag{2.19}$$

In the dirty limit [88], the T-dependence of ξ is given by Eq.2.18 whereas the length λ is given by

$$\lambda(T) = \lambda(0)/\sqrt{1-(T/T_c)} \tag{2.20}$$

where $\lambda(0) = \lambda_L(0)\sqrt{\xi_0/2.66l}$.

λ_L can vary from several thousands of angstroms down to less than a hundred. The T-dependence of λ_L follows the empirical form given by Eq. 2.10. $\xi(0)$ and $\lambda(0)$ are just the coeffiecients for the T-dependence of $\xi(T)$ and $\lambda(T)$ for $T \leq T_c$.

Lastly, the ratio between the two charcteristic lengths, the penetration depth and the coherence length, defines the G-L parameter for a superconductor

$$\kappa = \lambda/\xi \tag{2.21}$$

Thanks to the fact that both lengths, i.e., ξ and λ diverge at T_c, the parameter κ is independent on temperature when close to T_c. Superconductors are categorized depending on whether the value of κ is greater or smaller than $1/\sqrt{2}$. Superconductors fulfilling the condition $\kappa < (>)1/\sqrt{2}$ are termed as superconductors of the type-I (type-II).

Type-I Superconductors versus Type-II Superconductors

The primary difference between type-I and type-II superconductors resides in the way they react to an externally applied magnetic field as illustrated below in Fig. 2.3(b). In type-I superconductor there exists only one critical magnetic field B_c (the thermodynamic critical field). The superconductor entirely ejects magnetic flux lines from its interior for $B < B_c$. The perfect diamagnetism of the superconductor becomes completely annihilated when the applied magnetic field reaches the thermodynamic critical field B_c. The temperature dependence of the critical field B_c in type-I superconductors is nearly parabolic, and follows the form:

$$B_c(T) = B_c(0)[1-(T/T_c)^2] \tag{2.22}$$

where $B_c(0)$ is the extrapolated value of B_c at $T = 0$. In the MKS units system one can write

$$B = \mu_0(H + M) \tag{2.23}$$

Here M is the magnetization.

The Meissner effect implies that B is zero. This corresponds to $M = -H$. When $B > B_c$, the superconductor enters the normal phase with zero magnetization ($M = 0$). The meaning of the negative sign in the superconducting phase is that the conductor becomes a perfect diamagnet with the magnetic flux expelled from its inside by surface screening currents. Moreover, the superconducting phase can be also annihilated by passing an excessive current which produces a magnetic field at the surface of strength equal or greater than B_c. This limits the maximum affordable current to maintain superconductivity and therefore it is an important issue from the application point of view.

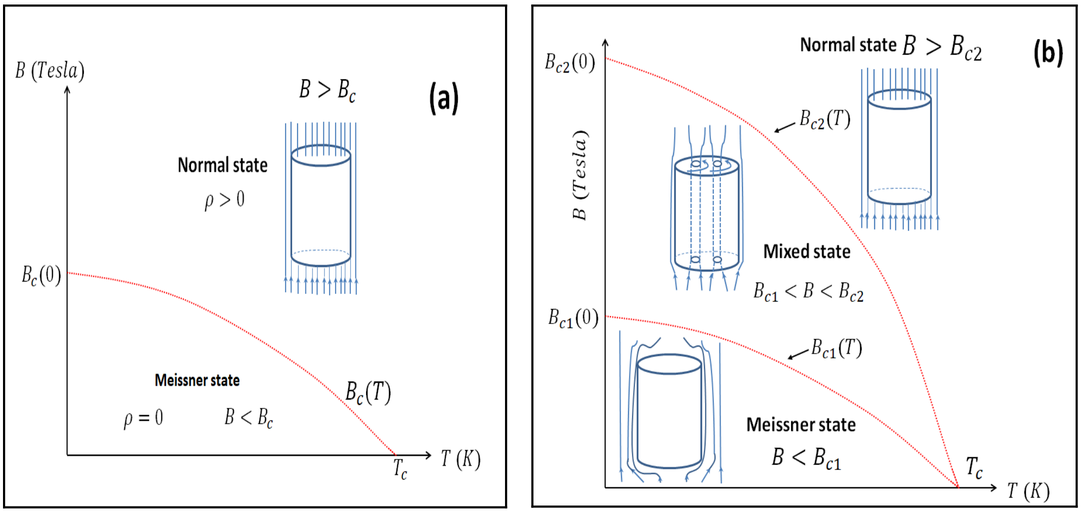

FIGURE 2.3: Phase diagrams of type I (a) and type II (b) superconductor. In(b), the magnetic flux penetration in the mixed state is shown in the interval ($B_{c1} < B < B_{c2}$). Below B_{c1}, the type-II superconductor behaves similar to a type-I superconductor (whose temperature dependence of the critical field B_c is given by Eq. 2.23 and shown in (a)). As B exceeds B_{c2}, the superconducting phase is replaced by the normal phase.

On the other hand, in type-II superconductor an additional mixed phase (Fig. 2.3(b)) exists between Meissner phase and the normal phase. The mixed phase in type-II superconductors is identified by two distinct critical fields. The first (lower) critical field, B_{c1}, is the minimum field value above which the magnetic field begins to partially enter the superconductor. The second (upper) critical field, B_{c2}, marks the complete second order-phase transition of the superconductor to the normal phase. In the mixed phase, $B_{c1} < B < B_{c2}$, the magnetic field enters the material in the form of flux tubes each of which carries a quantized magnetic flux

$$\phi_0 = h/2e = 2.07 \times 10^{-15} Tm^2 \tag{2.24}$$

where h is the Planck constant and e is the charge of the electron.

The flux tubes can be portrayed as vortices of flowing current circulating magnetic field lines threading the superconductor from the side of the boundary with vacuum (insulator). At the equilibrium, vortices adopt a particular configuration in order to minimize the free energy of the specimen. In conventional type-II superconductors, the diameter of a vortex is typically of the order $\approx 20 - 200nm$. It consists of a normal conducting core within which the magnetic field is large and the local superconductivity is supressed, surrounded by a superconducting region where a persistent ring supercurrent flows and thus the field is screened by this current from the remaining portion of the superconductor. The vortex has a radius λ_L whereas the vortex core is of radius ξ (typically of the order $\sim 10nm$). Every vortex is an axial symmetric formation. In the vortex core, the order parameter is zero on the vortex axis and tends to reach its equilibrium value at the distance ξ from the axis. As magnetic field increases from B_{c1} toward B_{c2}, the density of vortices increases and the inter-vortex distance is field-dependent. The electromagnetic region of the vortex suffers deformation when the vortices are of high density due to strong magnetic field or when vortices penetrate to a sample of small size ($<< \lambda_L$).

Within the G-L theory framework, the following relations between the critical magnetic fields, the magnetic penetration depth and the coherence length were obtained [88]

$$B_c = \phi_0/\sqrt{8}\pi\xi\lambda_L \tag{2.25}$$

$$B_{c1} = \phi_0/4\pi\lambda_L^2(ln(\kappa + 0.5)) \tag{2.26}$$

$$B_{c2} = \phi_0/2\pi\xi^2 = \sqrt{2}\kappa B_c \tag{2.27}$$

In Eq. 2.25, B_c is the critical field for Type-I superconductors. Note that the B_{c1} for type II-superconductors in Eq. 2.26 depends on κ logarithmically, so for low T_c superconductors which are characterized by very small values of κ ,the term κ may be dropped. On the other hand, the high- T_c superconductors are said to be strong type-II superconductors since they possess a tremendous κ value. As an example, the YBCO superconductor has $\kappa \approx 100$ because the coherence length is extremely short, on the order of 1-2 nm and λ_L is typically 150 nm. In general, in high-T_c superconductors, B_{c2} is very high (of the order of 100 Tesla) while B_{c1} is very small (of the order of 10-2 Tesla). From practical point of view, all technologically interesting materials such as Nb compounds, Chevrel phases (B_{c2} can reach up to 60 Tesla) or high-T_c oxides (B_{c2} can reach up to 150 Tesla) are type-II superconductors. The reason is that the generation of magnetic vortices keeps the cost in magnetic energy less than the gain in condensation energy. As a result, the overall free energy of the mixed superconducting phase remains, thermodynamically, more preferred than the normal phase even up to high fields.

Niobium (Nb) metal, the material from which thin films of the present study are made, belongs to the group of transition metals of the periodic table. It has body-centered cubic (bcc) crystal structure with lattice constant $a = 3.3$Å. Bulk Nb has superconducting phase transition temperature $T_c \approx 9.2$ K. Nb is one of the most important materials for superconducting technologies, from superconducting radio frequency (SRF)cavities [89], to superconducting circuits for sensitive sensing [90] and quantum informatics [91]. Plenty of experimental studies reported on measurements on different Nb samples, from almost perfect single crystals to disordered films [91–99].

The value of κ for Nb is found to be dependent on sample quality, for instance, $\kappa \sim 1$ is obtained for high purity bulk Nb samples [92], whereas for ultrathin single crystalline Nb film (thickness =20Å), κ value of about 14.5 is obtained [100]. We point out that the identification of the type of superconductivity was analyzed in detail in [101, 102]. It was argued that one has to use the ratio of the upper and thermodynamic critical fields, H_{c2}/H_c, instead of a conventional criterion based on the Ginzburg-Landau parameter, $\kappa = \lambda/\xi$. When $(H_{c2}/H_c) > 1$, the material can be then identified as a type-II superconductor where magnetic vortices form. Moreover, it was shown that the κ based criterion coincides with the thermodynamic criterion (H_{c2}/H_c) only at the superconducting phase transition temperature, T_c, and not even in the very close vicinity below T_c. In anisotropic superconductors, the same material can be type-I in one direction of the magnetic field, and type-II in another [101].

In the clean case, Nb is shown to behave as type-I superconductor. In [103] it is shown that for pure Nb, (H_{c2}/H_c) is far below 1 and therefore the sample is regarded as type-I superconductor. This is also supported by high-quality magneto-optical imaging of Nb single crystals with RRR = 500 which show unambiguously a clear structure of the intermediate state (with Meissner and normal domains) replacing the mixed state of Abrikosov vortices [99]. However, in the dirty limit, situation looks difficult since Nb is close to the crossover boundary and can be easily shifted into the type-II side by non-magnetic disorder via increasing the London penetration depth, λ, and shortening the coherence length, ξ. Magnetic disorder, on the other hand, pushes a superconductor into the reverse direction. Nb is susceptible to the disorder with its experimental residual resistance ratio $RRR \equiv R(300K)/R(T_c)$, ranging between 3 and 90000 [92, 95].

2.2.3 The BCS Theory

The BCS "microscopic" theory is the most successful theory of superconductivity, presented in 1957 by J. Bardeen, L. Cooper, and J. R. Schrieffer [6, 7, 104]. Before this theory comes out, H. Fröhlich had some speculations on the role of the electron-phonon interaction[105]; it has been suggested that this interaction might cause the formation of the superconducting state obtained experimentally and reported by Maxwell [106] and by Reynolds, Serin, Wright, and Nesbitt [107]. In accord with these experiments the superconducting critical temperature show dependence on the isotopic mass of atoms of the superconductors, the well-known isotope effect since isotopic effect is related to the mass of the vibrating ions that generate phonon. The experiments thus provided evidence on the relation between the electron-phonon interaction and superconductivity.

The superior success of the BCS theory is ascribed to the fact that it gives a proper explanation on the isotope effect, the zero resistance, the Meissner effect, and others in conventional superconductors. The basic idea of the BCS theory is that, at sufficiently low temperatures, conduction electrons beneath the Fermi surface may be scattered out of the Fermi surface by phonons; two scattered normal electrons may form a bound electron pair provided that the sufficiently weak interaction between them is attractive so that it overcomes the repulsive Coulomb force between the two electrons. To understand the electron-phonon interaction qualitatively, one may imagine an electron in a conductor moving through a lattice comprised of positive core ions as illustrated below in Fig. 2.4.

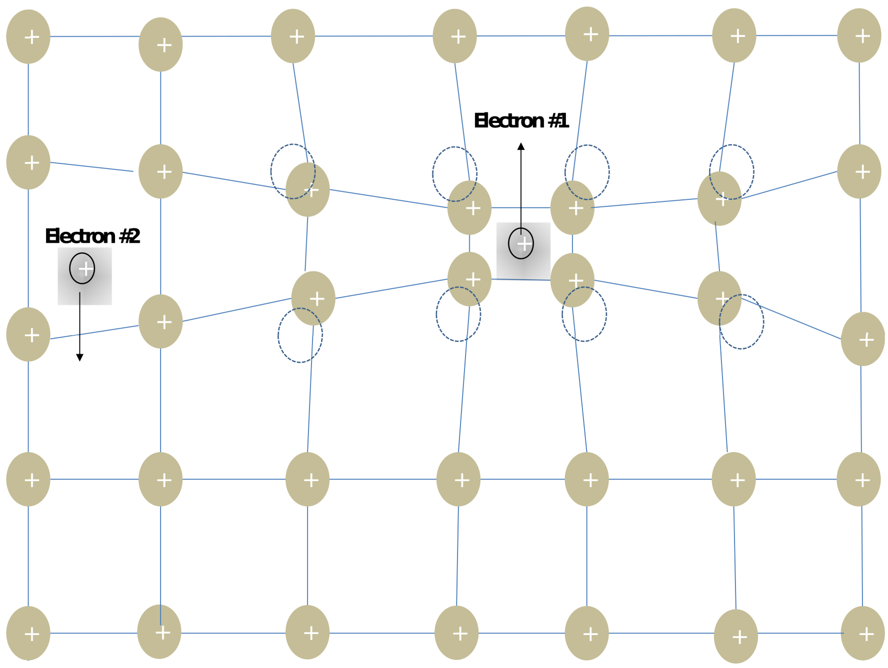

FIGURE 2.4: A schematic demonstration of the attractive interaction between two electrons through the lattice deformation. In the reciprocal space (k-space), the two electrons forming a bound electrons pair have equal and opposite spins and momenta, i.e, $(\overrightarrow{k}\uparrow, -\overrightarrow{k}\downarrow)$.

The electron will attract nearby positively charged ions what causes spatial deformation in the lattice. This in turn causes another electron, with opposite spin, to approach the region of higher positive charge density. Hence, the two electrons start to correlate to each other and form a bound pair which is called the Cooper pair. Cooper pair therefore has a single state with equal and zero total momentum (opposite momenta of the two electrons), opposite spins of the electrons and carries twice the charge of free electron ($2e$). Unlike normal electrons (fermions), Cooper pairs are boson-like particles that obey the Bose-Einstein statistics as they are all allowed to occupy the same state.

Since there is plenty of Cooper pairs in a superconductor, these pairs overlap strongly and collectively form a highly condensate state in such a way that all the pairs are described by a single coherent wave function. In a Cooper pair, the average distance between two electrons is of the order of the BCS coherence length (in the clean limit), given by [88]

$$\xi_0 = \hbar \nu_F / \pi \Delta(0) \tag{2.28}$$

where ν_F is Fermi velocity and $\Delta(0)$ is the zero Kelvins-superconducting gap. ξ_0 of a conventional s-wave superconductor is of the order a few hundred nanometers.

In the condensate state, the breaking of a Cooper pair will modulate the energy of the whole condensate (not just a single electron, or a single pair). Therefore, the energy needed to break an individual pair is related to the energy required to break all pairs. Moreover, the condensate as a whole, or any individual pair will not be influenced by the kicks (which are small at adequately low temperatures) from oscillating atoms in the conductor. Thus the paired electrons remain intact and collectively resist all kicks and supercurrent flow will experience no resistance. Thus, the collective behavior resulting from the condensation of Cooper pairs is a crucial requirement for superconductivity.

For type-I superconductors, in which the interaction between electrons is sufficiently weak (the so-called weak-coupling case), the BCS theory provides (independent of the details of the interaction) a relationship [88] between the zero-temperature gap, $\triangle(T = 0K)$, and the critical transition temperature, T_c,

$$2 \triangle (T = 0)/k_B T_c = 3.52 \tag{2.29}$$

which is a universal constant for type-I superconductors (i.e., independent of material). The value will be higher for superconductors with stronger electron-phonon coupling like the type-II superconductor. In the vicinity of T_c the relation asymptotes to [88]:

$$\triangle(T \longrightarrow T_c) \approx 3.06 k_B T_c \sqrt{1 - (T/T_c)} \tag{2.30}$$

Moreover, the BCS theory relates the T_c to the electron-phonon coupling potential V and the Debye cutoff energy E_D in the form [6],

$$k_B T_c = 1.134 E_D e^{-1/N(0)V} \tag{2.31}$$

where $N(0)$ is the density of states for the electrons at the Fermi level.

In case of niobium (Nb) as type-II superconductor, values between 3.6 and 3.8 for $2\triangle(T=0)/k_BT_c$ are obtained from experiments ([108], Ref.[121] in [109]), which are more close to the BCS value obtained for Sn and In, than to 4.3 and 4.6 obtained for the strong coupling superconductor Pb and Hg, respectively, obtained from tunneling experiments (Ref.[121] in [109]). This shows that these Nb may behave as intermediate coupling superconductor. In case of thin Nb films various ratios of $2\triangle(T=0)/k_BT_c$ have been reported. For example, in [110] in case of films with thickness between 20Å to 228Å ratio of 3.6 has been found, suggesting that Nb films behave as weak coupling superconductors. On the other hand, in[111] it has been shown that the ratio increase from 3.8 to 5 when thickness of the films decreases from 50Å down to 9Å. It is very likely that the film quality (determined by film deposition conditions) affects the results.

Although the BCS theory gave satisfactory interpretation of the superconductivity phenomenon in most conducting materials, researchers (such as Bernd T. Matthias) searching for novel superconducting compounds rarely relied on the "formal" theory. For type-II superconductors, however, some of the experimental results do not strictly obey the BCS theory predictions. Many theoretical derivations have been carried out in order to have an extension of the BCS theory. For example, [112] and [113] developed on theories of strong-coupling superconductors, (Type II superconductors).

2.2.4 The Josephson Effect

The Josephson Effect (JE) is one of the most appealing macroscopic quantum phenomena of superconductivity. The JE occurs when a super-current (I_s) tunnels through a thin layer forming a barrier between two relatively bulky superconducting electrodes (banks); collectively forming the so-called Josephson junction (JJ). In this subsection, we focus more on discussing some basic properties of weak links. The term "weak link" refers to the junction connecting the SC electrodes so that the critical current transporting through it is much less than that in the electrodes. As an example, Fig. 2.5 displays a simple sketch of the superconducting-insulating-superconducting (SIS) structure where the JE can take place. As shown, two SC electrodes are linked together via thin insulating layer of size L.

The current I_s, which flows through such SIS structure depends on the voltage (V) across the electrodes and on the phase difference (φ) of the order parameter between the electrodes given by

$$\varphi = \chi_2 - \chi_1 \tag{2.32}$$

where χ_2 and χ_1 are the phases of the superconducting order parameter $\triangle$ in the electrode.

$$\triangle_{1,2} = |\triangle_{1,2}| exp(i\chi_{1,2}) \tag{2.33}$$

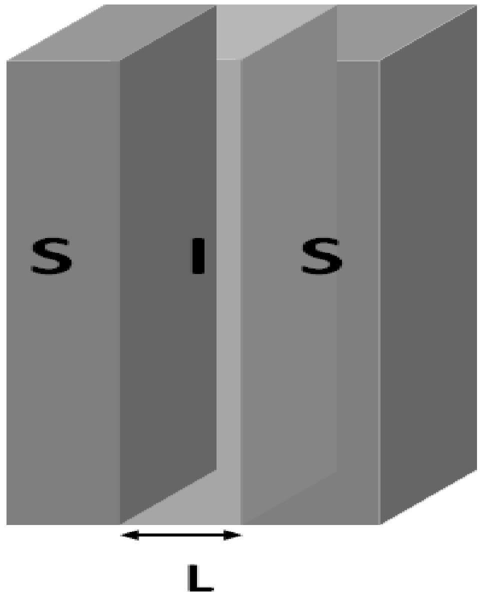

FIGURE 2.5: SIS structure forming a Josephson junction.

The "classical" current-phase relationship for a Josephson junction takes the simple form [114]:

$$I_s = I_c sin(\varphi) \tag{2.34}$$

where I_c is the critical current, or the amplitude of the supercurrent, I_s.

The phase (φ) is related to the voltage (V) across the electrodes by

$$d\varphi/dt = (2e/\hbar)V \tag{2.35}$$

Eqs.[2.34] and [2.35] qualitatively describe the JE but they show important differences. Eq. 2.34 is an approximate one, and various sorts of deviations of supercurrent from this dependence may occur in a SC weak link (of any type), for example with increasing the dimensions of the link. Furthermore, the constant current I_c in Eq. 2.34 is dependent on the material and geometry of the weak link, the material of the superconducting electrode, temperature and other factors. When the dimensions of weak links are sufficiently small, the JE takes place; a single-valued and 2π -periodic relationship exists between the supercurrent I_s and the phase difference (φ) of the electrodes. Moreover, in the superconductor the opposite currents are equivalent. Therefore, $I_s(-\varphi) = -I_s(\varphi)$,i.e., the function $I_s(\varphi)$ is symmetrical with respect to the origin[115]. As the dimensions of the weak link further increases, this relationship tends to deviate gradually from the Josephson behavior; mathematically, this appears in the form of corrections to the simple classical form given by Eq. 2.34. The deviation also depends on the material of the link (i.e., superconductor, normal metal, etc.).

On the other hand, Eq.[2.35] is derived on the basis of quantum mechanics. That Eq. 2.35 holds true to a high precision (however, it is not is universally applicable) has been demonstrated in experiment (see, for instance, [90, 116, 117]). In general, all the electrodynamic phenomena occurring at the Josephson links are divided into two main categories: stationary (dc) effects and nonstationary (ac) effects. This depends on whether the variables, including the phase difference (φ), vary with time or not.

In (dc) process, φ remains constant and hence there is no associated voltage across the JJ as revealed by Eq. 2.35. However, according to, a nonzero supercurrent (I_s) can flow through the junction. This current ($I = I_s$) is constant in time and less than the maximum, critical current (I_c), i.e,

$$V = 0, \varphi = const, I = I_s(\varphi), \mid I \mid \leq I_c \tag{2.36}$$

In nonstationary (ac) case, φ varies with time what leads to Josephson oscillations if the voltage at the contact has a dc component $\overline{V}$. As follows immediately from Eq.2.35, in this case the phase (φ) contains a component that increases linearly with time at a rate

$$w = d\overline{\varphi}/dT = (2e/\hbar)\overline{V}, f = w/2\pi = (2e/h)\overline{V} \tag{2.37}$$

Therefore, the supercurrent oscillates in time at a frequency w that is directly proportional to $\overline{V}$. In ac events, current components in addition to the supercurrent I_s possibly can flow through the junction. In addition, the I_s may depend not only on the instantaneous value of the phase φ but on the former variations of φ as well. This makes the ac case to be far more sophisticated than the dc case. In resistively and capacitively shunted Josephson junctions in a circuit [44], Josephson oscillations occurs since the externally applied current is distributed among the circuit components (the resistor, the Josephson junction and the capacitor, connected in parallel).

For the dc ($V = 0$) case, the $I_s(\varphi)$ relationship is permanently sinusoidal for tunnel junctions. For two identical SC electrodes ($\Delta_1 = \Delta_2 = \Delta$), I_c takes the form [114, 118]:

$$I_c = V_c/R_N, V_c = (\pi/2)(\Delta(T)/e)tanh(\Delta(T)/2k_BT) \tag{2.38}$$

where $\Delta(T)$ is the modulus of the superconducting gap Δ in electrodes made of the same material, and R_N is the normal state-resistance of the junction. The product I_cR_N is called the characteristic voltage of the junction V_c; it does not depend explicititly on any parameters of the barrier, and it is determined just by the temperature (T) and critical temperature (T_c) of the electrode through a function $\Delta(T) = k_BTf(T/T_c)$ [41, 110, 111, 119].

As derived from the microscopic theory [7], the quantity $\Delta(T)$ is almost constant at low temperatures:

At $T \lesssim 0.6T_c$

$$\Delta(T) \approx \Delta(0)\{1 - (2\pi k_B T/\Delta(0))exp[-\Delta(0)/k_B T]\}. \tag{2.39}$$

$\Delta(0) = (\pi/\gamma)k_B T_c$, $\gamma = 1.78$.

and falls off rapidly as

$$\Delta(T)^2 \sim k_B^2 T_c(T_c - T), at(T_c - T) \lesssim 0.1T_c \tag{2.40}$$

The maximum characteristic voltage (V_c) of the junction in the limit ($T \longrightarrow 0$) is determined by the critical temperature T_c, $max(V_c)[\mu V] \approx 240T_c[K]$.

Near T_c, the characteristic voltage behaves linealy with temperature with universal slope

$$V_c = (\pi/4)(\Delta^2/eK_B T) = \alpha(T_c - T), \alpha \approx 635\mu V/K \tag{2.41}$$

An example for the experimental deviation from Eq. 2.41 can be found in [37]. In Fig. 2.5, L denotes the basic geometrical length of the weak link separating the two electrodes. Simply, it is the dimension of the weak link in the direction of current flow. However; it is an effective length $L_{eff} \geq L$ rather than the length L that plays a pivotal role in the nonlinear electrodynamics across the link which in some way (depending strongly on the type of weak link) extends to a certain degree into the adjacent sections of the electrodes. L_{eff} is the distance within which the nonlinear effects in a weak link are localized. Weak links may be classified depending on the comparison of L_{eff} to the characteristic lengths of the link material, the coherence length ξ (within the link) and the mean free path l being most important among them [114]. Weak links are said to be short links if $L_{eff} \ll \xi$ and long links if $L_{eff} \geq \xi$. The response of the links to the tunneling current is very dependent on the mean free path l. For weak but dirty links l (the mean free path)$\ll \xi_0$ (the BCS coherence length) and both $|\Delta|$ and the supercurrent density (j_s) undergo significant changes.

Finally, we would like to point out that various theories on tunneling phenomena have been formulated on the basis of specific assumptions. For instance, in 1963 a complete theory was formulated for the dc case ($V = 0$) [120], and in 1966 a theory for arbitrary $V(t)$ was completed [121, 122]. In fact, these theories do not account for the effects of the thickness of the energy barriers compared to all other characteristic lengths in the superconductor (including the mean free path, l). Moreover, the theories postulate that critical current I_c through the junction is much weaker than the critical current of the electrodes what eliminates disturbances in the electrodes caused by the tunneling current. On the other hand, subsequent theories took into account the effect of finite geometric length L on the tunneling properties. For instance, in 1975 Kulik and Owelyanchuk proposed a theory (known as KO-1 theory, [123]) for the dirty case [$l \ll L \ll \xi$ (the coherence link of the weak link material)] and subsequently in 1977 they introduced another theory (KO-2 theory [124] for the clean case ($l \ll L, \xi$)). For the temperature dependence of the critical current for small weak links, these two theories meet with the AB (Ambegaokar-Baratoff) theory [120] on the approach to T_c whereas they show deviations at lower temperatures [114]. Finally, we point out that, recently, the dependence of global superconductivity on inter-island coupling in arrays of long diffusive SNS junctions (the junction is long provided that the junction length $L >$ the SC coherence length ξ_{SC}) has been studied by S. Eley et al [42]. In the study, in view of quasi-classical theory [125], it has been argued that the proximity coupling between islands does not depend on the SC gap energy, Δ, of the islands, but instead it depends on a different energy scale termed as Thouless energy, E_{Th} (inversely proportional to the time for the diffusion of electrons between islands in fractal superconductor; $E_{Th} \ll \Delta$). The quasi-classical theory tells that E_{Th} is the main energy scale that limits the critical current flowing through the junction length in an array of long or intermediate-length junctions. In chapter 5, we will address more the work of Eley et al and we will exploit it to interpret our experimental findings for thinner films which behave as arrays of Josephson junctions, however, in complicated manner.

2.2.5 Josephson junction in a circuit: The RCSJ model

For a Josephson junction in a circuit it is often suitable to use the RCSJ (Resistively and Capacitively Shunted Junction) model; the equivalent circuit of the junction is shown in Fig. 2.6

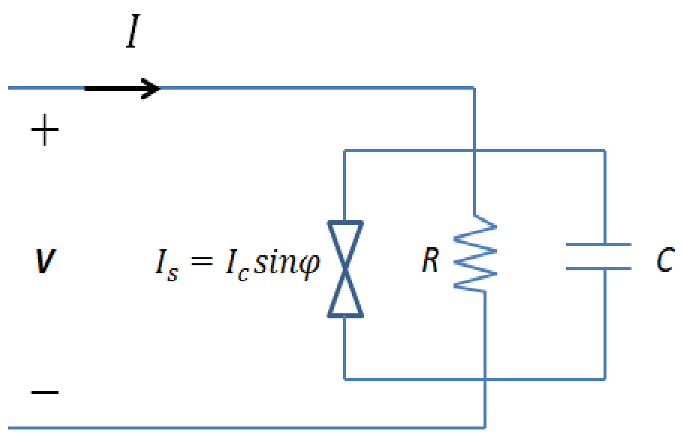

FIGURE 2.6: Resistively and capacitively shunted Josephson junction.

The externally applied current in the circuit is a superposition of three terms: the Josephson current, given by Eq. 2.34]; $I_s = I_c sin(\varphi)$, the shunt current given by $I = V/R(V)$; where R is a shunt non-linear resistance (it represents junction losses) which depends on V, and the capacitor with capacitance C which can transport a current; $I_{cap} = CdV/dt$. Consequently, the externally applied bias current I is given by

$$I = I_c sin(\varphi) + V/R + C\frac{dV}{dt} \tag{2.42}$$

By using $V = \hbar/2ed\varphi/dt$, we obtain a differential equation for the behavior of the Josephson phase difference:

$$I = \frac{\hbar C}{2e}\frac{d^2\varphi}{dt^2} + \frac{\hbar}{2eR}\frac{d\varphi}{dt} + I_c sin(\varphi) \tag{2.43}$$

By normalizing time t to $1/w_{J0}$ where $w_{J0} = \sqrt{2eI_C/\hbar C}$ is zero-bias plasma frequency, we get

$$\frac{d^2\varphi}{dt^2} + \alpha\varphi + sin(\varphi) = \eta \tag{2.44}$$

In Eq.2.44, $\eta = I/I_c$ is the normalized bias current and $\alpha = w_{J0}/(2eI_cR)$ is the normalized loss coefficient. A Josephson junction with phase φ has stored energy $(\hbar I_c)/2e(1 - cos(\varphi))$; the pre-factor $\hbar I_c/2e$ is the Josephson energy, E_J.

In order to quantitatively discuss the solution of Eq. 2.44 the pendulum analog is used as a simple way to visualize many properties of the junction[44]. Moreover, the electrodynamics of Josephson junctions may be equivalent to the motion of a fictitious particle whose coordinate is φ, moving in a tilted washboard potential [43, 44, 126], shown schematically in Fig.2.7.

The barrier height for the washboard potential, in Fig.2.7, is current-dependent according to [44]

$$\Delta U = 2E_J(\sqrt{1-\eta^2} - \eta\cos^{-1}\eta) \tag{2.45}$$

With applying a suitable, constant bias current, the particle can surpass the barrier height and escape from the well. For thermal activation (TA) mechanism of escape [43], the escaping rate of the particle is given by

$$\tau(t) = f\exp(-\Delta U/k_B T) \tag{2.46}$$

where f is the attempt frequency. The shallower the well, the sooner the escape occurs. The difference among three different particle-escape mechanisms, the TA, the macrosscopic quntum tunneling (MQT) and the phase diffusion is illustrated schematically in the inset of Fig.2(a) in Ref.[43].

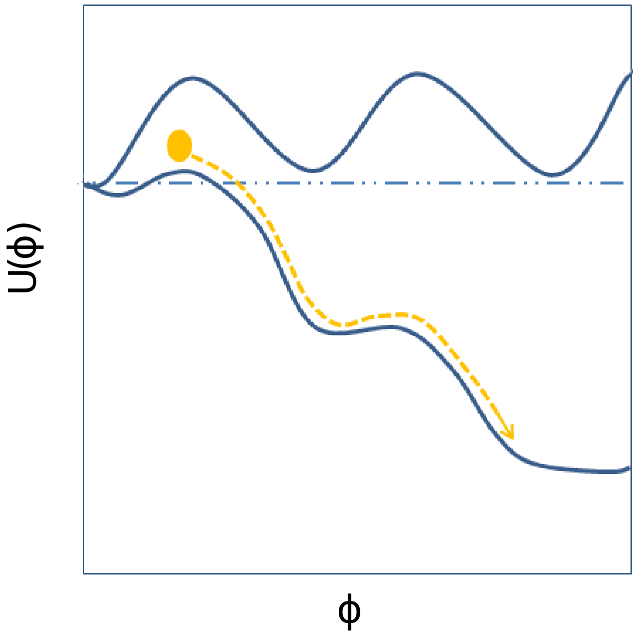

FIGURE 2.7: Variation of washboard potential with φ for zero bias case (upper) and non-zero bias case (lower). This schematic drawing is based on the figure presented in Ref.[44].

Chapter 3

Transport properties and phase transitions

In this chapter, we address distinct vortex dynamics phenomena associated with the superconducting-to-normal phase transition in both, the absence and in the presence of external magnetic fields. We mainly discuss the theoretical basis describing these physical phenomena. In particular, in zero magnetic fields, the topological phase transition in 2D systems occurs upon thermal dissociation of tightly bound spin vortices on the basis of the 2D-XY model. This will be addressed in Sec.3.1. On the other hand, in the mixed phase of type-II superconductor, the magnetic (Abrikosov) vortices may freeze at low temperatures into vortex glass, and melting of this glass phase upon warming can be verified using the scaling laws of the standard VG theory. This will be addressed in Sec.3.2. Finally, the nature of vortex pinning and thermal excitations responsible for vortex dynamics in the superconducting state may be studied with the aid of existing pinning theories such as collective pinning theory and strong pinning theory (Sec.3.3).

3.1 Berezinskii-Kosterlitz-Thouless phase transition

3.1.1 BKT transition description in 2D XY model-simple argument

2D XY models have been developed by physicists V. L. Berezinskii in 1971/2 [127], and J. M. Kosterlitz D. J Thouless in 1972/3 [23], and proposed to explain topological excitations in 2D neutral superfluids. Such models describe any 2D Coulomb gas [24]; Coulomb gas points to a coulomb attraction force between vortices (V) and antivortices (AV) in the phase below T_{BKT} so that V and AV spread over the 2D planes as a Coulomb gas (a nice diagram of BKT phase transition can be found in [128]). According to the descriptions, a thermodynamic instability should happen in which V-AV pairs, frozen at low temperatures, spontaneously dissociate into free vortices at a characteristic phase transition temperature, T_{BKT}. D. R. Nelson and Kosterlitz [**nelson**] have introduced a universal relation between the T_{BKT} and the superfluid sheet density. Subsequently, several experiments on superfluid-helium films confirming this prediction have been reported [26, 129].

The existence of the predicted V-AV dissociation instability in helium films is mainly because the interaction energy between vortex pairs varies logarithmically with the separation between them. J. Pearl [130] showed that thin superconducting films have analogous scenario wherein vortex pairs in the films have a logarithmic interaction energy out to the a characteristic length $\lambda_\perp = \lambda^2/d$ beyond which the interactions energy falls off as $1/r$. λ and d are the bulk penetration depth and the thickness of the film respectively. $\lambda_\perp$ plays the role of magnetic penetration depth for fields perpendicular to the film, and as it increases the diamagnetism in the SC state becomes of less significance. As $\lambda_\perp$ increases, vortices in the Superconducting films behave just like those in helium films.

In [23], Kosterlitz and Thouless have pointed out that the finite range logarithmic vortex interaction in a SC film annihilates the precise analogy to helium films. In [1], Beasley et al have shown that in that for SC systems with large $\lambda_\perp$, the situation can resemble the one for helium film with some existing discrepancies. They have shown that, as a result of the finite energy of a free vortex in a SC film, in equilibrium, a few free vortices will stay in the SC film below T_{BKT} along with the bound vortices-antivortices portrayed by Kosterlitz and Thouless. This in turn results in a broadening in the BKT transition which is also predicted to be the case in reality for helium films with finite energy of a free vortex. Above T_{BKT}, a plasma of free vortices exists and the situation in SC and helium films is quite similar provided that the means separation between vortices is less than $\lambda_\perp$. In the dirty limit, a simple formula has been derived which links the broadening in the resistive transition to the ratio of T_{BKT} to the mean-field temperature T_{MF} in high sheet resistance thin films. In the formula, the T_{MF} can be found from theories on fluctuation-enhanced conductivity above T_{MF}. After, B.I. Halperin and Nelson [131] proposed another formula for the temperature dependence of resistance from which one can extract both T_{MF} and $T_{BKT}(< T_{MF})$ which will be addressed in Sec. 3.1.2.

In statistical physics, the XY model is proposed as a classical spin model comprised of 2D normalized vectors (spins) equally distant from one another, forming a square spin lattice of spacing a. A short-range interaction exists between spins in the lattice so that only the next neighbor spins (i.e., four surrounding spins) interact with each other. The interaction prefers to align neighboring spins (the coupling constant $J > 0$) along one direction. The XY model-Hamiltonian H is given by [27]

$$\beta H = -J \sum_{\langle ij \rangle} \overrightarrow{S_i}\,\overrightarrow{S_j} = -J \sum_{\langle ij \rangle} \cos(\theta_i - \theta_j) \tag{3.1}$$

Where S_i, the spin on the site i in the lattice, is a classical planar vector. $< ij >$ denotes summation over all nearst neighubor sites and the θ_i denotes the angle of the spin on the i^{th} site relative to an arbitrary polar direction in the 2D vector space. β is the inverse of $k_B T$; k_B is Boltzmann constant and T is the temperature. Fig. 5.2 portrays a typical spin configuration for high temperature T and for T=0.

The BKT transition within the XY model is illustrated through spin configurations generated in the form of vortices, regarded as topological defects in the system. The vortices interact via a logarithmic interaction potential $\sim ln(r)$. As temperature T increases, thermal fluctuations become stronger and this increases the

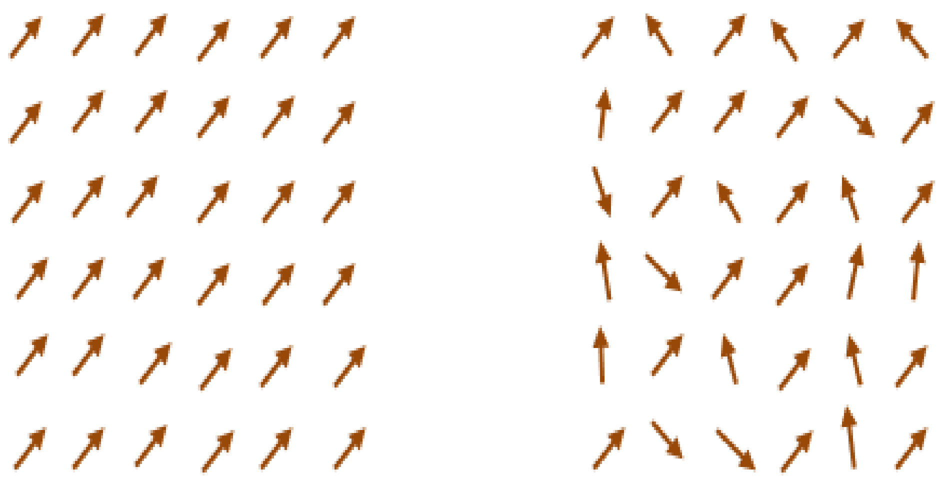

FIGURE 3.1: Typical spins configuration at high T (right) and at $T = 0$ (left).

FIGURE 3.2: Spin configuration for a vortex and an antivortex.

average spatial separation (r) between the bound vortices (with opposite vorticity) until they eventually unbind at the transition characteristic temperature (T_{BKT}). Fig. 5.3 portrays spin configurations of a vortex and anti-vortex which form pairs below T_{BKT}. At T_{BKT}, a second order phase transition takes place; the continuous rotational symmetry of the spin system (i.e. turning all spins at their position) is not broken spontaneously and the transition is not forbidden according to the Mermin-Wagner theorem [132]. According to the theorem, in low dimensions $(D \leq 2)$ with short range interaction, thermal fluctuations are powerful to inhibit spontaneous ordering as explained generally by the theorem, and in particular for the 2D O(N) models [133].

The transition occurs from a quasi-long range ordered phase and to a more disordered phase due to the annihilation (by low energy thermal excitations) of the large-scale coherence. A salient feature of the phase transition is the spatial decay of order parameter fluctuations, which alters from a power law behavior at all low temperatures to an exponential behavior above T_{BKT}. The turnover in behavior is a sign that the freed vortices disorder the system effectively to the extent that a breakdown of the low T approximation $(T < T_{BKT})$ for the correlation function occurs.

In a simple argument, unbinding of vortical pairs associated with a BKT transition in the XY model can be understood by considering the interplay between the self-energy of an isolated vortex and the entropy. The self energy for a single isolated vortex is given by [134]:

$$E_{vor} = \pi J ln(L/a) \tag{3.2}$$

where L is the system size (in lattice units) that is suffecient to accommodate a single free vortex and a is the spin lattice spacing. The entropy associated to a vortex creation is given by

$$S = ln(L^2/a^2) = 2ln(L/a) \tag{3.3}$$

which therefore can be calculated by considering the multiplicity of such spin configuration,(L^2/a^2), the vortex can be placed in the square lattice of dimensions L^2 (i.e, the vortex can be centered at every lattice side).

A system at thermal equilibrium tends to be in states with low free Helmholtz energy (F). The free energy associated to the creation of a vortex is given by

$$F = E_{vor} - TS = (\pi J - 2T)ln(L/a) = \pi J ln(L/a) - 2Tln(L/a) \tag{3.4}$$

Therefore the free energy diverges logarithmically in a system with infinite size $(L \to \infty)$.

Since the phase of the system depends on the the dominant term, Eq. 3.4 implies that the phase transition temperature is given by

$$T_{BKT} = (\pi/2)J \tag{3.5}$$

For $T < T_{BKT}$, $F \to \infty$ as $L \to \infty$. Therefore, free energy will be a minimum in the absence of free vortex. However, for $T > T_{BKT}$, $F \to \ -\infty$ as $L \to \infty$ what implies that system favors to decrease its free energy by creating a free vortex (via vortex unbinding). Indeed, for $T < T_{BKT}$, a high vorticity density exists (i.e., many V and AV are present in the system) and therefore, at $T > T_{BKT}$, a tremendous (an infinite) number of free vortices can proliferate in the system due to destroyed quasi long-range order of bound vortices available below T_{BKT}.

The constant J is a measure of the energy required to turn neighboring spins against each other at constant T. So, J is expected to decrease if the vortex system is already more disordered and turning spins against each other should cost less energy. The T_{BKT} changes depending on stiffness of the phase of the SC system, but the ratio $J(T_{BKT})/T_{BKT} = 2/\pi$ is a constant (i.e., system independent).

3.1.2 BKT transition and transport measurements

BKT transition occurs at the characteristics temperature T_{BKT}, below the mean-field transition temperature T_{MF}, $T_{BKT} < T_{MF}$. The thermal unbinding of V-AV pairs generates a finite resistance in the temperature range $T_{BKT} < T < T_{MF}$. In some cases, however, the signature of true BKT transition may be elusive, primarily for the following two reasons. Firstly, superconductors, at finite temperature, can have not only the vortical excitations described by the XY model but also quasi-particle excitations which limit the observation of various characteristics of the transition to a narrow temperature range between T_{BKT} and T_{MF}. Secondly, screening effects due to charged supercurrents [1] modify the logarithmic interaction between vortices needed to observe BKT physics. As a result, the nature of BKT transition in a superconductor becomes somewhat dissimilar to the expected behavior within the XY model.

In experiment, the BKT transition is commonly studied through the following two distinct approaches: when approaching the transition from above ($T > T_{BKT}$); the transition may be recognized from the Ginzburg-Landau (GL) SC fluctuations, encoded in temperature–dependent quantities, such as resistance or magnetization. In this approach, the information on BKT transition is carried by the temperature dependence of SC correlation length, $\xi(T)$, which diverges exponentially (Eq. 3.9) at T_{BKT}, in contrast to the power-law dependence expected by GL theory [17, 135]. A standard method used for the observation of BKT transition via determining its characteristic temperature, T_{BKT}, is to fit the experimental resistance data, $R(T)$, to the interpolation formula proposed by Halperin and Nelson (H-N) [33, 131]:

$$R(T)/R_N = 1/(1 + (\Delta\sigma(T)/\sigma_N)) = 1/(1 + (\xi(T)/\xi_0)^2) \tag{3.6}$$

where

$$\xi(T)/\xi_0 = A \sinh(b/\sqrt{t}) \tag{3.7}$$

Here, ξ_0 is the zero-temperature correlation length, $t = (T - T_{BKT})/T_{BKT}$ and A is a constant of order of two. R_N is the normal state resistance determined from experimental data. b is the most relevant parameter, determining the shape of resistance curve above T_{BKT} and it is related to vortex-core energy (μ) and connected to the interval $t_{MF} = (T_{MF} - T_{BKT})/T_{BKT}$ [17, 33]. According to theory, b is proportional to the energy scales μ and J_s (the 2D superfluid stiffness) and t_{MF} according to [17]:

$$b \sim (4/\pi^2)(\mu/J_s)\sqrt{t_{MF}} \tag{3.8}$$

For large μ, b becomes negligibly small characterizing T_{BKT} very close to T_{MF}. μ is usually estimated as the loss in condenstaion energy within a vortex core (of the size of the order of ξ_0) [136]. Fitting the experimentally measured $R(T)$ data and obtaining the value of b allows for determining the ratio μ/J_s. The XY model predicts that $\mu/J_s = 4.9$ [137].

On the approach to T_{BKT} from above ($T > T_{BKT}$), the SC correlation length, $\xi(T)$, behaves as [27]

$$\xi(T) \sim \exp(const./(T - T_{BKT})^{1/2}) \tag{3.9}$$

Or equivalently, the $R(T)$ data may be fitted to the exponential dependence form:

$$R(T) \approx const * R_N \exp[-2(c(T_{MF} - T_{BKT})/(T - T_{BKT}))] \tag{3.10}$$

Here, T_{MF}, T_{BKT}, and dimensionless constants *const* and c are adjustable (sample-dependent) fitting parameters.

In light of the BKT theory, The interval $(T_{MF} - T_{BKT})$ is governed by the proliferation of V-AV pairs which are thermally dissociated in the vicinity of the T_{BKT}. This difference between the transition temperatures becomes more pronounced in case of disordered systems thanks to the broadening of the normal-to-superconducting phase transition associated with a modified crossover from BKT-to-GL SC fluctuations.

An alternative way commonly used for the T_{BKT} extraction, which relays on the fact that in the vicinity of the T_{BKT}, i.e. for $T < T_{MF}$, Eq. 3.10 may be approximated by the relation $R(T) = R_0 \exp[-b_1(T - T_{BKT})^{1/2}]$. This leads to the following dependence [138]:

$$[dlnR(T)/dT]^{-2/3} = (2/b_1)^{2/3}(T - T_{BKT}) \tag{3.11}$$

The second method of studying BKT transition is by approaching the transition from below T_{BKT}; the superfluid phase stiffness J_s for a typical BKT transition is expected to jump discontinuously (the so-called universal jump) from a finite value below the T_{BKT} to zero, following universal relation given by Eq. 3.12. The superfluid stiffness $J_s(T)$ is an energy scale which is a measure of the impact of phase fluctuations in the SC state. It is related to the effective 2D superfluid density $n_s(T)$ and the effective mass m^* according to: $J_s = \hbar^2 n_s/4m^* = h^2c^2d/16\pi e^2\lambda^2$, where d is the film thickness and λ is the magnetic penetration depth. This condition may be verified by direct measurements of the penetration depth [17, 28, 33, 110] or by evaluation of the nonlinear exponent of the current-voltage (I-V) characteristics [50, 139]. In the experiments described in this thesis we will focus on this last method, i.e., evaluation of the I-V characteristics. In the low current limits ($I \to 0$), the I-V characteristics can be described by the relation $V \sim I^{n(T)}$, with $n(T)$ coupled to $J_s(T)$ via $n(T) = 1 + \pi J_s(T)/T$, Eq. 3.12. Within the BKT scenario it is expected that the temperature-dependent exponent $n(T)$ increases rather abruptly from 1 in the normal state to 3 at $T = T_{BKT}$ (at which the vortex-antivortex proliferation becomes entropically favorable as T increases), following the universal jump of the superfluid stiffness J_s from 0 to $2/\pi$ as T is reduced below T_{BKT} [140]:

$$J_s(T_{BKT})/T_{BKT} = 2/\pi \tag{3.12}$$

Indeed, this is typical behavior expected for systems with homogeneous SC state, i.e., systems which are free from defects that cause perturbation in the thermodynamics of the standard BKT phase transition. The temperature dependence of J_s is due to two effects: the existence of quasi particle excitations upon Cooper pair breaking above the SC gap and phase fluctuations of bound V-AV pairs below the T_{BKT}. The latter effect is usually negligible when the vortex core energy scale, μ, is large, such as in the case of superfluid films [26]. In conventional 3D superconductor, due to the abscence of BKT phenomenon, the 3D J_s jumps discontinously to zero at the supercondcuting transition temperature T_c. We point here that in [141] it has been reported that BKT transition is observed in 3D NbTiN film, due to disorder-induced 2D superconductivity hidden in the film.

We note here that the effect of disorder on the smearing of the J_s jump has been discussed in many experimental and theoretical studies [27, 36, 142], commonly assuming that the disorder in thin films results in fragmenting the SC state (see Fig. 3.3) due to localization effects, or that the fragmentation of the SC state is induced by extrinsic factors, due to various properties of the film substrates. Moreover, BKT transition has been studied and discussed in the context of proximity-Josephson physics, indicating the crucial role of superconducting proximity effects on the observation of the transition in Josephson junctions systems [37, 42, 143]. In this study (Chapter 5. Results and Discussion), we show that the primary reason for the behavior of the BKT transition in our Nb thin films is the film inhomogeneity triggered by the structural transformation upon changing film thickness (d). In previous study [49] by my colleagues, it is demonstarted that the Nb films undergo structural transformation, from amorphous structure for film thickness $d < 3$ nm, to mixed amorphous/polycrystalline structure for $3nm < d < 5nm$, and subsequently to a fully polycrystalline structure for $d > 5nm$. For $d < 5nm$, results show that the behavior of our inhomogeneous films resembles the behavior of Josephson junction arrays and the BKT physics turns more complicated as thickness decreases.

Fig. 3.3 shows schematically the behavior of vortex matter due to BKT physics (a) and sample inhomogeneity (b). In the BKT case, the vortices bound in pairs with opposite vorticity below T_{BKT} (top), get unbound by a sufficiently large excitation current I (bottom). This in turn creates additional voltage drop in proportion to the average density of the freed vortices what leads to nonlinear characteristics. However, in the case of inhomogeneous superconductors (b), the system segregates into puddles of various sizes with distinctive strength of the local SC condensate (top). Consequently, an applied current I may switch weak superconducting puddles into normal ones (bottom), contributing additional large broadening to the BKT transition, what complicates the extraction of T_{BKT} .

We point out that in order to have most reliable information on BKT transition from the $R(T)$ measurement, a constant measuring current of small magnitude $(I \to 0)$ is favored. This ensures eliminating the thermal effects which may be induced by high measuring currents. In I-V measurements, variable direct current (dc) is

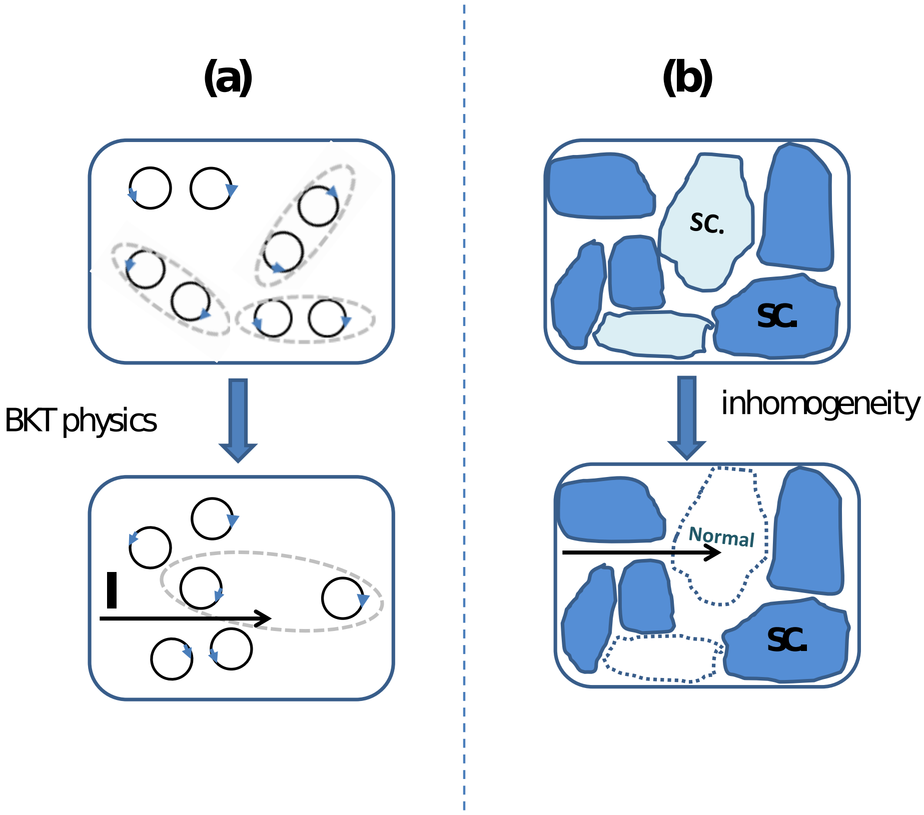

FIGURE 3.3: Schematic drawing illustrating difference between BKT physics in homogeneous superconductors (a) and the role of inhomogeneity (b). The arrow in the bottom figures indicates current. The drawing is based on the idea presented in Ref.[36].

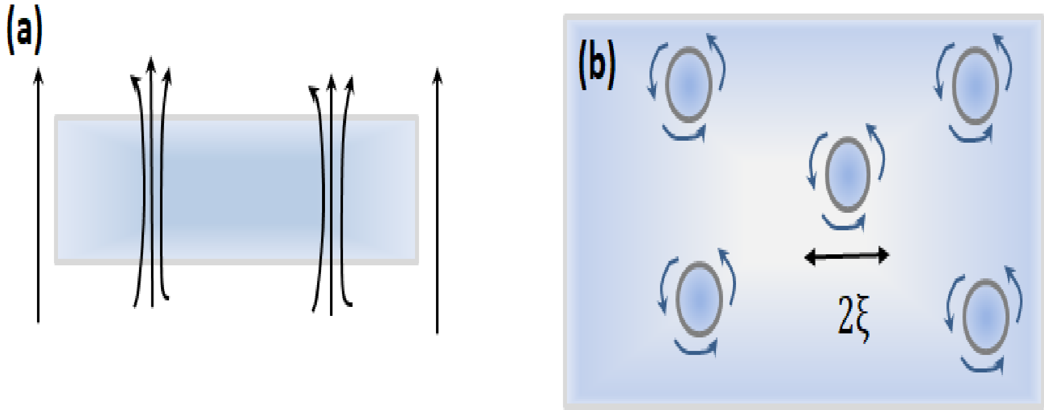

FIGURE 3.4: (a) Side view of magnetic vortices penetrating the normal cores inside the superconductor. Solid lines portray the applied magnetic field B lines (b) Top view; 2ξ is the estimated size of an individual vortex and the direction of the current circulating vortex core is shown.

used and the voltage drop across the sample is recorded as current changes what generates the linear and nonlinear isothermal I-V characteristics. The experimental procedures for all the $R(T)$ and I-V measurements of this study will be addressed in Chapter 4 (Experiment).

3.2 Vortex glass phase transition

A different interesting second-order phase transition observed in superconductors is a vortex glass (VG) transition. In the presence of external magnetic field, B, Abrikosov single-quantum vortices (field-induced) are introduced into the mixed phase of type-II clean superconductors (vortex lattice turns into vortex glass in dirty superconductor); each vortex carrying quantum of flux $\phi_0 = hc/2e$ and collectively forming a vortex-lattice of average density $a_0^2 = B/\phi_0$. The resulting vortex structure is driven by the current density j via the Lorentz force density $F_L = jB/c$ and the finite average velocity v of vortices generates a dissipating electric field $E = vB/c$. Fig. 3.4 displays a schematic of magnetic vortices penetrating into a type-II superconductor. An STM image of the formation of a triangular Abrikosov vortex lattice in $NbSe_2$ superconductor can be found in [144].

In defects-free superconductors, there is no vortex pinning. Therefore, flowing currents produce vortex motion resulting in finite ohmic resistance and destruction of superconductivity [45, 145]. However, in disordered superconductor or in the presense imperfections, vortex flow is impeded and vortex pinning takes place. Instead of long-range ordered vortex lattice, pinned vortices may be ordered at low temperatures on short distances, creating phase known as vortex glass (depending on the dimensions of the system; either 3D or 2D) at the phase transition temperature. The hallmark of the VG transition is that the fluid of vortex lines interacting with randomly distributed vortex-trapping centers undergoes on decreasing temperature a sharp thermodynamic transition into a truly superconducting VG glass phase. In theory, this implies a vanishing linear resistance with the divergence of energy barriers for vortices in response to any uniform applied current with density (j) which has a component normal to the vortex lines. This immediately produces vanishing dissipation, and hence zero resistivity indicating that vortices are frozen in the mixed phase.

Real materials contain defects what give rise to energetically favored places for the vortex lines and thus inhibit their mobility. The presence of random pinning or the introduction of quenched disorder can make the long-range crystalline order of the vortices unstable [146]. There are two main types of pinning: small-scale disorder from impurities, vacancies, etc and large-scale disorder from well-spaced grains, or twin boundaries, cracks, macroscopic inhomogeneity, etc. Thus, the correlation length for the crystalline positional order of vortices will be finite when there is quenched disorder present in the system. Small–scale disorder annihilates the long-range positional correlations of the vortex lattice what may lead to a superconducting VG transition. On the other hand, long-range disorder may leave the lattice structure intact out to long distances but can still dramatically impede macroscopic flux flow. Further discussion on this subject can be found in [45].

VG transition has been verified in 2D systems to occur at T =0 by means of the pure 2D vortex glass model [147, 148], indicating the absence of a finite-temperature VG transition. At $T > 0$, vortices start to partially form a liquid phase which deteriorates the rigidity of the vortex lattice, and thus a true VG phase describing the bulk system may no longer exist. Unfortunately, according to the proposed 2D-scaling method of the measured I-V characteristics, there is no specific theoretical prediction for the exponent describing the exponential temperature-dependence of the linear resistance due to thermal activation [149] what limits the applicability of the model and make it not easy to compare between different experimental studies. On the other hand, in case of 3D or quasi-2D systems experiments show that VG transition may occur at finite temperatures ($T > 0$); this is in accord with the expectations of theory for such systems. Upon the transition, melting of the glassy phase is driven by suffeciently large thermal fluctuations at temperatures above the transition characteristic temperature (T_g) in the low current limit ($I \to 0$) [150–155]. According to the standard VG theory, linear resistance, $R_{lin}(T)$ for ($I \to 0$), vanishes at T_g following the relation [45, 73]:

$$R_{lin} = (V/I)_{I \longrightarrow 0} \propto (T - T_g)^{\nu(z+2-D)} \tag{3.13}$$

where D is the dimensionality of the system. Here, ν is the static critical exponent of the vortex-glass correlation length and it diverges near T_g as $\xi_g \sim| T - T_g |^{-\nu}$, and z is the dynamic critical exponent for the correlation time $\tau_g \sim \xi_g^z$. Therefore, the logarithmic derivative of the resistance has a linear dependence on T according to Vogel-Fulcher relation given by [77, 156]:

$$\left(\frac{d(\ln R_{sq})}{dT}\right)^{-1} = \frac{1}{s}(T - T_g) \tag{3.14}$$

The slope is the inverse of $s = \nu(z + 2 - D)$ which reduces to νz for choosing $D = 2$. T_g and s can be estimated from the linear region of $(dlnR_{sq}/dT)^{-1}$ vs T. In the plot of $(dlnR_{sq}/dT)^{-1}$ versus T, T_g is recognized as the temperature T at which the extrapolation line crosses the T-axis indicating the vanishing of the linear resistance (R_{lin}) on the approach to the T_g from above.

Another popular way to study the VG transition is through the linear-nonlinear evolution of the current-voltage (I-V) characteristics. The isothermal nonlinear I-V characteristics in the vicinity of T_g can be scaled into two distinct branches by the following IV scaling laws:

$$\frac{V}{I(T - T_g)^{\nu(z+2-D)}} = f_{\pm}\left(\frac{I}{|T - T_g|^{\nu(D-1)}}\right), \tag{3.15}$$

where ν is the exponent of the vortex-glass correlation length, z is the dynamical critical exponent, D is the number of dimensions, and $f_{\pm}$ are the scaling functions above and below T_g. Above T_g (i.e., in the vortex –liquid phase), a finite linear resistance exists in the current limit, $I \rightarrow 0$ according to Eq.5.13 and the I-V curve becomes nonlinear for large I. At T_g, the I-V isotherm satisfies the power law:

$$V(I) \sim I^{(z+1)/(D-1)}. \tag{3.16}$$

Several experimental studies, in line with theoretical predictions, showed that z=[4-7] and ν=[1-2] are reasonable values for the occurrence of VG transition in both, 3D and quasi-2D superconductors [52–54, 157–159]. This holds true with the assumption that the resistance drops rapidly with decreasing current until it becomes nearly zero below the critical current. Furthermore, studies revealed that it is not always the case to have ν and/or z values within the theoretical bounds indicating that the VG branches obtained with the aid of standard IV scaling laws are non-universal [72, 75, 78–80]. Moreover, the existing discrepancies in the results among different studies suggest that more insights into the vortex matter are required for further understanding of the critical behavior of the phase transition.

Another alternative way to investigate the VG transition from I-V data analysis is to plot them on a double logarithmic (log-log) scale. For a typical VG transition, the expected turn over from finite resistance to a rapidly vanishing resistance is usually associated with obvious right to left curvature of the $V(I \rightarrow 0)$ characteristics. This can be better seen by plotting $dlogV/dlogI$ versus I (examples are shown in [52] for a 100 nm-Nb thin film grown on Si substrate) or $dlogE/dlogJ$ vs. J, where E is the electric field inside the sample and J is the current density as commonly done in literature. By doing so, the isothermal I-V curves for temperatures below the transition temperature $(T < T_g)$ are expected to turn upward demonstrating a power law behavior whereas for those from above $(T > T_g)$ are expected to turn downward demonstrating ohmic behavior in the low current limit $(I \rightarrow 0)$. However, the scenario can be somewhat different in the low I limit such as revealed by studies on the inhomogeneity effects. For example, as shown in [160], accounting for the finite size effects in the low-current density in YBCO films modifies the crossover to the ohmic behavior compared to YBCO single crystal. We will refer to the possible role of finite-size effects in our Nb films in Chapter 5.

3.3 Vortex Pinning and thermal creep phenomena

3.3.1 Strong pinning versus weak collective pinning scenario

The weak collective-vortex pinning theory has been developed in the wake of the high-T_c discovery [57, 161, 162]. According to theory [57, 163], in the mixed phase of type-II superconductors, weak collective pinning (WCP) occurs in the case of randomly localized atomically small, weak, and uncorrelated pinning sites. The pinning force acting on a single vortex flux line by an individual pinning defect vanishes and a collective action of many pins can pin a vortex which generates the average pinning-force density. This net pinning force is generated by fluctuations in the pinning energy. Moreover, theory predicts that the resulting critical current density J_c; the current density at which vortex de-pinning takes place, scales quadratically with the density of pins n_p (i.e., $J_c \propto n_p^2$). The depinning current density J_c is the maximum current density that a superconductor can carry without resistance [164]. In experiment, measuring J_c is a major key to evaluate the strength of vortex pinning in the low J limit. However, when thermal fluctuations are present (thermal vortex creep at finite temperature), J_c is no longer a distinct border separating a dissipative-free regime from a dissipative one in the SC phase. In particular, the dependence of the j_c on temperature according to WCP theory will be addressed in Sec. 3.3.2.

In contrast, in strong pinning (SP) scenario, vortex lines are plastically deformed by individual strong pins (defects) with sufficiently low density of pins (n_p) [165]. A competition between the force exerted by the pin on the vortex line and the vortex elasticity gives rise to a multi-valued solutions and therefore the averaged effective force $<f_{pin}>$ from individual pins is non-zero and the measured J_c is linearly proportional to $n_p<f_{pin}>$ [70].

Thermal creep phenomenon is portrayed as a small, finite directed motion of the vortex lines which creates dissipation in the SC state. This matter is interesting at low current density ($J \rightarrow 0$) where in this limit, the effect of self-fields can be ignored. The thermodynamic response to weak probe currents determines whether vortices constitute a realistic glass phase, characterized by infinite barriers against creep and hence resistance drops to zero as $J \rightarrow 0$ or whether they start to form a liquid phase with finite creep barriers, allowing vortex motion at any temperature ($T > 0$) such that resistance becomes finite as $J \rightarrow 0$. In the latter case, a mixed glassy-liquid phase may exist within a specific range of $J \rightarrow 0$. As J increases, vortex dynamics changes and a competition between the driving force ($\sim J$) and the temperature T exists until J crosses J_c, the threshold above which superconductivity breaks down. This thermodynamic evolution can be manifested by the evolution in the shape of the I-V characteristics rounding as J increases, which fundamentally governs the shape of the rest of characteristics above J_c.

In fact, the effects of thermal fluctuations have been studied and qualitative understanding of vortex-matter interaction for the weak pinning case has been developed [161, 166]. While some basic understanding of the differences between creep in the strong and weak pinning landscapes has been provided by studies of charge density wave pinning [167–170], and weak-to-strong pinning crossover has been discussed in [171, 172], the theoretical description of strong pinning has been achieved only recently by M. Buchacek et al [69–71].

The presence of the $T = 0$ excess-current characteristics (an experimental example is shown in figure 3 in [71]) that exhibits a linear flux-flow (FF) response at large currents (I) in the $V(I)$ characteristics is a hallmark of strong vortex pinning [60, 61]. Furthermore, the ideal strong pinning occurs in absence of thermal fluctuations (i.e., no thermal vortex creep) at $T = 0$. At finite temperatures ($T > 0$), thermal fluctuations emerge what generates, with increasing current, rounding (non-linear dynamic response) in the shape of the I-V characteristics describing vortex dynamics on the approach to the FF regime. In the past, it was believed that thermal creep effects persists up to driving force below the critical force (where pinning is finally overcome), i.e., $F < F_c$. This believe, however, is not confirmed by experimental studies on bulk superconductors [173, 174]. In [60] a step towards proper theoretical description of experimental results has been achieved, with conclusion that the pinning force persists even at drives beyond critical, $F > F_c$. Finally, recent novel work by Buchacek et al. [69, 70] shows that thermal effects generate a downward shift of the critical- (or depinning-) force density, while maintaining the shape of the excess-force characteristic, what confirms the presence of pinning and its thermal reduction at large drives $F > F_c$.

The theory [69, 70] provides quantitative results and precise expressions for the main parameters describing the effects of thermal fluctuations in the vortex pinning landscape. The theory [70] postulates that a type-II superconductor contains a low density of point-like defects that are sufficiently strong to act individually and pin vortices. By following the prediction of the theory [70] that the activation barrier energy depends on the pinning-force density rather than the driving current density J, a methodology for the extraction of the main parameters describing thermal fluctuations was proposed. A subsequent experimental test of the theory has been conducted on 2H-$NbSe_2$ and a-MoGe type-II superconductors and successful results have been published in the same year [71]. The main theoretical outcome of [70], which we exploit to analyze our experimental data, will be addressed in more detail in Sec. 3.3.3.

3.3.2 Critical current density and collective pinning theory

Before we further pursue the discussion on the newly developed strong pinning theory, we would like to discuss the influence of external parameters, namely, the temperature (T) and magnetic field (B) on the critical current density, J_c, on the basis of weak collective pinning theory. This will be useful for the interpretation of our results as will be shown in chapter 5 (Results and Discussion). According to the theory, two types of vortex pinning mechanism may be identified depending on the nature of the spatial variations associated with the defects (pins) present in the superconductor [67]. The spatial variations can be either in the Ginsburg-Landau (GL) coefficient (α) associated with disorder in the SC transition temperature (T_c) and/or in the charge carrier mean free path (l) near lattice defects. This results in two types of vortex pinning which are commonly known as δT_c pinning and δl pinning.

In the δT_c-type, spatial variations of T_c generate spatial modulations of the linear and quadratic terms of the GL free energy functional $\alpha|\psi|^2 + (\beta/2)|\psi|^4$ (Eq. 2.12) while in δl-type variations of the mean free path only affect the modulus of the gradient term, $|\bigtriangledown\psi|^2$, through variations in the effective mass tensor [67].

On the basis of collective pinning theory, the temperature dependence of normalized J_c in a single vortex pinning regime can be described by [67, 175]:

For the case of δT_c pinning, theory predicts that:

$$J_c(t)/J_c(0) = (1-t^2)^{7/6}(1+t^2)^{5/6} \tag{3.17}$$

and for δl pinning:

$$J_c(t)/J_c(0) = (1-t^2)^{5/2}(1+t^2)^{-1/2} \tag{3.18}$$

where $t = T/T_c$ and $J_c(0)$ is the de-pinning current density at $T = 0$.

Correspondingly, the temperature dependence of the vortex pinning energy, U_c, is characterized by the following relations, [3.19] and [3.20] for δT_c and δT_c types respectively:

$$U_c(t)/U_c(0) = (1-t^2)^{1/3}(1+t^2)^{5/3} \tag{3.19}$$

and

$$U_c(t)/U_c(0) = (1-t^2)^4 \tag{3.20}$$

Eqs. 3.17 and 3.19 predict that normalized J_c and normalized U_c, respectively, grow faster with T decreasing below the T_c in case of δT_c-type pinning compared to δl pinning (this is illustrated in Figs. 3 and 4 in Ref.[67]).

In spite of the distinctive nature characterizing each pinning mechanism, some studies have reported on the coexistence of δl and δT_c types of pinning in the same system [76, 172]. If both pinning mechanisms coexist, then the $J_c(t)$ may be written as a superposition of Eqs. 3.17 and 3.18. On the other hand, several studies have reported on vortex pinning through studying the magnetic field (B)-dependence of J_c [176–178]. In this study, we focus more on the temperature dependence of the J_c and the U_c in order to get a complete comprehension of different vortex phenomena.

3.3.3 Thermal vortex creep and Strong pinning theory

In this subsection, we briefly review the formalism of the strong pinning theory in [70, 71] and discuss the main quantitative theoretical results describing vortex dynamics in the presence of thermal fluctuations. In particular, we will consider the formulas which we used for the analysis of our experimental data obtained from I-V measurements in this study (Chapter 5. Results and Discussion).

Before we start the discussion, we remind that in view of Fig. 3.4, the formulation of the strong pinning theory assumes that the superconductor contains a small density of randomly distributed strong pins so that a single pin is individually capable of pinning a vortex.

According to the theory, through injecting the bulk of the superconductor with a current of density (J), the resulting force-velocity ($F - v$) characteristics for the vortex statics and dynamics in the mixed phase derives from the dissipative force-balance equation for the bulk vortex system [71]:

$$\eta v = F_L(J) - F_{pin}(v, T) \tag{3.21}$$

T is the temperature, J is the current density and v is the mean velocity of vortex lattice. $F_L(J)$ is the driving Lorentz force and $F_{pin}(v, T)$ is the average pinning force density, the quantity of major importance according to the theory. η denotes the Bardeen-Stephen viscosity per unit volume and has the form:

$$\eta \approx BH_{c2}/\rho_n c^2 \tag{3.22}$$

Here, B is the applied magnetic field, H_{c2} is the upper critical field, ρ_n is the normal-state resistivity and c is light velocity.

According to Eq.3.21, in the absence of thermal creep ($T = 0$) and at low velocities, the theory predicts a nearly constant pinning-force density $F_{pin} \approx F_c$, F_c (the critical force density), over a large range of velocities [60, 61], in agreement with Coulomb's law of friction. At finite temperatures ($T > 0$) and for small J, the $F_L(J)$

then can be compensated by $F_{pin}(v = 0, T)$ and vortices in the mixed phase remain pinned, (i.e., $v = 0$). A finite vortex velocity, $v \approx [F_L(J) - F_c]/\eta > 0$, only appears at larger drives. As a result, we find the excess-current characteristics with vanishing dissipation (voltage) below the critical (de-pinning) current density $J_c = cF_c/B$ and a shifted Ohmic branch above (see Figure 1 in [69], also Figure 3 in [71]).

According to the theory, in the presence of thermal creep, vortices departure their pinning sites in the form of activated creep-type motion, characterized by an energy barrier $U(v)$ which relates to the average velocity $v(J)$ of the bulk vortex system via the self-consistent Arrhenius law:

$$U(J, v) \approx k_B T ln(v_{th}/v) \tag{3.23}$$

k_B is the Boltzmann constant, v_{th} is the thermal velocity scale, related to an attempt frequency for thermal de-pinning and derived within strong pinning theory in [69, 70]. As v approaches v_{th}, thermal fluctuations turn insignificant and the $v - J$ characteristics join the $T = 0$ excess-current characteristics.

In the theory, the energy barrier $U(J)$ is important in two limit. At weak drives ($J \longrightarrow 0$), the response of the vortex lattice depends on the defects action scenario. In the context of weak pinning theory, the barriers $U(\mathrm{j})$ either remain finite or diverge via $U(J \rightarrow 0) \propto J^{-\mu}$ characterizing a vortex-liquid or a vortex-glass phase, respectively [57]. Strong pinning theory, however, predicts that [69, 70], for large saturating barriers ($U(J) \gg T$) in the limit $J \longrightarrow 0$, the resistance becomes exponentially small, and exhibits an activated behavior (a specific form of creep at low drives) with finite barrier what replaces the glassy response of the vortex lattice by an ohmic one. Indeed, this is the dynamic response of vortex system predicted at high T in the vicinity of the vortex glass-melting line. The corresponding regime is usually known as thermally assisted flux flow (TAFF) regime which may cross to the FF regime on the increase of temperature.

Within this TAFF regime the vortex system may be portrayed as a highly viscous liquid with a (plastic) relaxation time that is comparable to the typical pinning time [56]. As implied by its name, the resistance is thermally assisted, i.e., $R_{TAFF} \propto R_{FF} \exp(-U_0/k_B T)$, R_{FF} is the flux-flow resistance, and U_0 is the finite activation barrier. Thus, within the framework of strong pinning, the superconductor loses its characteristic property of dissipation-free transport of the current. We point here that U_0 links to the condensation energy (proprtional to the coherence length), thus, the creep in high T_c superconductors is very strong due to short coherence length [179] and high temperatures T compared to low T_c superconductors.

On the other hand, at strong drives, as J approaches the critical drive ($J \rightarrow J_c$), the barriers are expected to vanish as, $U(J) = U_c(1 - J/J_c)^{\alpha}$; the exponent α depends on the pinning model [70, 165]. Indeed, in presence of thermal fluctuations, the critical current density J_c is reduced to a de-pinning current density $J_{dp}(T)$ separating flat and steep regions of the high $j - v$ characteristics (figure 3 in [71]).

Another central result provided by the strong pinning theory is the following expression for the vortex velocity-drive ($v - J$) characteristics:

$$v/v_c = J/J_c - 1 + [k_B T/U_c) ln(v_{th}/v)]^{2/3} \tag{3.24}$$

The derivation leading to the simple form of Eq. 3.24 is based on the force-dependence of the barrier energy which assumes the form

$$U[F_{pin}(v,T)] \approx U_c[1 - F_{pin}(v,T)/F_c]^{3/2} \tag{3.25}$$

Eq.[3.25] tells us two important things. First, the theory provides further insight that the relevant force in this simple form of the barrier's scaling law is not the usual driving Lorentz-force density $F_L \propto J$ (that would result in a standard form of $U(J)$) but it is the velocity-dependent average pinning force density, $F_{pin}(v,T)$. Second, as J approaches J_c, the barriers vanish with an exponent $\alpha = 3/2$, which is universal for any smooth pinning potential [71].

Combining Eqs.[3.25] and [3.21], we replace $F_{pin} = F_L - \eta v$ to obtain the dependence of the barrier energy on the drive j and velocity v through the form

$$U[F_{pin}(v,T)] \approx U_c[1-(F_L - \eta v)/F_c]^{3/2} = U_c[1-(J/J_c - v/v_c)]^{3/2} \equiv U(J,v) \tag{3.26}$$

Equations [3.23] and [3.25] combine into a velocity and temperature-dependence of the $F_{pin}(v,T)$, in the following form

$$F_{pin}/F_c \approx 1 - [(k_B T/U_c) ln(v/v_{th})]^{2/3} \tag{3.27}$$

For $T > 0$ and $F_L(j \to 0) = F_{pin}(v \approx 0, T)$, the velocity ratio v/v_c can be neglected and the characteristics described by Eq. 3.26 are equivalent to the Arrhenius law with a barrier exponent $\alpha = 3/2$. Indeed, within this approximation, the driving force $F_L/F_c = J/J_c$ is balanced by the pinning force $F_{pin}/F_c = (k_B T/U_c) ln(v_{th}/v)]^{3/2}$ and $v - j$ characteristics are described by Arrhenius law with a barrier $U(J) = U_c(1 - J/J_c)^{3/2}$.

Inserting the expression for $F_{pin}(v,T)$ into the equation of motion [3.21], and dividing by F_c, one arrives at the simple form given by [3.24]. To arrive at Eq. 3.24, the definition of the free flux-flow velocity $v_c = F_c/\eta$ at F_c is utilized. U_c is the activation barrier energy (velocity-dependent term) and it is of inverse proportion to the thermal velocity parameter v_{th}/v_c as predicted by the theory.

Eq. 3.24 describes the turnover of vortex dynamics from creep-type into flow-type response that dominate at low and high j, respectively. It captures the small vortex velocity at subcritical drives below the critical current ($J < J_c$), far below the critical current ($J \ll J_c$), the the $v - J$ rounding of in the critical region, and the beginning of the smooth sub-ohmic region.

Here, we note that the calculation leading to Eq.3.24 is based on Kramer's rate theory [180, 181] with the assumption that $U_c \gg k_B T$. Indeed, as will be shown in Chapter 5 (Results and discussion), this condition is fulfilled for the investigated films of this study. According to Eq. 3.23, the velocity dependence of the barrier energy restricts the applicability of Eq. 3.27 to velocities $v < v_{th}/e$, e is the natural exponent.

By relating the theoretical result, Eq. 3.24, to the current $I = AJ$ and voltage $V = LE$; $E = Bv/c$ is the electric field within the sample, using the sample length L and cross sectional area A and the definition of the free flux-flow voltage at I_c, $V_c = R_{FF} I_c$, we arrive at the creep-flux flow interpolation formula:

$$V = R_{FF}(I - I_c) + V_c \left[\frac{k_B T}{U_c} ln \left(\frac{v_{th}}{v_c} \frac{V_c}{V} \right) \right]^{3/2}. \tag{3.28}$$

The result given by Eq. 3.28 can be compared to the experimental data obtained from the I-V measurements. It involves the parameters I_c,R_{FF}, $U_c/k_B T$, v_{th}/v_c which are necessary for describing vortex dynamics. In experiment, these main parameters can be obtained as follows:

At large voltages (V) which indicate flux flow-type dynamics, thermal creep shuts down; the second term in Eq. 3.28 describing creep vanish and the I-V characteristics reduce to the simple form describing the excess-current characteristics $V = R_{FF}(I - I_c)$, from which I_c and R_{FF} can be obtained. In a next step, the I-V data can be rescaled so that $V \longrightarrow V/V_c = v/v_c$ and $I \longrightarrow I/I_c = J/J_c$ in order to be in the form of Eq. 3.24. This rescaling induces a data collapse in the asymptotic region (Fig.3(a) in [71]); the deviations appearing in the transition region then are due to creep. From these deviations, one can extract the two remaining parameters $U_c/k_B T$ and v_{th}/v_c through a careful fit to the data in the transition region.

Th example shown in Fig.3, [71], demonstrates the successful observation of thermal creep in 2H-$NbSe_2$ sample via measuring the isothermal I-V characteristics (red data points) in a perpendicular magnetic field B =1 T. The data are taken at the temperatures T = 4.8, 5.0, 5.2 and 5.5 K (with T increasing from right to left). The average inter-vortex distance $a_0 \approx 45nm$ is small compared to the sample thickness d and hence the standard strong pinning theory for three-dimensional (3D) bulk pinning is applicable. As T increases further, thermal fluctuations become more relevant and thus a remarkable rounding in the characteristics in the critical region near voltage onset is produced and the extrapolated $T = 0$ excess-current characteristics are approached at larger drives. The fits are shown up to velocity where activation barriers, $U(j, v)$, remain larger than thermal energy ($k_B T$).

On the other hand, figure 8 in the same study shows the analysis of the activation barriers $U(F_{pin}(v, T))$ for 2H-$NbSe_2$ sample. The data are represented as $-ln(v/v_c) = U/k_B T + \gamma$ versus $J/J_c - v/v_c = F_{pin}(v, T)$. Fits of the activation barrier $U(F_{pin})$ to Eq. 3.26 are shown for two different exponents $\alpha = 3/2$ and $\alpha = 1$. The fits outside the range $v \leq v_{th}/e$ are also shown. For the sake of extracting the reduced energy $U_c/k_B T$, it should be noted that the most appropriate portion of the curve which describes thermal creep had been selected and discussed.

Chapter 4

Experiment

4.1 Sample preparation

4.1.1 Sample fabrication

Niobium (Nb) layers and silicon/niobium/silicon (Si/Nb/Si) trilayers thin films were made in the laboratory of The Johns Hopkins University (JHU), USA, using magnetron ion sputtering technique in in high vacuum chamber at room temperature. The samples were grown by my advisor Prof. Marta Z. Cieplak with the help of Leyi Zhu (a graduate student at JHU).

In magnetron sputtering (Fig. 4.1), the chamber is first evacuated to a high vacuum to help minimize the partial pressures of all background gases and possible contaminants in the sputtering chamber. Once the base pressure in a very high vacuum is reached, a sputter gas, such as argon (Ar) in our case, is flowed into the chamber and a pressure control system is used to regulate the total pressure (typically in the millibar range). A high electric field is applied between the cathode (sitting right behind the sputtering target) and the anode (connected to the chamber as electrical ground) in order to generate the plasma. The positively charged atoms of the sputtering gas are now accelerated towards the negatively charged cathode, leading to high energy collisions with the surface of the target. Ions momentum transfer is associated with each collision and therefore atoms at the target surface are ejected into the surrounding space with high kinetic energy that is enough for arrival at the substrate surface. The substrate is most often polarized with a high negative potential $(0.5 - 3KV)$ to attract and supply the ions with appropriate kinetic energy.

Unlike typical sputtering (non-magnetically enhanced), in magnetron sputtering, large magnets (placed behind the target) are used to trap the electrons in the plasma at or in the close vicinity of the target surface. The magnetic field applied at right angles to the electric field causes the trapped electrons to move in spiral motions until they collide with a spattering gas atom. This increases the number of electrons that take part in ionization process what increases the efficiency of ionization and therefore a lower Ar pressure ($\sim 0.5mbar$) may sustain plasma. This upgrades film quality as less Ar atoms will be incorporated into the deposited film. Moreover, the confinement of the electrons prevents damage which would be caused by direct impact of these electrons with the substrate or growing film. This ultimately leads to creating layers of high purity and homogeneity that are characterized by good adhesion to the substrate.

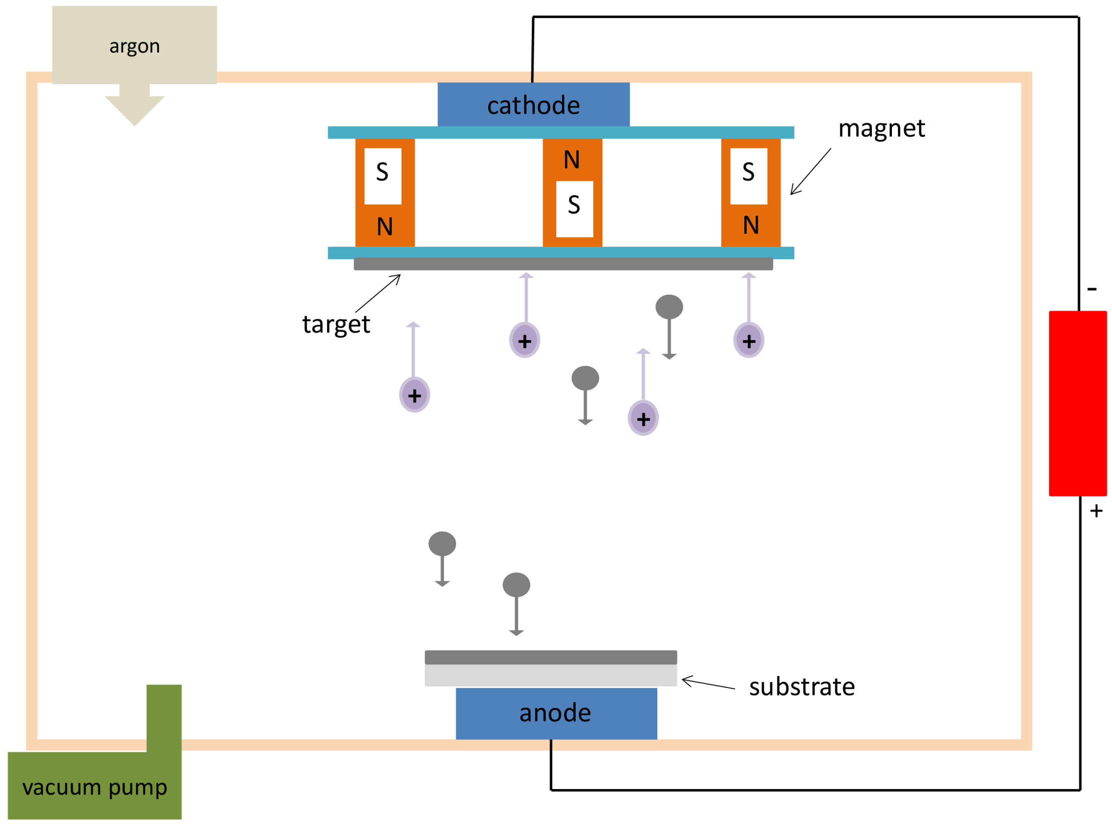

FIGURE 4.1: Schematic of the magnetron sputtering chamber.

Fig. 4.2 shows a schematic diagram of a tri-layer Si/Nb/Si on glass substrate. The deposition sequence was as follows: a layer of silicon with a thickness of about $d \approx 10nm$ is first deposited, followed by the deposition of Nb layer with a nominal thickness from $0.1nm$ to $50nm$, and on the top, another Si layer ($d \approx 10nm$). The Si layer between Nb layer and the substrate prevents the diffusion of oxygen from the substrate behind to niobium whereas the layer on the Nb surface prevents the diffusion of oxygen from the atmosphere.

The deposition rate was calibrated by depositing samples ($d \approx 50nm$) at different deposition current, I, and then by measuring the layer thickness using low-angle diffraction. Since the thickness of Nb has been changed in a wide range, it turned out to be necessary to change the deposition current. This is because prolonged deposition time results in increased density of impurities incorporated into Nb layers. For this reason thicker layers (d between 2 nm and 50 nm) have been deposited at large current, $I = 150mA$. On the other hand, in case of very thin Nb layers (d <2 nm) large current results in poor control of the layer thickness. Therefore, current has been decreased down to $75mA$ for the deposition of thin films.

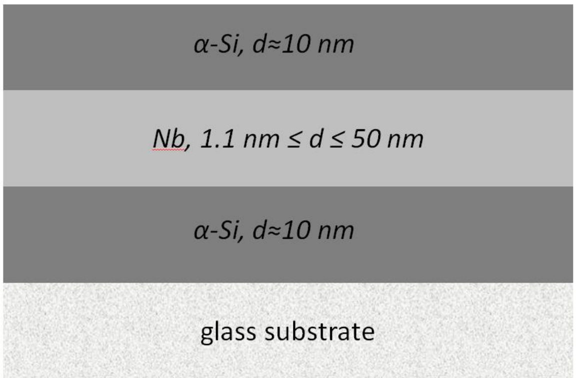

FIGURE 4.2: Schematic of the Si/Nb/Si trilayer.

4.1.2 Sample characterization

X-ray Diffraction

X-Ray Diffraction (XRD) is an efficient method, used for determining the crystal structure of materials. It is very useful in characterizing bulk crystal structures and chemical phase composition. Materials may be categorized as crystalline materials (can be single crystal or polycrystalline) or amorphous materials. Crystalline materials are comprised of atoms arranged in a regular ordered pattern in 3D space. There exist seven well-known crystal systems, which are: cubic, tetragonal, orthorhombic, rhombohedral, hexagonal, monoclinic and triclinic. In particular, we remind that niobium (Nb) has a cubic lattice with bcc structure, space group Im$\bar{3}$m.

Parallel atomic planes intersecting the unit cell are used to define directions and distances in the crystal lattice. Fig. 4.3 shows a schematic of x-ray diffraction. d is defined as the distance between adjacent planes of atoms forming the lattice. The orientation and the spacing (d) of these planes are defined by three characteristic integers h,k,l termed as Miller Indices. The (hkl) designate a crystal face or family of planes throughout a crystal lattice. Polycrystalline materials may contain a multitude of small single crystal regions. These regions are called grains and they are separated by grain boundaries and may have different shapes, sizes and orientations. On the other hand, materials with out periodic structure where atoms are stacked in an irregular manner are called amorphous materials; they do not exhibit sharp distinctive peaks of diffraction in the XRD pattern.

Based on the well-known Bragg's Law, Eq. 4.2, information on the spacing between atomic planes can be obtained when constructive interference (indicated by peaks in the XRD spectrum) occurs. Knowing the spacing of crystallographic planes by diffraction methods, the crystal structure of materials can be identified. For a special case, the plane spacing of cubic crystal is related to the lattice parameter (a) by the following equation:

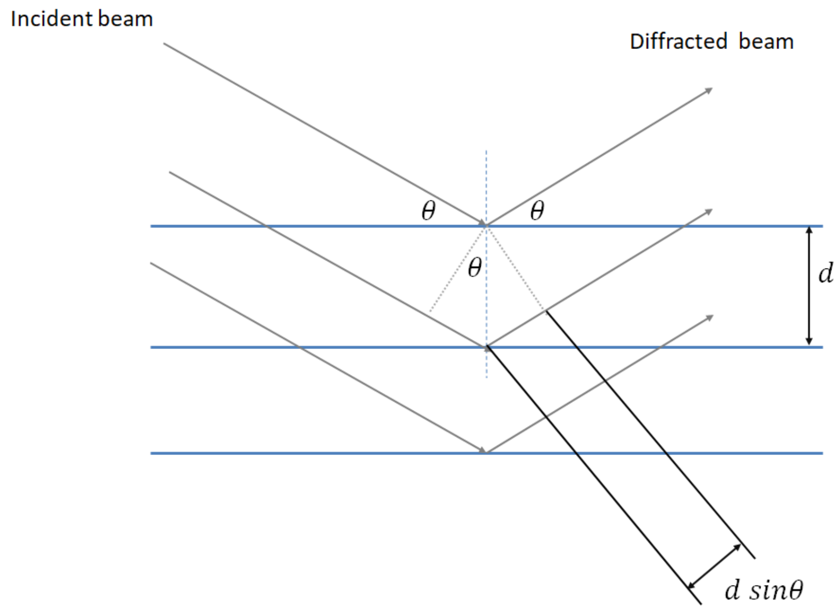

FIGURE 4.3: X-ray diffraction.

$$d_{hkl} = a/\sqrt{h^2 + k^2 + l^2} \tag{4.1}$$

From Bragg's law for the constructive interference,

$$n\lambda = 2d_{hkl}\sin\theta \tag{4.2}$$

Where n is the diffraction order ($n = 1, 2..$) and λ is the x-ray radiation wavelength.

Substituting Eq.4.1 into Eq.4.2 we obtain,

$$\sin^2(\theta) = n^2\lambda^2(h^2 + k^2 + l^2)/4a^2 \tag{4.3}$$

Structural analysis of all the samples in this study was carried out in the SL1.3 IF PAN laboratory using a high-resolution Philips XPert MRD diffractometer with copper- $K\alpha$ radiation tube, wavelength = 1.540598Å. Diffractograms were measured in the so-called $\theta - 2\theta$ configuration (Fig. 4.4(a)). The X-ray beam falls down on the layer at some angle θ and enters the analyzer at a detector angle of 2θ, so the XRD spectrum of a sample is recorded as beams-intensity (I) versus 2θ. Our polycrystalline Nb films show a distinctive intense peak indexed as (110) which locate at $2\theta \approx 38$ deg. in the XRD spectrum. The intensity decreases and the peak gets broadened as Nb film thickness, d, decreases indicating increased amorphous phase contribution. As thickness changes, we estimated the full-width at half maximum (FWHM) of the (110) intensity peak (Fig. 4.4(b)). The XRD measurements of all our samples were performed by Dr. Roman Minikayev at the laboratory of SL 1.3, the institute of Physics, PAS.

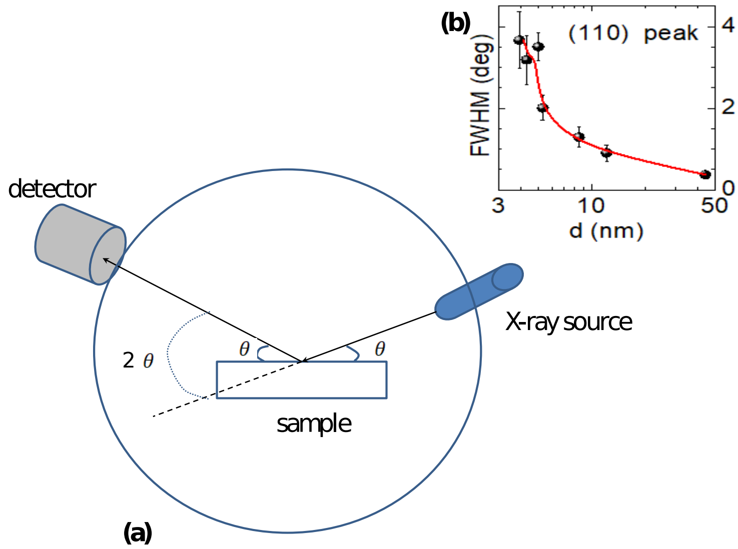

FIGURE 4.4: (a) Simple schematic of the main components of the XRD measurement chamber, (b) shows d-dependence of FWHM for (110) peak in the x-ray diffraction spectrum of our Nb films.

X-ray reflectivity measurement

X-ray reflectivity (XRR) measurement is a powerful tool used for determining the electron density, layer thickness, interface and surface roughness of a single and multi- thin layer systems. It can determine a layer thickness between 1Å-400nm and roughness between 0-20Å. The operating principle of the XRR technique is similar to the X-rays diffraction (XRD) measurement. It requires a proper optical alignment of the sample between the X-ray source and detector. X-rays of wavelength (λ) are bombarded to hit the sample and the detector (Fig. 4.4(a))) records the intensity (I) of the scattered rays. Changing the incidence angle (θ) and scanning the intensity versus 2θ can provide an oscillatory behavior which is sample dependent. From these oscillations in the I vs. 2θ curve one can determine the layer thickness, etc.

If the incident x-ray angle is too small, all coming x-rays can be reflected from the surface of the material through total external reflection. This special angle of incidence angle is called the critical angle (θ_c) which depends on the electron density of the material and the sample layered structure. The more electronic density, the more reflection occurs as each electron serves as a scattering center for the incoming rays.

If $\theta > \theta_c$, then the incident x-rays start to penetrate into the material with an angle called transmission angle (θ_{trans}) and therefore less reflected photons are recorded by the detector. Thus, reflection from the lower and the upper surfaces of the film occurs and the interference of the reflected rays creates periodically repeating interference fringes called "Kiessig fringes" which explains the oscillatory behavior of the XRR curve for $\theta > \theta_c$. In the curve, depending on θ, the interference can be constructive (maxima) or destructive (minima) (see Figures 1 or 2 in [182]). The recorded intensity is proportional to a quantity called the reflection (R) which is θ and θ_c dependent and explains the behavior of I vs. 2θ and the shape of the generated XRR curve.

The Reflectivity from ideal flat surfaces is calculated with Fresnel reflection. When displayed on the 2θ scale, the distance between two successive maxima or minima in the oscillatory behavior of the XRR curve represents $\triangle 2\theta$ which provides an estimate of $\theta \approx \triangle\theta$ and the layer thickness (d) can be simply calculated using Bragg's law (Eq. 4.2)(see also https://www.youtube.com/watch?v=ndzaA9AmI9M). In [183], a modified Bragg's law derived based on the geometrical optical theory has been proposed for accurate determination of the thickness of monolayer or multilayer film.

For multilayer films, reflectivity is also calculated by the formalism developed by Parratt which can be used in a recursive manner [184]. The formalism is used in commercial XRR simulation programs for determining thickness of each layer, etc. In real measurements, the surfaces and/or interfaces of thin films are not smooth and roughness causes diffuse (or off specular) scattering and the intensity of the specular reflection is reduced. Thus, the intensity of the Kiessig fringes and the intensity of the entire reflectivity curve decrease as roughness increases in the layered system. Fig. 4.5 shows example of the XRR data, obtained for our 4.3 nm thick-Nb film. The analysis results reveal less thickness homogeneity and more surface roughness when compared to thicker films. All the XRR measurements and subsequent calculations for all our samples were performed by Dr. Roman Minikayev at the laboratory of SL 1.3, the institute of Physics, PAS.

4.1.3 Preparation of samples for transport measurements

Prior to performing any transport measurements, the fabricated Si/Nb/Si samples layers were etched into a "Hall-bar" structure (see Fig. 4.6), using photolithography followed by ion beam etching process. The principle of ion beam etching is similar to the sputtering process described previously in (Sec.4.1.1) with the difference that the sample is placed on the cathode to etch the material. The gas in which deposition took place was gas SF6, and the pressure in the vacuum chamber during etching was 5×10^{-2} mbar. For the photolithography process, a thin layer of photoresist (MICROPOSIT S1818 G2 brand) is applied to the sample surface and then dried in an oven at a temperature $T = 115$ for 15 minutes. Afterwards, an appropriate shadow mask with Hall bar geometry is applied to the surface of the photoresist covering the top of the sample, followed by illumination with UV radiation using LSB721 200 W Hg(Xe) Arc lamp (ozone free). After these proper treatments, the layer can be etched. Finally, after etching, the photoresist is washed with acetone.

4.2 Transport measurements setup

In this section we discuss the setup we used for performing measurements down to 2 K, namely, a Quantum Design Physical Property Measurement System (PPMS). The PPMS is used for most of the transport measurements in this study. Measurements

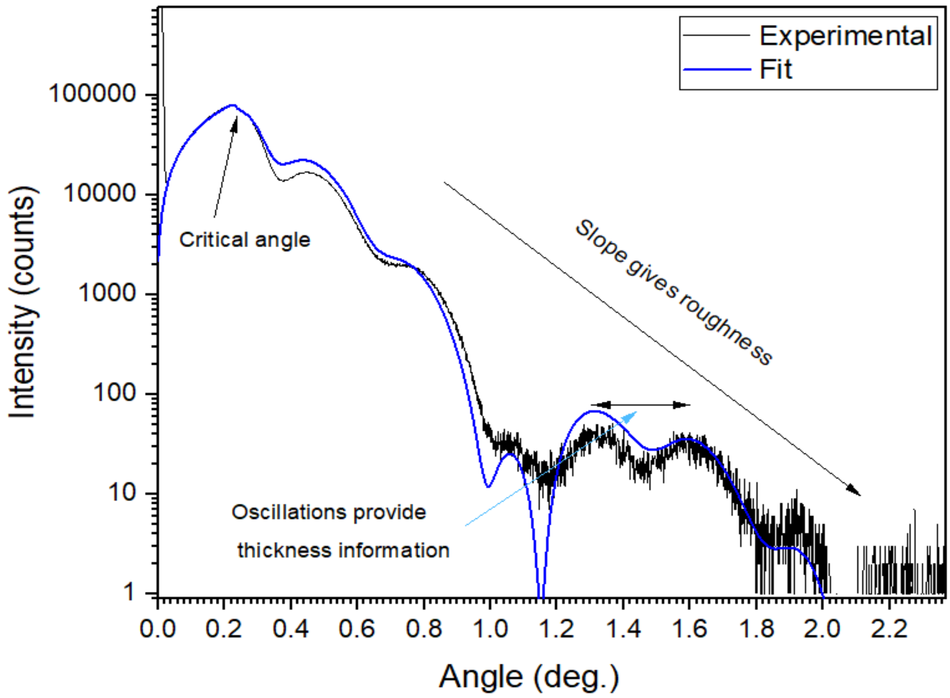

FIGURE 4.5: Intensity versus angle for 4.3 nm-Nb film sandwiched between to silicon wafers (Fig.4.2). Black curve represents experimental data and the blue one was obtained using the commercial fit software.

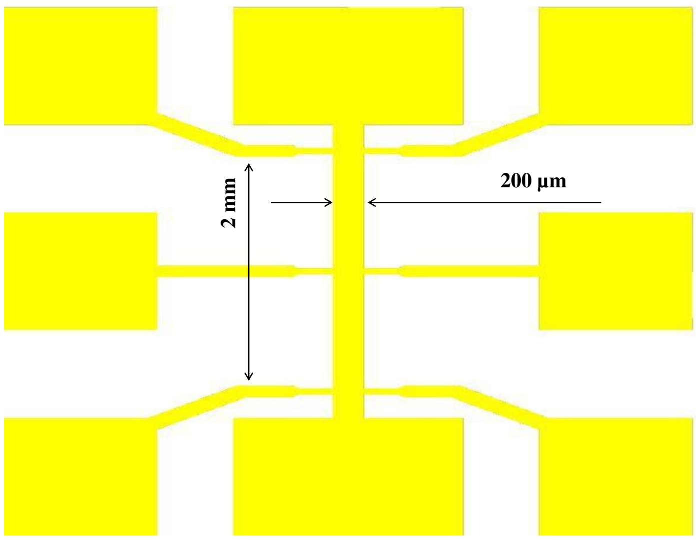

FIGURE 4.6: Schematic representation of the hall-bar structure.

which require temperatures below 2 K were performed using dilution refrigerator, discussed at the end of this chapter (Sec. 4.4). Fig. 4.7 shows a snapshot of the PPMS and displays its components, which work integratively, and together assist running the experiment.

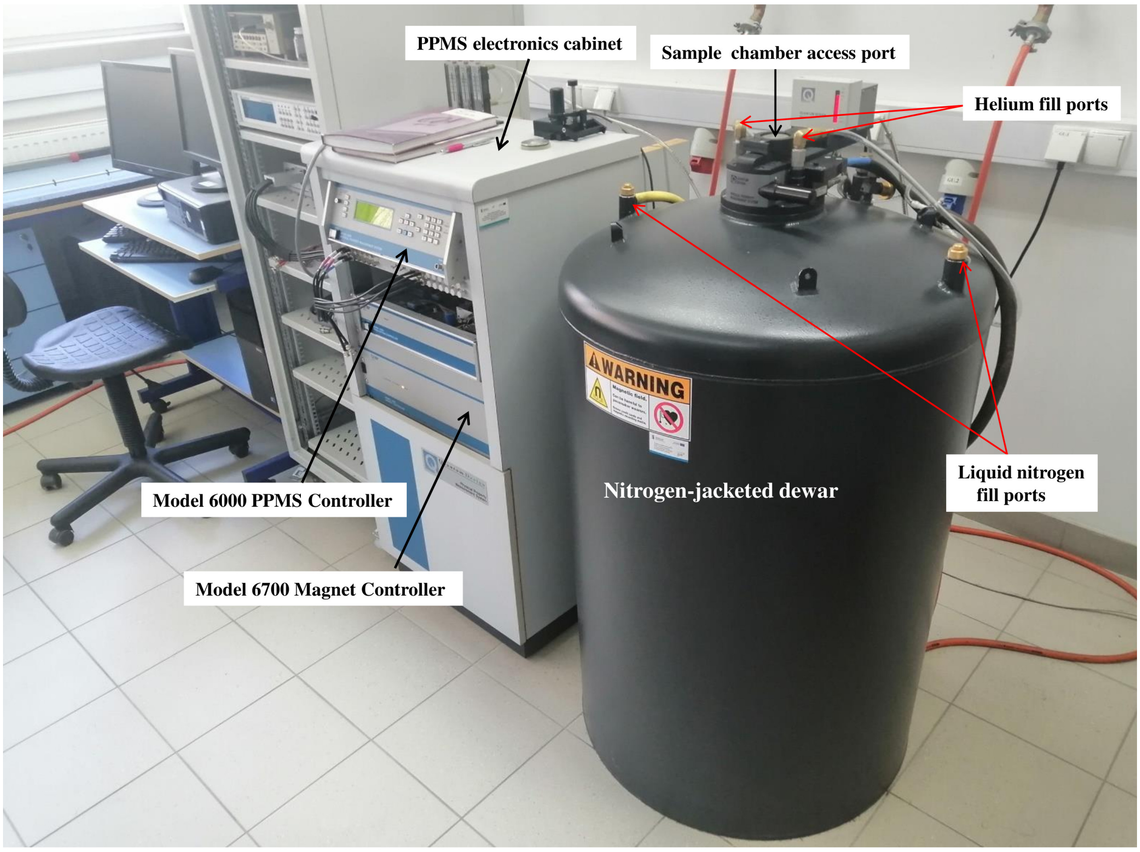

FIGURE 4.7: An overview of the PPMS used for our measurements.

Here, we would like to briefly discuss our PPMS integrated components shown in Fig. 4.7. The first major component is the Nitrogen-jacketed dewar (48 Liters capacity) which contains the liquid-helium bath (87 Liters capacity) in which the PPMS probe (will be discussed further) is immersed. Thanks to the reflective superinsulation property, the dewar helps to minimize helium consumption what partially contributes to the operating efficiency of the dewar. The dewar is associated with a liquid-nitrogen transfer adapter (L-shaped tube) to facilitates the liquid-nitrogen fill procedure. As indicated in the figure, there are two liquid-nitrogen-fill ports on the top of the dewar. A second major PPMS component is called the PPMS probe, a sophisticated device with delicate components, which is immersed in the liquid-helium bath inside the dewar. It is constructed in a way that does not allow heat exchange between the sample chamber and the helium bath and minimizes radiative power loss into the helium bath. A third major component of the PPMS is the sample chamber. At the very bottom of the chamber there exists a multi-pin connector that contacts the base of an installed sample puck (Fig. 4.7). A heater and two thermometers and are located right below the sample puck connector. This proximity helps maintain close thermal contact with the puck and sample during experiment. There is a region in between the sample chamber and the inner vacuum tube called the cooling annulus. An impedance assembly activates (deactivates) the flow of helium into the cooling annulus via switching off (on) the assembly heater.

The PPMS is purchased with a 9-Tesla longitudinal magnet (a superconducting solenoid made of a niobium–titanium alloy embedded in copper) immersed in liquid helium. The magnet controller (Fig. 4.7), either the Model 6700 or the Model 3120 can to be switched into the magnet circuit so that the magnetic field can be changed. The Model 6000 PPMS Controller (Fig. 4.7) is an integrated user interface that hosts the PPMS electronics and the valves for gas contolling. The front panel of the controller contains a power button, a display screen (which displays the temperature, magnetic field, pressure, helium level, etc) and others. Moreover, as shown, the PPMS contain the Model 6700 Magnet Controller which uses different approach modes to control the magnet charging and discharging. The electronics cabinet (Fig. 4.7) holds the Model 6000 and Model 6700 controllers, the vacuum pump, power strip in addition to extra hardware and electronics which may be useful with some PPMS options. The vacuum pump operates continuously to control pressure in the sample chamber and to aid thermal control. Valves in the Model 6000 controller regulate the vacuum and the gas-flow rates. Finally, the top part of the probe is called the *probehead*. It contains the two helium-fill ports and all the connection ports for attaching gas, vacuum, and electrical lines from the Model 6000 PPMS Controller. Moreover, it includes the access port into the sample chamber.

Fig. 4.8 shows the sample puck which holds the sample for experiment. The puck is constructed of oxygen-free high-conductivity copper that ensures high thermal uniformity. It has been gold-plated to prevent oxidation. The base of the puck contains 12 solder pads through which electrical leads (supplied by us) establish contact with the sample. These solder pads are connected (via hard-wiring) to a set of 12 pins on the base of the sample puck. When the puck is installed, the 12 pins connect to the sample-puck connectors located on the base of the PPMS sample chamber and then ultimately to the pins of the gray-ringed Lemo connector on the probe head. The puck is keyed in order to insure a proper alignemnet of the electrical connectors. The system thermometers and heaters are located directly below the installed puck, so temperature control is intimately related to the temperature of the sample. Every PPMS option includes a number of pucks, so one can use different pucks to mount different samples. One also may configure each puck for a different type of experiment.

In order to verify a sample contact with the puck, a puck-wiring test station (Fig. 4.8(c)) is used. It contains a puck connector, and 12 banana jacks; all wired in series for probing purposes. In order to verify proper electrical connection of the sample (via checking undesired shorts, poor connections, and so on) before inserting the puck into the sample chamber, a digital voltmeter can be used. After the sample is mounted, the voltmeter probes have to be connected to the proper numbered Banana jacks.

Eventually, after mounting the sample on the puck and soldering the electric leads to the appropriate solder pads, the puck is ready for insertion into the sample chamber by following some careful procedure. Following proper insertion of the sample puck through the sample chamber access port (Fig. 4.7), a top-plate assembly which includes the components for sealing the sample chamber is used.

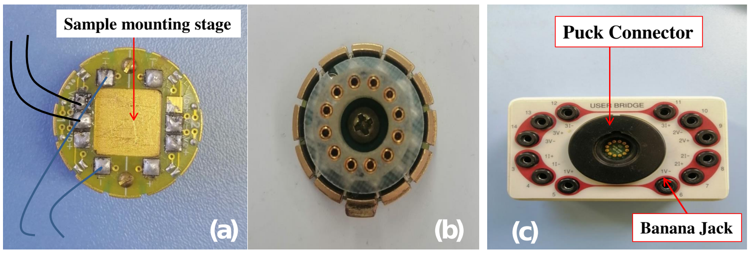

FIGURE 4.8: (a) sample puck; black (blue) lines indicate voltage (current) leads, respectively. Electric leads soldered to the appropriate solder pads are connected to the sample after mounting (b) Bottom view of the sample puck. (c) Puck-wiring test station (Top view).

4.3 Measurements

Measurements in this study, in zero and finite external magnetic fields, are obtained with the aid of AC Transport Measurement System (ACT) option upon completing the electrical connections to the PPMS-Probe head. The ACT option includes a precision current source and a precision voltmeter in a package to be used alongside with the base PPMS platform. The ACT option supports various types of electrical transport current measurements including those which require using a DC current. Typically, measurements are made by driving a probe current through the sample and then the potential drop in one direction across the sample is measured. Before measuring, a sample mounted on the sample puck should be ready for insertion into the sample chamber which has to be well-sealed after. Results of measuremnts and other related parameters are stored in specified ACT measurement data files. In the following, the experimental details of the transport measurements that are relevant to our studies will be discussed.

4.3.1 Resistivity measurements

The ACT option supports four-terminal AC current resistivity measurements. In four-terminal measurements, two leads pass a measuring current (I) through the sample and two separate leads are used to measure the voltage drop (V) across the sample (See Fig. 4.9). Compared to two-probe method (Fig. 4.10), the current through the sample and the potential drop across the sample can be known with high accuracy as the voltage leads draw very little, “ideally” no current, so that the effects of lead and contact resistance are eliminated. Ohm’s law is used for calculating the resistivity of the sample (Fig. 4.9). The sample resistivity (ρ) is given by

$$\rho = VA/Il \tag{4.4}$$

Where l is the voltage leads separation and A is the cross-sectional area through which the current passes. In Fig. 4.9, it should be noted that the current and voltage leads do not contact the sample at the same point. In case the current and voltage leads contact the sample at the same point, lead resistance is eliminated but contact resistance still affects the measurement results. Therefore, it is recommended to perform true four-wire measurements with the ACT option in order to take advantage of the instrument's sensitivity. The ACT software records resistivity in units which can be configured. Fig. 4.10 differentiates between both probe methods which can be used for measuring the sample resistance (R). V_1, V_2 indicate the voltage drops on the contacts. The subscripts $+$, $-$ in $I_{\pm}$ indicate the direction of the measuring current flowing though the sample.

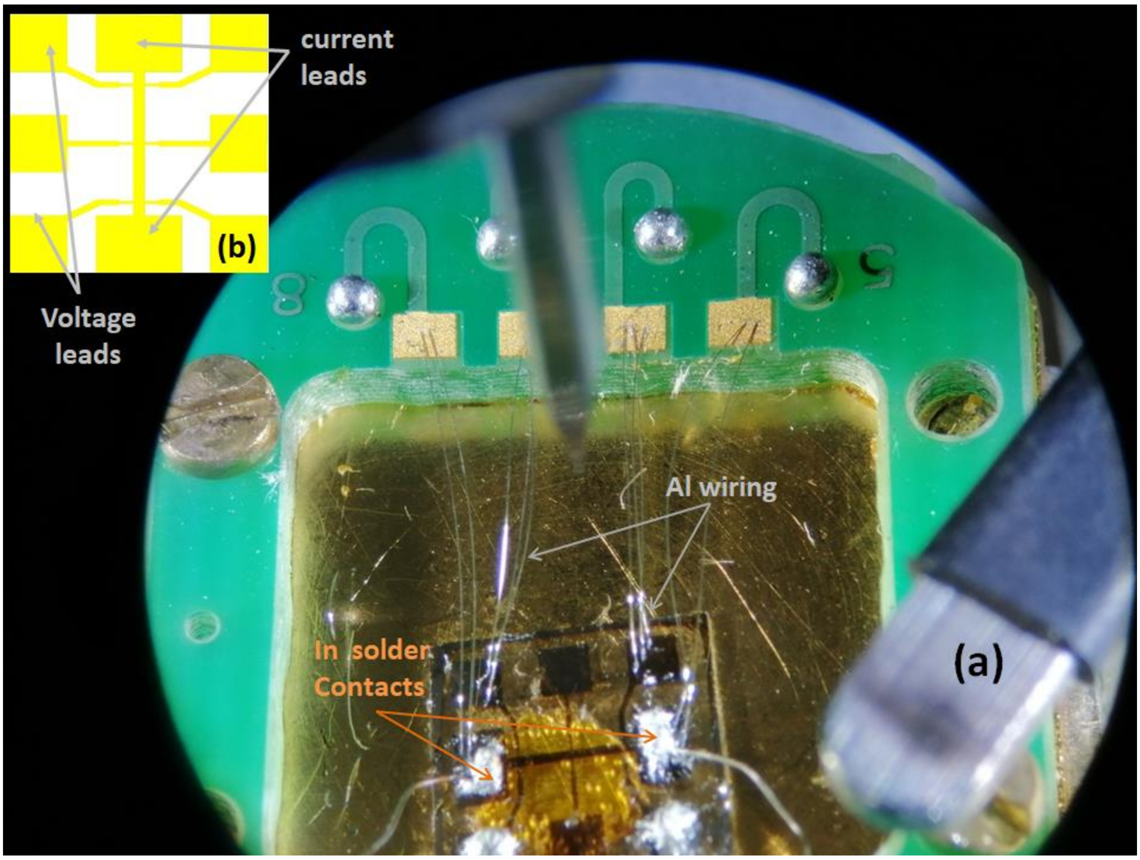

FIGURE 4.9: Sample preparation for transport measurements. (a) A four probe wiring performed on Nb thin film (with hall-bar structure mimicked in (b)) mounted on a sample puck. The wiring was performed using aluminum (Al) thin wires and, independently, using Indium (In) solder contacts on purpose so we test the influence of the wiring material on the transport measurements results; we found similar results, (b) schematic of the hall-bar structure indicating the locations of attaching the current and voltage leads.

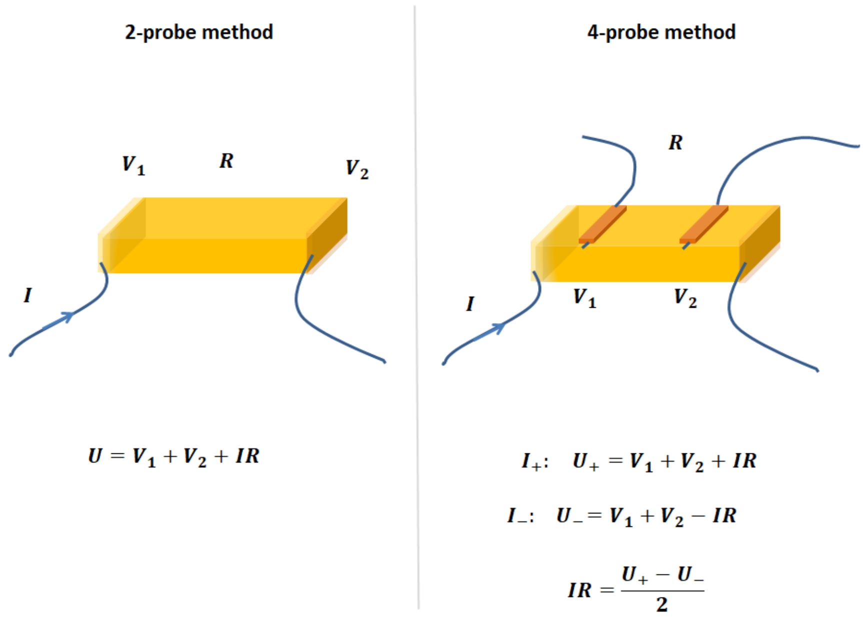

FIGURE 4.10: Four-probe method versus two-probe method.

4.3.2 Current-Voltage (I-V) measurements

The ACT option traces voltage versus current voltage for samples connected to either channel 1 (for sample 1) or channel 2 (for sample 2) on the Model 7100 AC Transport Controller. Physical connections to the sample are made in a similar way as for resistivity measurements (Fig. 4.9).

In $I - V$ measurement, dc current (I) goes through the sample and may be ramped up or down in small detached steps. The current can start at zero and ramp up to a defined maximum positive or negative current or reversely (i.e., it may start at the specified maximum current and ramp down to zero). The Model 7100 provides up to 2 Ampere current. While the current I is ramped, the associating voltage drop V across the sample is measured and reported. Throughout the current ramp pattern, a discrete number of current and voltage readings is taken, and an $I - V$ curve plot is thereby created. An isothermal $I - V$ curve demonstrates the response of a sample at fixed temperature to the passing current. This may be of particular interest when nonlinear behavior exists such as in our study. We point here that the PPMS system provides fully automated temperature control and the temperature instability is of the order of 10^{-4} K what gives reliability to the measured data.

We note that once the ACT software is started, it automatically measures the power line frequency. Each $I - V$ data point is obtained over an integral number of line cycles in order to reject power line noise. Furthermore, the “Remove Voltage Offsets” setting can be used to measure the zero-excitation baseline voltage prior to each $I - V$ measurement and then subtract this voltage from the entire set of $I - V$ data. In order to take an $I - V$ measurement curve, one has to define the measurement by a series of settings. A particular attention has to be paid to the settings that help to protect the sample such as setting the “power limit” and the "voltage limit".

The "Constant Current Mode" has to be activated if the Model 7100 is going to operate in constant current mode, also recognized as high-impedance mode. Constant current mode is the default operating mode as it is the preferred mode for most applications. In the constant current mode, the potential drop across the current leads is adjusted in order to maintain a desired current through the sample, regardless of sample resistance. The Model 7100 is not a perfect current source when the low-impedance mode is opted. This is because the available current decreases as the potential drop increases across the current leads and the actual current is equivalent to the requested current only when the sample resistance is so low in comparison with the Model 7100 current drive source impedance. Low-impedance mode may be useful when an $I-V$ curve might be multiple-valued in the current I. Fig. 4.11 compares the behavior of the current in both operating modes.

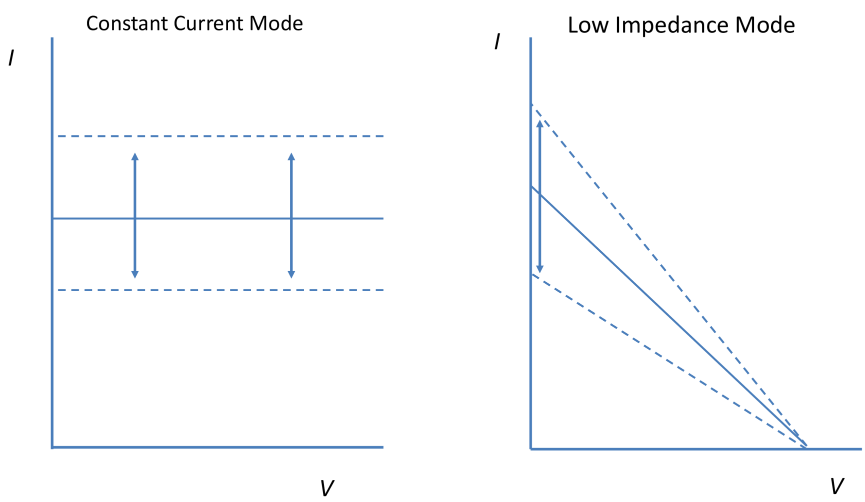

FIGURE 4.11: The available current as a function of voltage drop across the current leads. The dashed lines indicate how the current behaves when the current setting is changed.

Our experimental investigations showed that the PPMS (with the automatic voltage offset subtraction) does work well in case of thicker polycrystalline samples, which are more or less homogeneous. However, in thinner samples (d <4 nm) we approach the situation when inhomogeneities, in form of extended grain boundaries, start to work as Josephson junctions, what may produce superconducting diode effect. This may produce very strange, non-reproducible measuring effects when using automated measurements by PPMS. In addition, the PPMS measures down to 2 Kelvins only what limits our measurement range of temperature for thinner samples, in particular, those which require measuring in the millikelvins range. This is the reason why in case of thinner samples we decided to use another setup (will be discussed next) with separate current source, lock-in amplifier with preamplifier, etc., in which measuring parameters are defined by user, not automated as in PPMS.

4.4 Dilution Refrigerator

Here, we briefly discuss the dilution refrigerator, the technique we used for our transport measurements at very low temperatures (millikelvins).

4.4.1 Technical description

The 3He/4He dilution refrigerator operates in a closed-loop cooling system and uses the heat of mixing of those two isotopes of helium, 3He and 4He, to obtain cooling and thus enabling measurements down to millikelvin temperatures [185]. At temperatures below 870 millikelvin (precise temperature depends on the 3He concentration) the 3He-4He mixture separate sponteneousley into two phases: concentrated phase (i.e., 3He rich phase) and dilute phase (3He poor phase). The concentrated phase becomes pure 3He (100% 3He) while in the dilute 4He rich phase (93.4% 4He) there remains 6.6% of 3He. Because of a boundary between the phases and since the enthalpy of 3He in the concentrated phase is smaller than in the dilute phase, energy is required (endothermic process) to move 3He particles from the concentrated to the dilute phase. In a dilution refrigeration process this energy is taken from a well isolated environment so cooling will take place. In principle, the cooling provided by the dilution unit is based on the 3He requiring heat when pumped into the dilute phase, which provides cooling in the environment this happens in. In the dilution unit, the isolated environment where the mixing of the Helium isotopes occurs is called the Mixing Chamber. That's where the phase boundary (separating concentrated and dilute phases) is located, and where the cooling occurs when the 3He is pumped through the phase boundary. Other main components of the dilution unit (see Fig. 4.12) are the still chamber, the continuous flow heat exchanger (in the form of a spiral), and the step heat exchangers.

The mixing chamber connects to a still chamber, which distils the 3He from the 4He due to the difference in vapor pressure (3He > 4He). Heat must be applied to the still to increase evaporation (To avoid rapid cooling to a temperature where the vapor pressure in the still chamber becomes very low and the pumps cannot effectively circulate 3He and hence the circulation stops). As 3He has larger vapor pressure than 4He, this process distils 3He out of the mixture (the 3He concentration in the gas phase is $\sim$90). More power to the still indicates a higher circulation rate, thus resulting in higher cooling power. In a steady state operation, 3He comes to the dilution unit pumped with a gas handling system (GHS). It enters the dilution unit precooled first by the pulse tube cryocooler (since there is no necessity for external supply of cryogenic liquids) down to about 3 kelvin, and through the main flow impedance in the still chamber. From there it proceeds to the continuous flow heat exchanger and subsequently to the step heat exchangers, which cool the 3He going to the mixing chamber. From the mixing chamber the 3He goes into the still chamber and evaporates in a gaseous phase through a still pumping line, eventually returning back to the start of the process (through the GHS in which 3He is purified and then pumped back into the condensation line). As 3He vapor is pumped from the liquid inside the still, the 3He concentration in the liquid will decrease. The difference in 3He concentration between the still and the mixing chamber results in an osmotic pressure gradient along the connecting tube. This pressure pulls 3He (up to the still)

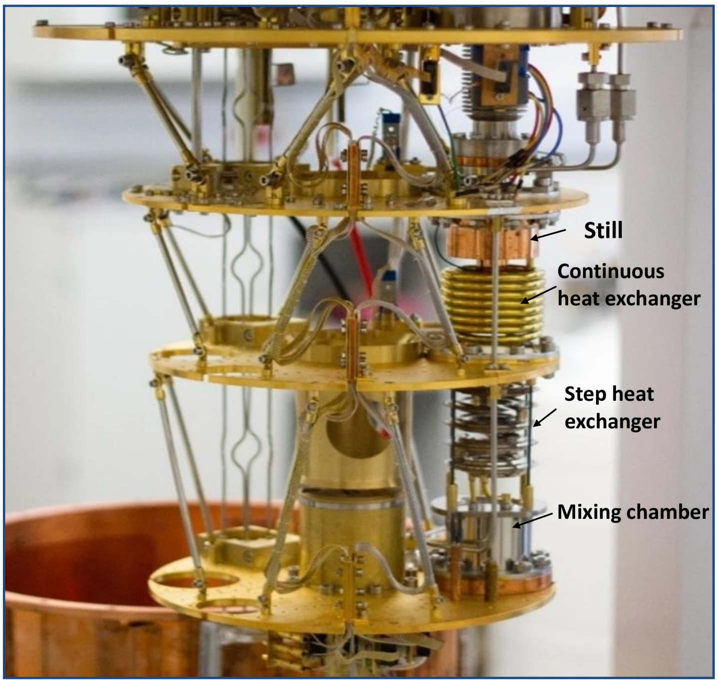

FIGURE 4.12: Dilution unit of the refrigerator (AGH University of Krakow) used for our millikelvin transport measurements.

from the mixing chamber. The efficiency of the dilution refrigerator is determined by the efficiency of the heat-exchangers. The ingoing 3He should be cooled by the outgoing 3He (from the still) as much as possible. The available cooling power is determined by the circulation rate of 3He. The larger the flow, the larger the cooling power, provided that the heat-exchangers can handle the increased flow rate.

The 3He/4He dilution refrigerator whose dilution unit is shown in Fig. 4.12 allows reaching and stabilizing temperatures in the range [10 mK-30 K]. Cooling power at 100 mK is 200 μW, and at 20 mK is 4 μW. The integrated superconducting magnet allows for generating the magnetic field up to 14 T. The unique system of sample exchange allows changing the sample at a temperature of 10 K. Thus, the time needed to replace and cool the sample to 100 mK is about 72 hours. The refrigerator is equipped with 2 bundles of 12 pairs of wires for DC current measurements. One bundle is made of constantan and the other one (superconducting) is made of Cu/NbTi. There are also 8 coaxial cables allowing to perform AC measurements up to 500 MHz. The temperature measurement is carried out using the RuO_2 thermometers calibrated in temperature range from 50 mK up to 30 K. Measuring at temperatures <50 mK to a high degree of accuracy is possible by using a CMN reference thermometer and a superconducting cascade thermometer SRD1000. The thermometer is approximately 1 cm away from the sample, located on the cold finger (in the mixing chamber of the refrigerator) where the sample is placed. For four-probe measurements, the sample is mounted on a puck and wired same as shown in Fig. 4.9.

Chapter 5

Results and Discussions

5.1 Evolution of BKT phase transition in disordered Nb films

5.1.1 Temperature dependence of resistance

In this sub-section we discuss inhomogeneity effects in the SC state, mainly on the observation of BKT phenomenon in disordered Nb thin films through the temperature dependence of resistance. There are two distinct types of SC fluctuations which possibly coexist in a wide variety of 2D systems; namely, the Ginzburg-Landau (GL) fluctuations and BKT fluctuations. The choice of the GL-mean field transition temperature, T_{MF}, is a well-known problem in the analysis of the fluctuation study. Various criteria for determining the T_{MF} have been considered in the literature [186–189] such as (i) midpoint of the resistive transition i.e., 0.5 R_N (R_N is the normal-state resistance), (ii) 0.9 R_N, etc. In this study, we use the formula proposed by Aslamsov and Larkin (AL) [190, 191] to estimate T_{MF} for our films in the absence of magnetic field. According to AL theory, T_{MF} can be estimated through the fluctuation induced 2-dimensional excess conductivity (known as paraconductivity) above T_{MF} in the temperature dependence of resistance according to:

$$[R_{sq}^{-}1 - R_N^{-}1]^{-1} = a((T - T_{MF})/T_{MF}) \tag{5.1}$$

where a is some constant (sample-dependent).

In Fig.5.1, we display, on a linear-linear scale, the normalized sheet resistance (R_{sq}/R_N) of Nb films with different thickness (d) as a function of temperature (T) measured in the absence of external magnetic field (B=0).

As shown in Fig.5.1 the normal-to-superconducting (NM-SC) phase transition shifts toward lower temperatures T along with increased normal state resistance (see results in Table 5.1) when d decreases. We also observe that the top parts of the transitions become increasingly broadened on the decrease of d.

Using the $R_{sq}(T)$ data from Fig. 5.1, we display in Fig. 5.2(a-f) the results for the evolution of T_{MF} with decreasing d. T_{MF} is estimated from the linear extrapolation

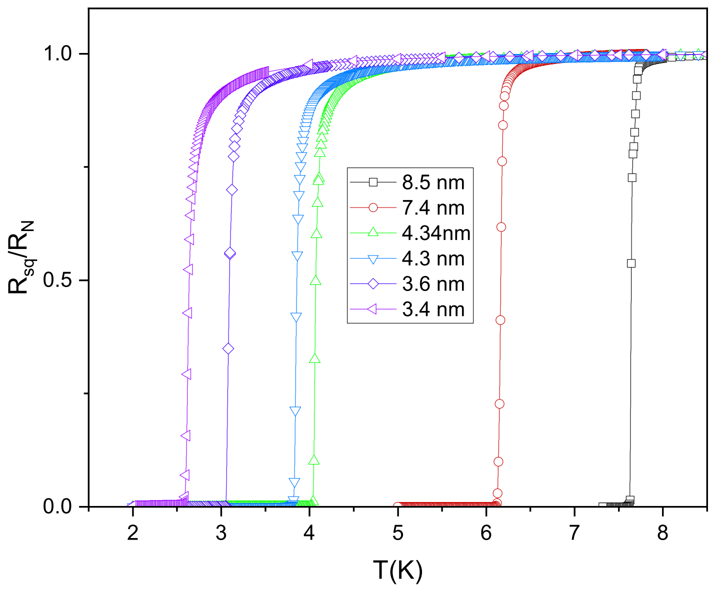

FIGURE 5.1: Temperature dependence of sheet resistance $R_{sq}(T)$ (normalized to R_N)for Nb films with different thickness d. Measurements were performed at different measuring currents ($I = 0.5$ mA, 0.2 mA, 0.2 mA, 0.05 mA, 0.1 mA, 0.03 nm for d =8.5 nm, 7.4 nm, 4.34 nm, 4.3 nm, 3.6 nm, and 3.4 nm respectively).

using Eq. 5.1. As shown, fitting lines intersect the T-axis at T_{MF}. Interestingly, 8.5 nm-film shows a step-like resistive behavior close to normal state (the inset of Fig. 5.2(b)) which we could not observe neither for the thicker film (d=44 nm) nor for thinner films (d <8.5 nm). Using Eq. 5.1, two sets of the $R(T)$ data which together build up the step-like resistive behavior can be extrapolated separately (dashed blue and dashed green extrapolation lines) thus pointing out two distinct transition temperatures separated by ∼0.058 K. This suggests that exotic phenomenon may mediate the AL fluctuations probed at 0.5 mA current. This in turn suggests different origins of inhomogeneity effects on the NM-SC phase transition in 8.5 nm-film. The possible origin of the step-like resistance behavior will be addressed later in the text. When d decreases further, we can see in Fig. 5.2(c, d) some encircled portions of the data which do not show step-like features upon phase transition. In the discussion of Sec.5.1.2 (current-voltage characteristics) we will refer back to this issue and show that turbulences in the $R(T)$ dependence in the vicinity of T_{MF} may be better inferred from the nonlinear behavior of current-voltage characteristics. In particular, we demonstrate that the step-like features we obtain in $R(T)$ behavior may originate from phase slip (PS) phenomena, which can cross to GL and BKT fluctuations as d decreases in a non-trivial way. In $R(T)$ measurement, unveiling the characteristic features of such phenomena in presence of film inhomogeneity is believed to be dependent on the fixed current used for measurements. This is likely why for thinner samples, Fig. 5.2(c-f), we do not observe these features while they may be manifested in current-voltage measurements (Fig. 5.13(b)). In general, in $R(T)$ measurements, the magnitude of current driven into a sample plays crucial role in disclosing the various possible effects of present inhomogeneity on transport properties.

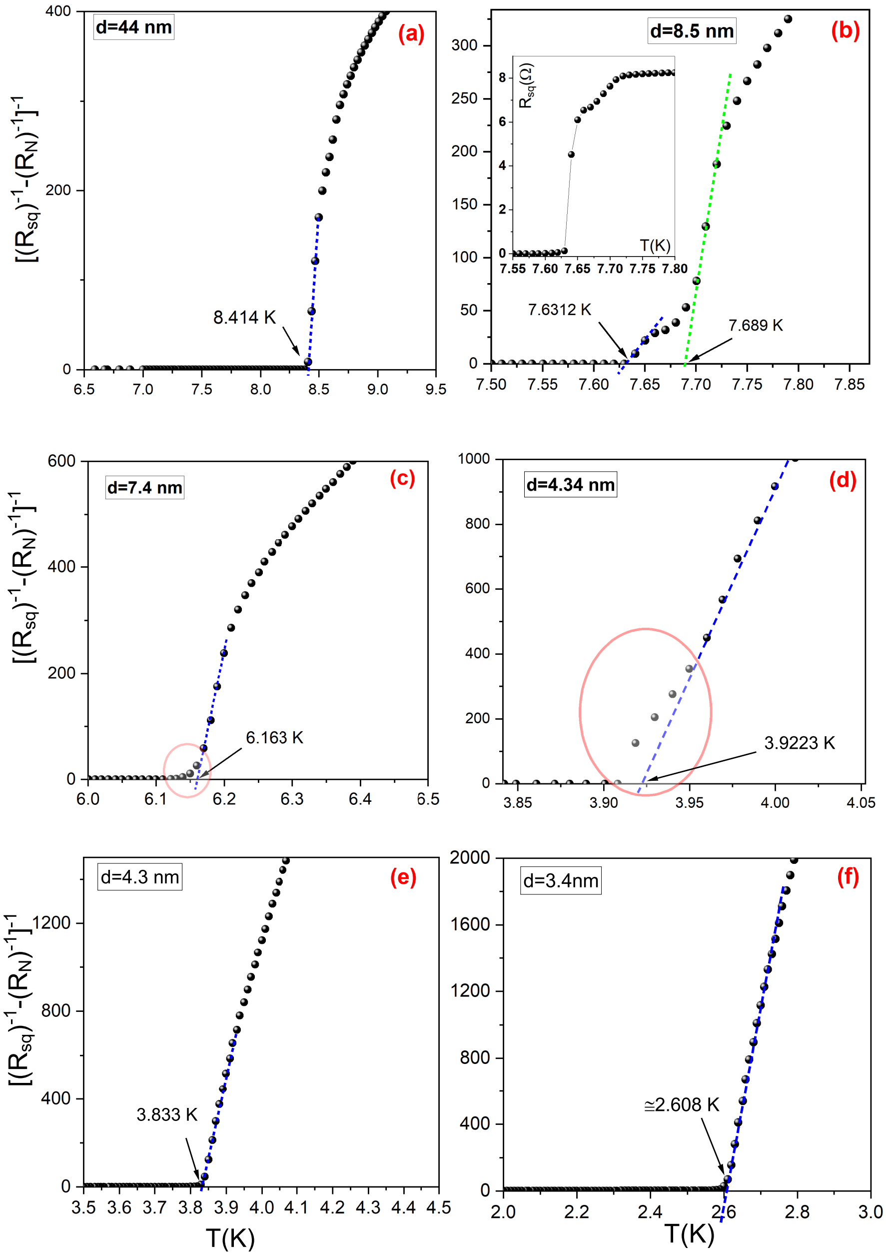

FIGURE 5.2: Estimation of T_{MF} using AL-method for Nb films of different thickness (d). The dashed lines (blue and green) represent linear extrapolation fits to the data indicated by (black) points, crossing the T-axis at T_{MF}. Results for T_{MF} are also summarized in Table 5.1.

Fig.5.3 illustrates another analysis method of $R_{sq}(T)$ dependence for three Nb films (investigated already using AL-method). We recall Eq. 3.10, an approximate interpolation formula for the T-dependence of the resistance, $R_{sq}(T)$, proposed by Halperin and Nelson (H-N) where the T_{MF} and BKT transition temperatures (T_{BKT}) are related by the following equation:

$$R_{sq}(T) \approx const * R_N exp\left(-2\left(c\frac{T_{MF}-T_{BKT}}{T-T_{BKT}}\right)\right) \tag{5.2}$$

The T_{MF}, T_{BKT}, and dimensionless constants *const* and c are adjustable (sample-dependent) fitting parameters and R_N is determined from experimental data. The values of the T_{MF} and T_{BKT} resulting from the fits are shown inside the figure.

In clean samples, the T-fluctuation region above T_{BKT} is usually dominated by AL fluctuations, while BKT fluctuations are limited to a narrow range in the vicinity of T_{BKT}. Within this range, the resistance decreases exponentially. The interval ($T_{MF}-T_{BKT}$) is governed by the proliferation of vortex-anti vortex (V-AV) pairs which are thermally dissociated in the vicinity of T_{BKT} under the influence of the bias current. This interval turns to be more prominent for disordered films due to broadening of the NM-SC phase transition associated with a modified crossover from GL to BKT SC fluctuations. As we can see in Fig. 5.3 , the obtained values for T_{MF} and T_{BKT} for the films are barely differentiated from one another when fitting the data using relation 5.2. In addition, in case of 8.5 nm film these values fell between two different temperatures extracted using AL-method. Thus, it appears that the relation given by 5.2 is too simplified for the proper description of the data.

In the following we use more sophisticated equation suggested by Halperin and Nelson, which does not require fitting of the T_{MF}, but instead allows to fit parameter b, which is related both to the difference between T_{MF} and T_{BKT}, and to the vortex-core energy (estimated as the loss in the condensation energy within a vortex core of the size of the order of the BCS correlation length [136]. Using Eq. 3.6-3.8 from chapter 3, we have:

$$\frac{R_{sq}(T)}{R_N} = \frac{1}{1+(A\sinh(\frac{b}{t}))^2} \tag{5.3}$$

with $t = (T-T_{BKT})/T_{BKT}$.The constant A is chosen to be 2 for all films. If no vortical fluctuations, $A = 0$. b and T_{BKT} are free fitting parameters. b is the most relevant parameter to determine the shape of resistance above a BKT transition and it is connected to the interval $t_{MF} = (T_{MF}-T_{BKT})/T_{BKT}$ and the vortex-core energy (μ) [33]. According to theory, b is proportional to the energy scales μ and J_s (the 2D superfluid stiffness) and t_{MF} according to Eq. 3.8; $b \sim (4/\pi^2)(\mu/J_s)\sqrt{t_{MF}}$.

The BKT correlation length $\xi(T) \sim A\sinh(b/\sqrt{t})$ is expected to interpolate in a continuous way between the BKT regime and the GL-regime. The BCS-GL theory predicts that of $\xi(t)$ diverges as power law at T_{MF} whereas BKT theory predicts its divergence asymptotically, i.e., exponentially at T_{BKT} according to $\xi(T > T_{BKT}) \sim \exp a/(T-T_{BKT})^{1/2}$ [27]. In presence of disorder, such as in the case of films studied

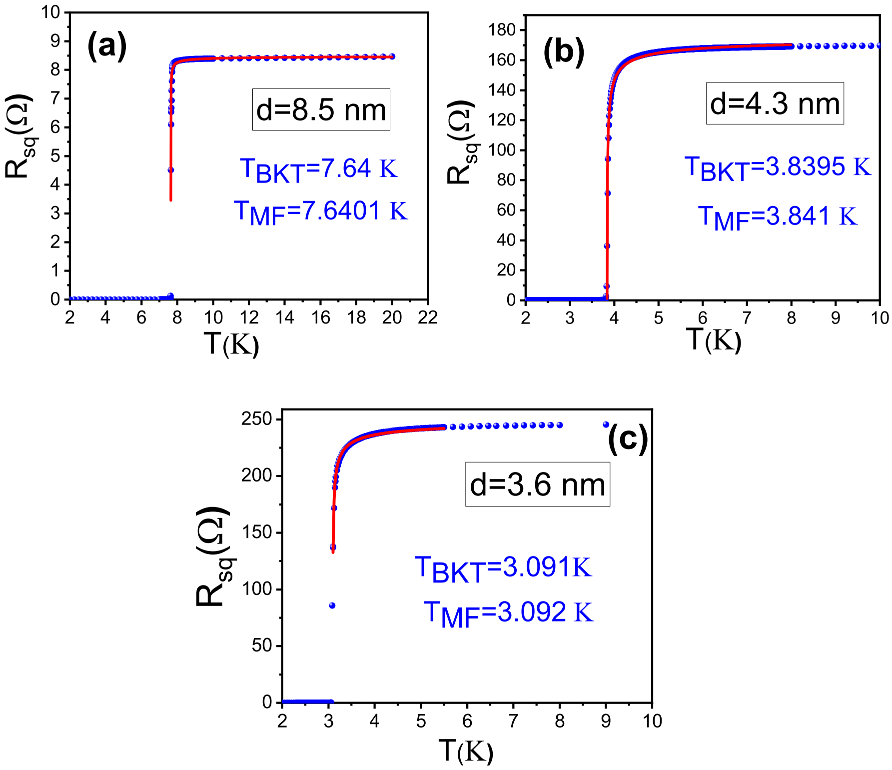

FIGURE 5.3: $R_{sq}(T)$ for Nb films with different d. The (red) solid lines correspond to theoretical fits of Eq. 5.2 to the data indicated by (blue) points. T_{BKT} and T_{MF} values are given in the figures.

here, scenario gets complicated and careful understanding is required. The fits of Eq.5.3 to the resistance data for all films are shown by red lines in Fig. 5.4(a), while in Table 5.1 we present the parameters obtained from the fits, R_N , b ($\sim$ vortex-core energy) and T_{BKT}.

The plots of resistance on the logarithmic scale (Fig. 5.4(a)) reveals distinctive difference between three films with larger thickness (d=8.5 nm, 7.4 nm 4.34 nm) and three thinner films (d=4.3, 3.6 and 3.4 nm). Thicker films show relatively narrow transitions and very low resistance at low T. On the other hand, the transition is much more broadened in case of thinner films. We also note that, as d decreases, the resistance in the limit of low temperatures saturates at finite (not zero) level. This signals the possible development of the fractal superconductivity, in which superconducting regions do not encompass uniformly whole sample, but create inhomogeneous mixture of superconducting islands immersed in non-superconducting background.

In Table 5.1, the evolution of the parameter b with decreasing d shows that b increases with increased inhomogeneity effects as d decreases. If we use the formula given by Eq.3.8 for our films and use the values of b we obtained for from the $R(T)$ fits, we can obtain values for μ/J_s as shown in Fig. 5.4(b). The values which we obtain for thicker films are significantly smaller than these predicted by the XY model (for which μ/J_s=4.9 [137]), but they increase with decreasing d. Very similar behavior of parameter b has been obtained for thin NbN films [17]. Comparison of the results of the penetration depth measurements discussed in [17] confirmed small

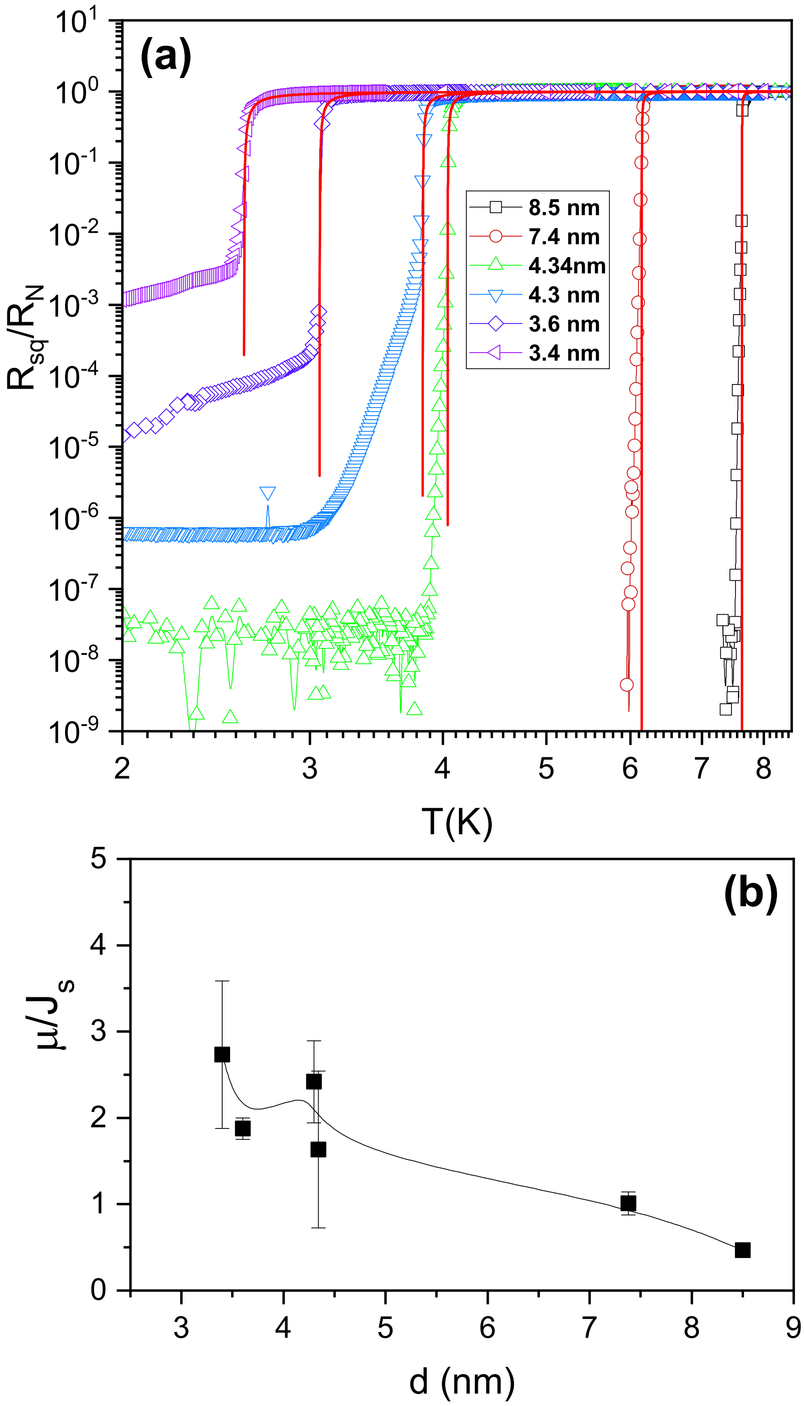

FIGURE 5.4: (a) Normalized sheet resistance $R_{sq}(T)/R_N$ versus T (of Fig. 5.1) on a log-log scale for Nb films with different thickness (d= 8.5 nm, 7.4 nm, 4.34 nm , 4.3 nm, 3.6 nm and 3.4 nm). The (red) solid lines correspond to theoretical fit of Eq. 5.3 to the experimental data indicated by (colored) points. (b) μ/J_s calculated using ($b \sim (4/\pi^2)(\mu/J_s)\sqrt{t_{MF}}$) versus film thickness (d); in the formula we used T_{MF} obtained from AL-methodand T_{BKT} obtained from ($R(T)$ fits using Eq.5.3.

d (nm)	T_{MF} (from AL method) (K)	R_N (Ω)	b (unitless)	T_{BKT} from $R(T)$ (K)	T_{BKT} from $I-V$ (K)
44	8.414	2.079	0.0121	8.393	Not meaured
8.5	$T_1 = 7.689$, $T_2 = 7.631$	8.437	0.013	7.632	between 7.62-7.63
7.4	6.163	38.19	0.017	6.154	between 6.075-6.084
4.34	3.922	147.3	0.037	3.905	between 3.8-3.824
4.3	3.833	169.67	0.041	3.829	3.1
3.6	3.07	274.1	0.047	3.060	≈ 1.65
3.4	2.608	377.4	0.057	2.602	Not measured

TABLE 5.1: Results for R_N, b, and T_{BKT} obtained from theoretical fits of Eq. 5.3 to experimental data shown in Fig. 5.1 for Nb films with different d. All fits were performed with selecting A =2. We also summarize the results for T_{MF} estimated using AL-method. In particular for d =8.5 nm, we have slightly different two values for T_{MF} (T_1 ≈7.69, T_2 ≈7.636 K) obtained using the effective medium approximation (EMA) (see discussion on EMA). Moreover, we show the results for the evolution of the BKT-like phase transition temperature (denoted as T_{BKT}) extracted from the analyses of the low $V(I)$ characteristics of all indicated films (Sec.5.1.2)

values of for μ; it is shown that such value is indeed expected in BCS superconductor. Moreover, the increase of μ/J_s with increasing disorder (Fig. 5.4(b)) is also similar to that reported for NbN [17]; it is due to the fact that the loss of the condensation energy within the vortex core becomes energetically more expensive in disordered superconductor.

In order to test validity of our T_{BKT} extraction, we have used the extrapolation method [138], described by Eq. 3.11 in Chapter 3, which relies on linear T-dependence of the quantity $[dlnR_{sq}(T)/dT]^{-2/3}$. This procedure results in plots shown in Fig. 5.5, from which we obtain T_{BKT} values almost identical to those found from Eq.5.3. An interesting and remarkable feature seen in the figure is the appearance of finite value of the quantity $[dlnR_{sq}(T)/dT]^{-2/3}$ below the T_{BKT} in films with d <4.3 nm. Mathematically, it results from tiny but finite value of the R_{sq} at low temperatures, which is not expected in case of true BKT transition. The finite value of R_{sq} suggests that the SC state in these thinner films becomes increasingly inhomogeneous, so that the current used for these measurements, however small, destroys superconductivity locally. Since the data presented in Fig. 5.5 has been measured down to 2 K only, we cannot exclude the possibility that resistance will eventually drop to zero at lower T. As will be discussed in next subsection, the extension of IV measurements of films with $d < 4.3$ nm down to millikelvin region indeed indicates persistence of finite residual resistance below T_{BKT} specified in Fig. 5.4, which, however, eventually decreases to zero. As will be discussed, this behavior is attributed to the Josephson coupling (JC) between superconducting islands.

Now, in order to gain more insights into the phase transitions in our films, we select 8.5 nm-film as a reference sample to understand the evolution of BKT transition as thickness decreases. But before we proceed further, we would like to comment briefly on the induced inhomogeneity in superconductors with granular or non-granular type structures. Historically, the term "granular" has been used to describe materials in which SC islands are immersed in the non-SC (usually insulating) matrix; inhomogeneity in such materials is structurally evident, and frequently leads

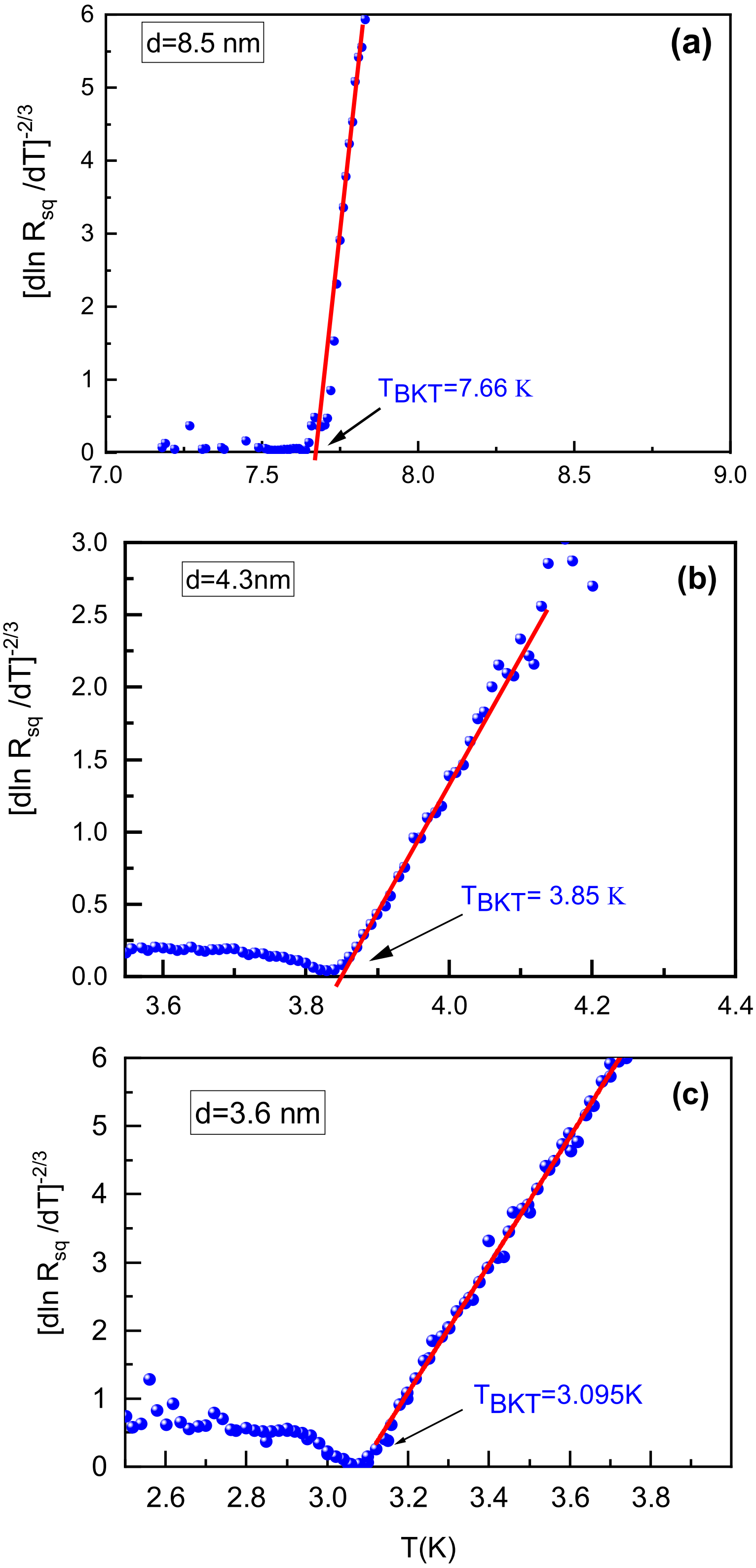

FIGURE 5.5: $[dlnR_{sq}(T)/dT]^{-2/3}$ versus T for Nb films with d=8.5 nm, 4.3 nm and 3.6 nm. T_{BKT} (marked in the figures) are derived by extrapolation of the linear section as indicated by continuous (red) lines.

to non-monotonic temperature –dependence of resistance. As studies of SC materials progressed, it turned out that even materials which appear to be structurally homogeneous may show presence of inhomogeneity, e.g., high-T_c superconductors in which weak links contribute to Josephson junctions. In high-T_c superconductors, the coherence length is short, so these materials are more sensitive to disorder on small scale. In conventional superconductors, the coherence length is quite large, so they are less sensitive. Furthermore, studies using scanning tunneling spectroscopy measurements [14, 192] have shown that even when disorder in the system is homogeneous, the system shows an intrinsic tendency towards the formation of spatial inhomogeneity in the SC state. This matter has to be taken into account while analyzing the BKT transition.

In Fig. 5.6, we show, on linear-linear scale, the sheet resistance of as a function of temperature for 8.5-nm film (a) and 7.4 nm (b). In (a) we observe a two-step NM-SC phase transition in 8.5 nm-film which we do not observed in 7.4-nm film (b). When it comes to granular systems, such two-step resistive phase transition is often explained by "granular" nature of the film in the form of randomly distributed nanoscale SC grains separated by grain boundaries [38, 193–195]; the transition is explained as evolution of local superconductivity into global superconductivity with decreasing temperature where the inhomogeneous nature of the samples may be caused by the differences in the grain size what affects the broadening features of the transition. Such scenario may be valid for thinner Nb films ($d < 5$ nm) in our case since our Nb films reveal transformation from polycrystalline structure ($d >$5 nm) into amorphous structure ($d <$5 nm) until it becomes completely amorphous at $d \approx$3.3 nm [81]. In next subsection (5.1.2) we will show that the two-step transition in 8.5 nm-film has a different origin and it is generated by phase slip phenomenon, triggered by the dimensionality of the film.

Now, let us turn more attention to Region I and Region II where the double-step resistive behavior is manifested for 8.5nm-film (Fig. 5.6(a)). Indeed, as will be demonstrated, we could reproduce the resistance behavior as T decreases including both regions (I, II) using the effective medium theory (EMT). EMT approximation (EMA) is a statistical approach useful in describing fractal superconductivity by means of modeling the superconductor to a random-resistor-network; at a given temperature T, each resistor may be metallic or superconducting-like in response to the applied measuring current. Fig. 5.7 show that the $R(T)$ data (including those belonging to Regions I and II) can be well-fitted using the following $R(T)$ formula, which reveals the existence of two distinct sets of the SC puddles [196, 197]:

$$R(T) = R_N \left[w_1 erf\left(\frac{T - \overline{T_{c1}}}{\sqrt{2}\gamma_1}\right) + w_2 erf\left(\frac{T - \overline{T_{c2}}}{\sqrt{2}\gamma_2}\right) + 1 - w_1 - w_2 \right] \tag{5.4}$$

Here R_N is the normal sheet resistance, $\overline{T_{c1,2}}$ is the random local critical temperature for each puddle in the first/second set of the puddles; assumed to have a Gaussian shape distribution, with mean $\overline{T_{c1}}$, $\overline{T_{c2}}$ and width γ_1, γ_2, respectively. The weight w of the T_c statistical distribution represents the fraction of the SC puddles (i.e., w_1 for puddles with $\overline{T_{c1}}$ and w_2 for puddles with $\overline{T_{c2}}$ and the non-SC fraction $(1-(w_1+w_2))$ represents the metallic background. For the case w_2 =0 we have only

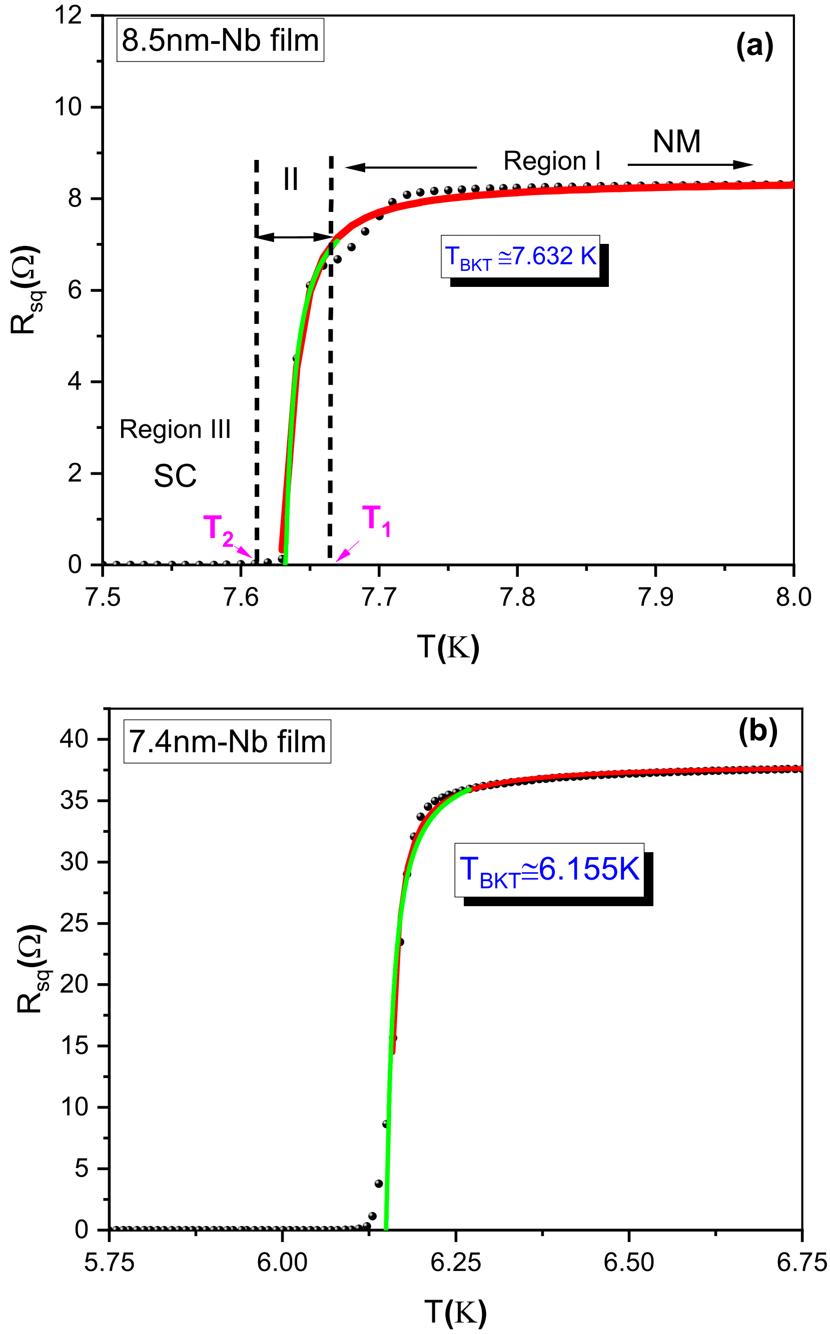

FIGURE 5.6: Two-step NM-SC phase transition of 8.5 nm Nb film revealed by using $R(T)$ characteristics. Green solid line in (a) shows a fit of the data in Region II to H-N formula Eq. 5.3 since such region is generally the one expected to best describe the BKT [39]. This is further shown by the tendency of the red fitting curve to skip the data for Region I and continuing to Region II. This suggests an intrinsic phenomenon mediating the GL-to-BKT crossover. This will be addressed further in the text. T_1 is the temperature separating Region I from Region II as indicated. $T_2(< T_1)$ is the temperature separating Region II from the superconducting region denoted by Region III. (b) NM-SC transition for 7.4 nm-film where no step-like resistance behavior as in thicker film can be observed. Red and green lines represent H-N fits in attempts to mimic the fits in (a).

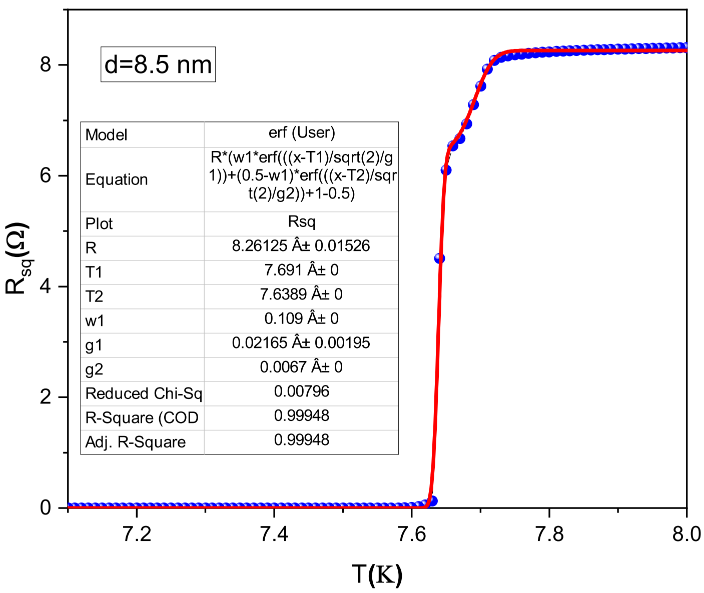

FIGURE 5.7: Fit of the $R_{sq(}T)$ data for8.5 nm-film using EMA.

a single Gaussian distribution, describing the SC transition at $\overline{T_{c1}}$. The SC fraction can percolate in the system only if $((w_1 + w_2) \geq 1/2)$ (the weight $1/2$ is the threshold for homogenous distribution of SC puddles describing the weakly percolating case), and only then the percolative SC transition marked by vanishing effective resistance R may take place at the temperature $T_p \leq \overline{T_c}$. We point out that EMA has been also discussed elsewhere [17, 36, 196, 198] .

Our EMA analysis using Eq. 5.4, in the weakly percolating case (w =0.5), yields two distinguished SC transition temperatures ($T_{c1} > T_{c2}$), thus indicating a two steps-phase transition to the normal state. The T_{c2} =7.638 K, locates in Region II but on the verge of the SC phase ($T < T_2$) shown in Fig. 5.6(a), is the one with the most-dominant statistical SC weight fraction ($w_2 \approx 0.4, \gamma_2 \approx 0.007$) of the statistical ensemble characterizing the film. On the other hand, the $T_{c1} = 7.691$ K ($\approx T_1$) which is characteristic of the rest of the SC percolation weight ($w_1 = 0.5 - w_2 \approx 0.1, \gamma_1 \approx 0.02$) locates in Region I on the verge of the "normal" phase. This in turn confirms that the SC-NM phase transition is fundamentally described by Region II (where T_{c2} locates) for the film. We point out here that modulating γ in experiment is expected to smoothen out the step-like transition feature in the resistance obtained for our film. We note here that T_{c1} is almost identical to T_1 from the AL-method, see Fig. 5.2(b). Furthermore, we note that T_{c2} (7.638 K) is close to the values for T_{MF} estimated using the AL-method (i.e., T_2 =7.631 K in Fig. 5.2(b)) and H-N model (7.636 K) analyses. This reveals how different T-fluctuations statistical models (i.e., EMA, AL-method and H-N) tend to capture the T_{MF} describing puddles of the most SC weight fraction. Hence, we conclude that T_{MF} =7.63(4) K, estimated from analyses of Region II using these models, is the temperature at which the major SC phase of the bulk undergo the very first mean-field transition towards the normal phase in 8.5 nm-film. The remaining issue concerns the nature of the possible BKT transition preceding the mean-field transition ($T_{BKT} < T_{MF}$). This will be addressed more in

Sec. 5.1.2.

Likewise, by following similar procedures and fitting the $R(T)$ data for thinner films (d <8.5 nm) using the different statistical approaches discussed above, we may observe the effects of film inhomogeneity on transport characteristics. As shown in the inset of Fig. 5.8(a), 7.4 nm-film demonstrates that in the $R(T)$ regime expected to describe the BKT-to-GL crossover, the data does not strictly follow the EMA fitting curve but rather continue smoothly towards the normal state as T keeps increasing. However, as shown when displayed on logarithmic-linear scale, the data adhere to the fitting curve except those which shows clear deviation as T drops below 6.078 K. Fig. 5.8(b) demonstrate the current-induced discrepancy in the $R(T)$ behavior for 3.4-nm film suggesting that the SC state is fragile towards an applied current, so one can expect a very low superfluid stiffness. This also suggests that the intrinsic non-conductive paths alter with changing the magnitude of the small measuring current in experiment. Consequently, the validity of statistical model, e.g., "random-resistor-network" model [36] and the renormalization group (RG) apparatus [33] may need to re-considered in order to account for the perturbations in the sharp features of the NM-SC transition caused by increasing the current on the expense of present inhomogeneity effects. This becomes more important when a comparison between theoretical and experimental results is held. In general, due to the potential sensitivity of a sample to the measuring current in $R(T)$ measurements, intrinsic inhomogeneity effects resulting in smearing the sharp features of BKT transition may be better described by direct measurements or commonly through the I-V measurements. Measuring the nonlinear I-V characteristics provides more insights into the nature of turbulences in the coherence of the quasi long-range order characterizing a BKT phase.

Fig.5.8(c) shows our attempts to fit the $R_{sq}(T)$ data (measured at I =0.03 mA) for 3.4 nm-film. The green curve shows the fitting result if we assume a two-step transition (similar to 8.5 nm-film) is occurring in the film. We can notice deviations of the data from the curve in the vicinity of the normal state. The red curve shows the result if we assume a single transition temperature characterizing the whole film. As evident from the inset figure, when plotted on a logarithmic-linear scale, we can notice the failure of our fits using EMA. Similar failures were also found when fitting the data measured with reduced current ($I = 10\ \mu$A) for the same film. Indeed, inferior EMA fits were found for all films with d <7.4 nm indicating that EMA is not the most-suitable approach for describing inhomogeneity effects on the phase transitions occurring in these films.

5.1.2 Current-voltage characteristics

GL-to-BKT fluctuations and phase slip line phenomenon

Now, we switch the discussion to the results obtained from evaluating the nonlinear current-voltage characteristics (IVCs) measured for our films. Before we further proceed our discussion on BKT transition, we first would like to firm our understanding on the step-like behavior seen from the $R(T)$ measurement for 8.5 nm-film. But this time, we will look at the problem from the perspective of IV measurements. We

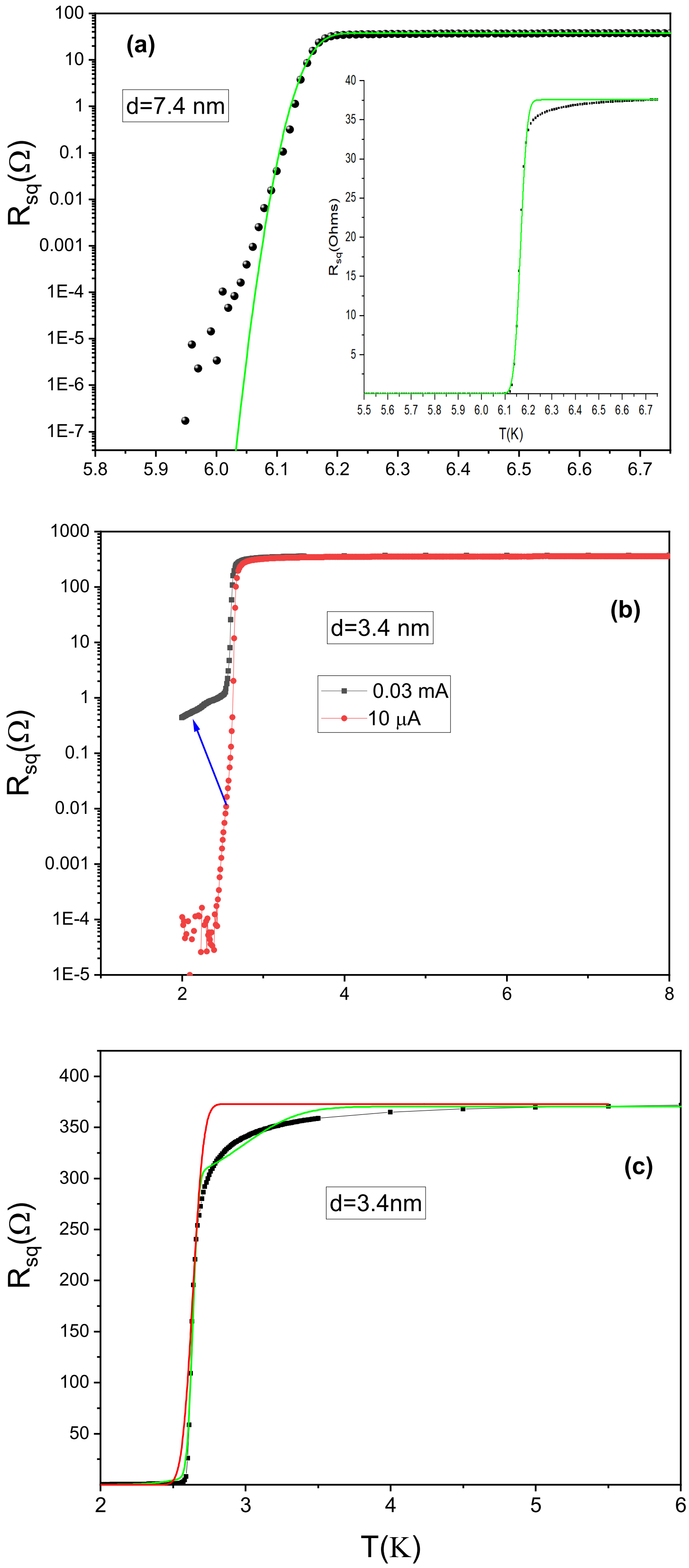

FIGURE 5.8: Results for $R_{sq}(T)$-fits using EMA for Nb films with d=7.4 nm (a) and d=3.4 nm (c). (b) Current-dependent $R_{sq}(T)$ measured for 3.4 nm-film.

aim to understand the meaning of the phase transition temperatures $T_{c1} > T_{c2}$ (with $w_1 < w_2$ obtained from EMA), below which BKT phenomenon may occur (Table 5.1).

Figures 5.9(a) and 5.9(b) shows the non-linear IVCs for 8.5 nm-film measured in zero external magnetic field (B =0 T) and in field (B =0.2 T). The voltage (V) is displayed on the vertical axis of the plot while the current (I) is displayed on the horizontal axis. In the figures, I_{c1} denotes the critical (de-pairing) current (required for breaking Cooper pairs completely). Interestingly, above I_{c1} and as T increases toward the T_{MF}, we notice the emergence of intermediate resistive states in the form of multiple consecutive steps with resistance (voltage) below the normal state-resistance ($V \sim I$). The series of the critical currents ($I_{cn}; n = 2, 3, ..$) denote the currents separating subsequent resistive states intermediating the SC-NM phase transition for an I-V isotherm. Most-likely, such resistive states mark the formation of so–called phase slip lines (PSLs); high current-induced kinematic vortices which are commonly recognized in wide SC films (width $w \gg \xi_0$(BCS coherenc elength)) [199–203]. Numerical simulations suggest that the PSLs effect is caused by rivers of fast moving vortices and antivortices that annihilate in the middle of the sample [57, 58]. Nice visualization of a real effect has been obtained for films of Sn and InSn using scanning laser microscopy [54]. The PSL effect is different from the phenomenon of phase slip centers, which occurs in narrow SC wires with width w much smaller than the coherence length or magnetic penetration depth. We had estimated $\xi(0) \approx$ 11 nm (sec. 5.2) and $\lambda(0) \approx$ 73 nm; on increasing temperature up to $T/T_c = 0.97$ these parameters increase to about 63 nm and 430 nm, respectively, which is well below sample width ($w = 200\ \mu$m), so that the PSL effect is a more likely cause of the observed behavior. Fig. 5.9(b) displays visible PSLs characteristics for 8.5 nm-film, which emerge on the approach to T_{MF} as thermal energy, $k_B T$, increases in the presence of constant, perpendicularly applied magnetic field (B =0.2 T). As T increases, in zero field and in field, the resistive states merge due to getting broadened since the effective size of the sample (within which electrodynamics of phase slip phenomenon occur) in units of the two characteristic lengths (the coherence length $\xi(T)$ and magnetic penetration depth $\lambda(T)$) gets reduced; thus it becomes difficult for the sample to accommodate more PSLs [204].

In the following, we attempt to evaluate the possible effects of phase slip (PS) phenomena on the observation of BKT transition in 8.5 nm-film below the mean field transition ($T < T_{MF}$). Therefore, we decided to generate the $R_{sq}(T)$ curve with the aid of IV measurements. If we use the IVCs data plotted in Fig. 5.9 and plot the isothermal resistance $R = V/I$ versus the scan current (I) we obtain the following $R(I)$ characteristics shown below in Fig. 5.10,

The dotted vertical (black) line in the figure indicates that the readings of the resistance (V/I) of all indicated isotherms are taken at I =0.5 mA, the same static current we used in $R(T)$ measurement. Fig. 5.11 shows a comparison between the sheet resistance $R_{sq}(T)$ measured using resistance measurement at 0.5 mA and the one generated using I-V measurement according to Fig. 5.10. As we can see, the results are almost the same what confirm the step-like behavior of the resistance characterizing NM-SC phase transition in 8.5-nm film.

In view of the previous discussions, we note here that the step in the resistive

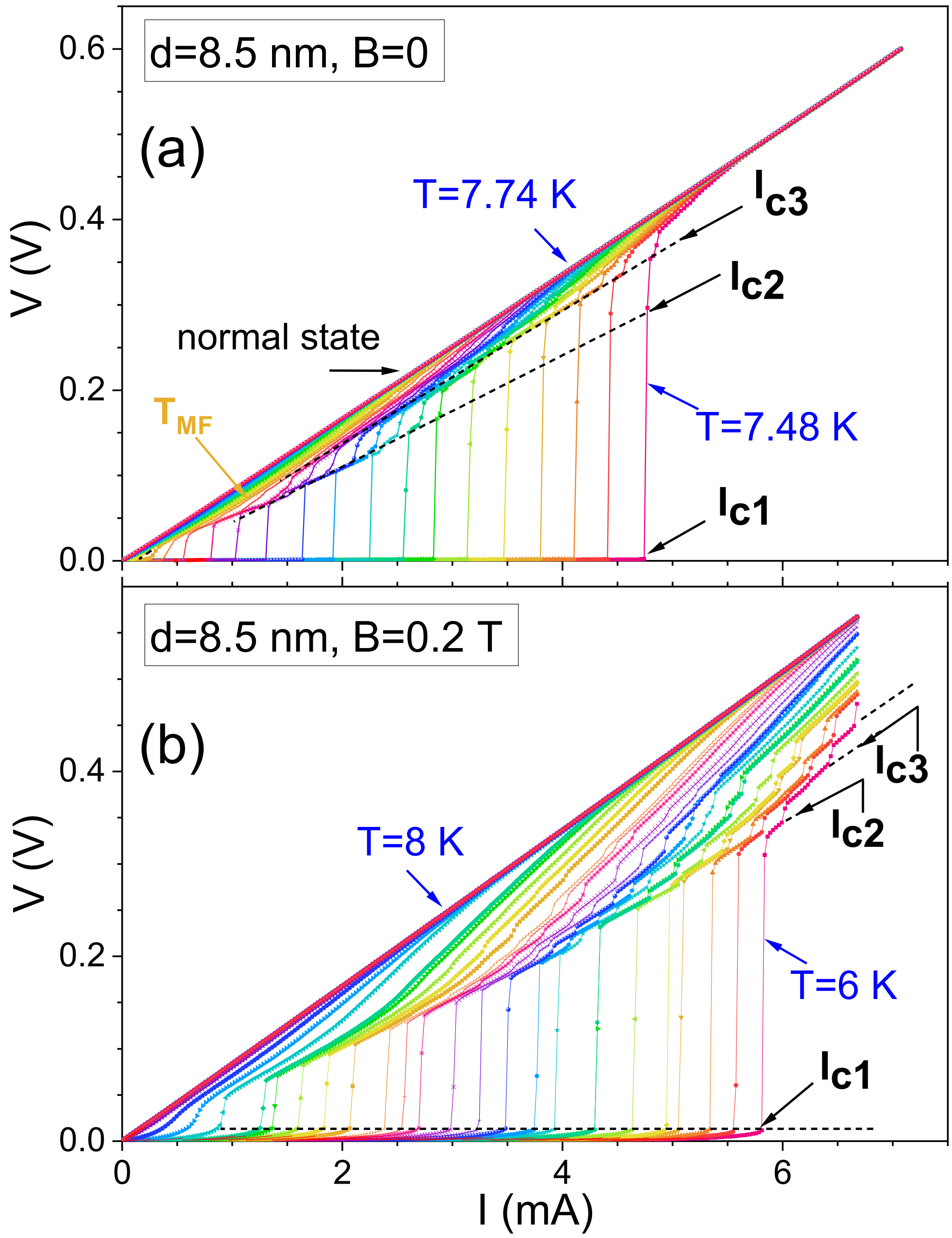

FIGURE 5.9: Intermediate resistive states in the I-V characteristics for 8.5 nm-Nb film at B =0 T (a) and 0.2 T (b). The consecutive measurement temperatures are sepearted by 10 mK in (a), and by 50 mK in (b). The black dashed lines in the figures indicate the locations of sequential critical currents (I_{cn}; n = 1, 2, 3, ...) separating successive resistive states in each I V isotherm.

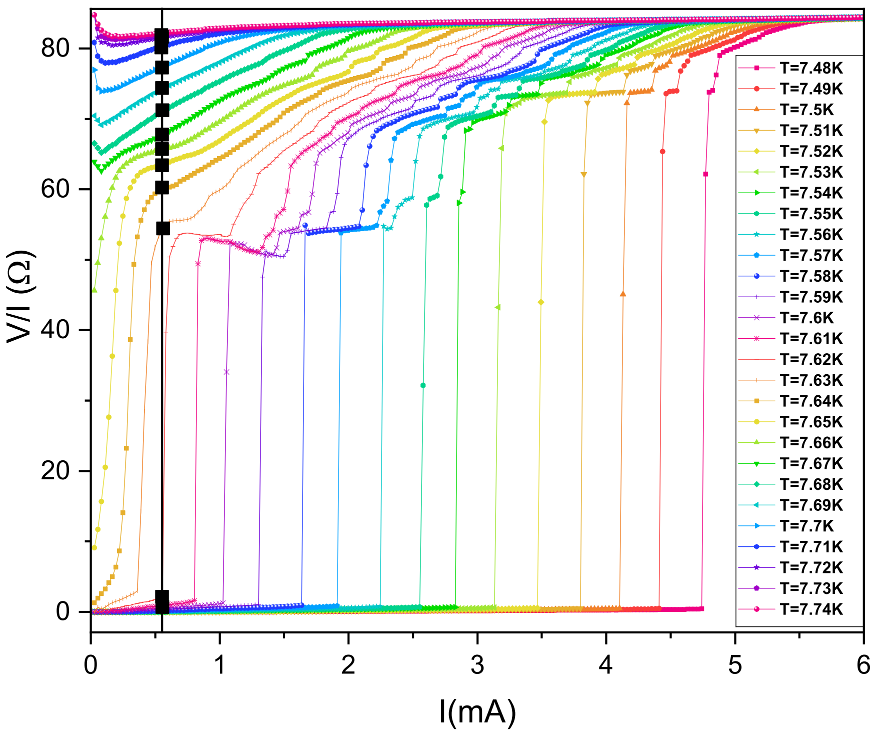

FIGURE 5.10: Resistance (V/I) versus I derived from the IVCs shown in Fig. 5.9.

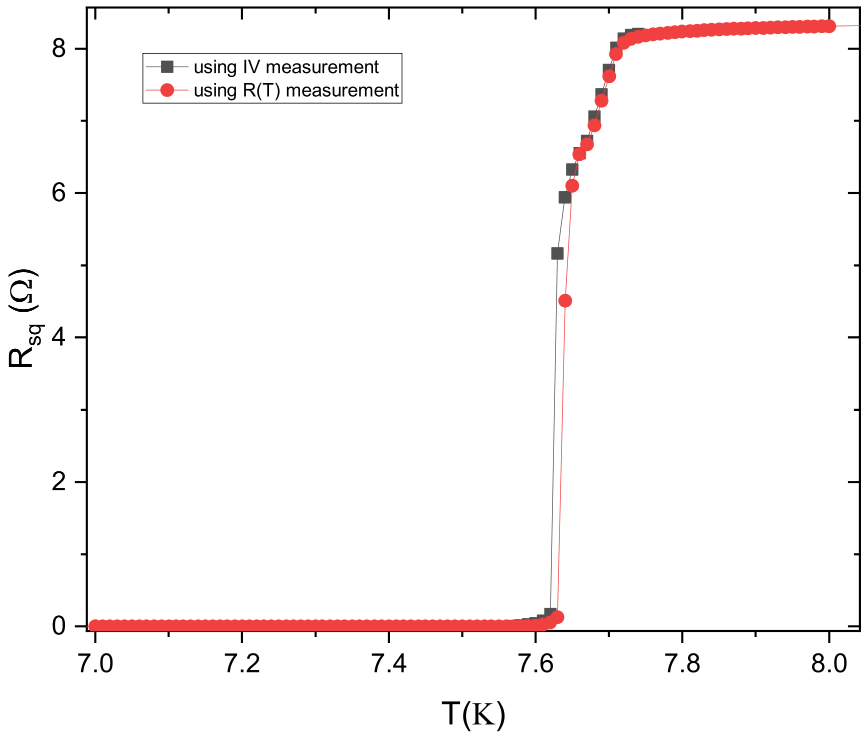

FIGURE 5.11: Sheet resistance, $R_{sq}(T)$, measured for 8.5 nm-film using two types of transport measurement; $R(T)$ and I-V measurements.

transition towards the normal state (labeled by Region I which possibly merge to Region II in Fig. 5.6), represent thermally induced resistive states which are characteristic of PSLs. Consequently, T_{c1} (=7.691 K from EMA and belong to Region I in Fig. 5.6) most-likely acts as the transition temperature of the phase dominated by these PS events at lower temperatures (possibly extending to Region II) towards the purely normal metal phase ($V \sim I$) with increasing T. Hence, the potential BKT transition in 8.5 nm-film may be partially masked by these PS events (under fixed current density) in the vicinity of the mean-field transition. If so, this in turn adds perturbation to the divergence of the correlation length expected at T_{BKT}. Thus, we look further carefully into the BKT problem in 8.5-nm film from the perspective of I-V measurement as will be demonstrated. In fact, both, BKT and phase slip (PS) are complex phase-fluctuation phenomena of difficult experiments, particularly when both phenomena coexist in presence of non-conductive paths in a system. In [205], an evidence of the emergence of both BKT and PS effects in granular NbN films (thinner than 15 nm) has been shown, suggesting a 2D (due to BKT) to quasi-1D (due to PS) dimensional crossover in the same system. Moreover, in [206], the roles of hot-spots (local zones characterized by temperatures higher than T_c and hosted by weak links among SC puddles) and Larkin Ovchinnikov type flux-flow instability on the observation of BKT transition in $KTaO_3$ (111) based superconductor has been addressed.

We point that in ordinary polycrystalline and amorphous superconducting films, it may be not that simple to observe PSLs [207]. Among the experimental challenges [202] are prohibiting the formation of Abrikosov vortices by keeping adequately high energetic barriers at the edges [208] and ensuring good heat dissipation since at high current densities Joule heating may easily smear the current-voltage characteristics [209].

Fig. 5.12 shows, on a log-log scale, the nonlinear evolution of the IVCs in zero field for 8.5 nm-film. BKT theory predicts a typical behavior of the power law $V \sim I^{n(T)}$ with n increasing rather abruptly from 1 in the normal state to 3 at $T = TBKT$, following the universal jump of the J_s from 0 to $2/\pi$ as T falls below T_{BKT} according to Eq.3.12; $n(T) = 1 + J_s(T)/T$. This is true in case of clean (homogeneous) systems with bound (V-AV) in a zero-resistive state below T_{BKT}. However, in presence of inhomogeneity, I-V measurements for our films reveal two distinct IVCs regimes where the $V(I)$ power law behavior differs somewhat from theoretical predictions (see also Fig. 5.13 and Fig. 5.14). For our convenience, from now on, we call these regimes the high $V(I)$ regime (with IVCs characterized by voltage, say, above 10^{-4} V for all films) and the low $V(I)$ regime (IVCs with voltage below 10^{-4} V) of all films. The analyses of both $V(I)$ regimes is primarily intended to capture inhomogeneity effects on the nonlinear behavior of $V(I)$-power law expected for a BKT transition, within a reasonable range of investigation.

In Fig.5.12, we mark by dotted rectangle the concerned region of low $V(I)$ data in which $ln(V)$ is proportional to $ln(I)$. In this region $I(V)$ follows power-law ($V \propto I^{n(T)}$) for all isotherms, with the power $n(T)$ increasing with decreasing T. As we can see in the figure, at high T the I-V dependence tends to be more ohmic which may be described by n value approaching 1, independent of the value of the current, as expected for normal state. According to the BKT scheme, it is expected that n increases rather abruptly from 1 in the normal state to 3 at $T = T_{BKT}$, following the universal jump of the J_s from 0 to $2/\pi$ as T falls below T_{BKT} according to; $n(T) =$

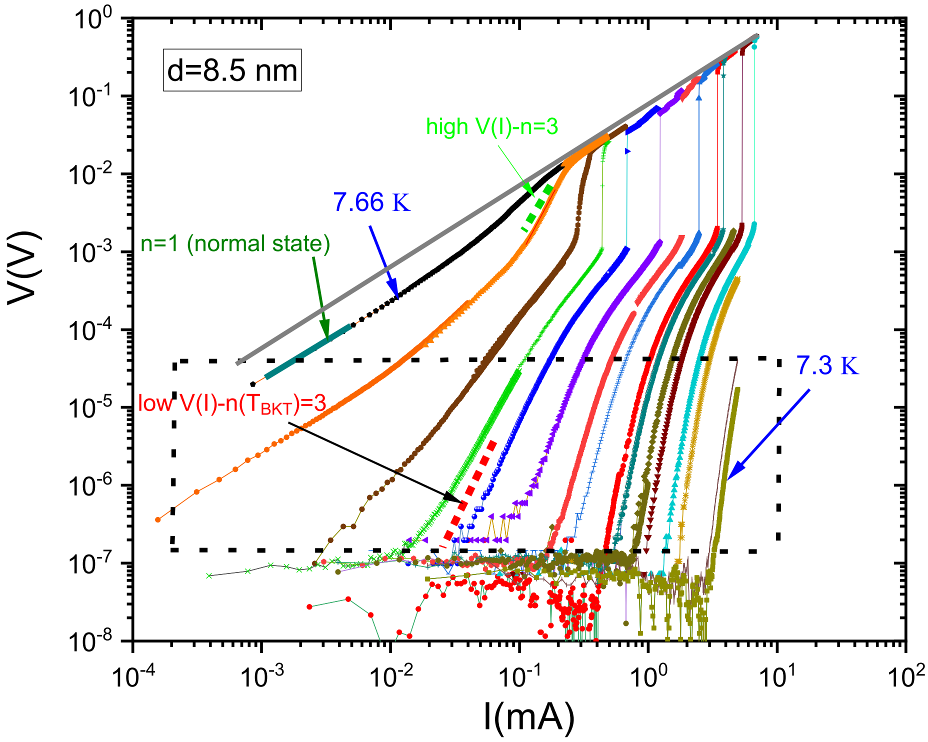

FIGURE 5.12: logarithmic current-voltage characteristics for 8.5 nm-film. The dashed rectangle shows low $V(I)$ regime with power-law behavior. Red (green) dashed lines are drawn at n =3 in the low-V (high-V) regions.

$1 + \pi J_s(T)/T$.

As temperature decreases, n increases, and at the lowest temperature vanishing dissipation is expected in the limit of low currents, implying divergence of n on the approach to T =0. While the increase of n from 1 to 3 is not very abrupt but gradual, nevertheless the increase of the value of the slope n is indeed visible in Fig. 5.12, so we can estimate that the T_{BKT} falls within the range 7.62 K and 7.63 K at n =3, as shown by dashed red line inside the dotted rectangle. This value is slightly lower than the value extracted from H-N formula (≈7.632 K). One may expect a more typical BKT scenario for thicker films with increasing homogeneity until the transition becomes invalid upon crossing from 2D-to-3D superconductivity.

Note that in the region of the plot above the rectangle, i.e. at higher V ($> 10^{-4}$ volts) for each isotherm, the values of V show saturation before jumping abruptly to high value in the normal state. This saturation indicates the occurrence of free flux flow (FF) with increasing current. As T increases, the jump broadens upon approaching the normal state. Interestingly, on the verge of the normal state the isotherm in the high-V range acquires "n =3" slope, as indicated by dashed green line in the plot. This isotherm corresponds to a temperature of ∼7.65 K which is higher than the one obtained from the low $V(I)$ analysis (T_{BKT}=7.625 K). In both high $V(I)$ and low $V(I)$ regimes the transitions from n =3 to n =1 take place at nearly similar low currents indicating rapid jump to the mean field-temperature (n =1). At first glance, this seems to provide a single interpretation of BKT physics from the perspectives of low $V(I)$ and high $V(I)$ analyses for the $V(I)$-power law behavior. However, it is important to understand that the dynamics of vortex fluid is completely different in the low-V and high V-regimes. In the high V-regime the apparent n =3 transition occurs on the verge of flux flow approach to normal state, in the presence of large density of vortices excited by both high current and high temperature; and therefore it cannot reflect true BKT transition. In the low $V(I)$ regime, the (V-AV) pairs ($T < T_{BKT}$) become thermally dissociated with increasing the current (I) and the vortex system is set into motion as I keeps increasing followed by unstable flux flow (FF)-type motion preceding the abrupt jump to normal state. In particular, as T increases on the approach to T_{BKT}, the dissipation in the SC state at low currents is expected to be dominated by BKT-like phase fluctuations where the role of self-field (i.e., current-induced) vortices may be ignored. As a result, one can safely discuss (BKT-to-GL)-like fluctuations in the vicinity of the transition from the perspective of low $V(I)$ measurements. This also secures our $V(I)$-based calculations for the temperature dependent superfluid stiffness $J_s(T)$ (shown later in Fig. 5.14) where the temperature dependent-fluid carrier density $n_s(T < T_{BKT})$ is expected to describe a globally coherent SC phase in 8.5 nm-film. Moreover, the sharp features in the $J_s(T)$ vs. T behavior we obtained for the film are revealed by the closeness of the T_{BKT} and T_{MF} values and the finite but small value of b shown in Table 5.1. The value of b gets even smaller as d increases above 8.5 nm (such as for 44 nm-film), indicating further approach toward the clean limit of 2D superconductivity.

In order to conclude and summarize our discussion for 8.5 nm-film, the film reveals distinct inhomogeneity effects on transport properties in the vicinity of BKT phase transition. The crossover from GL-to-BKT phase fluctuations in the $R(T)$ dependence, probed experimentally with 0.5 mA current, is mediated by PS events. However, the possible BKT phase transition in the film still can be described within the BKT scheme either from $R(T)$ measurement, or alternatively from IV measurements. The small value for the parameter b characterizing the film (Table 5.1) might be calculated over GL-BKT fluctuations crossover in presence of PS fluctuations but not over a pure GL-BKT crossover; if this is true, then the value of parameter b we obtained from fits of $R(T)$ data may not be so strictly used to estimate μ/J_s using Eq. 3.8. In $R(T)$ measurements, PS phenomena may be attenuated if smaller current is used. In I-V picture, instead of the abrupt jump expected for clean systems, the gradual change of the $V(I)$-nonlinear exponent $n(T)$ in the vicinity of T_{BKT} is a clear manefistation of present inhomogeneity and therefore smearing in the typical behavior of supurefuluid stiffness, $J_s(T)$, occurs. However, to a good approximation, BKT transition in the film may be characterized by a single T_{BKT} ($T_{BKT} < T_{MF}$) value what may signal the global coherence of both; the amplitude and the phase fluctuations upon the transition in the film. In case of existing links coupling the SC puddles, we then conclude that the induced non-conductive paths result in a weak perturbation to the global SC condensate strength which allows for the observation of textbook-like BKT transition with semi-sharp features (Fig. 5.14).

Role of enhanced inhomogeneity on BKT transition

We now turn our discussion to the increasing role of inhomogeneity on smearing BKT transition in thinner samples as d decreases below 8.5 nm. If we go back to Fig. 5.4, we can notice that the $R(T)$ data for 7.4 nm and 4.34 nm-films exhibit, on log-log scale, a similar behavior as the one for 8.5 nm-film. This seemingly suggests that the impact of inhomogeneity present in these films on transport properties is not much different from the one observed for 8.5 nm sample. However, closer examination of $R(T)$ and I-V indicates important differences.

Fig. 5.13(a,b) show the nonlinear evolution of the IVCs in zero external magnetic field for 7.4 nm and 4.34 nm-films, respectively. We show that the evolution of the nonlinearity in IVCs resembles to that of 8.5 nm-film: with decrease of T we observe the increase of the slope of the $V(I)$ on a log-log scale in the small V regime. However, we also observe that the region of power-law dependence in the low $V(I)$ regime (dashed rectangles) is restricted to smaller I and V, particularly at low T. Still, we can identify isotherms in the vicinity of n =3 (indicated with red dashed lines). We also find that the T_{BKT} extracted from the low $V(I)$ regime is markedly lower than that obtained from $R(T)$ analysis (Table 5.1). This discrepancy becomes even more profound as d decreases, pointing to the role of enhanced inhomogeneity on modifying the shape of IVCs, captured in the form of further gradual modification on the typical $V(I)$-power law predicted by theory.

The (black) arrows in Fig. 5.13(a) point to the IVCs characterized by the slope n =1 (indicating normal phase) for $T >$ 6.164 K (below which we start indeed to have n >1 in the low $V(I)$ regime). This exemplifies the gradual transformation of the slope $n \approx$1 (normal state) into $n \approx$3 leading to a non-typical $V(I)$ power law behavior (This gradual change is in stark contrast to the "jump" predicted by standard BKT theory, and clearly indicates growth of inhomogeneity) as film thickness decreases. Such transformation into the slope $n \approx$3 within a reasonable small current window may break down as disorder further increases. In Fig. 5.13(b), we note that the IVCs of 4.34 nm- film showcase intermediate resistive states between

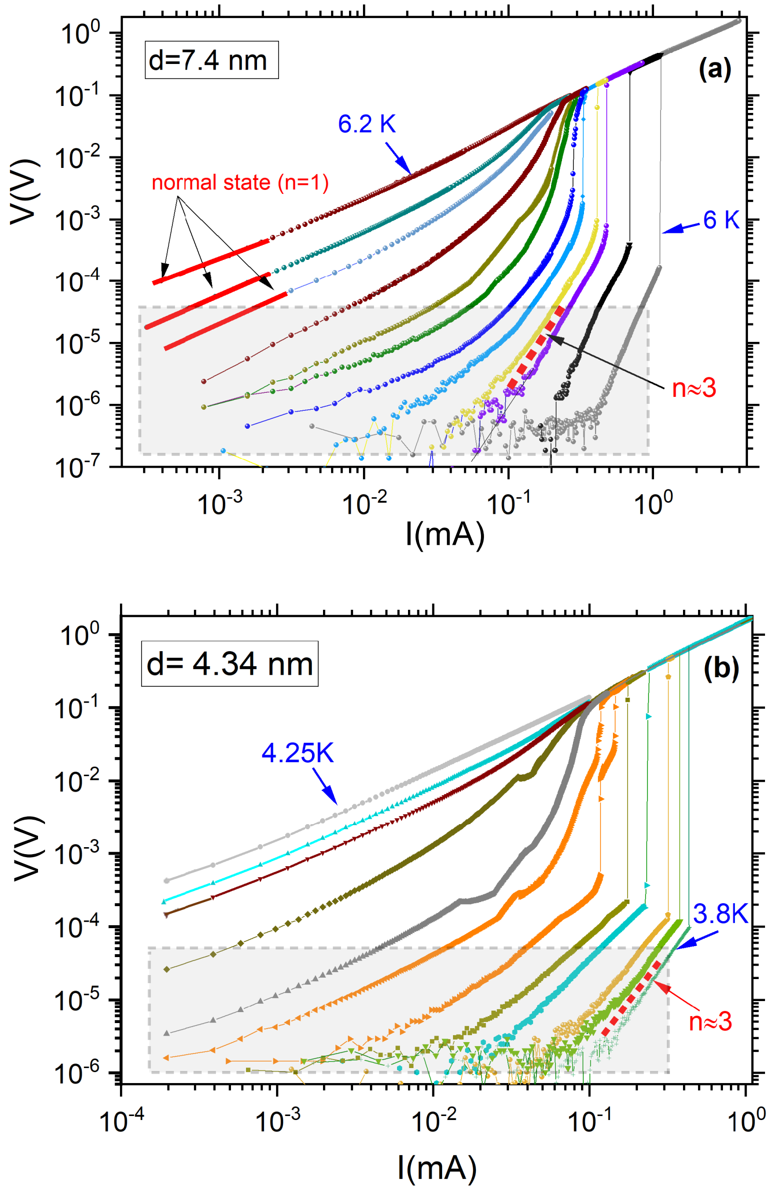

FIGURE 5.13: IVCs measured in absence of magnetic field (B =0), plotted on log-log scale for 7.4 nm-film (a) and for 4.34 nm-film (b). The $V(I)$-slope $n \approx 3$ is found between [6.085 -6.075 K] and [3.825-3.8 K] in (a) and (b), respectively.

superconducting and normal states as T approaches T_{MF} from below. In view of previous discussion on 8.5 nm-film, this may suggest the occurrence of some non-linear thermodynamic events (which could differ in nature from PSLs) triggered by the intrinsic film inhomogeneity. Such events are not clearly visible in the IVCs for 7.4 nm-film suggesting a strong link between them and the possible granular nature of the film. Moreover, we remind that in $R(T)$ measurements, no step-like behavior was seen for these films. Most-likely the reason is that the "fixed" currents used in $R(T)$ measurements (I =0.2 mA for both, d =7.4 nm and d =4.34 nm) do not induce thermal (i.e., T-dependent) these events (the events are either obscured or suppressed by the magnitude of the used current). Hence, the finite T_{BKT} obtained from H-N fits (listed in Table 5.1), for all films of this study ($d \leq$8.5 nm) might not represent a phase transition driven purely by GL-BKT fluctuations but rather we refer to them as (GL-BKT)-like fluctuations due to being modified by inhomogeneity and possibly induced phenomena (such as PSLs in 8.5 nm-film) which may be more complicated as d decreases.

As d decreases, the evolution from n =1 towards n =3 with decreasing T becomes slower, illustrating the influence of growing inhomogeneity on the BKT transition. This is nicely visible in the dependence of $n(T)$ in Fig. 5.14, in which we observe that relatively rapid increase of n on lowering T in 8.5 nm-film is replaced by gradual smearing of data towards lower T in films with smaller d; pointing to the enhanced incoherence of the quasi-long range order in SC state expected for typical BKT transition.

Now, if we follow the standard BKT scheme which concerns the power law behavior of the IVCs below universal T_{BKT}, in the low I limit, the isotherm for T_{BKT} obtained from the analysis of the low $V(I)$ regime is primarily the one expected to first follow the dependence $V \propto I^{n(T)}$with $n(T_{BKT})$ =3. As d decreases ($d \leq$ 8.5 nm), whenever IVCs with the slope $n \cong$3 is observable in the low $V(I) \propto I^{n(T)}$ regime, this likely indicates that inhomogeneity gives rise to a non-erasable remnants of the BKT phase transition, while it generates smearing of the transition what makes it difficult to precisely identify T_{BKT}. By following the most common assumption on mesoscopic scale-fractal superconductivity, inhomogeneity in our films, enhanced with decreasing d, possibly exists in the form of SC puddles with different strengths of SC condensate or SC puddles immersed in non-SC matrix [33, 210]. The spatially distributed GL and BKT phase fluctuations across the film map signals a weakened logarithmic interaction between vortices (chapter 3), and I-V measurements capture this in the form of slower change of the slope $n(T)$ in the vicinity of T_{BKT}. When our films become granular (d <5 nm; polycrystalline-to-amorphous structural transformation occur), they behave as Josephson junctions arrays (as will be dicussed later) where scenario turns more complicated as T decreases below T_{MF}.

In Fig. 5.14 we show the T-dependences of the $V(I)$-power law-exponent n and of the superfluid stiffness J_s, estimated using the formula $n(T) = 1 + \pi J_s(T)/T$ within the low $V(I)$ characteristics regimes (Fig. 5.12 and Fig. 5.13). We point out here that calculating the J_s may be valid only for describing the effects of phase fluctuations in films with d not far below 8.5nm (so to say, for d >4.3 nm), where calculating the slope $n \cong$3 is possible and $R(T)$ behavior follows similar trend as shown in Fig. 5.4. We limit our results on the J_s smearing down to temperatures, T, not far below T_{MF} due to lack of measurements at lower temperatures. We postpone

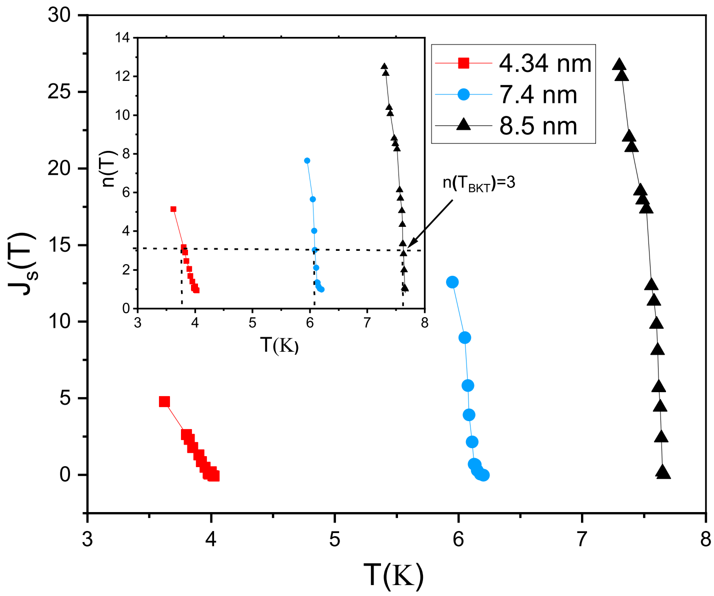

FIGURE 5.14: Superfluid stiffness $J_s(T)$ versus T extracted from the low $V(I)$ regime for films with different thicknesses. Inset shows the $V(I)$-exponent $n(T)$ versus T. Error bars are within data point size. Black horizontal dashed line marks n =3 while the vertical dashed lines points to smearing in $n(T)$ as it evolves from n =1 to n =3 (horizontal line), thus pointing to smearing in smearing in $J_s(T)$ as shown.

discussing the scenario for films with d <4.3 nm to the next subsection (Inhomogeneity effects and Josephson behavior) since stiffness in thinner samples may not rapidly increase when T is lowered and proximity effects may not induce rigid superconductivity in the metallic matrix. We will rather have more insights through evaluating the T-dependence of the critical (switching) currents using IVCs as T decreases below T_{MF}.

As anticipated, the universal jump in $J_s(T)$ from normal to SC state is smeared with decreasing d indicating the local distribution of J_s over the film. The smearing of $J_s(T) \sim \lambda^{-2}(T)$ as d decreases is due to evolution in both, phase and amplitude fluctuations what fundamentally modifies the putative GL-to-BKT fluctuations crossover for our films. As seen in the figure, 8.5 nm-film demonstrates sharp transition characteristics compared to thinner films. This is with the note that PS events (discussed before) may not play important role in smearing the calculated J_s, caused by the cutting off the asymptotical divergence of the correlation length predicted at T_{BKT}. As d decreases with enhanced inhomogeneity and localization effects, the stiffness energy scale becomes more comparable to the Cooper pairing energy ($J_s > \Delta(T)$), in contrast to homogeneous systems, in which J_s greatly exceeds Δ, $J_s \gg \Delta(T)$ [5]. This is with keeping in mind that the screening effects of repulsive Coulomb interaction between conducting electrons reduces as d decreases. In fact, the gradual decrease towards higher T has been described by the BCS theory through tha gap dependence of J_s [50]. We also point that the distribution of $\Delta(T)$

has been evaluated for granular superconductors, for example through direct studies of the temperature dependence of the magnetics penetration depth, $\lambda(T)$, [36, 41, 110].

Inhomogeneity effects and Josephson behavior

We now turn to discussing thinner films ($d \leq 4.3$ nm) which show increasing finite resistance at low temperature as d decreases (Fig. 5.4(a)). Fig. 5.15(a) shows the nonlinear evolution of the IVCs for 4.3 nm-film. The IVCs of this film seems to demonstrate an intermediate case thus classifying our Nb films into two categories, films with ($d >$4.3 nm) and films with ($d <$4.3 nm). The $V(I)$-slope $n \cong$3 still can be observed for 4.3 nm-film. However, the nonlinear $V(I)$ evolution as T decreases reflects strong inhomogeneity effects when compared to thicker films. This is inferred from the enhanced gradual evolution of the slope $n =$1 into $n \cong$3 (Fig.5.15(b)) along with the modified shape of nonlinear IVCs. As will be illustrated, even for films with $d <$ 4.3 nm (such as 3.6 nm-film) it turned out that of $n \cong$3 still may be detected in the low $V(I)$ regime. As d decreases further and further, observing the slope $n \approx$3 within a reasonable range of low-current limit as $T < T_{MF}$ becomes more elusive in view of standard BKT scheme.

Further decrease of the films thickness, down to $d =$3.6 nm, results in dramatic change in the I-V characteristics in comparison to thicker films. This is illustrated in Fig. 5.16(a) where we plot, on linear-linear scale, the isothermal IVCs (for T in the range 1.1 K to 2K) for 3.6-nm film under two opposite bias current polarities ($\pm I$). We observe that, as T decreases, two different critical (switching) currents arise: at smaller current I_{c1}, the voltage jumps from zero to some intermediate value, and, at larger current, I_{c2}, the voltage jumps up to a normal state (normal voltage at 1 K is equal to about 0.2 K, and it is not visible on this figure). We note that the switching currents I_{c1} appears to be different dependent on current polarity, while I_{c2} is similar for both polarities (we will discuss it later). As temperature is increased from 1K the switching current I_{c1} becomes broadened and disappears altogether above about 1.7 K-1.8 K.The observation of two switching currents is in a stark contrast to the IVCs displayed in Fig. 5.15(a) for the film with $d =$4.3 nm; in which only one critical current (jump to normal state) is seen. It is important also to underscore the fact that the sequence of just two switching currents is different from the PSL feature present in Fig. 5.9, in which characteristic staircase of many switching currents in consecutive temperatures is seen. Preceding somewhat further examination of the data, we propose a following tentative interpretation of the two switching currents. Since below I_{c1}, the resistance is equal zero, I_{c1} is the current which breaks global coherence in the sample. Between I_{c1} and I_{c2} there are regions which are superconducting, and regions which are normal (details later), while at I_{c2} the system jumps into normal state.

Fig.5.16(b) shows the differential resistance (dV/dI) versus current (I) for 3.6 nm-film at two different temperatures: 1 K and 1.4 K. The switching currents I_{c1} and I_{c2} are visible at $T =$1 K as large peaks. As T increases to 1.4K, additional, prominent differential peak appears between two previously found peaks; we call this additional switching current I_{c12}; it always follows the sequence $I_{c1} < I_{c12} < I_{c2}$.

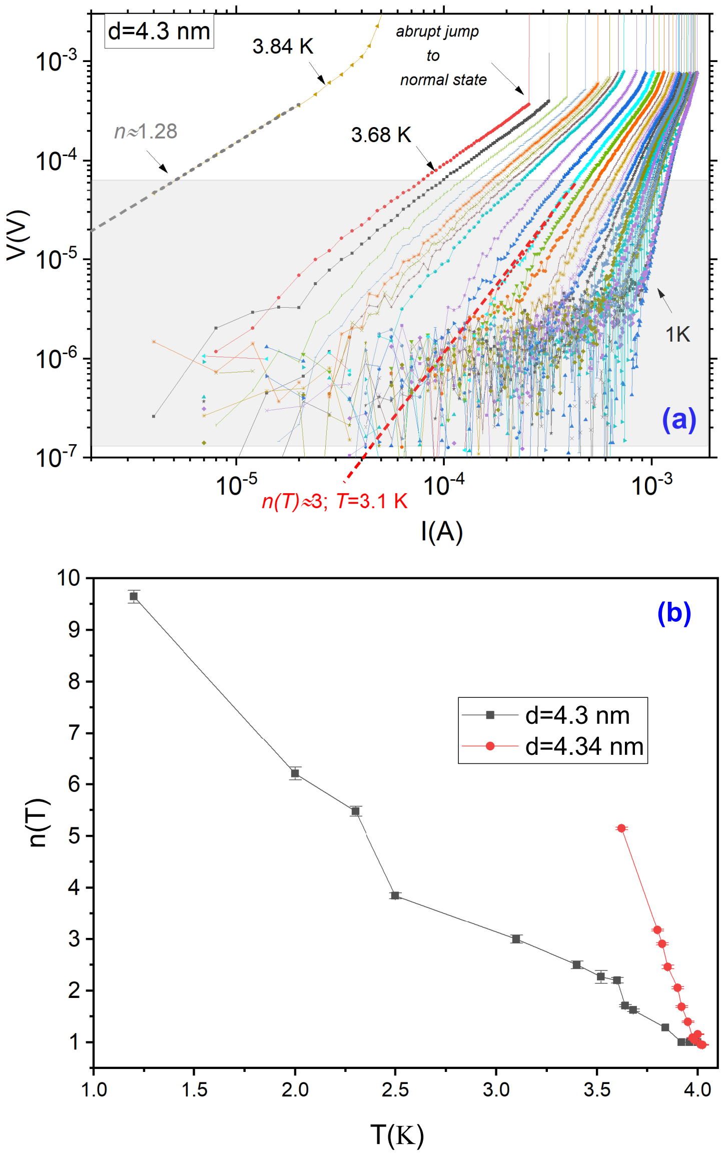

FIGURE 5.15: Logarithmic IVCs for 4.3 nm- film thicknesses (B =0 T). The dashed (red) line is drawn at n ≅3 in the low-V region. (b) Comparison between the smeared behavior of the slope $n(T)$ as T decreases for 4.34 nm-film and 4.3 nm-film, extracted from the low $V(I)$ regimes (rectangle areas) in Fig. 5.13(b) and Fig. 5.15(a) respectively. Unless shown, error bars are smaller than the point size.

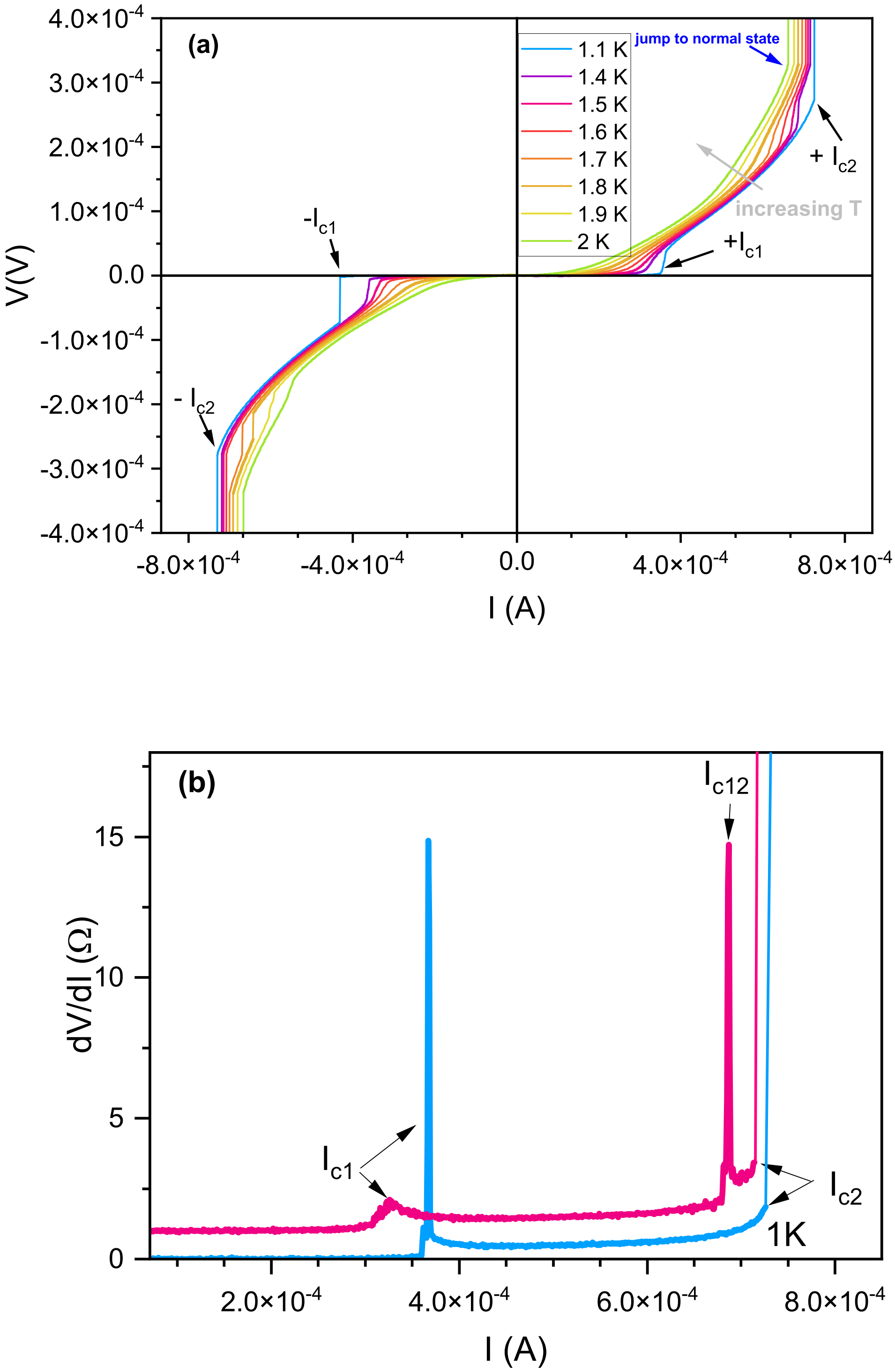

FIGURE 5.16: (a) IVCs for 3.6 nm-film (B =0 T) measured under different current polarities ($\pm I$); the locations of the switching currents I_{c1} and I_{c2} for 1.1 K are pointed out. (b) Differential resistance (dV/dI) versus $+I$ measured at T =1 K and 1.4 K. The curves are offset, for clarity. A differential peak emerges at I_{c12} for T=1.4 K while such a peak is absent for 1 K.

In Fig. 5.17 we show the $V(I)$-hysteresis loop measured for 3.6 nm-film at T =1 K. The current I is first swept from zero up to 1.5 mA (as shown by black data), next from 1.5 mA to -1.5 mA (shown in red), and finally, from -1.5 mA to zero (green). Colored arrows point to the current sweep direction. In 5.17(a), the voltage saturates at 1 V due to used amplifier with high magnification for investigation of the SC state. We mark the position of I_{c2}which we found it to be of identical magnitude ($\approx$ 7.35X10^{-4} A) for both current polarities. In 5.17(c) we zoom the IVCs in 5.17(a) so we can look more closely into the $V(I)$-hysteresis behavior. As we can see, the first switching event to the next voltage state with increasing current occurs at current, I_{c1}, I_{c1} seems to have different magnitude for $\pm I$. We will refer back more to this issue later in the text. Finally, we note that on decreasing current, from 1.5 mA down to zero (or from -1.5 mA to zero) the voltage drops back to original zero state at current I_r (return current, marked in the figure), which is much smaller than I_{c2}. In order to evaluate the origin of this difference, we have measured the stability of temperature during current sweep, as shown in 5.17(b). As we can see, in both directions ($\pm I$), as I exceed the value for I_{c2}, the temperature becomes unstable and increases rapidly up to about 4.5 K while increasing current. On decreasing sweep down to I_r, the temperature returns back to stable 1 K. This indicates that hysteresis observed during the sweep above I_{c2} is caused by heating of the film due to the approach to normal sate. We also note that during the sweep across the first switching current, I_{c1}, there is no change of temperature; this is related to the fact that the resistance of the film in the current range between I_{c1} and I_{c2} is relatively minor, so the flowing current does not induce sample heating.

Despite the unusual observation of two critical (switching) currents, it is interesting to examine the question if any feature resembling BKT transition may be observed in this case. Looking for such transition, we have to restrict the considerations to the region of currents just below I_{c1}, i.e., to the region of currents, which may produces putative V-AV dissociation. Guided by this idea we display in Fig. 5.18(a), on log-log scale, the nonlinear +IVCs ($+I$ polarity) measured for 3.6 nm-film in the range T =[0.7 K-3 K], B =0 T. Black arrows point to temperatures and the black dashed line denotes the slope n $\cong$3, obtained in the vicinity of 1.7 K. Fig. 5.18(b) shows the results for the exponent $n(T)$ versus temperature T, calculated using the +IVCs shown in Fig. 5.18(a) and the -IVCs ($-I$ polarity) when plotted (not shown) on log-log scale as absolute V versus absolute I. We point here that the slope $n(T)$ was calculated over IVCs with I in the range below I_{c1}. The IVCs for ($\pm I$) shows minimum voltage of the order of 10^{-6} to 10^{-7} V. As we can see, the slope n $\cong$3 is observed at T $\approx$1.75 K for $-I$ polarity while it is observed at $\approx$1.7 K for $+I$ polarity, demonstrating slight difference in the results. Analysis for +IVCs shows T_{MF} which agrees with one listed in Table 5.1 (Sec. 5.1.1), observed with measuring $R(T)$ with $+I$ (I is constant during measurement). On the other hand, analysis for -IVCs points to T_{MF} slightly larger than for $+I$ case (we did not measure $R(T)$ with reversing the polarity of the constant current which we used in $R(T)$ measurements). Smearing in the T-dependence of J_s behavior related to $n(T)$ within standard BKT scheme as $n(T) = 1 + \pi J_s(T)/T$, is enhanced noticeably as T increases above 1.7(5) K ($\approx$0.5(5) T_{MF}). As T decreases below 1.7 K (n $\approx$3), $n(T)$ starts to raise, pointing to global coherence of the whole film.

In order to visualize the evolution of IVC's in a broad temperature and current range the I-V measurements (in zero field) were performed down to 0.1 K. In Fig.

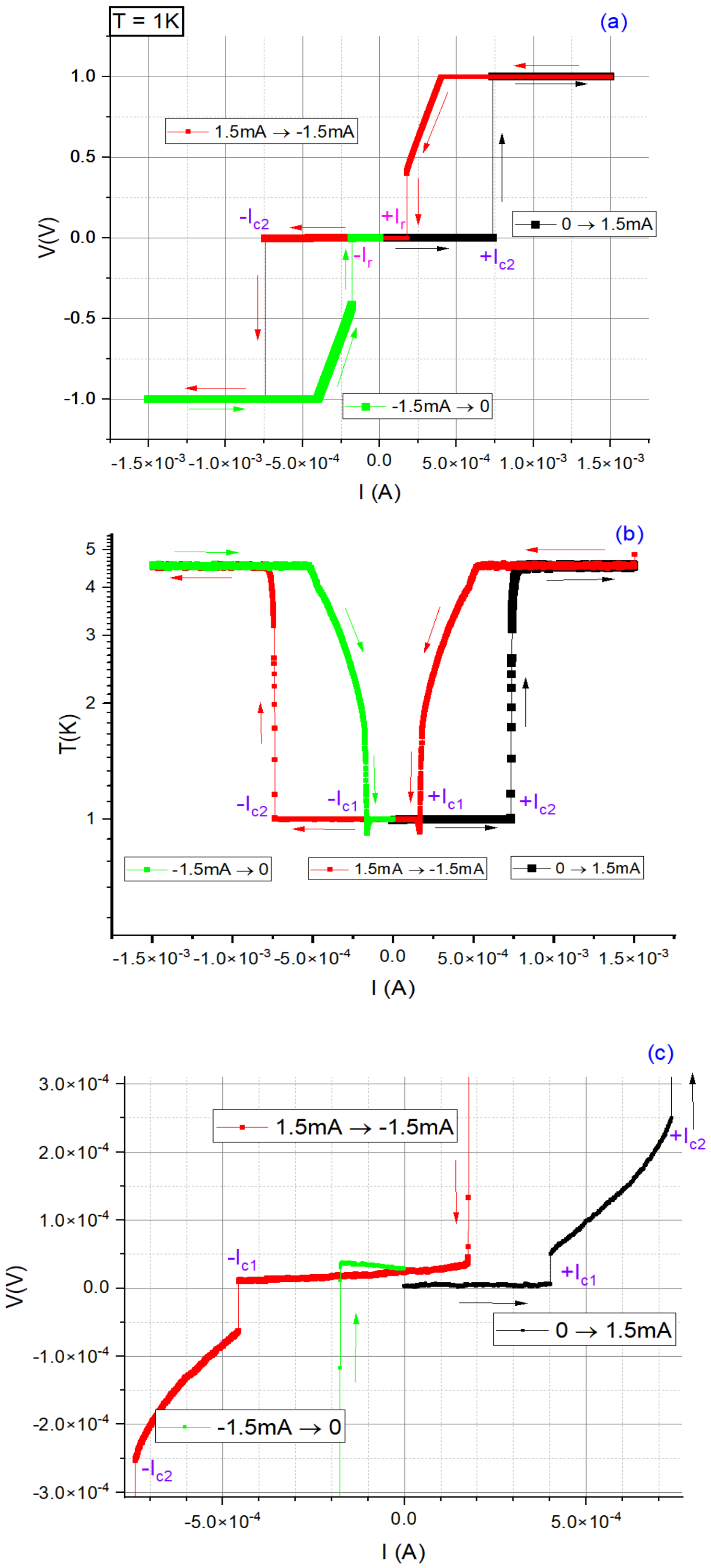

FIGURE 5.17: (a, c) $V(I)$-hysteresis behavior measured at 1K for 3.6 nm-film (B =0 T). (b) Temperature instability obtained during hysteresis measurement.

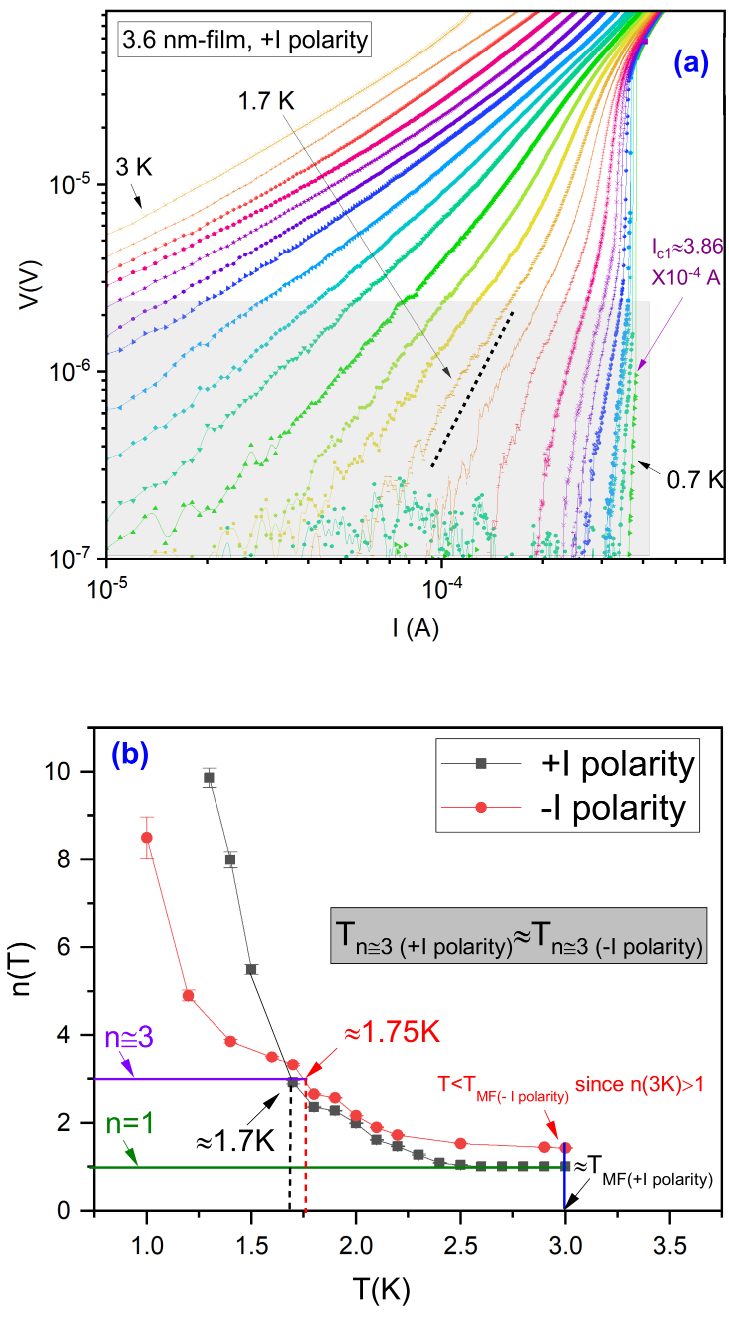

FIGURE 5.18: (a) Logarithmic +IVCs in the low $V(I)$ regime for 3.6 nm-film. (b) Behavior of $V(I)$-exponent, $n(T)$, calculated for polarities ($\pm I$)

5.19(a) we show evolution of differential resistance versus current for both polarities, calculated from IVC's in the T-range 1K to 3K (the data below 1K are very similar to 1K data, indicating no or weak dependence of the critical currents on temperature at lower T). Consecutive curves in the figure are measured every 0.1 K, and they are shifted upwards for clarity. As we can see, as current, I, increases we observe peaks in the dV/dI vs. I, marking the positions of the switching currents at which resistance (voltage) switches to the next resistive $V(I)$-state in the IVCs. As T increases, the size, and the shape of peaks change. Peaks translate into dips in the conductance dI/dV versus voltage, shown up to 3 K in Fig. 5.19(b). Interestingly, a new feature is visible in this plot, which is absent in Fig. 5.19(a). Namely, when temperature falls below 1.7K (for negative side), or 1.4K (for positive side) the voltage measured at I_{c12}, and, simultaneously the voltage at I_{c2} drops down by substantial factor and remains at the low level down to lowest T. On the other hand, as T drops below 1K, the dV/dI vs. I follows the behavior same as for 1 K, indicating the saturation behavior of the switching currents. We point here that in (a) and (b) the $V(+I)$ curves for 1.2 K and 1.3 K are incomplete due to measuring errors.

In Fig.5.20(a) we show the T-dependence of the successive switching currents, I_{c1}, I_{c12}, and I_{c2}. The data for I_{c1}, I_{c12}, and I_{c2} were carefully read off from the peak positions in dV/dI versus I; an example of assigning these currents to the corresponding peak positions is shown in Fig. 5.19(a). Note that when defining peak positions, we may use two different notations: either we may read the value of the current at the peak onset (which we call "Base"), or we may read it at the peak maximum ("Max."). While "base" and "max." values are easy to define in case of I_{c1}, in case of I_{c2} it is possible to extract "base' only; while "base" is difficult to define in case of I_{c12} peaks, which become very broad with increasing T. For this reason we show in Fig. 5.20 "base" values of I_{c2}, "max." values of Ic12, both values of I_{c1}, in order to emphasize slightly different T-dependence of both values. Error bars denote the range within which the switching currents may be identified. As we can see for the currents I_{c12} and I_{c1} ($+I$ polarity), error becomes smaller with decreasing T, thus pointing to narrow peaks in the dV/dI vs. I so that switching currents to the next voltage states becomes better defined.

An intriguing feature which we can observe in Fig. 5.20 is that the T-dependence of the current at which the jump to normal state occurs shows saturation as T decreases below $T \approx 0.5\ T_c$. Of particular interest, the saturation progressively extending to very low temperatures tends to occur in $I_{c1}(T)$ and $I_{c12}(T)$ behaviors as well. Another very peculiar behavior is observed in Fig. 5.20(b), which shows voltage read at the critical currents I_{c2} and I_{c12} (voltage at I_{c1} is extremely small, and it is difficult to read it from our data). The peculiarity is that the voltage measured at I_{c2} drops down, from about 0.32 mV to 0.275 mV, and this happens in the vicinity of the temperature at which global superconductivity occurs ($T \sim 1.7$ K). We also observe that peaks at I_{c12}, which are single at high temperatures, split into double peaks as T decreases. Below we discuss how all these behaviors may be interpreted, at least qualitatively, in the framework of Josephson junction array (JJA) physics.

Since the films considered in this work do not display any tendency to approach insulating state at $T = 0$ (at least in zero magnetic field), we look into descriptions of JJA systems with superconductor-normal-superconductor (SNS) junctions. It is important to recall here that the previous structural study of the films identical to studied here, presented in [81, 211] reveals a transition from polycrystalline into

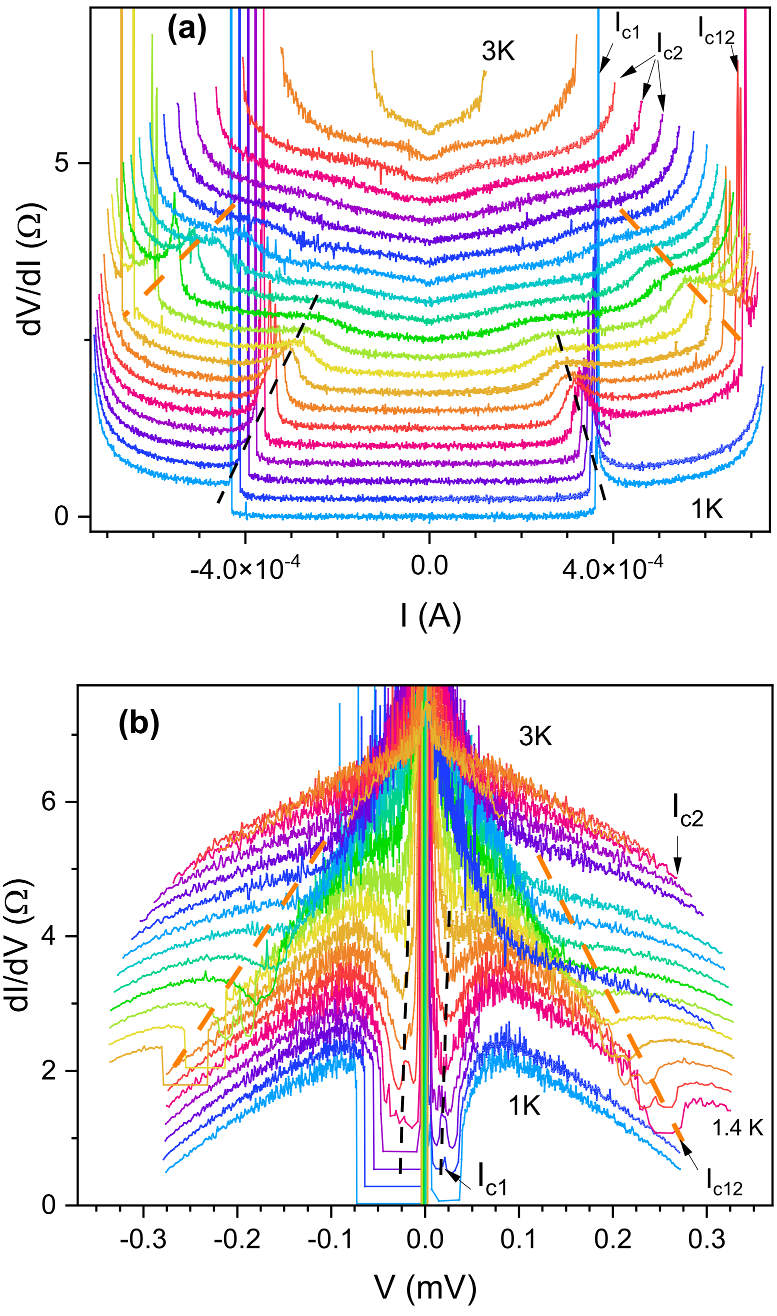

FIGURE 5.19: (a) Differential resistance dV/dI vs. I for 3.6 nm-film (B =0 T, T =1 K-3 K; T-step=0.1 K). Black arrows denote I_{c2} ; the current at which abrupt jump to normal state occurs, and to $I_{c12} < I_{c2}$ in the isothermal IVCs. We erased the lines connecting I_{c2} to the normal state for better vision. Black dashed lines points roughly to the evolution of the resistance peaks observed at the first switching current I_{c1}. Orange dashed lines points roughly to the evolution of the resistance peaks observed at current I_{c12} ($< I_{c2}$). (b) Differential conductance dI/dV vs. voltage (V). Dashed lines demonstrate the dI/dV evolution with voltage V which corresponds to I_{c1}, I_{c12} and I_{c2} as indicates by arrows.

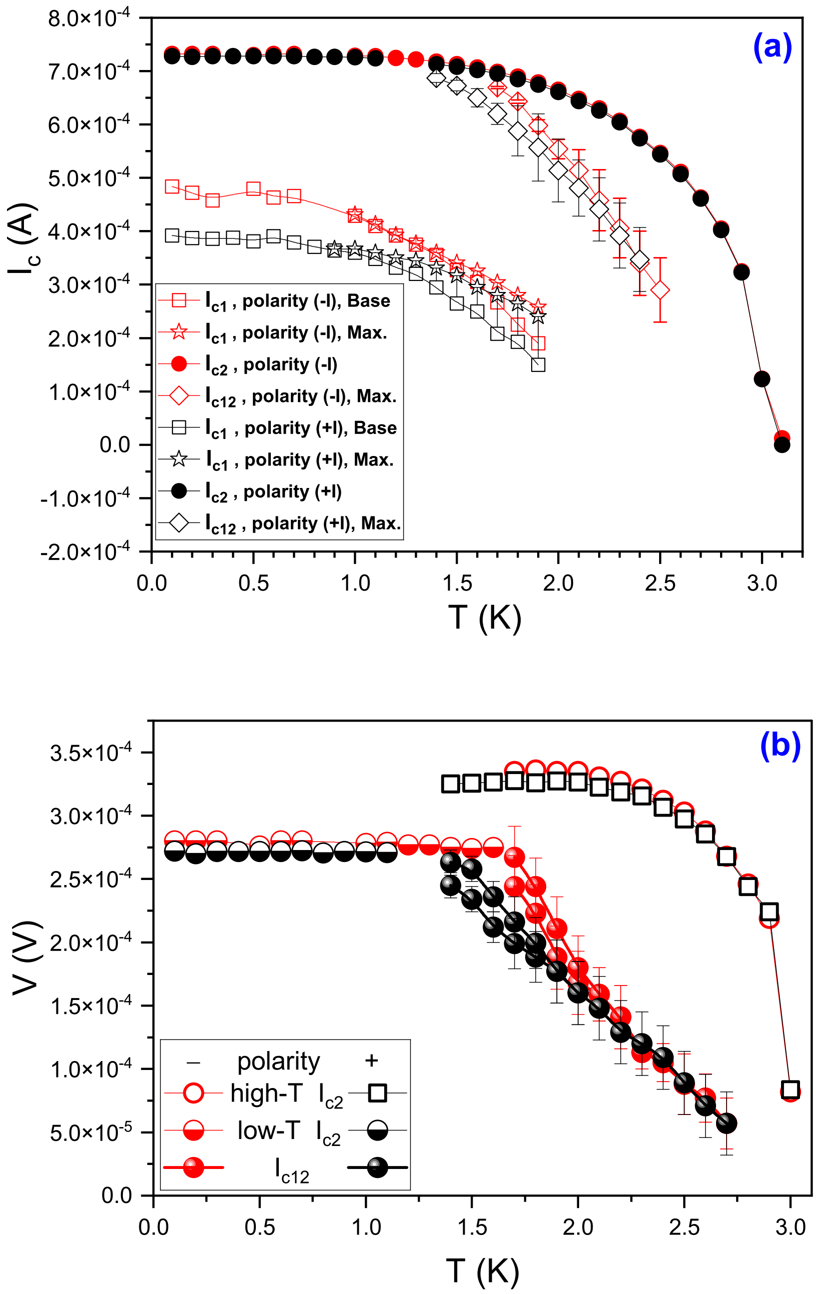

FIGURE 5.20: T-dependence of critical (switching) currents, I_{c1}, I_{c12} and I_{c2} for 3.6 nm-Nb film under both bias polarities ($\pm I$), B =0 T. "Max." denotes the readings (indicated by symbols) taken from the maximum resistance of the differential peak while "Base" denotes the reading taken at the onset of the peak position. (b) T-dependence of voltage, $V(T)$, at switching currents I_{c12} and I_{c2} for both polarities.

amorphous structure in the vicinity of d =3 nm, therefore it is reasonable to expect that films with thicknesses around 3 nm contain polycrystalline grains (islands) immersed in the amorphous (metallic) background. While both constituents of this system are Nb-based, they likely differ in various properties. For example, while thick Nb films show positive sign Hall coefficient, in the thinnest films negative contributions become evident at lowest T, suggesting that the nature of carriers may be different in SC islands and the amorphous metallic part. Nevertheless, in order to simplify our description, we leave this problem to consider in future studies, and discuss now the known results of JJA with SNS junctions.

One of the first attempts to describe such systems is the phenomenological theory of, Lobb, Abraham and Tinkham (LAT) [212, 213]. This model considers SC islands with dimensions larger than SC coherence length; these islands couple via proximity effects across SNS junctions, and the system is always approaches SC state in the T =0 K limit [214]. There are, however, other possibilities for the T =0 limit, namely, metallic, non-superconducting state; such systems have been considered theoretically, and observed experimentally [210, 215]. Recent studies try to evaluate how the T =0 state of the system is determined by basic system parameters, such as island-to-island distance, or island size; the study is based on the investigation of Nb islands deposited on the gold (Au) films [38, 42]. Before turning to our work, in the following we briefly describe the results of Nb/Au study.

In Fig. 5.21 we schematically illustrate the experimental results of temperature dependence of the resistance of Nb/Au film. The arrays were investigated under constant island diameter and variable edge-to-edge spacing (L) between islands. The islands were regarded as mesoscopic islands (island diameter is comparable to the dirty-limit superconducting coherence length; $\xi_{SC} \approx$ 27nm estimated for Nb). As we can see, the curve shows a two-step resistance (voltage) versus temperature and thus the width of the normal to superconducting phase transition is subdivided into distinct regimes. In the figure, T_1 is the temperature at which the normal state of the islands (region I) undergo the very first superconducting transition (by crossing to region II) which gradually evolves into the whole film transition at T_2 with decreasing temperature.

Pictures display three islands, each limited to four grains for simplicity. In region I, the Nb islands are normal metals. In region II, the phase of the grains (represented by black arrows) starts to be coherent within each island (although there is not yet inter-island phase coherence). At T_1, Cooper pairs diffuse from the Nb into the Au, and the resistance drops. The grains have intra-island Josephson coupling J and nearest-neighbor inter-island coupling J′(indicated by red squiggly lines). In region III, J has saturated, but J'continues to increase as the normal metal coherence length, $\xi_N \sim 1/\sqrt{T}$, increases. $\xi_N = \sqrt{\hbar D/2\pi k_B T}$; $\hbar$ and k_B are the Planck and Boltzmann universal constants, respectively, D is the normal metal diffusion constant ($D = v_F l_e/3$; v_F is the Fermi velocity and l_e is the elastic mean free path) and T is the temperature. In region IV, ξ_N becomes comparable to the island spacing, and the entire system of film and islands progresses towards having global phase coherence. As T is further decreased, the film undergoes a transition (referred to it as BKT transition in their case) to superconducting state at T_2. It has been found that T_2 depends on the island spacing as $1/L^2$ but qualitatively, both T_1 and T_2 depend also strongly on islands height. The $R(T)$ behavior for Nb-arrays [42] with different island spacing (L in nm) is shown in Fig.1(a) in [42].

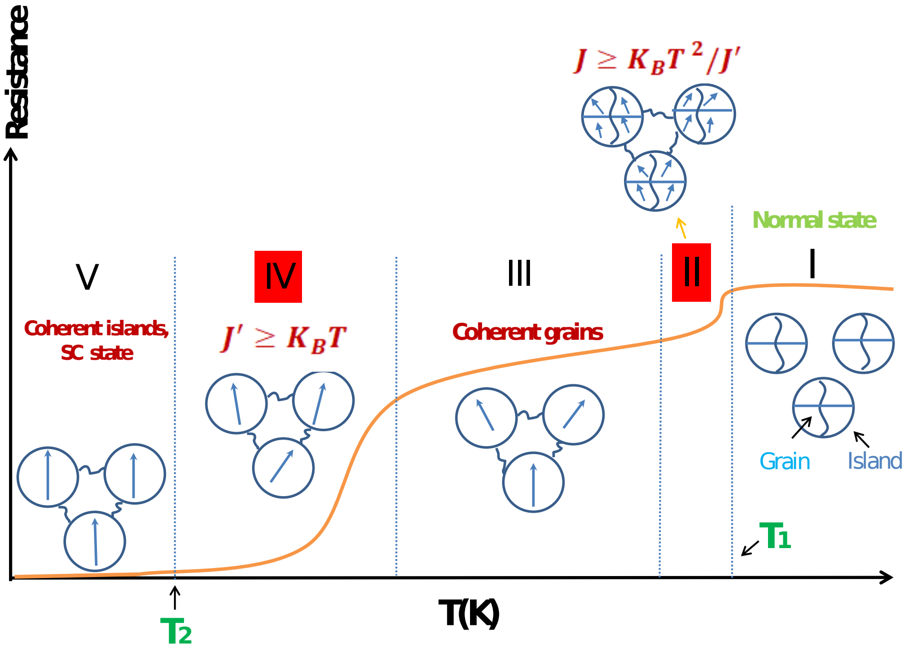

FIGURE 5.21: Schematic illustration of the temperature dependence of resistance in Nb islands on Au film (based on results presented in Refs.[38, 42]). Pictures in different regions are described in the text.

To compare this description to our experimental results, we show in Fig. 5.22 the sheet resistance as a function of temperature, $R_{sq}(T)$, for 3.6 nm-Nb film. The inset shows a step-like resistance behavior observed as T decreases. In analogy to the $R(T)$ behavior illustrated in Fig. 5.21, the first transition at about T =3 K, shaded by yellow, corresponds to region II whereas regions III and IV are shaded by light blue. While in this $R(T)$ measurements we do not observe a second transition at lower T towards global superconducting state, from the analysis of I-V data (Fig. 5.18) we know that it occurs at about T_c =1.7 K. Thus, we conclude that the resistance of our film resembles very closely the behavior observed in JJA reported in [38]. We point here that region III and IV for our film possibly merge together due to the magnitude of measuring current (0.1 mA) we have used in $R(T)$ measurement. Moreover, it is important to point out that, in contrast to fixed distances between islands in experiment presented in [38, 42], the sizes of islands and distances between them are likely random in the case of our films. Therefore, proximity effects may couple some islands in the temperature range between the first transitions observed at T =3 K and the global transition of the array at T_c =1.7 K. This is confirmed by the fact that the peak at critical current I_{c1} does not disappear strictly at the temperature of 1.7 K, as would be expected based on the T_{BKT} found in Fig. 5.18, but persists, albeit broadened up to at least 1.9 K (see Fig. 5.20). Finally, we note that similar $R(T)$ behavior is seen in the case of thinner film with d =3.4 nm, as shown in Fig. 5.4(a).

It is important to mention that the I-V measurements performed on Nb/Au films [42] show features features similar to the results of our experiment, i.e., two critical currents, where the lower critical current is the critical current of the whole array. As listed in Ref.[42] the samples studied in [42] exhibit large island spacing L, at

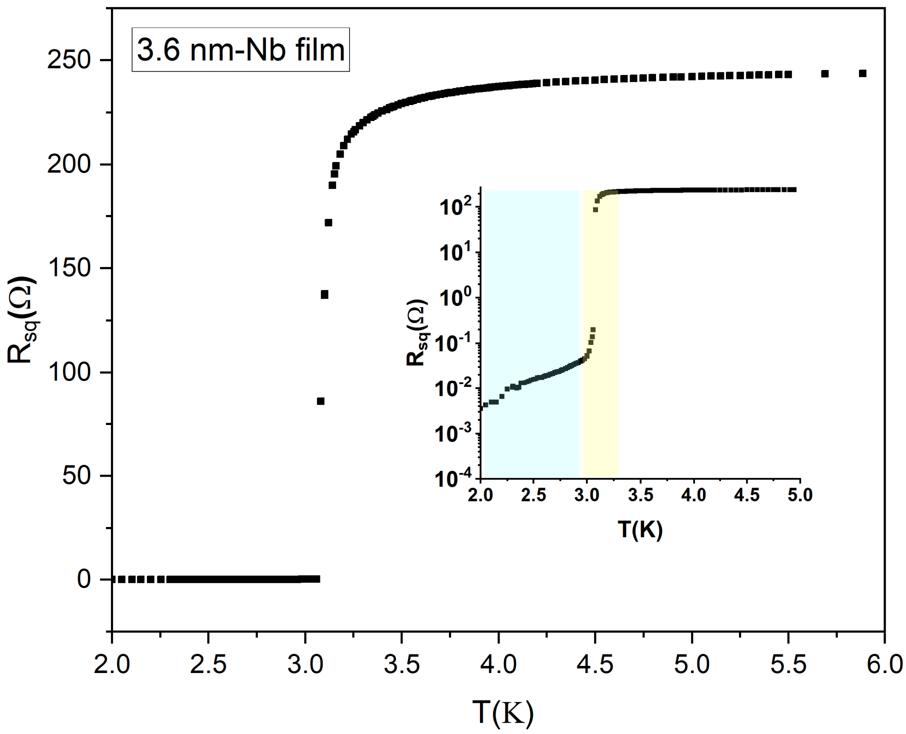

FIGURE 5.22: Sheet resistance versus temperature for 3.6 nm-Nb film, $B = 0$ T.

least seven times larger than the SC coherence length of Nb islands, estimated in that work as equal to 27 nm. The junctions of that type, called long (diffusive) junctions, display interesting features: the transition temperature of the array, T_c, is not governed by the SC gap energy of the islands (Δ), but by much smaller Thouless energy, which is inversely proportional to the time it takes normal electrons to diffuse between islands; $E_{Th} = \hbar D/L^2$ (D is diffusion constant of normal metal). A consequence of this is that the temperature dependence of the critical current of the array, I_c, is not related to the T-dependence of Δ, but it is described by very different equation relation to E_{Th}. Indeed, in [42] it is shown that $I_c(T)$ follows predictions for long diffusive junctions, first derived by Dubos et al [125].

Based on the similarity of our I-V results and the results for Nb/Au system [38, 42] we believe that I_{c1} we observe is the critical current for the global superconductivity achieved in the system, which consists from both SC islands, and metallic junctions with proximity-induced superconductivity, while I_{c2} is the critical current at which the system returns to normal state ($V \sim I$). Since in the region between I_{c1} and I_{c2} the resistance is non-zero, while SC state exists in the islands, it is tempting to associate I_{c2} with the critical current of the islands. However, this may not be exactly true, because, as temperature is lowered below the T_c onset of the islands, the proximity effect immediately starts to operate in the areas surrounding the islands, and, therefore, the T-dependence of I_{c2} may be modified. Later in the text we will return to detail discussion of both critical currents. Before we do that, it is important to point out two differences between our results and the results for Nb/Au array described in [42].

First of these differences is the existence of third switching current, I_{c12}, which is not observed in Nb/Au arrays. As shown in Fig. 5.20 this feature exists in intermediate T-range, between I_{c1} and I_{c2}. Voltage related to this feature approaches voltage at I_{c2} at high temperature (Fig. 5.20(b)). On decreasing T peaks at I_{c12} first split into two peaks each, and this is followed by the approach to the low$T$-voltage at I_{c2}. This approach occurs, as already pointed out, in close vicinity of global superconducting temperature. Trying to understand the origin of I_{c12} feature, we note that one of the basic differences between our films and the sample Nb/Au is the variable size and distances between SC islands, which likely exist in our films, in contrast to well-defined parameters of Nb/Au arrays. This means that in our films there are probably plenty of junctions with different junction length L, both larger and smaller than the coherence length of Cooper pairs on Nb islands. In the case $L > \xi$ we expect that long junction-behavior, similar to what has been discussed for Nb/Au, and this is what would result in I_{c1} differential peaks. On the other hand, at high temperature, when ξ becomes longer, the inverse situation likely occurs ($L < \xi$), long junctions becomes irrelevant for transport, while short (possibly intermediate) junctions take over. A characteristic property of diffusive junctions is the possible existence of multiple Andreev reflection (MAR), which may contribute to the additional peaks in the I-V curves [216]. So we tentatively assign I_{c12} peaks to MAR effect; more details will be discussed later.

The second difference between our results and these of Nb/Au arrays is the polarity dependence of the observed peaks in both I_{c1} and I_{c12} peaks. While it seems that no polarity dependence exists for I_{c2}, the voltage measured at I_{c2} show that this is not exactly the case; the effects becomes stronger with decreasing temperature.

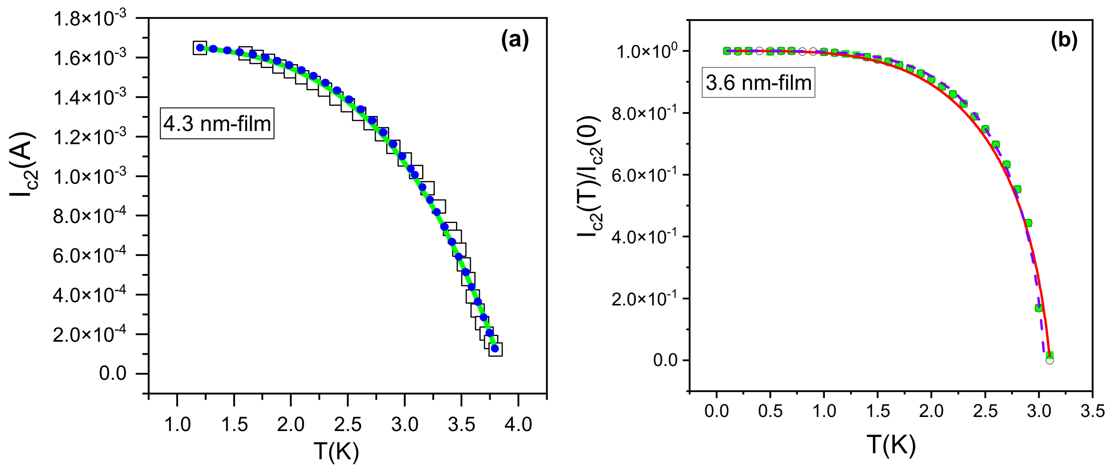

FIGURE 5.23: (a)T-dependence of the critical current I_{c2} for 4.3 nm-film. The data (squares) are fitted using Eq. 5.5 (green solid line) and Eq. 5.7 (blue dotted line). (b) Normalized $I_{c2}(T)$ (green points) for 3.6 nm-film. Solid red and dashed blue lines shows results obtained while attempting to fit the data using Eq. 5.6 and Eq. 5.7.

In the following, in an attempt to support our tentative understanding of three switching currents, we discuss in more detail their behaviors. We first turn attention to the T-dependence of the critical current I_{c2}, at which the system is turned normal; since the approach to normal state is also well defined in the thicker (4.3 nm) film, we compare the behaviors observed in thicker (4.3 nm) and thinner (3.6 nm) films. In Fig. 5.23(a), we show the data (empty squares) for the T-dependence of the current I_{c2} for 4.3 nm-Nb film. We use the IVCs shown previously in Fig. 5.15(a) to read off the values of I_{c2}. We find that the data in the whole T-range may be fitted (green solid line) using the following phenomenological formula for the T-dependence of the critical current [37, 41, 217],

$$I_c(T) = I_c(0)\left[1 - \left(\frac{T}{T_c}\right)^4\right] \tag{5.5}$$

It has been shown that Eq. 5.5 describes the T- dependence of the critical currents for several 2D arrays of small Josephson junctions [41] and for strongly disordered ultrathin Sn and Bi films (with sheet resistance below 500 ohms) produced by quenched condensation[37]. In this last case the Sn and the Bi superconducting films were modeled into resistively and capacitively shunted Josephson junction array (JJA) using the classical RCSJ model (sometimes known as the Steward McCamber model) [40, 44] where the Josephson coupling energy is greater than the charging energy ($E_J \gg E_c$). In chapter 2, the RCSJ model is introduced (Sec. 2.2.5).

This in turn shows that our film does not truly behave as BCS-like superconductor since it is predicted that, in BCS-like superconductors, as T increases, the Cooper-pairing energy gap $\Delta(T)$ tends to vanish as $\sqrt{1-(T/T_c)^4}$. Close to T_c, $\sqrt{1-(T/T_c)^4} \approx 2\sqrt{1-T/T_c}$which is consistent with the behavior of BCS gap $(\Delta(T)/\Delta(0) \approx 1.74\sqrt{1-T/T_c})$ [37]. This is not the case for our film as the gap dependence $\Delta(T) \approx \sqrt{1-(T/T_c)^4}$ extends to cover temperatures far below T_c.

The blue "dotted " line in Fig. 5.23(a) shows our attempts to fit the T-dependence of I_{c2} using a relation for weak–coupling superconductor, which has been found to be fulfilled in case of niobium films of various thicknesses [17, 28, 50, 110]:

$$\frac{Ic(T)}{Ic(0)} = \frac{\lambda^{-2}(T)}{\lambda^{-2}(0)} = \frac{\Delta(T)}{\Delta(0)} \tanh\left[\frac{\Delta(T)}{2k_B T}\right] \tag{5.6}$$

where k_B is Boltzmann's constant, λ is the magnetic penetration depth and Δ is the superconducting gap at a given temperature T. The normalized gap is approximated by [218]

$$\frac{\Delta(T)}{\Delta(0)} \approx \left[\cos\left(\frac{\pi}{2}\left(\frac{T}{T_c}\right)^2\right)\right]^{1/2} \tag{5.7}$$

The fits, using $I_c(0)$, $\Delta(0)$ and T_c as fitting parameters, reproduce data very well, practically indistinguishable from the phenomenological relation [5.5]. From the fit we get values of $\Delta(0)$ =0.8 meV, and T_c =3.88 K (close to T_{MF} in Table 5.1). The value of $\Delta(0)$ is somewhat higher than $\Delta(0) = 0.65$ meV, reported for Nb films of comparable thickness by Park et al [111] (note that in this last reference it has been found that Nb ultrathin films are not strictly weak coupling i.e., $\Delta(0)/k_B T_c$ =1.97 for thickness of about 4.3 nm).

Turning now to the case of thinner film, shown in Fig. 5.23(b) we find that attempts of similar fitting of Eqs. 5.6 and 5.7 does not work. In order to limit the amount of fitting parameters, we have normalized the data by $I_{c2}(0)$. When using exact dependence given by Eq. 5.7 the best fit achieved (shown by red curve) deviates from the data; moreover, the fitted curve in this case cannot be improved, because it becomes insensitive for $\Delta(0)$ exceeding 1.4 meV. We have tried to modify Eq. 5.7 by replacing exponent 2 by a free fitting parameter. Such a fit (shown by dashed line) seems to give a better result, but the extracted $\Delta(0)$ is equal to unreasonably large value of 2 meV (while based on [111], using $Tc \approx 3.08$ K, $\Delta(0)/k_B T_c \approx 2$ it should be about 0.53 meV).

The inadequacy of the BCS fit is not very surprising; it signifies a changing nature of the phase coherence with decreasing temperature. Since on decreasing T the coherence length in the SC islands becomes shorted, the short Josephson junctions which couple SC islands at high T are effectively turned off at low T, and instead, coupling by long junctions takes over. This leads to a distinctive value of SC gap, which in case of long junctions is induced in normal metal; this gap (called also "minigap") is smaller than full SC gap induced by proximity effect in short junctions [219].

We can extract directly the value of the minigap (we call it Δ^*) at low T, from the dependence of voltage at the critical current I_{c2}, which has been shown in Fig.5.20(b).

This value at lowest T is equal to about 0.285 meV (it is slightly different for two current polarities due to the SDE). Note that using as T_c the temperature of the global coherence (1.7K) and the factor $\Delta^*/k_B T_c = 2$ from [111] (for sample with thickness d =3.6 nm), we get very close value of Δ^* =0.293 meV, what nicely confirms this interpretation. Furthermore, we suggest that the jump in the voltage measured at I_{c2}, which is evident in Fig. 5.20(b) on the approach to the global coherence temperature (∼1.7K) results from abrupt switching of SC gap, from larger SC gap existing in the high T-region of short JJ, into smaller Δ^* in low-T region of long JJ; just above the jump this larger gap, Δ, is equal to 0.375 meV. Notice, however, that even large Δ in short–JJ region does not follow BCS-like T dependence given by Eq. 5.6 and Eq. 5.7. The reason is most likely caused by the fact that the length of short junctions, which dominate the behavior at high T, varies with temperature; therefore we cannot fit the curve with one constant value of $\Delta(0)$; in other word, effective pairing interaction is affected much more strongly by the surrounding landscape of SC islands and junctions than in the case of regular BCS superconductor. Note that this type of behavior cannot be simulated by an artificial JJA with fixed geometrical parameters; it is only possible to have it in a JJA with variable length of the JJ.

We now turn to evaluating properties of I_{c1} switching current. First, we considered the evolution of the isothermal dV/dI versus I, as I increases starting from zero at very low temperature. We have experimentally performed 700 I-V measurements at T =0.7 K; measurements for the negative current polarity ($-I$) were performed separately after measurements for the positive current polarity ($+I$). After every single measurement we heat to a normal-state temperature (>3.1K) and then cool back again to 0.7 K and run the next measurement. Results from 700 measurements interestingly reveal stochastic switching of the critical current I_{c1}. Fig. 5.24 shows the switching current distribution (SDC) as a function of the switching current (I_{c1}), calculated for positive and negative current polarities.

Aside from the stochastic switching of the I_{c1} for each current polarity, there is a clear difference between positive and negative SDC, confirming diode effect. While we cannot pin at the moment exact effect responsible for SDE in case of our film it seems that the intrinsic sample inhomogeneity, with the mixture of long and short JJ, may be responsible. Polarity dependence of the nonreciprocal current response in IV characteristics; $I(V) \neq -I(-V)$ is called the superconducting diode effect (SDE). SDE is very often driven by broken (or reduced) inversion symmetry and broken time symmetry in different systems, including Josephson Junctions systems, in zero and non-zero magnetic fields, therefore, it can be useful in technological applications [220]. Observing SDE in systems without time-symmetry breaking is very rare [221]. The intrinsic mechanism that causes SDE in junction-free bulk superconductors has been recognized as the nonreciprocity of the depairing critical current and the underlying mechanism of the supercurrent nonreciprocal tranport may be better understood in engineered systems [220]. Questioning the possible origins of SDE in our comlicated film, we point that in [222], a theoretical work has been introduced, suggesting that, in both classical and quantum heterojunctions systems, the SDE could be simply induced by the difference in the charging energy; due to the difference in the charge accumulation on both sides of the junction. Moreover, controlling Andreev-bound states in the normal metal barrier or weak links in a Josephson junction can help controling the diode effect [223]. The role of self-field vortices caused by nonuniformuty in both the critcial current and the bias current distribution is also possible [224–226].

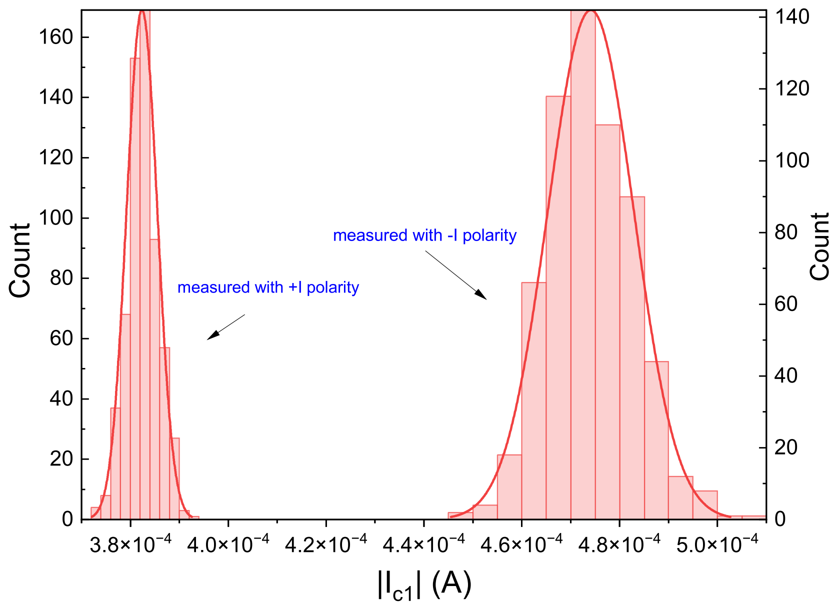

FIGURE 5.24: SCD (bars) for 700 switching events measured at T = 0.7 K, B =0 T under polarity ($\pm I$). Gaussian distribution is assumed (Red fitting lines); switching to next resistive state occurs at I_{c1} with distribution maximum at 3.824×10^{-4} A for the positive I polarity and at $4.74\times^{-4}$ A for the negative I polarity (the values for the standard deviation σ are 3.14×10^{-6}, 8.79×10^{-6} for positive, negative polarities respectiviely).

Turning now to the stochastic behavior, we note that it has been reported, for example, in [43] indicating a Josephson-like dynamics of the $LaAlO_3/SrTiO_3$ interface discussed within the classical RCSJ model. As already mentioned in Sec.2.2.5 the dynamic of JJ in RCSJ model is equivalent to a particle moving in a tilted washboard potential, with particle escape from potential well given either by thermal activation (TA) or macroscopic quantum tunneling (MQT) process. In in [43] it has been pointed to the possibility of the macroscopic quantum tunneling (MQT) effect (possibly with phase diffusion) that may describe the saturation behavior in the switching current observed at very low temperatures. Moreover, we point that Nb-InAs-Nb and high T_c-$Bi_2Sr_2CaCu_2O_{8+\delta}$ moderately damped Josephson junctions have been studied in [126] where thermal activation (TA) process is the governing dynamics mechanism and leads to critical current behavior characterized by faster growth at low temperatures in comparison with MQT mechanism. Moreover, in finite (non-zero) magnetic field, stochastic behavior of nonreciprocal critical current has been reported, for instance, for Al/InAs nanowire [227]. In Fig. 5.20(a), we can notice that the T-dependence of I_{c1} approximately shows similar behavior for both current polarities what may roughly point to a similar escaping mechanism, however unclear, to the next voltage state.

Here, we point that from Eq. 2.43 (chapter 2), the junction capacitance C is inversely proportional to the spacing between SC banks. Besides, from Sec. 2.2.4 (The Josephson Effect), we remind that for links with various dimensions, deviations from the simple classical form given by Eq. 2.34 occur, with the note that the critical current and preceding currents are link-geometry dependent and not only depend on the instantaneous value of the SC phase ϕ but depend also on the former variations of the phase [114].

We have also studied the hysteresis behavior in absence of external magnetic field (B =0 T) via increasing current I above the switching current I_{c1} and then returning back (decreasing current) to the same resistive state at I_{r1} (so-called re-trapping current). Fig. 5.25 shows the results of hysteretic behavior of our film at temperatures T=0.1 K and 0.4 K. As we can notice from figures (a) for 0.1 K, scanning current starting from I =0 to $+I = 5X10^{-4}A$ and then back to I =0, then following through I =0 to -5×10^{-4} A and then back again to I =0 results in a hysteresis loop of the same size if we reverse the scenario (i.e., starting from $I = 0$ to $I = -5 \times 10^{-4}$ A , etc as shown in figure (b)). The current sweep direction is indicated by arrows in the figures.

The green loops (and right scale) show temperature dependence of the system (measured close to the sample) during the sweeps. It is clear that there is some Joule heating during the sweep, however, unlike the jump to normal state at I_{c2} switching current, the jump at I_{c1} does not influence heating in the system, which warms up with the same steady increase both below and above I_{c1}. This suggest that hysteresis at I_{c1} is not related to heating. The values of the switching current (I_{c1}), the re-trapping current (I_{r1}) are show in the figures. Fig. 5.25(c) shows that at 0.4 K, the size of hysteresis loops remains almost the same as for T =0.1 K. However, we observe that I_{c1}/I_{r1} is at both temperatures slightly smaller (closer to the value of 1) for positive polarity than it is in the case of negative polarity.

Fig.5.26 shows the hysteresis results for the temperatures T =0.7 K, 1.1 K and 1.5

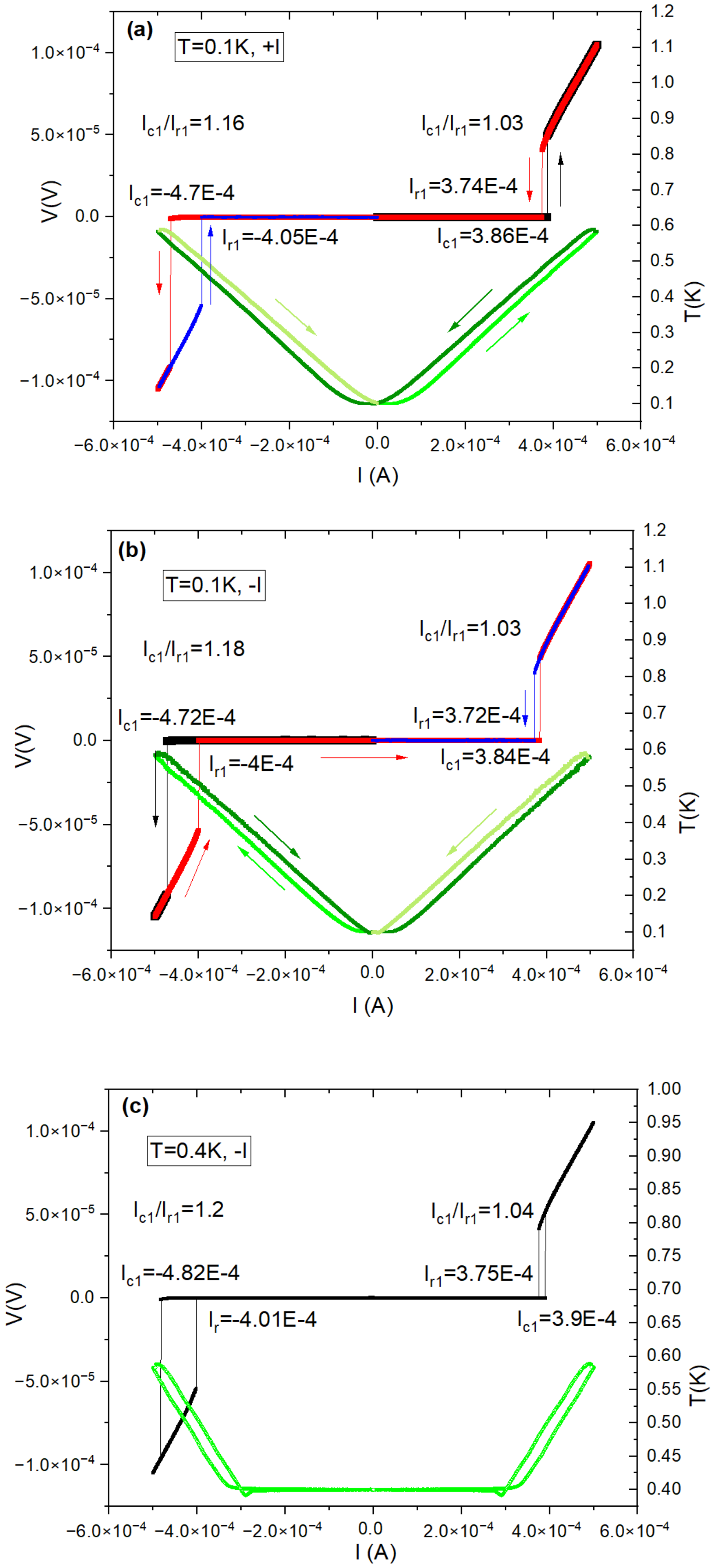

FIGURE 5.25: Hysteresis loops in the IVCs (a, b) for T =0.1 K and (c) for 0.4 K measured for 3.6 nm-Nb film, B =0 T.

K. At 0.7 K, as shown from figures (a) and (b), the hysteresis loop for negative current polarity remains almost the same as at lower temperatures (0.1 K and 0.4 K). However, on the $+I$ side, the ratio I_{c1}/I_{r1} is almost unity as I_{r1} becomes identical to I_{c1}. As T increases, we can see that at 1.1 K no hysteresis is seen on the $+I$ side whereas it remains visible on the $-I$ side in figures (c) and (d); the size of full hysteresis loop is almost constant. As T increases further and further, the loop size for the $\check{}I$ side diminish and start to disappear such as shown for $T = 1.5$ K in Fig. (f).These evaluations indicate that there is a rough correlation between presence of hysteresis and the approach to the temperature, at which global coherence is achieved ($T \sim$1.7 K). This correlation could be expected based on RCSJ model, because hysteresis in this model is related to the quality factor Q (inversely proportional to the damping); $Q = w_{p0}RC \geq 1$, $w_{p0} \sim 1/C$ is the Josephson plasma frequency [126]. When temperature is increased above the global coherence temperature, the capacitance coupling between islands rapidly diminishes and quality factor decreases to 1. However, we note that hysteresis disappears at slightly lower T than the occurrence of global coherence, moreover, the SDE is quite pronounced in the hysteresis in experiment, where it is somewhat obscured in the analysis of the nonlinear $V(I)$-dependence (Fig. 5.18). This may suggest that RCSJ is two simplified to describe present system or there is no one-to-one correspondence between BKT and RCSJ modeling.

In the following we discuss the T-dependence of the switching current I_{c1}, as obtained in our experiment in the film with d =3.6 nm. The critical current in case of long junction has been evaluated theoretically [125]; it has been found to follow quasi-classical equation for the single, diffusive SNS junction:

$$I_{c1}(T) = a\frac{E_{Th}}{eR_N}\left(1 - b\exp\left(\frac{-aE_{Th}}{3.2k_BT}\right)\right) \tag{5.8}$$

where R_N is the normal resistance and the parameters a and b depends on Δ/E_{Th}. E_{Th} is inversely proportional to the islands spacing L and the diffusion time of electrons between islands ; $E_{Th} = \hbar^2 D/L^2$. At T =0 (zero temperature), and for the true long-junction limit ($\Delta/E_{Th} \longrightarrow \infty$) the product $eR_N I_{c1}$ is proportional to E_{Th} as follows [125]

$$eR_N I_{c1}(T = 0) = 10.82E_{Th} \tag{5.9}$$

In the opposite limit, i.e., Δ/E_{Th} approaches zero, that is, in short diffusive SNS junctions, as $T \to 0$, we have the following dependence [114, 228]

$$eR_N I_{c1} \cong 2.07\Delta(T \to 0) \tag{5.10}$$

Equations 5.9 and 5.10 show that it is the smallest of the two energies, Δ and E_{Th}, that limits the critical current in diffusive SNS junctions. In general, in the region between long and short junction limits, the critical current at T =0 transforms gradually from relation given by Eq.5.9 to the one given by Eq. 5.10. Many experiments have been performed to test validity of Eq.5.8, all of them for systems with junctions

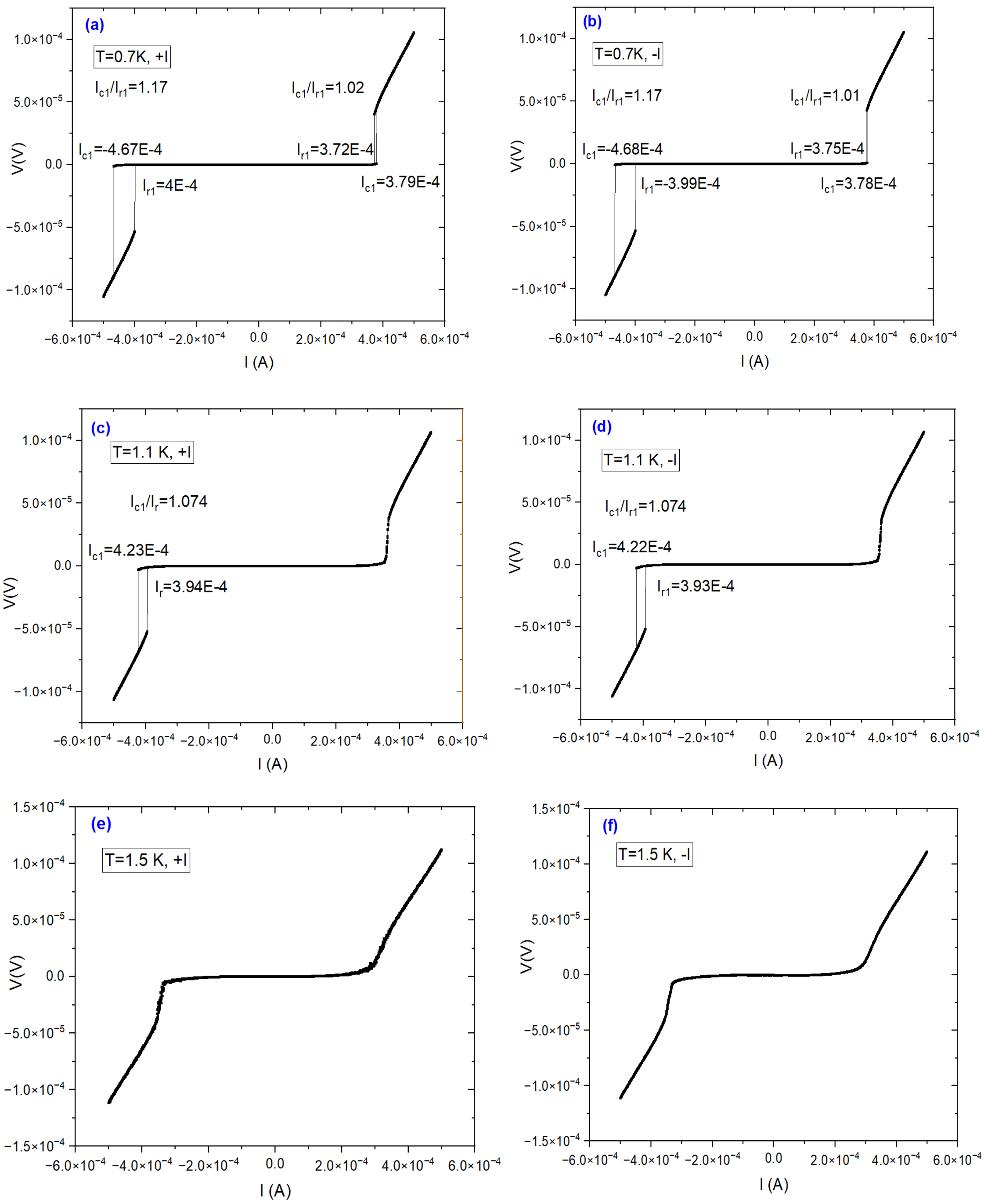

FIGURE 5.26: Hysteresis loops in the IVCs measured for 3.6-nm film for the temperatures T =0.7 K, 1.1 K and 1.5 K, B =0 T.

of fixed, known junction length L [219]. In particular, the relation [5.8] has been used in [42]to interpret the T-dependence of I_c of Nb/Au JJA; qualitative agreement has been found.

Unlike the previous experiments, the system which we study here contains many junctions with variable (unknown) lengths L. Still, we may test the validity of relation [5.8] in our case by modifying slightly this relation. First we normalize I_{c1} to its T =0 value (measured at T =0.1 K), $I_{c1}(0)$. Next, we introduce new constant C^*, defined as $C^* = a/L^2$, whereas a is the constant from relation [5.8], and L is the junction length. Using this substitution, and the definition of $E_{Th} = \hbar D/L^2$ (where D is the diffusion coefficient of the normal metal), we replace Eq. 5.8 by

$$I_{c1}(T)/I_{c1}(0) = 1 - b\exp\left(\frac{-\hbar D}{3.2k_B}\frac{C^*}{T}\right) \tag{5.11}$$

Once the D is known, we can fit this relation to the data for $I_{c1}/I_{c1}(0)$, treating b and C^* as fitting parameters. The value of D may be estimated from the known relation $D = v_F l/3$, where $v_F = 2.73 \times 10^7 cm/s$ is the Fermi velocity, and l is the mean free path, estimated based on the R_N value. For polycrystalline films we have $\rho_N l = const$, where $\rho_N = R_N d$ is the resistivity, and $const = 3.7 \times 10^{12} \Omega cm^2$ for crystalline niobium [229]. For amorphous films a modification relating const to residual resistivity has been proposed [230], and we use it for our estimate. We get $D = 0.52 cm^2/s$, and, based on this value, the Thouless energy $E_{Th} = (34 meV nm^2)/L^2$.

Fig. 5.27(a) shows the data for I_{c1} (both polarities, as the base value) and the relation [5.11] fitted to it. The fitted values of b are 3.46 and 4.15 for two different polarities, while C^* is 0.029 and 0.032, respectively. The constant b obtained from the fits is somewhat larger than the value 1.3, expected for long junction limit ($(\Delta/E_{Th}) \sim \infty$) [125]. Nevertheless, T-dependence predicted by quasi-classical model for long junctions is followed reasonably well in the T-range below 1.7 K, and slightly deviates at higher T. We can even get an estimate of the L value acceptable from the point of view of long junction behavior; the reasoning behind this is illustrated in Fig. 5.27(b), in which we plot the dependence of E_{Th} on the junction length L, given by the relation $E_{Th} = (34 meV nm^2)/L^2$. Using the limits expected in case of long junctions, we can add to this plot the maximum value of E_{Th}, which would be equal to gap value at low T, i.e., Δ^* =0.285 meV. We can also calculate a value of a parameter, $a = C^* L$, using fitted C^* parameter; and we add to the plot a limiting value of E_{th} for a =10.82 (expected for infinite (Δ/E_{Th})); the shaded area shows the range of possible L value in our film, falling in-between 11 nm and 18 nm. Note that for these L values a is in a range between 3.6 and 10.82 while the ratio of Δ^*/E_{Th} falls between 1 and 3, therefore the average junctions appears to be close to intermediate junctions length, rather than to a limiting long junction length. Our estimation results suggest that the energy scale E_{Th}, comparable to Δ, may govern the switching events (to next voltage states) by limiting the irreversible current I_{c1}, therefore governing the shape of the rest of IVCs as current further increases. This with keeping in mind that, eventually, the T-dependence of I_{c2} (switching current to normal state) is independent of the current polarity ($\pm I$).

Of course, all these considerations are based on very approximate estimate of D

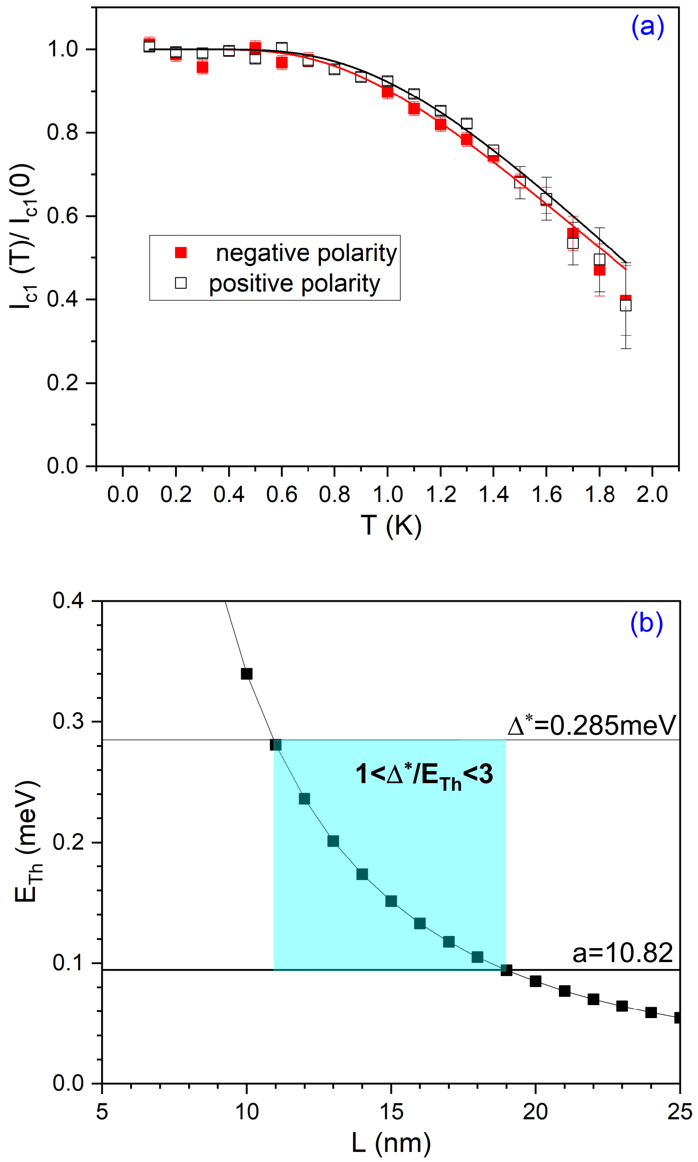

FIGURE 5.27: (a) Fits of normalized $I_{c1}(T)$ versus T (for 3.6 nm-film, B =0 T) using Eq. 5.11. (b) Variation of E_{Th} with junction length L.

value, and, on the assumption that the T-dependence may be described by a formula for a single junction. The fact that we are dealing with JJA instead, is vividly shown by the dependence on current polarity. We believe that the complicated interplay of many junctions may be responsible for the diode effect.

Now, after discussing the behaviors of I_{c1} and I_{c2}, let us pay more attention to the switching current I_{c12} ($I_{c1} < I_{c12} < I_{c2}$), which is visible in the T-range 1.4-2.5 K (Fig. 5.20). As we have already suggested, this switching current may be related to multiple Andreev reflection (MAR) features. MARs is a retro-reflection mechanism of the quasi-particles (electrons/holes) at the interfacial boundary of diffusive Josephson junctions [216, 231]. MARs are usually characterized by a sequence of resonances, dips (minima) /peaks (maxima), in the differential resistance (conductance) versus current or voltage, thus developing a subgap structure (SGS). The appearance of SGS in a SNS junction due to MARs has originally been explained by Klapwijk et al [232] in a model that does not include normal scattering. Following that, an appealing model called the Octavio-Tinkham-Blonder-Kapwijk (OTBK) model [233] has been introduced by Octavio et al where they study MARs across N/S interface using Boltzmann equation approach; the strength of the barrier affects the shape and order of the resonances and their evolution with temperature. The model assumes elastic scattering process at the N/S interface and no scattering events are assumed to occur in the normal region. In the same study, it has been also shown that normal scattering enhances the MARs resonances even at T =0 K state. Here, we point that for Nb Arrays on Au film (long junctions) in figure 2(a) of [42], dip-to-peak oscillations are somewhat visible (in particular, for the case of 540 nm islands spacing) in the dV/dI versus I; although no comments on the possible role of Andreev reflections or other possible technical origins. Andreev reflections have been also studied in systems which are not of SNS-type junctions [231, 234].

The condition that is often exploited to demonstrate a well-developed SGS from the IV measurements of Josephson junctions system is given by [231]

$$eV = 2\Delta(T)/N \tag{5.12}$$

Here V is the voltage, e is the electron charge, and N =1, 2, 3... represents the N^{th} order-Andreev reflection. In the SGS, Δ represents the gap which could be either the SC gap, Δ_{SC} , for the SC electrodes (banks) of the junction or the induced gap ($\Delta^* < \Delta_{SC}$) in the non-SC part of the junction. An example which points to the relative peaks/dips characterizing Andreev reflections governed by both gaps is shown in the calculated SGS for Nb/InAs/Nb weak link system where InAs behaves as two dimensional electron gas (2DEG) [234].

An important theoretical work [235] shows that the shape of the MAR resonances in the differential conductance spectrum depends on the relative length of the junction with respect to the coherence length; theory predicts sharp peaks for short junctions ($L \ll \xi$), evolving into less obvious features with increasing junction length. Comparison of our results to the previous experimental and theoretical work is a difficult task, because, unlike all other cases, here we study the JJA with collection of junctions of various lengths. Nevertheless, some observations can be made.

In order to proceed, we re-plot in Fig. 5.28(a) the differential conductance versus voltage for some selected temperatures for two current polarities, and in (b) the voltage at critical current I_{c2} and at I_{c12} maxima versus temperature. Let us first state that we know from the values of the T_c (T_c onset at 3.08 K, and global coherence temperature, 1.7 K) that two different gap scales exist. The large gap, related to 3.08 K onset, if interpreted according to BCS theory, would lead to $\Delta(0)$ =0.53 meV, while smaller gap, at 1.7 K, with $\Delta^*(0)$ ≅0.29 meV. As we see in Fig. 5.28(b) the smaller gap $\Delta^*(0)$ is indeed observed in the lowest T (split by diode effect). On the other hand, large gap is seen only at high T. In the vicinity of the T_c onset we can fit BCS theory prediction $\Delta(T) = \Delta(0)1.74\sqrt{1-T/T_c}$ to the data measured at critical current current I_{c2}, and from this fit we get $\Delta(0) = 0.48 \pm 0.05$ meV. However, $\Delta(T)$ does not follow BCS theory; instead, it saturates at the value of about 0.33 meV just above the temperature of the transition to global coherence.

Let us now turn to the presumed MAR features. As we see in Fig. 5.28(a) the drop of conductance at $\Delta^*(0)$ is clearly seen at lowest T =0.1 K(slightly different for both polarities). As T increases above the global coherence T (equal to about 1.4 K and 1.7 K for positive and negative polarities, respectively), we observe two effects. First the drop of conductance at high voltage shifts suddenly to about 0.33 meV (which may be identified with Δ, compare Fig.5.28(b)). Secondly, at somewhat smaller voltage, a broad minimum of conductance appears which we identify with MAR. These two features, lower voltage MAR minimum and high-voltage conductance drop (Δ) evolve differently with increasing T. The high voltage drop (Δ) remains at roughly constant level up to about T =2 K, and then it starts to move to smaller voltage. On the other hand the MAR minimum evolves first into well-defined double peak (best seen at T = 1.9K for negative polarity). At still higher T, T >2, it changes into shallow and broad minimum on the conductance curve, without any sharp features characteristic for MAR. This continuous evolution of the MAR feature strongly suggests that it represents T-dependence of Δ^*. High-T broadening of MAR minimum likely results from thermal broadening when thermal energy k_BT exceeds Δ^*; this happens for T >2K. However, even for T > 2K we can still identify the position of this broadened minimum; it shifts approximately linearly towards smaller voltage with increasing T, as depicted in Fig. 5.28(b); eventually , it seems to approach $\Delta(T)$ curves close to the T_c onset. Moreover, as T decreases, we do not exclude totally the possible emergene of gaps which could be fractions of E_{Th}; such gaps were reported in [219]. Note that at 2 K, at which MAR feature becomes reasonably well-defined, we find approximate relation $\Delta \sim 2\Delta^*(0)$. Thus, vicinity of T =2K is the only temperature, at which we are able to observe something resembling SGS expected by theory for single junction (Eq. 5.12). We mark this temperature by green dashed line in Fig. 5.28(b).

Trying to interpret these observations, we propose the following scenario. In our JJA system at the T_c onset the SC state is confined to SC islands. As T is decreased, proximity effect develops in the intermediate surrounding of the SC islands. The closest SC islands couple via proximity effect, producing larger SC areas, but with suppressed Δ. Since the coherence length is large, many junctions with widely different L, all following the condition $L \ll \xi$, contribute to transport, but sharp MAR features cannot be observed due to thermal broadening ($\Delta^* < k_BT$). Nevertheless, broadened MARs contribute to the shallow minimum on the conductance curve, indicating development of the small $\Delta^* < \Delta$. Small Δ^* grows linearly with decreasing T, in contrast to the suppression of large Δ; coexistence of these energy scales suggest

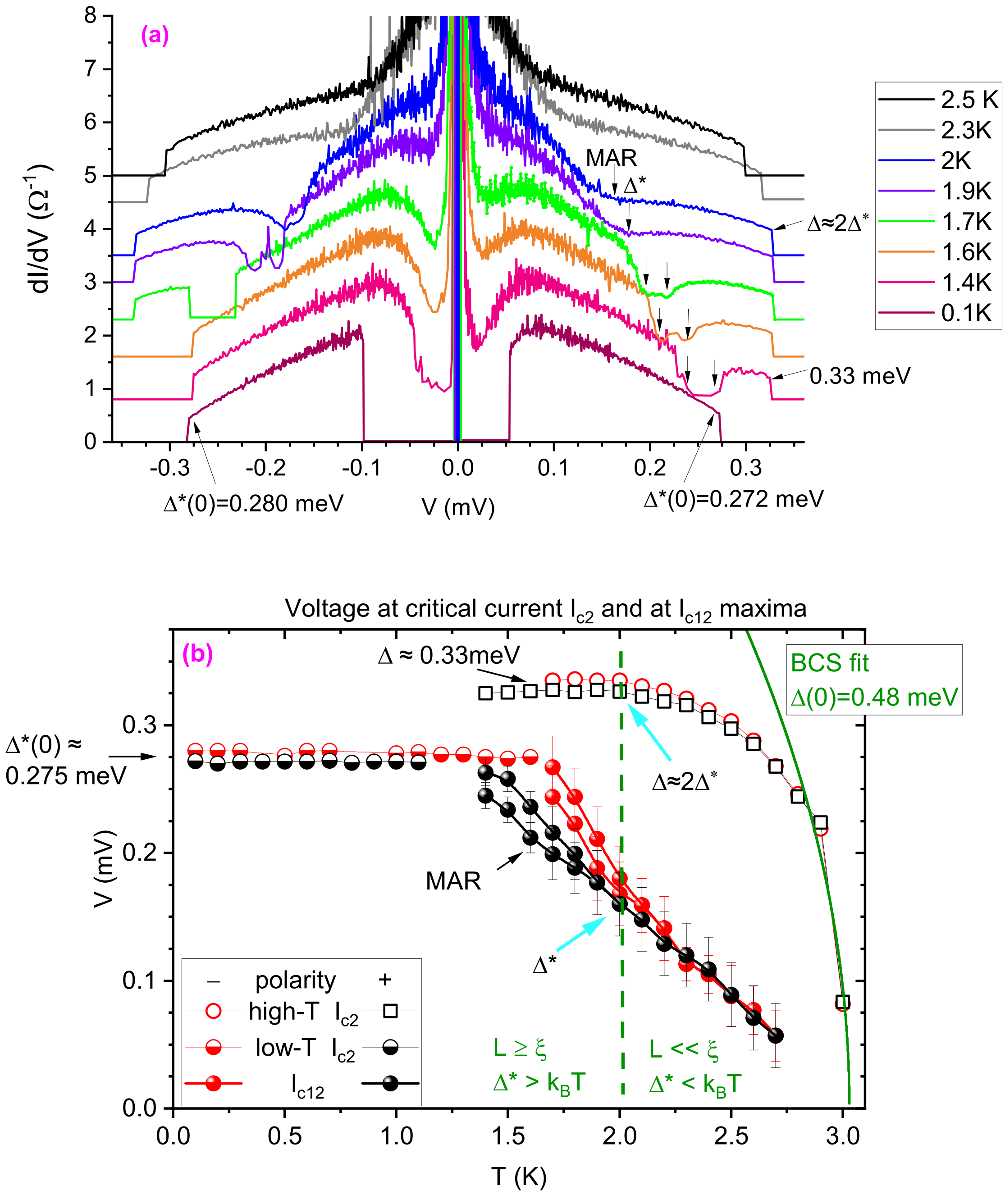

FIGURE 5.28: Conductance dI/dV vs. V (a) and V (measured at I_{c2} and at I_{c12} maxima) vs. T with pointing to the possible MAR features (b) in 3.6 nm-film (B =0 T). Curves for different T in (a) are shifted upward for better visibility.

inhomogeneous mixture of areas with different coupling between SC islands. This region of short junctions persists down to about 2K (to the right of the green line in Fig. 5.28(b)). To the left of this line we enter MAR region, in which MAR features are well defined, because now $\Delta^* > k_B T$. The decrease of the coherence length, which reaches about 18 nm at 2K, suggests that intermediate junctions ($L \geq \xi$) start to play increasingly important role. In this region proximity coupling depends on the normal metal coherence length, which increases with decreasing T, leading eventually to global coherence.

Finally, we would like to point that as d keeps decreasing below 3.6 nm, however unstudied, it may turn out that $J_s < \Delta(T)$ and the SC phase suppression to be driven by phase fluctuations of non-BKT type which may dominate over amplitude fluctuations of the order parameter (whose modulus related to carrier density n_s). Among the possible scenarios (which are beyond our study) is that there may be a largely spaced but small SC-like grains will be formed describing anomalous SC to metal transition where the Cooper pairing energy $\Delta(T)$ may remain finite. As for the case of SC puddles in a metallic sea, the Andreev scattering of electrons from the SC-metallic boundary becomes ineffective for the case of small order parameter on a single puddle [210].

5.2 Vortex dynamics in presence of external magnetic field

Before we start our discussion for this section, we point that the majority of the content of this section has been reported by us before in [236]; "Reprinted with permission from: Sameh M. Altanany, I. Zajcewa, T. Zajarniuk, A. Szewczyk, and Marta Z. Cieplak, Physical Review B 109, p.214504, (2024). Copyright (2024) by the American Physical Society".

5.2.1 Vortex glass transition and scaling laws

In this section, we present and discuss the results for evaluating the VG phase transition (Sec. 3.2, Chapter 3) in thicker Nb films, namely, the films with d=44 nm, 8.5 nm and 7.4 nm. As illustrated previously in Sec. 5.1, these films reveal less inhomogeniety effects in the superconducting state, due to smaller amount of disorder compared to thinner samples. In Fig.5.29 we display on a double logharithmic scale, the temperature dependence of the normalized sheet resistance R_{sq}/R_N for three Nb films with d = 7.4 nm, 8.5 nm, and 44 nm, in the presence of applied magnetic field B. B is applied perpendicular to the film plane and ranges between zero and 1.6 T. R_N is the normal state-sheet resistance selected at T =10 K. In Table 5.2, we list the R_N and other physical parameters determined at $B = 0$, the phase transition-critical temperature T_c at $R_{sq}/R_N = 0.95$, and ΔT_c, the width of the transition defined by criterion 10% to 90% of R_N. As evident, the T_c decreases and the ΔT_c broadens when d decreases. Such feature can be also manifested with increasing the magnetic field, so that the region at which the resistance drops to zero shifts gradually to lower T.

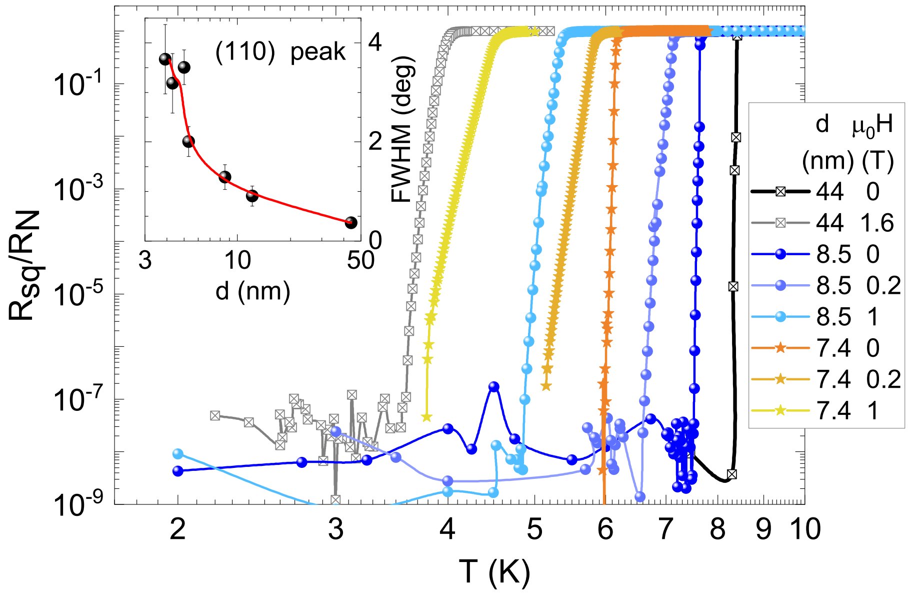

FIGURE 5.29: Normalized sheet resistance R_{sq}/R_N versus T on a double-log scale, measured at B in the range 0 -1.6 T for Nb films with d = 44 nm, 8.5 nm, and 7.4 nm. Inset shows d-dependence of FWHM for (110) characteristic peak in X-ray diffraction spectrum, [236].

By utilizing the values of the T_c and the upper critical field, H_{c2} (defined at $R_{sq}/R_N = 0.95$), measured at small magnetic fields ($B_\perp$) in the vicinity of the T_c, we estimate the value of the zero temperature-upper critical field, $H_{c2}(0)$, and the in-plane coherence length $\xi(0) = [\Phi_0/2\pi H_{c2}(0)]^{1/2}$ according to the pair-breaking theory [88, 100], $H_{c2}(0) = 0.825\, dH_{c2}/dT|_{T_c}\, T_c$. Here Φ_0 is the quantum of magnetic flux $=$ 20.68 Gsμm^2. The estimated values of the $\xi(0)$, shown in Table 5.2, show agreement with the parameters of similar films studied in [49]. Figure 5.30 shows example of fitting the $H_{c2}(T)$ data for 8.5 nm-film using the Baumgartner et al model [237, 238], an accurate model which matches the Werthamer-Helfand-Hohenberg (WHH) model [121, 239]. Black squares and red circules denote the experimental data for $H_{c2}(T)$ obtained from $R(T)$ measurements based on the criterion $R_{sq}/R_N(T = 10K) = 0.95$ and $R_{sq}/R_N(T = 10K) = 0.50$ respectively. Both criteria yields $\xi(0) \approx 11nm$ and zero field-superconducting phase transition tempratures T_c =7.647 K(blue solid line; in agreement with with the T_{MF} in Table 5.1) and T_c =7.54 K (green dashed line). Since the out-of-plane coherence length is likely to be smaller than $\xi(0)$, and coherence length in bulk Nb is 39.5 nm, we predict that in external magnetic fields, films behave as two-dimensional (2D) or quasi-2D systems. This may be also inferred from the BKT transition behavior in abscence of magnetic field.

In the following, in order to verify the nature of possible VG transition in the zero-resistive state in these films, we hold a comparison between the results for the experimental data obtained from the $R(T)$ and IVC measurements and the predictions of VG theory [45, 240]. We start the analysis with the temperature dependence of resistance measured at fixed current (I). In the context of VG theory, the VG phase in the superconducting state is characterized by the vanishing linear resistance (R_{lin}) while approaching T_g from above [77, 156], in the very low current limit ($I \longrightarrow 0$) [45, 73]; we recall Eq. 5.13 in chapter 3

d (nm)	R_N (Ω)	T_c (B=0) (K)	ΔT_c (K)	T_{BKT} (K)	$-dH_{c2}/dT\|_{T_c}$ (mT/K)	$\xi(0)$ (nm)	B (T)	T_g (K)	$z \pm 0.5$	$\nu \pm 0.7$
7.4	38.22	6.29	0.07	6.084	621	10.1	0.2	5.4	3.1	2.1
							0.6	4.5	4.2	2.7
							1	3.7	5.4	3
							1.5	2.9	5.4	2.7
8.5	10.69	7.71	0.059	7.625	442	10.8	0.1	7.15	3.75	2.2
							0.2	6.82	4	3.1
							1	5.0	5.5	2.2
							1.5	3.87	6	2.3
							2	2.65	4.9	2.7
44	1.96	8.43	0.032	8.4	378	11.2	1	5.35	6	1.5
							1.6	3.48	6.3	1.7

TABLE 5.2: Parameters of Nb films: film thickness d, normal sheet resistance R_N at 10 K, T_c (at R_{sq}/R_N=0.95) and the transition width ΔT_c (both at $B = 0$), T_{BKT} determined from IVC at $B = 0$, slope $dH_{c2}/dT|_{T_c}$ determined from linear fits to the upper critical field H_{c2} in the vicinity of the T_c, coherence length $\xi(0)$, VG transition temperature T_g and critical exponents z and ν from I-V scaling analysis. The uncertainty of the T_g value is $\sim \pm 0.25$ in the case of thinnest film, and $\sim \pm 0.2$ in case of remaining films.

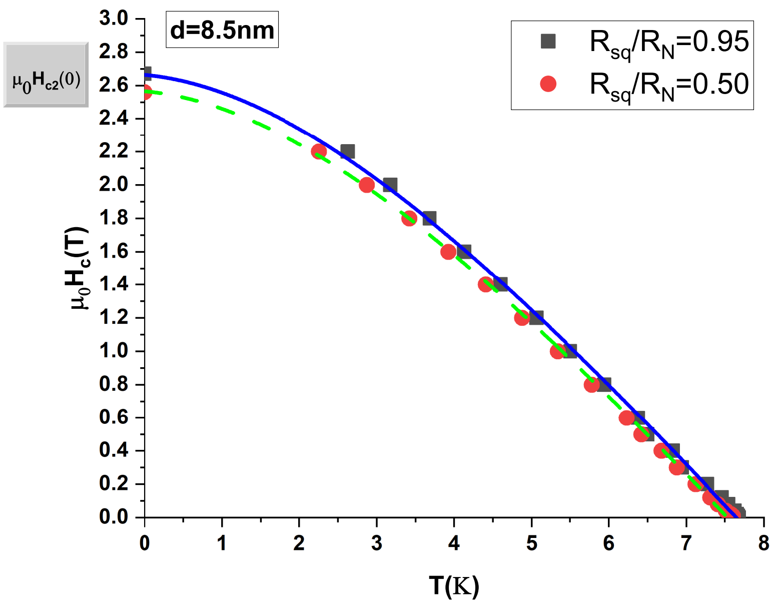

FIGURE 5.30: Theoritical fits of the temperature dependence of the upper critical field, $H_{c2}(T)$, measured for 8.5 nm-film.

$$R_{lin} = (V/I)_{I \longrightarrow 0} \propto (T - T_g)^{\nu(z+2-D)} \quad (5.13)$$

where D is the dimensionality of the system, ν is the static critical exponent of the VG correlation length, which diverges at T_g according to $\xi_g \sim |T - T_g|^{-\nu}$, and z is the dynamic critical exponent for the correlation time $\tau_g \sim \xi_g^z$. Accordingly, the recognized method to extract the T_g and the exponents (ν,z) for the critical behavior of the transition [77, 156] is to examine logarithmic derivative of the sheet resistance which should follow linear T-dependence in the vicinity of the T_g, from Eq.[5.14] we have

$$\left(\frac{d(\ln R_{sq})}{dT}\right)^{-1} = \frac{1}{\nu(z+2-D)}(T - T_g) \quad (5.14)$$

In Figure 5.31 we show the results for the quantity $[d(\ln R_{sq})/dT]^{-1}$ plotted versus T for 8.5 nm and 7.4 nm-films. The $R_{sq}(T)$ has been measured in several magnetic fields and using the low drives, I=0.5 mA in (a) and 0.2 mA in (b). As illustrated, all curves exhibit linear portions below certain temperature T^*. This temperature may set the upper limit of the critical region associated with the VG thermodynamic transition [77, 158]. We mark the fits to the linear portions by dashed lines with the slopes, which gives the inverse of $\nu(z + 2 - D)$, reduced to νz for $D = 2$. From the intersection of the dashed line with the T-axis we determine the value of T_g, which we will call T_g^R, as marked in Fig. 5.31. However, since the current used during measurement is finite (not zero), and since the presence of disorder may generate distinct vortex behaviors in spatially limited areas of the films, the T_g^R determined in this way may not indicate true T_g value as defined by Eq. 5.13. For further insights into vortex behavior, in the following, we continue our investigations via analyzing the data for IVC's of the films.

In Figure 5.32 we show on a log-log scale the IVC's measured for different constant temperatures at fixed magnetic field, $\mu_0 H$ = 1 T in two thinner films. Arrows point to the approximate positions of the IV isotherms corresponding to T^* and T_g^R in the resistance analysis. The $V(I)$ isotherms measured at highest T reveal linear dependence, i.e., $V \sim I$, in the whole current range, indicating normal phase. As T goes down to T^* the linear $V(I)$ dependence survives in the range of very low-current, but then it turns into nonlinear with further increase of the current. As T keeps decreasing below T^* the linear dependence becomes no longer observed. Instead, the $V(I)$ dependence for low currents turns completely into power-law behavior, with the slope on the log-log scale increasing while approaching T_g^R. The change of slope with increasing current, is best seen in areas shaded by light green; we will show in more detail in Sec. 5.2.3 that the data in these areas are impacted by the thermal vortex creep, and they are well described by strong pinning theory, which with increasing current predicts the shape of the nonlinear IVC in the presence of thermal fluctuations [69–71]. We point that the isothermal slope is not constant over the full current range, but it turns smaller at high drives, suggesting the approach to the flux flow region preceding the abrupt switch to the normal state. As shown in Fig.5.32(a) the jump in this film does not lead straightforwardly to a normal phase ($V \sim I$), but rather to an intermediate resistive state(s), with resistance below normal state-resistance. Such non-equilibrium behavior has been pointed out earlier in Sec.

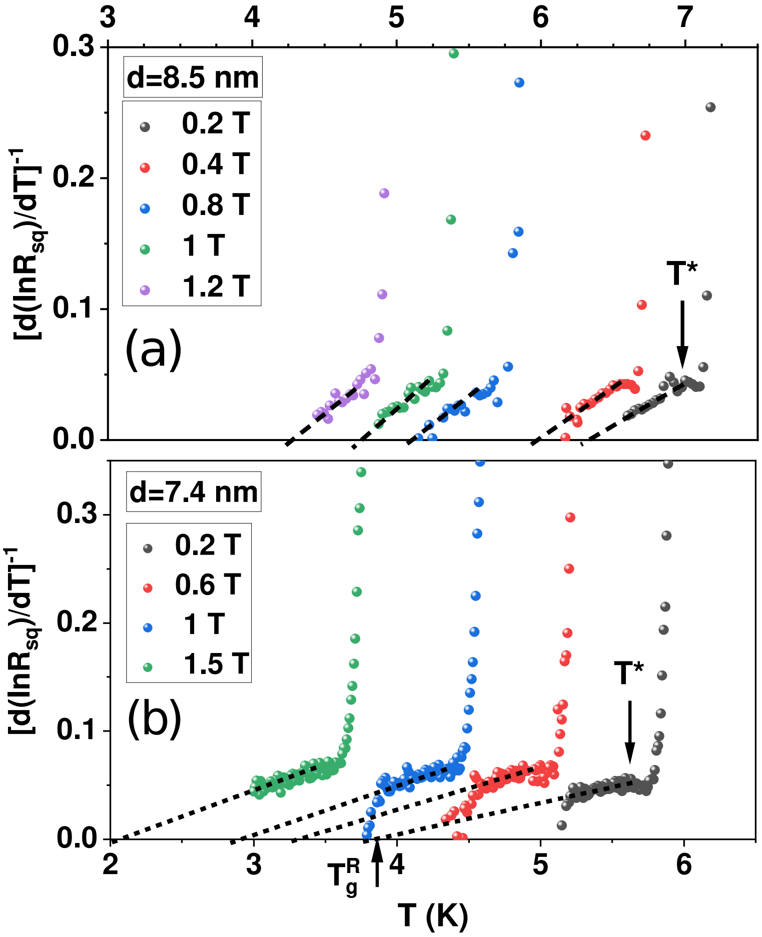

FIGURE 5.31: (Color online) $[d(\ln R_{sq})/dT]^{-1}$ for several magnetic fields for films with $d = 8.5$ nm (a) and $d = 7.4$ nm (b). T^* defines the upper limit of the critical VG region, and the dashed lines represent fits using Eq. 5.14 at $T < T^*$. The glass temperature, T_g^R, is the temperature at which the dashed line cross with the T-axis, [236].

5.1 (see Fig. 5.9); the most probable origin of this thermodynamic behavior is PSLs; in particular, small magnetic field, which broadens slightly the transition and shifts whole series of jumps to lower temperature, seems to be more suitable for observation of this effect. We continue focusing our discussion on vortex dynamics in the SC state (i.e, below I_{c1} labeled in Fig. 5.9).

In order to explore the vortex behavior in the SC state, it is instructive to proceed first with the common way of the IVC data analysis using the VG theory-$V(I)$ scaling laws in order to validate the VG picture. The scaling law predicts that the I-V curves in the vicinity of the T_g can be scaled into two distinct branches ($f_{\pm}$) below and above the T_g,

$$\frac{V}{I(T-T_g)^{\nu(z+2-D)}} = f_{\pm}\left(\frac{I}{|T-T_g|^{\nu(D-1)}}\right), \tag{5.15}$$

At the T_g the I-V isotherm should satisfy the power law:

$$V(I) \sim I^{(z+1)/(D-1)}. \tag{5.16}$$

Now, the problem which could be encountered during the analysis using the $V(I)$ scaling laws is the appropriate selection of the T_g value. Let us point out first that the T_g^R isotherms may be already impacted by thermal creep effects (especially in case of thinner film), and this invalidates scaling. Hence, either the T_g is greather than T_g^R, or the scaling in the present case is not valid at all.

In order to settle this issue we select the T_g by following the standard procedure; we plot the derivative $d(\log V)/d(\log I)$ as a function of current I, and seeking the temperature T_g, at which this plot follows a horizontal line, separating data sets with opposite concavities on decreasing I, downward at $T > T_g$, and upward at $T < T_g$ [80]. In Figs.5.33(a) and 5.33(b) we show the results of this procedure for two thinner films at $B = 1$ T; the black horizontal lines show the chosen data sets, what identifies the T_g and the z value, while following Eq. 5.13 the plot (in the insets) of R_{lin} versus $T/T_g - 1$ on log-log scale gives value of the exponent ν. The T_g estimated in this way is substantially above the T_g^R; corresponding isotherms are marked in Fig. 5.32. Figs. 5.33(c) and 5.33(d) show the collapse of the data after applying scaling procedure, which sounds reasonably good in first of these figures, and somewhat less satisfactory in the latter. The values of T_g, z and ν for different magnetic fields are listed in Table 5.2, where we include also the data for thickest film (d=44 nm). By comparing the values of the critical exponents obtained by this procedure with those predicted by theory and reported previously for quasi-2D scaling ($z = 4 \sim 7$ and $\nu = 1 \sim 2$) [52–55, 158, 159], we find that in case of two thinner samples the z values fall within the range of expectations, whereas values of ν are consistently somewhat too high.

However, it is important to point out that the selection of the proper sets of data in order to define the T_g is somewhat tricky, especially in case of the film with $d = 7.4$ nm; for this film the difference between upward and downward curvature is very

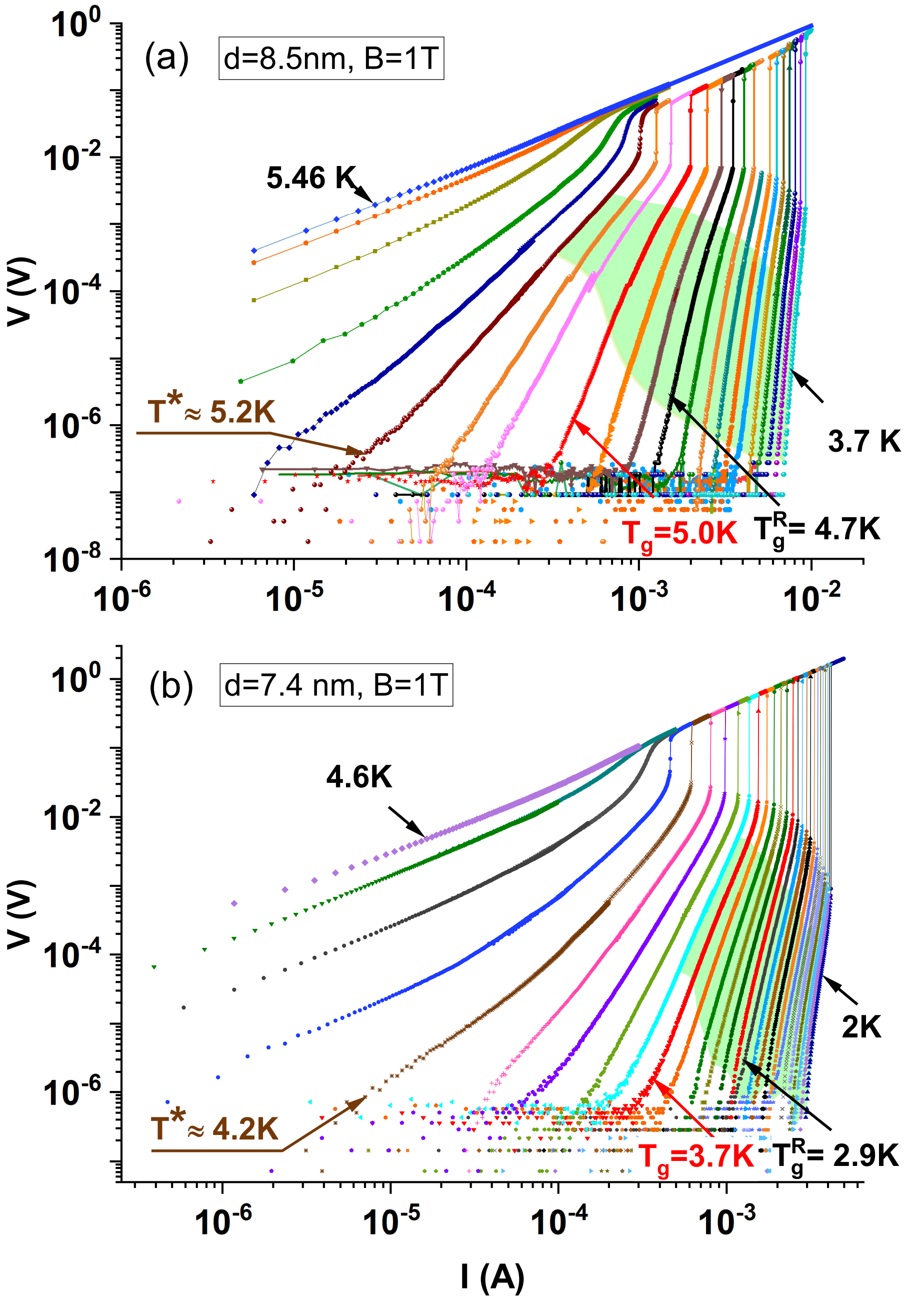

FIGURE 5.32: IVC'c at various T and $B = 1$ T for 8.5 nm-film, measured at T in the range 3.7 K-5.46 K (a), and for 7.4 nm-film, measured at T in the range 2 K-4.6 K (b). The black and red arrows point to the $V(I)$-isotherms at T_g^R's and T_g's determined by resistance and IVC's analysis, respectively. The light green areas in highlights the regions in which strong pinning theory [70] describes satisfactorily the IVC's, [236].

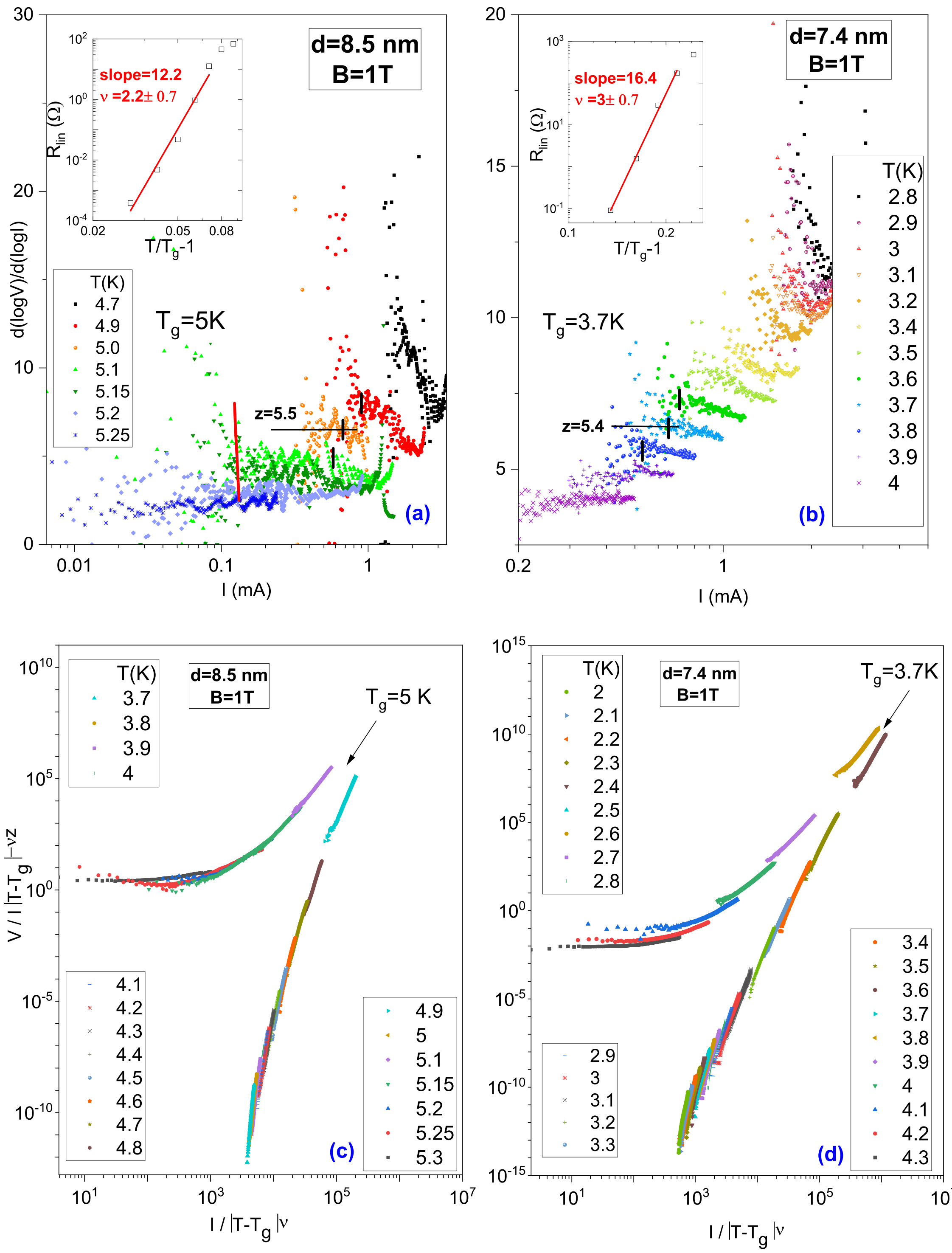

FIGURE 5.33: $d(logV)/d(logI)$ versus I for 8.5 nm-film (a) and 7.4 nm-film (b) at the magnetic field of 1 T. The black, horizontal lines indicate data sets at T_g, the black, vertical lines mark the onsets of creep revealed by strong pinning analysis, and the red, vertical line in (a) shows the I_{min} above which finite size effect is negligible. The insets in (a) and (b) show R_{lin} versus $T/T_g - 1$. (c-d) Quasi-2D VG scaling of the $I - V$ curves in the indicated temperature range in the vicinity of T_g demonstrating the two dynamic branches at B=1 T for d=8.5 nm (c) and 7.4 nm (d), [236].

gradual and this increases the uncertainty in identifying the T_g of the film. Moreover, the procedure may be influenced by two effects. First, finite-size effect may result in modifying the shape of the $V(I)$-isotherms, thus leading to Ohmic tails at current density smaller than about $J_{min} \sim k_B T/(2\pi\Phi_0 d^2)$ [241, 242]. In the present case this translates into minimal current $I_{min} \sim 0.12$ mA for 8.5 nm film (and even smaller value for 7.4 nm film), shown in Fig. 5.33(a) by dashed red vertical line, above which this effect is likely negligible; thus, we can safely ignore it. More complexities arise from the presence of thermal fluctuations (creep), which impacts the data at large drives as shown by green shadow in Figs. 5.32(a) and 5.32(b). In order to observe better approximate creep boundaries at temperatures close to the T_g we mark them by short, vertical, black lines in Figs. 5.33(a) and 5.33(b). It is obvious that the presence of creep, particularly in case of thinner film, imposes restrictions on the data available for scaling analysis. Hence, our considerations suggest rather marginal applicability of scaling procedure in the ultrathin Nb films, despite apparent validity suggested by Figs. 5.33(c) and 5.33(d).

We point that the marginal applicability of scaling analysis does not imply that the VG phase does not exist in the films (vanishing voltage (resistance) is obvious at small current values). Rather, it refers to enhanced inhomogeneity with decreasing film thickness. Different forms of disorder may contribute to this effect. For instance, the proximity of the niobium-silicon (Nb-Si) interface may result in small admixture of Si ions into Nb layer, creating point defects, and the surface layer in which these defects are available plays an increasingly important role on the decrease of film thickness. In the next section, we will demonstrate that the disorder which has the most effect on SC phase in the films is related to imperfect fusion of polycrystalline grains. Such grains, developing during the process of film growth, coalescence into smooth film with the increase of film thickness. In case of very thin films this coalescence gets imperfect, generating therefore amorphous regions at the grain boundaries. This enhances the role of disorder as d decreases, what may likely constitute fractal superconductivity at some smaller d. In the present case of polycrystalline films the SC phase still appears to be globally coherent at low T, but the disorder stimulates vortex creep appearing with increasing current.

In Fig.5.34(a) we showcase the phase diagram for these films at small currents (below the creep boundary) with vertical and horizontal axes normalized to $\mu_0 H_{c2}(T = 0)$ and $T_c(B = 0)$ values, respectively; gray-black lines indicate H_{c2} (determined at $R_{sq}/R_N = 0.95$) and color lines indicate the T_g. Note that the H_{c2} increases with decreasing d (with very tiny difference between two thinner films), while the T_g decreases, with substantial difference between two thinner films. Therefore, while the disorder reinforces upper critical field, it decreases noticeably the range of VG phase with expanding the region of vortex liquid (VL) phase between the VG and the normal phase. It may be anticipated that further decrease of d will lead to destoying the VG phase. Most likely, this will proceed via fragmentaion of the SC state into segregated islands immersed in the metallic background, leading to so-called anomalous metallic state, which has been previously observed in the limit of very small d [49].

In Fig. 5.34(b) we showcase the dependence of the separation between T_{BKT} (determined at zero magnetic field) and the T_g on the magnetic field for three films. Theoretically, for small magnetic fields, it has been predicted that $T_{BKT} - T_g \sim H^{1/2\nu_0}$,

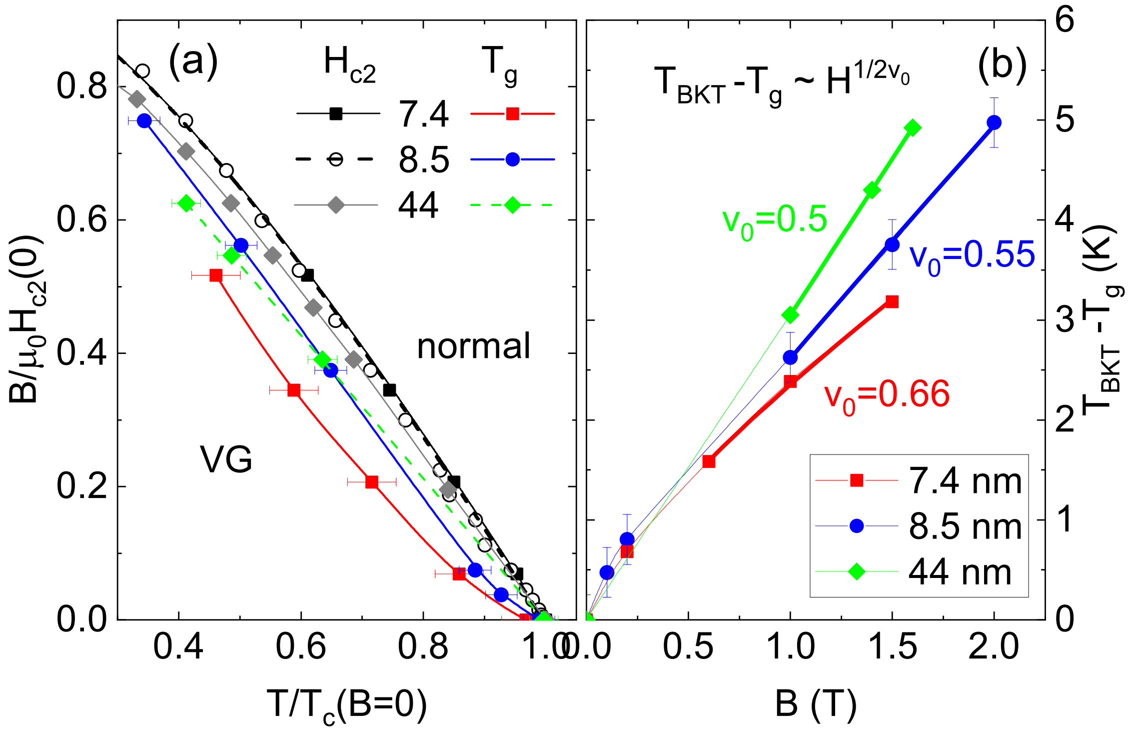

FIGURE 5.34: (a) Phase diagram for films with different d, with vertical and horizontal scales normalized to $\mu_0 H_{c2}(0)$ and $T_c(B = 0)$, respectively. (b) Behavior of the temperature difference $T_{BKT} - T_g$ as a function of magnetic field for films with different d; points are experimental data, lines show fits to power law with exponent ν_0, [236].

where ν_0 is the static critical exponent in zero-field [45]. In the temperature difference in the formula, we replaced the mean field temperature by T_{BKT} due to their proximity as demonstrated in Sec. 5.1. In the past this relation has been used for estimaing the value of static exponent in high-T_c superconductors, and it has been argued that the values of ν_0 obtained in these experiments, 0.66 [242] and 0.5 [241], are in agreement with the 3D-XY model or mean-field theory, respectively. For our case, upon decreasing d, the exponent shows evolution, from 0.5 in thickest film, to 0.66 in thinnest one. Since our films apparently behave as 2D systems with substantial pinning effects, the meaning of this finding is not that clear, apart from the fact that it indicates an effect of disorder on the correlation length in the VG phase.

5.2.2 Vortex dynamics and strong pinning theory

In this section we present a more detailed evaluation of vortex dynamics in the SC state at drives below I_{c1} in the presence of magnetic field. We focus on the region characterized by vortex creep, which we mark previously by light green color in Fig.5.32. Fig. 5.35(a) displays several examples of the IVC measured in this region at different temperatures in case of 8.5 nm-film at fixed magnetic field $B = 1$T. This type of IVC, called "excess-current characteristics", have been observed for type-II superconductors with strong vortex pinning [62, 64–66, 176]. The theoretical description of strong pinning by a small density of pins at $T = 0$ predicts a nearly linear-response (flux-flow) at large drives ($I > I_c$), that is shifted from $I = 0$ by the critical current I_c [60, 61]. Thermal fluctuations becomes important at finite temperatures ($T > 0$) and flux creep is enhanced. This modifies the observed features in three different ways: the I_c is reduced to a vortex depinning current (T-dependent), the rounding appears in the vicinity of it, and thermally assisted flux flow shows up at very small drives, $I << I_c$ [69–71]. In Fig. 5.35(a) the red lines represent theoretical fits of the data in accordance with the predictions of this theory [71], which will be discussed further in the text.

In Fig. 5.35(b), we show the method for extracting the I_c value from experimental data. Through the linear fit to the data at large drives just before the abrupt jump to normal state we define the depinning drive I_c and the flux-flow resistance R_{FF}, given by $V \approx R_{FF}(I - I_c)$, as indicated by red line (several data points just before the jump are omitted in the fit, since they may be already influenced by the approach to flux-flow instability). We point that in some systems with flux instability nonlinear behavior of flux flow resistance has been observed, ascribed to the process of dynamic ordering of vortex lattice in the flow region, as reported for 100 nm thick Nb films characterized by moderate strong pinning [243], or for other films [244]. Such feature leads to a peak or a broad maximum in the differential flux flow resistance preceding the instability of the flux flow. The inset to Fig. 5.35(b) provides an evidence of the absence of this feature our films.

In Fig.5.36(a-c), using the I_c and the films dimensions, we show the temperature dependence of the critical current density J_c for films with different thickness measured for different magnetic fields. For a given magnetic field, the data for J_c are plotted versus temperature reduced with respect to the SC transition temperature T_c, $t = T/T_c$. In all cases the dependencies (as shown by black lines) are very well described by the formula displayed in Fig. 5.36(c),

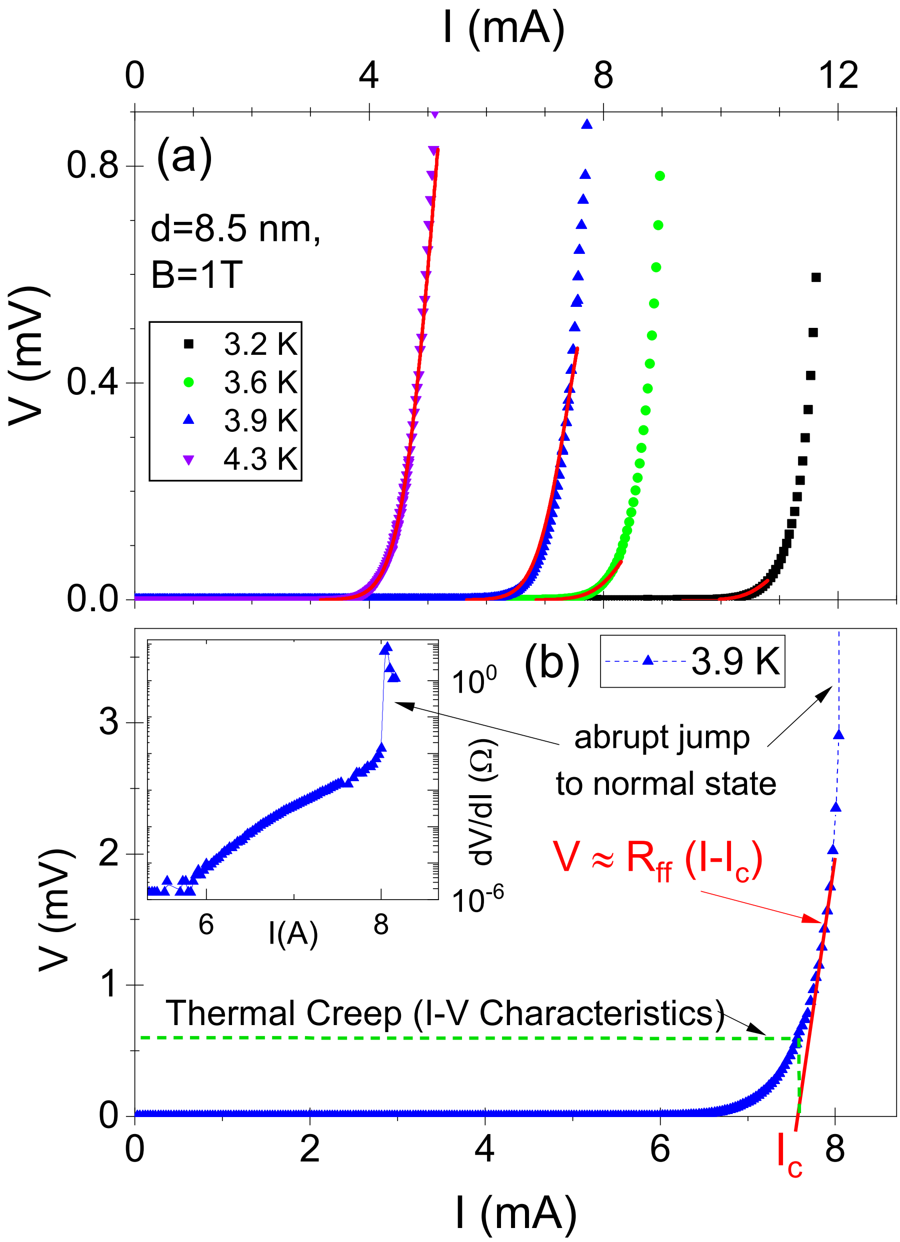

FIGURE 5.35: (a) $I-V$ characteristics measured for 8.5 nm-Nb film at a constant magnetic field $B = 1$ T and temperatures T from 3.2 K to 4.3 K. Red lines are fits to the $V(I)$ data based on the prediction of strong pinning theory [70] (see text for details). (b) Thermal creep and excess $(I-V)$ characteristics for 3.9 K under the same conditions in (a) demonstrating the linear response at large driving currents preceding the abrupt jump to normal state. Thermal creep is restricted to the confined zone (dashed green rectangle) and the red, straight line defines I_c and R_{FF}. Inset in (b) shows monotonic increase of differential resistance dV/dI with increasing I, [236].

$$J_c = J_{c0}(1 - t^2)^m, \tag{5.17}$$

where J_{c0} is the critical current density at $T = 0$, and m is the exponent characterizing the t-dependence. The behavior described by Eq. 5.17 is frequently observed in the region of high temperatures in type-II superconductors, either crystals or films [172, 245–248]. The origins are attributed to spatial variations of the coefficients in Ginzburg-Landau functional, which may be associated either with the fluctuation in the T_c (δT_c pinning) or with the fluctuation in the mean-free path of carries (δl pinning). In the framework of weak collective pinning, it has been shown that these two distinct pinning mechanisms are charcterized by different exponents m, 7/6 for δT_c, and 5/2 for δl [67]. However, some experiments reveal that this result holds also in the strong pinning scenario, such as in the case of thin FeSeTe films [172].

The parameters J_{c0} and m obtained from the fits in the present experiment are shown in the insets to Figs. 5.36(a) and 5.36(b) versus the reduced magnetic field. Considering first the inset to Fig. 5.36(a) we find that the J_{c0} value is high, ranging at $B = 1$ T from about 0.3 MA/cm^2 in the thinnest to about 8 MA/cm^2 in the thickest film, confirming strong, d-dependent pinning. The magnetic field dependence of J_{c0} in case of the thinnest film is well described by a power-law dependence, $J_{c0} = J_{c0}(0)(1 - B/\mu_0 H_{c2})^p$, with exponent $p = 1.55$ and the $J_{c0}(0)$ coefficient equal to about 6×10^5 A/cm^2. We note that this dependence is close to mean-field theoretical relation with $p = 3/2$, for other disordered SC films as recently described in [176]. Note, however, that in our experiment this is an extrapolation from relatively high temperatures ($t > 0.4$), so we cannot truely comment on actual low-t behavior. An interesting thing as shown in the inset to Fig. 5.36(a) is that this relation is different in case of thicker films. In particular, the data for film with $d = 8.5$ nm cannot be fitted by the same relation in the whole H-range. This is a first sign that the pinning nature depends on the film thickness and magnetic field.

In the inset to Fig. 5.36(b) we display the dependence of the exponent m on the film thickness. In the thinnest film m is about 1.3 and it is nearly field-independent, in the thickest film it equals to about 2.2, for 8.5 nm-film the value of m falls in-between, varying from the 1.25 at small B up to about 2 at high B. The exponents which we get from the fits are close to the theoretically predicted values for δT_c pinning in the thinnest film, and for δl pinning in thickest film, while they suggest gradual switching from one mechanism to the other in the 8.5 nm-film (we wonder here about the potential link between the pinning type and the PSLs behavior, in the vicinity of T_c, with increasing field). We summarize all these findings by plotting in Fig. 5.36(d) the normalized critical current density, J_c/J_{c0} as a function of t for all films and magnetic fields. We observe that all data points for the thickest and the thinnest film are aligned nicely along two curves, $(1 - t^2)^{2.2}$ and $(1 - t^2)^{1.3}$, respectively, while data for film with intermediate thickness shift from δT_c towards δl line with increasing magnetic field.

Further insight into this behavior is provided through evaluating the $I - V$ data by using strong pinning theory, recently introduced by Buchacek *et al.* [69, 70], subsequently applied to interpret the experimental data in case of 2H-$NbSe_2$ single crystals and a-MoGe films [71]. As discussed earlier in Sec.3.3 of Chapter 3, the main idea of this theory is that the thermal fluctuations modify the pinning force

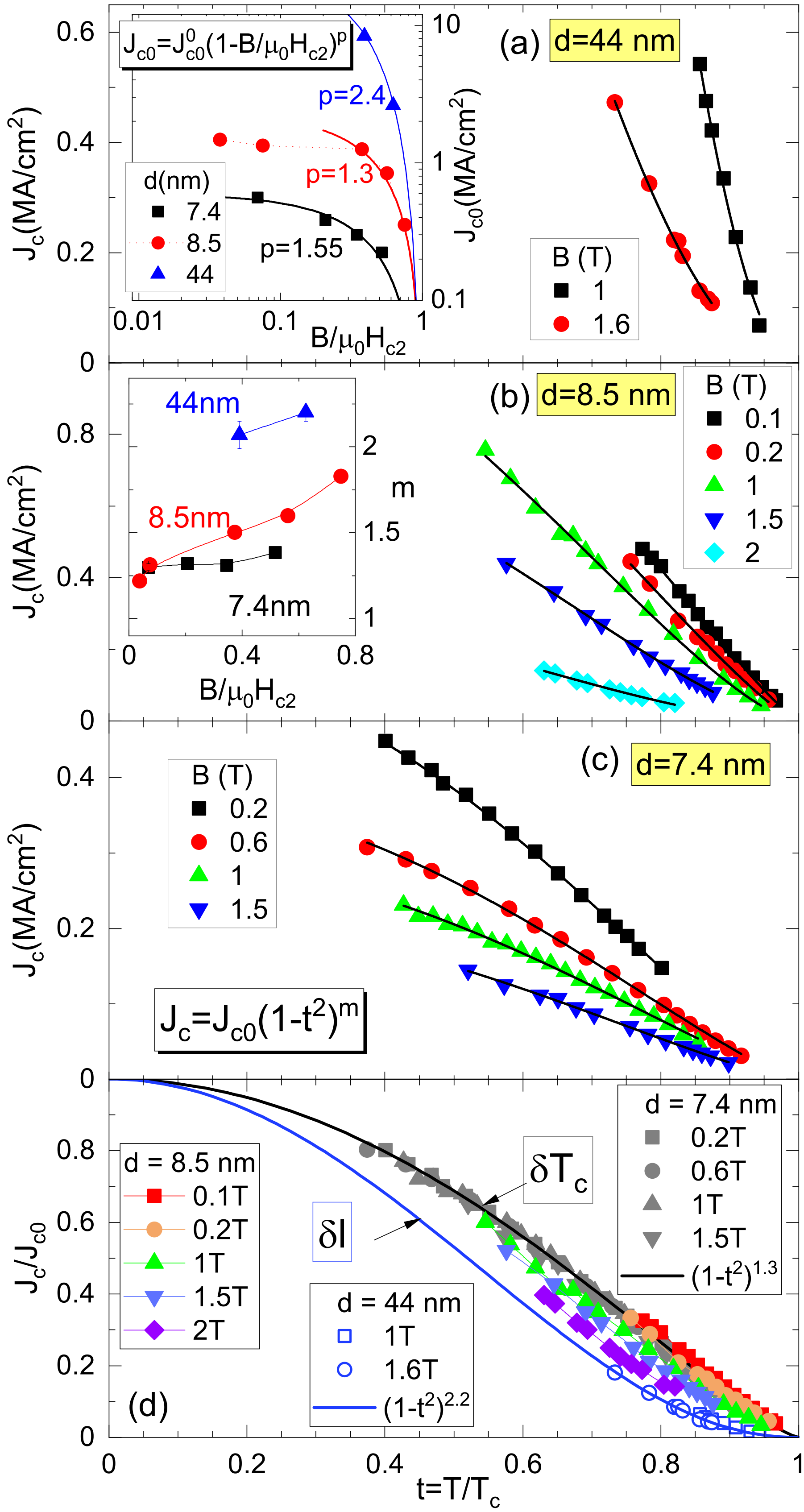

FIGURE 5.36: J_c versus reduced temperature $t = T/T_c$ at different magnetic fields for 44 nm-film (a), 8.5 nm-film (b), and 7.4 nm-film (c). The lines show Eq. 5.17 fitted to the data. (d) J_c/J_{c0} versus t for all films and magnetic fields. Continuous lines display Eq. 5.17 with exponents m equal to 2.2 (blue line) and 1.3 (black line), characteristic for δl and δT_c pinning, respectively. Insets in (a) and (b) show the dependence of J_{c0} and m, respectively, on reduced magnetic field for films with different d (unless shown, the errorbars are smaller than the point size), [236].

acting on vortices. At zero temperature, thermal fluctuations are absent and the vortex velocity v is obtained from the dissipative equation of motion, in which viscous force density $-\eta v$ is given by the balance between the Lorentz force density $F_L(J,B)$ driving the vortices and pinning force density due to defects $F_{pin}(v,T)$, $-\eta v = F_L(J,B) - F_{pin}(v,T)$. Here η is the Bardeen-Stephen viscosity per unit volume ($\eta = BH_{c2}/\rho_n c^2$, where ρ_n is resistivity in the normal state, and c is the velocity of light). At small velocities v and in the absence of creep F_{pin} is approximately constant. This does not hold true at non-zero temperature $T > 0$, when thermal fluctuations stimulate vortices to escape from pinning sites, so that F_{pin} becomes velocity dependent in the presence of flowing current. This gives rise to fluctuation-modified activation energy barrier against vortex creep, which now depends on F_{pin}, $U[F_{pin}(v,T) \approx U_c[1 - F_{pin}/F_c]^\alpha$, where F_c is the critical force density, while exponent α and the coefficient U_c depend on the pinning type; in the strong pinning theory $\alpha = 3/2$ for any smooth pinning potential. Eventually, this leads to the following modified current-voltage relation, which may be directly compared with experiment [71],

$$V = R_{FF}(I - I_c) + V_c \left[\frac{k_B T}{U_c} ln \left(\frac{v_{th}}{v_c} \frac{V_c}{V} \right) \right]^{1/\alpha}. \tag{5.18}$$

Here I_c, R_{FF} and V_c are experimentally-accessible parameters (I_c is the depinning current, R_{FF} is the flux flow resistance, and the their product is the voltage $V_c = R_{FF} I_c$). The two parameters $U_c/k_B T$ and v_{th}/v_c are characteristic for thermal creep behavior and they can be extracted from the fit of Eq. 5.18 to the data from experiment. The barrier U_c (T and B-dependent) should satisfy the relation $U_c \gg k_B T$ (k_B is the Boltzmann constant), which is a basic assumption in the derivation of Eq. 5.18. v_c is critical (free flux-flow) velocity, and v_{th} is thermal velocity scale, at which vortices traverse pins fast so that the barrier slowing down the motion becomes irrelevant. In Fig. 5.35(a) we show the fits of Eq. 5.18 to the data for 8.5 nm-film nm at $B = 1$ T, with α assumed equal to 3/2. In Fig. 5.37(a), the fits are shown for the case of rescaled coordinates V/V_c versus I/I_c.

One can alternatively extract the creep parameters using the relation

$$-ln\left(\frac{V}{V_c}\right) = \frac{U_c}{k_B T}\left[1 - \left(\frac{I}{I_c} - \frac{V}{V_c}\right)\right]^\alpha + \gamma, \tag{5.19}$$

where $\gamma = -ln(v_{th}/v_c)$. Fig. 5.37(b) shows plots of this relation fitted to the same experimental data set as in Fig. 5.37(a), using $\alpha = 3/2$. Both ways provide consistent results for creep parameters; in all cases the extracted U_c follows the condition $U_c \gg k_B T$. The fitted lines shows deviation from the data at large $I/I_c \gtrsim 0.9$, likely indicating some admixture of flux flow to the creep. In Fig. 5.38 we display the results for the velocity ratio v_{th}/v_c versus reduced temperature t for three different films ($B = 1$), comparing between the creep exponents α=1 and 3/2. The fitting range for ($J/J_c - v/v_c = I/I_c - V/V_c$) shifts to higher J in case of α=1 (see Fig.5.39; $J/J_c - v/v_c > 0.6$ (blue solid line)) and cuts-off in the fits occurs as J increases for the data outside the range of validitiy (i.e., for $v < v_{th}/e$ (blue dashed line); e is the natural exponent). According to [71], careful fits with α=1 in the high current region

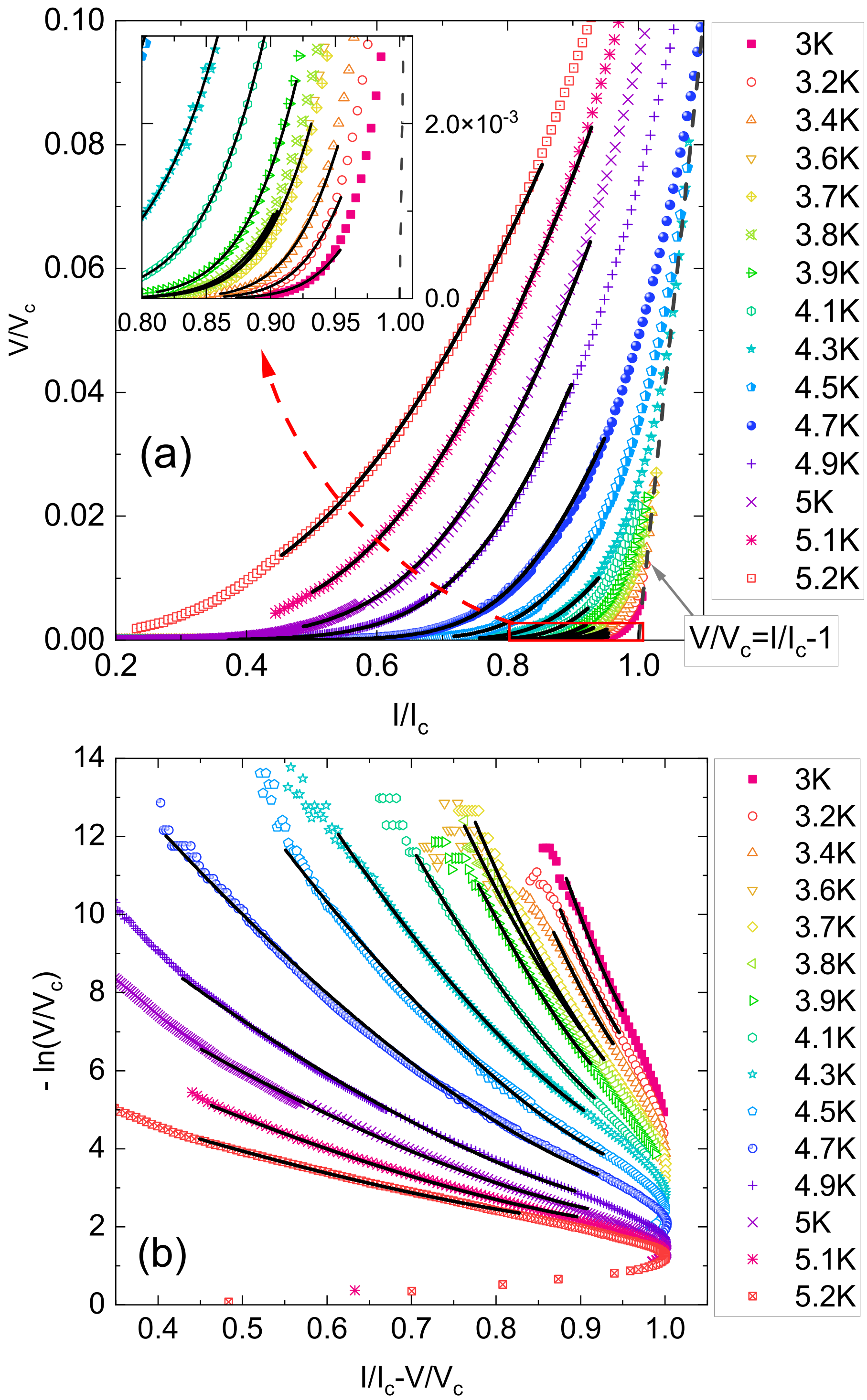

FIGURE 5.37: Data for 8.5 nm-film measured at $B = 1$ T at various temperatures, plotted as V/V_c versus I/I_c (a) and as $-ln(V/V_c)$ versus $I/I_c - V/V_c$ (b). Lines in (a) and (b) show Eqs. 5.18 and 5.19, respectively, fitted to the data, [236].

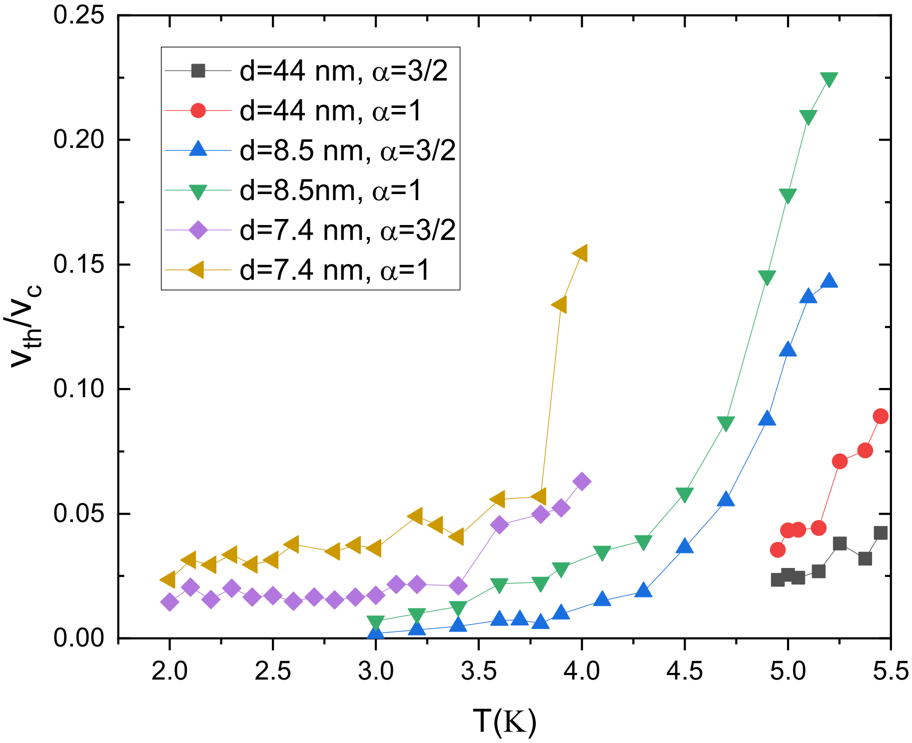

FIGURE 5.38: v_{th}/v_c versus t for different exponents α, calculated using Eq. 5.18 for different Nb films (B =1 T).

gives the proper values for v_{th}/v_c.

Figs. 5.40(a-c) and 5.40(a1-c1) show thermal creep parameters, U_c and v_{th}/v_c, respectively, extracted from the fits for different magnetic fields and plotted versus $t = T/T_c$ for films with different d. The values of v_{th}/v_c are rather small, but they increase with the approach to the T_c, in agreement with theoretical predictions [71].

The most interesting are the results for activation barriers U_c, which in the T-range studied here appear to follow functional behavior given by the relation

$$U_c = U_{c0}(1 - t^2)^n, \tag{5.20}$$

which resembles t-dependence of J_c given by Eq. 5.17, but with different characteristic exponents n. If we start from the results for the film with $d = 44$ nm [Fig.5.40(a)] we find that $U_c(t)$ for both magnetic fields may be described by the same exponent $n = 1.7$. This exponent is smaller than $m = 2.2$ exponent in $J_c(t)$ dependence. We note here that the pinning mechanism in 44 nm-film relates to the VG behavior (VG and vortex pinning theories both use $V(I)$ characteristics) characterized by the critical exponents ν and z whose values are listed in Table 5.2 (same applies to thinner samples).

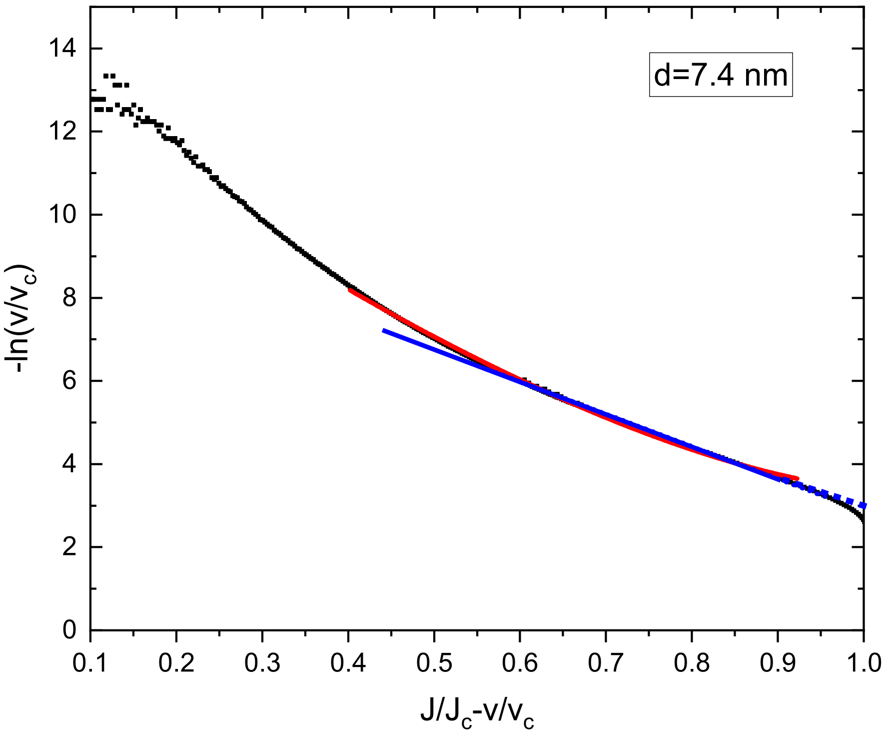

FIGURE 5.39: Analysis of activation barriers for 7.4 nm-Nb film, with data for $B = 1.0$T, T =3.8 K represented by black dots. Shown are the $J - v$ data represented as $ln(v/v_c) = U/k_BT + \gamma$ versus $J/J_c - v/v_c = F_{pin}/F_c$. The activation barrier $U(F_{pin})$ is fitted to $U(F_{pin}) = U_c(1 - F_{pin}/F_c)^\alpha$ for different exponents $\alpha = 3/2$ (red) and α =1 (blue; the fit outside the range of validity $v < v_{th}/e$ is continued with dashed line).

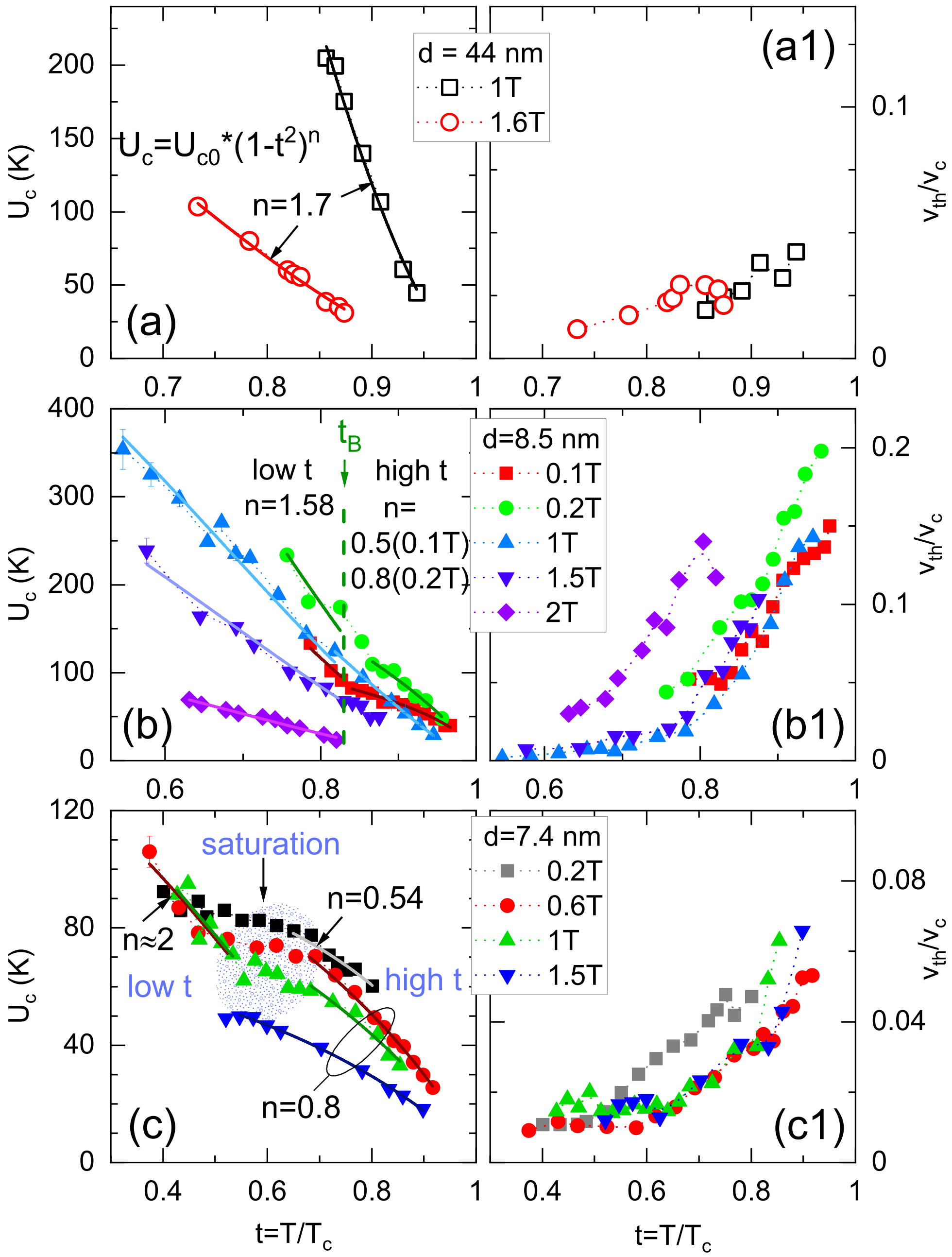

FIGURE 5.40: Creep parameters U_c (a-c) and v_{th}/v_c (a1-c1) versus $t = T/T_c$ for $d = 44$ nm (a,a1), 8.5 nm (b,b1) and 7.4 nm (c,c1) at different magnetic fields. Unless shown, errorbars are smaller than the point size. Continuous lines in (a-c) show fits of Eq. 5.20, with n value specified in the figure. Dashed green, vertical line in (b) shows the boundary at $t_B = 0.83$, shade in (c) shows saturation region, [236].

In case of film with 8.5nm-film [Fig. 5.40(b)] situation is more complex. In contrary to the $J_c(t)$ dependence, which could be fitted with a one exponent m in the entire t-range for a given magnetic field, the t dependence of the U_c varies in the vicinity of $t_B = T/T_B = 0.83$ (indicated by a green dashed line in the figure), from the one with exponent $n = 1.58$ for all magnetic fields at low t, to the one with field-dependent and much smaller $n < 1$ at hight t. Finally, in [Fig.5.40(c)], for the thinnest film with $d = 7.4$ nm the $U_c(t)$ dependence reveals three distinguished regions: high t region, in which data may be fitted with Eq. 5.20, with $n = 0.54$ for the lowest magnetic field, and $n = 0.8$ for all higher fields; the intermediate t region, roughly for $0.5 \lesssim t \lesssim 0.7$, in which saturation of the U_c is observed (marked in the figure by shadowed area), and low t region, in which the U_c again increases with decreasing t, and n is about 2 (too small amount of data points prevents more exact fitting in this range). This behavior of the U_c, which is more complicated in two thinner samples, differs a lot from much simpler form of the J_c. This is unsurprising, because the extraction of the U_c is performed in a wide range of creep, so that it provides much more information than the single value of the critical current density J_c.

In Fig. 5.41(a) we show coefficient U_{c0} (U_c at $t = 0$), extracted from the fits, as a function of reduced magnetic field. In case of two thinner films two distinguishable sets of U_{c0} are obtained, one in high-t, and one in low-t range (in case of thinnest film low-t data could be fitted for intermediate fields only). In case of $d = 8.5$ nm film these U_{c0} data sets differ by a factor of 4 at low magnetic field, but approach each other on increasing field. This in turn suggests that at low magnetic field the mechanism of pinning is different in the low-t and in the high-t range, while at high magnetic fields the mechanism remains the same .

In order to gain thorough understanding of the behavior which we observe for the $U_c(t)$, in Fig. 5.41(c) we made a plot of U_c/U_{c0} versus t for different films and magnetic fields. The continuous lines show the function $(1 - t^2)^n$ with various values of n, ranging from 0.5 (red line), through 0.8 (green) and 1.58 (purple), up to 1.7 (blue line). The data for film with $d = 44$ nm, shown by open points, align with blue line. All data for $d = 8.5$ nm, measured in various B and fitted at low t with a single function with $n = 1.58$ (solid color points) align with purple line in the low-t region, up to the boundary at $t_B = 0.83$ (shown by dashed line). At $t > 0.83$ the data start to progressively deviate from this common line, with deviation growing with decreasing magnetic field. On the other hand, we can re-plot these high-t data using U_{c0} calculated from fits in high-t region. This is shown by half-filled symbols for data measured at two lowest magnetic fields, 0.1 T (red diamonds), and 0.2 T (green triangles); these data nicely fit lines with $n = 0.5$ (red) and $n = 0.8$ (green), respectively. Finally, we add to the graph the data for film with $d = 7.4$ nm (solid black-grey points), which were fitted in the high-t range: the data measured at lowest magnetic field (0.2 T) fell close to the red line, in agreement with the value of $n = 0.54$ determined by the fits, while data measured at higher fields ($n = 0.8$) align with green line. As t decreases and approaches region of saturation of the U_c at $t \lesssim 0.7$, the data deviate downwards from red and green lines (to avoid confusion the data at still lower t, with fitted $n \sim 2$, are not shown).

Following our previous discussion on the behavior of the $J_c(t)$ we hereby propose to interpret these findings as the evidence of two distinct pinning mechanisms, δl in case of large n ($n > 1$), and δT_c when n is small $n \approx 0.5$. In accord with such

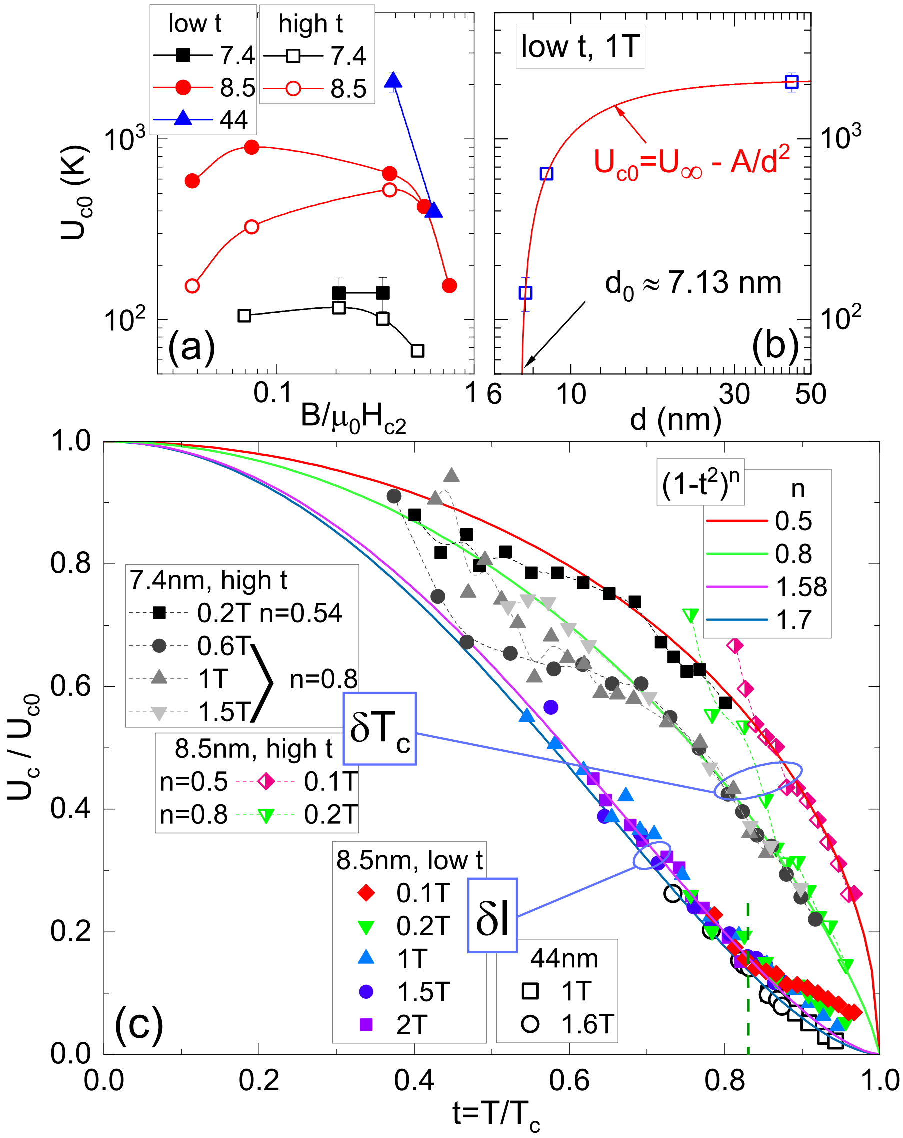

FIGURE 5.41: (a) U_{c0} versus $B/\mu_0 H_{c2}$ in low t (solid points) and high t (open points) range, for films with d equal to 7.4 nm (black squares), 8.5 nm (red circles), and 44 nm (blue triangles) (unless shown, the errors are smaller than the point size). (b) U_{c0} versus d extracted from low-t data measured at 1T; continuous line shows fit to the expression shown in the figure. (c) U_c/U_{c0} versus t for d= 44 nm (open points), 8.5 nm (low-t region: solid color points, high-t region: half-filled points), and 7.4 nm (grey-black solid points) for various magnetic fields. Continuous lines show function $(1-t^2)^n$, with $n = 0.5$ (red), 0.8 (green), 1.58 (purple), and 1.7 (blue), [236].

proposal, the results for thickest film signals observation of δl pinning. However, in thinner films the pinning of δT_c-type is present in high-t range, near the T_c, as evidenced by red line in Fig. 5.41. Little transformation of the exponent n from 0.5 into 0.8 upon increasing magnetic field in the high-t range suggests that while δT_c pinning remains the primary mechanism in the vicinity of the T_c, some admixture of δl pinning may occur. This is further supported by a gradual coalescence of two different U_{c0} values at high magnetic field in case of 8.5 nm-film, as shown in Fig. 5.41(a).

Qualitatively, such interpretation would be in agreement with the precedent theoretical descriptions of pinning mechanisms, which predict that the U_c/U_{c0} increases rapidly with T decreasing below the T_c in case of δT_c pinning, and increases much slower in case of δl pinning [67]. Our observation of smaller n exponents for U_c than m exponents for the J_c may also be in line with the expectation that in case of single vortex pinning the relation exists between the activation barrier and critical current density, $U_c(T,B) \sim J_c^{1/2}(T,B)$ [67]. However, the functional dependencies which we found, given by Eqs. 5.17 and 5.20, are different from detail predictions of Ref.[67]. This is unsurprising since these predictions postulated weak collective pinning scenario, which is not truely the present case. Nevertheless, more recent theoretical evaluation of several pinning models based on strong pinning theories finds qualitatively similar faster growth of δT_c pinning than the δl pinning with the t decreasing below 1 [68], although the detail functional behavior observed in our experiment is different from predicted by this theory.

It is intriguing to evaluate the U_{c0} dependence on d in the range of low-t, in which, in accord with our proposition, single pinning mechanism δl exists. In Fig. 5.41(b) we plot U_{c0} for data measured for all films in presence of field $B = 1$ T. The data indicate that rapid suppression of the U_{c0} occur with decreasing d. We find that it is consistent with the dependence $U_{c0} = U_\infty - A/d^2$, where U_∞ is the value of U_{c0} at large film thickness and A is a constant. This dependence predicts that $U_{c0} = 0$ at $d_0 \approx 7.13$ nm. While we have two few data points to verify the precise values of all constants (including exponent in d^2), it is obvious that the U_{c0} may drop to very small values at finite film thickness, so that the δl pinning may disappear at d just below the thickness of our thinnest film.

Our observations are summarized in the form of phase diagrams, which we propose for two thinner films in Fig. 5.42 (note that the horizontal scale in these graphs is T/T_c $(B = 0)$). The figure underscores dramatically distinctive nature of pinning in two thinner films. For 8.5 nm-film [Fig. 5.42(a)] the boundary between low-t and high-t regions, roughly at constant t_B, translates into dashed, green line marked as T_B, which approaches T_g-line on increasing magnetic field. The area in which δT_c dominates (shown in orange color) is very narrow, and it is confined mainly to low magnetic fields and high T; at fields larger than 1 T it cannot be identified any more, indicating that δl mechanism (shown by green color) becomes dominating. This feature suggests that the density of defects which cause δT_c pinning is rather limited in this film, so that at magnetic fields $B \gtrsim 1$ T the density of vortices outweighs the density of δT_c pins, and δT_c mechanism stops to play a leading role. On the other hand, in case of $d = 7.4$ nm film [Fig. 5.42(b)] the δT_c pinning persists up to the highest magnetic field measured, what suggests that the density of δT_c pins has increased significantly. In addition, on decreasing temperature, instead of δl pinning, we observe saturation region, delineated in the figure by two dashed lines, T_1 at high

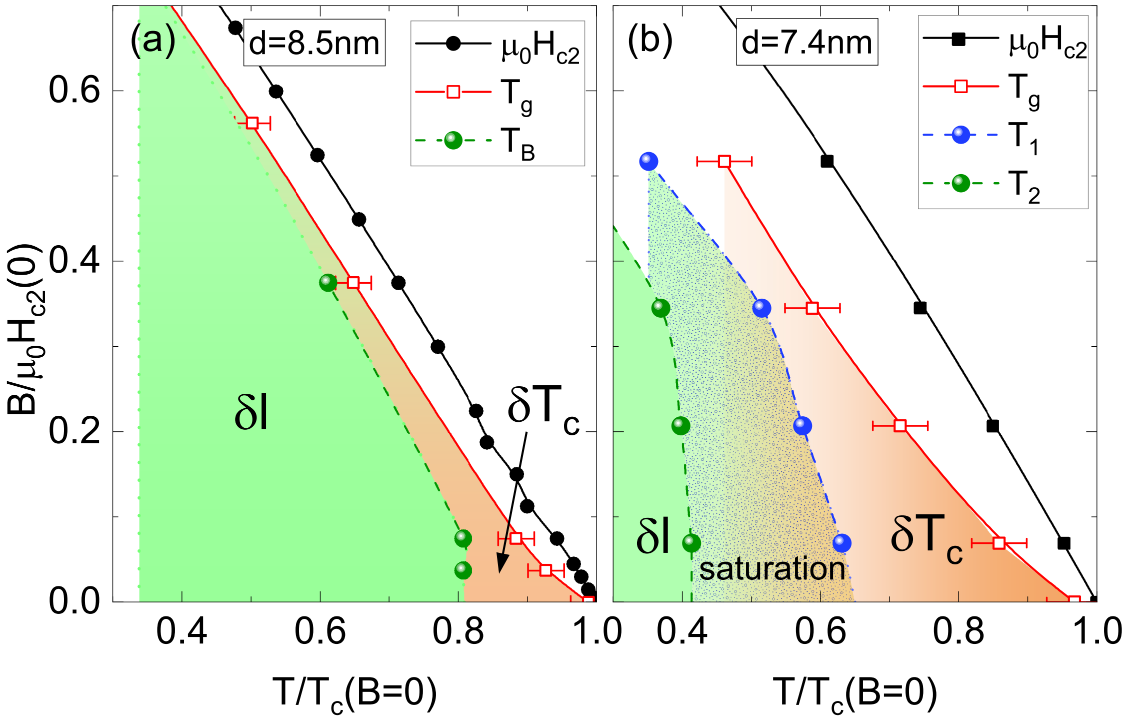

FIGURE 5.42: Phase diagrams for 8.5 nm-film (a) and 7.4 nm-film (b), with $\mu_0 H_{c2}$ (full black points) and T_g (open red points). In (a) dashed green line marks boundary at T_B, in (b) T_1 and T_2 mark the boundaries of the saturation region, [236].

T, and T_2 at low T. Finally, at $T < T_2$ the δl pinning most likely takes over, based on n value close to 2.

We now turn to discussing the possible origins of two different pinning mechanisms, and the saturation region in thinnest film. Point defects, e.g., those generated by small interdiffusion of Si atoms into Nb layer, may be eliminated from considerations, as such defects, of the atomic size, does not lead to strong pinning effects. Instead, more extended defects, of the size of about coherence length (11 nm in the present case) should be considered. In polycrystalline thin films, which grow by island growth, the most common defect structure contributing to strong pinning originates from the grain boundaries. The polycrystalline grains, of the size 3-5 nm, have been observed formerly by means of transmission electron microscope in the films deposited by magnetron sputtering, similar to the films we study; indeed, scattering from grain boundary produces specific dependence of the normal-state resistance on the film thickness, $R_N \sim d^{-2}$ [49].

During the process of film deposition the formation of islands is initiated first, followed by the islands coalescence into smooth film. This however leaves slight depression in between the grains, resulting in small surface modulation. Experiments on imaging of Nb films with thickness of about 30-80 nm indicate that such modulation, of the lateral size comparable to the coherence length, and of the height not exceeding 10 % of film thickness, forms efficient pinning sites in films [249]. Therefore, we believe that the δl pinning, which we observe in the thickest film ($d = 44$ nm), results from spatial variation of the mean free path induced by such thickness modulation. However, as the thickness of the films decreases the coalescence of the grains in the film turns less perfect. This leads to a formations of narrow amorphous regions at some grain boundaries. The density and size of such amorphous regions, distributed stochastically across the film, will increase on the decrease of film thickness. Such regions are potentially the main source of the depressed T_c, so they will result in δT_c pinning mechanism.

Note that we propose to link the origin of both pinning mechanisms to the same structural imperfections in the films, i.e. grain boundaries, however, with the decrease of film thickness some of these imperfections, of random distribution, evolve into amorphous inclusions. This interpretation suggests that the region in the phase diagram, in which δl pinning is the sole mechanism responsible for pinning of vortices, should be rapidly suppressed on decreasing film thickness, so that at some film thickness d_0 the δl pinning will be completely replaced by a mixture of δl and δT_c mechanisms. This picture is consistent with the d-dependence of U_{c0} estimated from low-t region and displayed in Fig. 5.41(b).

Finally, we should address the origins of the saturation region in the phase diagram of the thinnest film. Since the saturation happens close to the boundary between δT_c and δl regions, it is natural to suspect that the competition between two different mechanisms of pinning is responsible for this effect. In the vicinity of the boundary the activation barriers produced by these two types of pins become very close. This likely leads to frustration in the pinning landscape, what facilitates easier creep of vortices, and is reflected in saturation of the U_c. The effect is strong in case of thinnest film, because the density of amorphous regions at grain boundaries is large in this film. On the other hand, in thicker film with $d = 8.5$ nm much smaller density of amorphous grain boundaries produces very narrow saturation region, which is not observed in experiment.

Chapter 6

Conclusions and future directions

The subject of this thesis is the study of the evolution of the superconductivity of ultrathin films of niobium (Nb) as the film thickness, d, is reduced from 44 nm down to 3.6 nm. Such thickness reduction is known from previous studies [49] to induce structural transformation from polycrystalline structure at $d \geq 5$ nm to amorphous structure at $d \leq 3$ nm, what introduces inhomogeneity to the superconducting state in the films. Two aspects of superconducting properties have been evaluated here, the Berezinskii-Kosterlitz-Thouless (BKT) phase transition in zero magnetic field and the vortex dynamics in the presence of magnetic field. The experimental methods used here are the measurements of the resistance $R(T)$, and I-V characteristics (IVC) of the films.

$R(T)$ and IVCs in zero magnetic field, together, unveil the evolution of phase fluctuations induced by reduced dimensionality and enhanced structural disorder. We have used several distinct superconducting fluctuations-statistical models (Aslamazov-Larkin, Halperin-Nelson, effective medium theory) to analyze the $R(T)$ data and to extract two temperatures characterizing transition to superconducting state: mean field (T_{MF}) and BKT (T_{BKT}) transition temperatures. The analysis of these approaches, together with IVC's analysis indicates that, as d decreases, the superconducting transition is influenced by the vortex core energy μ (modified with disorder) and inhomogeneity present in the films. This leads to gradual smearing of the T-dependent superfluid stiffness, $J_s(T)$. Two interesting deviations from typical behavior of superconducting transition are observed. First, in 8.5 nm film at large current the transition to normal state proceeds via intermediate resistive states; we believe this effect is due to phase slip phenomenon, expected in case of wide samples at large current drives. Secondly, as d is reduced below 5 nm, the IVC typical for continuous superconducting state, with one critical current, transforms into unusual IVC with three distinct, consecutive critical currents, and superconducting diode effect. We attribute this transformation to breaking of continuous superconducting state into separate superconducting islands immersed in the metallic matrix. The analysis of the T-dependence and statistics of these critical currents indicates close correspondence with Josephson junction arrays (JJA), but with many distinct variable junction lengths; the three critical currents may be identified (starting from the high-current side) as a transition to normal state in the islands, a peak related to multiple Andreev reflection, and the transition to global superconducting state. The diode effect is likely related to the charging effect in JJA, but full understanding of it has to be postponed to future studies.

A separate part of the study focuses on vortex dynamics in films with d between 7.4 nm and 44 nm; the data are obtained in perpendicular magnetic field. Standard methods, including scaling laws, are applied to identify the vortex glass (VG) transition temperature. While quasi-2D VG transition is confirmed in case of the thickest film, with scaling exponents firmly within theoretically expected and previously reported values, the presence of creep in thinner films complicates this identification, resulting in large uncertainty in the putative VG transition temperature and scaling exponents. The creep regime is subsequently analyzed using recent strong pinning theory [71]. The T-dependence of the activation energy for vortex pinning U_c, extracted from this analysis, reveals two quite distinct regimes of pinning, which we propose to identify with δl and δT_c-type of pinning. The first of these regimes, δl, with slow increase of the U_c/U_{c0} below $T/T_c = 1$, is observed in thickest film. As the film thickness decreases, the second regime (δT_c) appears, characterized by faster growth of the U_c/U_{c0} below $T/T_c = 1$. We link these two different regimes with the grain boundaries existing in the films, which in thicker film produce carrier scattering, while in thinner films gradually evolve into amorphous inclusions, leading to local depression of the T_c. Experimentally obtained T-dependence of the U_c does not strictly follow existing theoretical predictions, what calls for more theoretical studies of the subject.

Bibliography

[1] M. R. Beasley, J. E. Mooij, and T. P. Orlando. "Possibility of Vortex-Antivortex Pair Dissociation in Two-Dimensional Superconductors". In: *Phys. Rev. Lett.* 42 (17 1979), pp. 1165–1168. DOI: 10.1103/PhysRevLett.42.1165. URL: https://link.aps.org/doi/10.1103/PhysRevLett.42.1165.

[2] V. J. Emery and S. A. Kivelson. "Importance of phase fluctuations in superconductors with small superfluid density". In: *Nature* 374.6521 (1995), pp. 434–437. ISSN: 00280836. DOI: 10.1038/374434a0.

[3] C Panagopoulos et al. "Superfluid response in monolayer high-T c cuprates". In: *Physical Review B* 67.22 (2003), p. 220502.

[4] B Nachumi et al. "Muon spin relaxation studies of Zn-substitution effects in high-T_c cuprate superconductors". In: *Physical review letters* 77.27 (1996), p. 5421.

[5] Pratap Raychaudhuri and Surajit Dutta. "Phase fluctuations in conventional superconductors". In: *Journal of Physics: Condensed Matter* 34.8 (2021), p. 083001.

[6] J. Bardeen, L. N. Cooper, and J. R. Schrieffer. "Theory of Superconductivity". In: *Phys. Rev.* 108 (5 1957), pp. 1175–1204. DOI: 10.1103/PhysRev.108.1175. URL: https://link.aps.org/doi/10.1103/PhysRev.108.1175.

[7] J. Bardeen, L. N. Cooper, and J. R. Schrieffer. "Microscopic Theory of Superconductivity". In: *Phys. Rev.* 106 (1 1957), pp. 162–164. DOI: 10.1103/PhysRev.106.162. URL: https://link.aps.org/doi/10.1103/PhysRev.106.162.

[8] M Cyrot. "Ginzburg–Landau theory for superconductors." In: *Rep. Progr. Phys. 36: No. 2, 103-158(1973).* (Jan. 1973). DOI: 10.1088/0034-4885/36/2/001. URL: https://www.osti.gov/biblio/4578140.

[9] Amit Ghosal, Mohit Randeria, and Nandini Trivedi. "Inhomogeneous pairing in highly disordered s-wave superconductors". In: *Phys. Rev. B* 65 (1 2001), p. 014501. DOI: 10.1103/PhysRevB.65.014501. URL: https://link.aps.org/doi/10.1103/PhysRevB.65.014501.

[10] Yonatan Dubi and Massimiliano Di Ventra. "Thermospin effects in a quantum dot connected to ferromagnetic leads". In: *Phys. Rev. B* 79 (8 2009), p. 081302. DOI: 10.1103/PhysRevB.79.081302. URL: https://link.aps.org/doi/10.1103/PhysRevB.79.081302.

[11] B. Keimer et al. "From quantum matter to high-temperature superconductivity in copper oxides". In: *Nature* 518.7538 (2015), pp. 179–186. ISSN: 14764687. DOI: 10.1038/nature14165. URL: http://dx.doi.org/10.1038/nature14165.

[12] V. J. Emery and S. A. Kivelson. "Superconductivity in Bad Metals". In: *Phys. Rev. Lett.* 74 (16 1995), pp. 3253–3256. DOI: 10.1103/PhysRevLett.74.3253. URL: https://link.aps.org/doi/10.1103/PhysRevLett.74.3253.

[13] Benjamin Sacépé, Mikhail Feigel'man, and Teunis M. Klapwijk. "Quantum breakdown of superconductivity in low-dimensional materials". In: *Nature Physics* 16.7 (2020), pp. 734–746. ISSN: 17452481. DOI: 10.1038/s41567-020-0905-x. arXiv: 2007.15870. URL: http://dx.doi.org/10.1038/s41567-020-0905-x.

[14] Mintu Mondal et al. "Phase Fluctuations in a Strongly Disordered *s*-Wave NbN Superconductor Close to the Metal-Insulator Transition". In: *Phys. Rev. Lett.* 106 (4 2011), p. 047001. DOI: 10.1103/PhysRevLett.106.047001. URL: https://link.aps.org/doi/10.1103/PhysRevLett.106.047001.

[15] Madhavi Chand et al. "Phase diagram of the strongly disordered *s*-wave superconductor NbN close to the metal-insulator transition". In: *Phys. Rev. B* 85 (1 2012), p. 014508. DOI: 10.1103/PhysRevB.85.014508. URL: https://link.aps.org/doi/10.1103/PhysRevB.85.014508.

[16] Mintu Mondal et al. "Enhancement of the finite-frequency superfluid response in the pseudogap regime of strongly disordered superconducting films". In: *Scientific Reports* 3.1 (Feb. 2013). ISSN: 2045-2322. DOI: 10.1038/srep01357. URL: http://dx.doi.org/10.1038/srep01357.

[17] Mintu Mondal et al. "Role of the Vortex-Core Energy on the Berezinskii-Kosterlitz-Thouless Transition in Thin Films of NbN". In: *Phys. Rev. Lett.* 107 (21 2011), p. 217003. DOI: 10.1103/PhysRevLett.107.217003. URL: https://link.aps.org/doi/10.1103/PhysRevLett.107.217003.

[18] G. Lemarié et al. "Universal scaling of the order-parameter distribution in strongly disordered superconductors". In: *Phys. Rev. B* 87 (18 2013), p. 184509. DOI: 10.1103/PhysRevB.87.184509. URL: https://link.aps.org/doi/10.1103/PhysRevB.87.184509.

[19] Thomas Dubouchet et al. "Collective energy gap of preformed Cooper pairs in disordered superconductors". English. In: *Nature Physics* 15.3 (Mar. 2019), pp. 233–236. ISSN: 1745-2473. DOI: 10.1038/s41567-018-0365-8.

[20] A. Kremen et al. "Imaging quantum fluctuations near criticality". In: *Nature Physics* 14.12 (Dec. 2018). Publisher Copyright: © 2018, The Author(s)., pp. 1205–1210. ISSN: 1745-2473. DOI: 10.1038/s41567-018-0264-z.

[21] Wei Liu et al. "Dynamical study of phase fluctuations and their critical slowing down in amorphous superconducting films". In: *Phys. Rev. B* 84 (2 2011), p. 024511. DOI: 10.1103/PhysRevB.84.024511. URL: https://link.aps.org/doi/10.1103/PhysRevB.84.024511.

[22] Bing Cheng et al. "Anomalous gap-edge dissipation in disordered superconductors on the brink of localization". In: *Phys. Rev. B* 93 (18 2016), p. 180511. DOI: 10.1103/PhysRevB.93.180511. URL: https://link.aps.org/doi/10.1103/PhysRevB.93.180511.

[23] J M Kosterlitz and D J Thouless. "Ordering, metastability and phase transitions in two-dimensional systems". In: *Journal of Physics C: Solid State Physics* 6.7 (1973), p. 1181. DOI: 10.1088/0022-3719/6/7/010. URL: https://dx.doi.org/10.1088/0022-3719/6/7/010.

[24] Petter Minnhagen. "The two-dimensional Coulomb gas, vortex unbinding, and superfluid-superconducting films". In: *Rev. Mod. Phys.* 59 (4 1987), pp. 1001–1066. DOI: 10.1103/RevModPhys.59.1001. URL: https://link.aps.org/doi/10.1103/RevModPhys.59.1001.

[25] David R. Nelson and J. M. Kosterlitz. "Universal Jump in the Superfluid Density of Two-Dimensional Superfluids". In: *Phys. Rev. Lett.* 39 (19 1977), pp. 1201–1205. DOI: 10.1103/PhysRevLett.39.1201. URL: https://link.aps.org/doi/10.1103/PhysRevLett.39.1201.

[26] DJ Bishop and JD Reppy. "Study of the superfluid transition in two-dimensional He 4 films". In: *Physical Review B* 22.11 (1980), p. 5171.

[27] Ilaria Maccari, Lara Benfatto, and Claudio Castellani. "The BKT universality class in the presence of correlated disorder". In: *Condensed Matter* 3.1 (2018), pp. 1–10. ISSN: 24103896. DOI: 10.3390/condmat3010008. arXiv: 1802.03315.

[28] Jie Yong et al. "Robustness of the Berezinskii-Kosterlitz-Thouless transition in ultrathin NbN films near the superconductor-insulator transition". In: *Phys. Rev. B* 87 (18 2013), p. 184505. DOI: 10.1103/PhysRevB.87.184505. URL: https://link.aps.org/doi/10.1103/PhysRevB.87.184505.

[29] Lara Benfatto, Claudio Castellani, and Thierry Giamarchi. "Berezinskii–Kosterlitz–Thouless Transition within the Sine-Gordon Approach: The Role of the Vortex-Core Energy". In: *40 Years of Berezinskii–Kosterlitz–Thouless Theory*. WORLD SCIENTIFIC, July 2013, 161–199. ISBN: 9789814417648. DOI: 10.1142/9789814417648_0005. URL: http://dx.doi.org/10.1142/9789814417648_0005.

[30] L. Benfatto, C. Castellani, and T. Giamarchi. "Kosterlitz-Thouless Behavior in Layered Superconductors: The Role of the Vortex Core Energy". In: *Phys. Rev. Lett.* 98 (11 2007), p. 117008. DOI: 10.1103/PhysRevLett.98.117008. URL: https://link.aps.org/doi/10.1103/PhysRevLett.98.117008.

[31] L. Benfatto, C. Castellani, and T. Giamarchi. "Doping dependence of the vortex-core energy in bilayer films of cuprates". In: *Phys. Rev. B* 77 (10 2008), p. 100506. DOI: 10.1103/PhysRevB.77.100506. URL: https://link.aps.org/doi/10.1103/PhysRevB.77.100506.

[32] S. Raghu et al. "Vortex-dynamics approach to the Nernst effect in extreme type-II superconductors dominated by phase fluctuations". In: *Phys. Rev. B* 78 (18 2008), p. 184520. DOI: 10.1103/PhysRevB.78.184520. URL: https://link.aps.org/doi/10.1103/PhysRevB.78.184520.

[33] L. Benfatto, C. Castellani, and T. Giamarchi. "Broadening of the Berezinskii-Kosterlitz-Thouless superconducting transition by inhomogeneity and finite-size effects". In: *Phys. Rev. B* 80 (21 2009), p. 214506. DOI: 10.1103/PhysRevB.80.214506. URL: https://link.aps.org/doi/10.1103/PhysRevB.80.214506.

[34] Adrian Gozar et al. "High-temperature interface superconductivity between metallic and insulating copper oxides". In: *Nature* 455 (2008), pp. 782–785. URL: https://api.semanticscholar.org/CorpusID:4419436.

[35] Andrea D. Caviglia et al. "Electric field control of the $LaAlO_3/SrTiO_3$ interface ground state". In: *Nature* 456 (2008), pp. 624–627. URL: https://api.semanticscholar.org/CorpusID:4425367.

[36] G. Venditti et al. "Nonlinear $I-V$ characteristics of two-dimensional superconductors: Berezinskii-Kosterlitz-Thouless physics versus inhomogeneity". In: *Phys. Rev. B* 100 (6 2019), p. 064506. DOI: 10.1103/PhysRevB.100.064506. URL: https://link.aps.org/doi/10.1103/PhysRevB.100.064506.

[37] K. Das Gupta et al. "Critical currents and vortex-unbinding transitions in quench-condensed ultrathin films of bismuth and tin". In: *Phys. Rev. B* 66 (14 2002), p. 144512. DOI: 10.1103/PhysRevB.66.144512. URL: https://link.aps.org/doi/10.1103/PhysRevB.66.144512.

[38] Serena Eley et al. "Approaching zero-temperature metallic states in mesoscopic superconductor–normal–superconductor arrays". In: *Nature Physics* 8 (2011), pp. 59 –62. URL: https://api.semanticscholar.org/CorpusID:30410791.

[39] Bikash Gajar et al. "Substrate mediated nitridation of niobium into superconducting Nb2N thin films for phase slip study". In: *Scientific Reports* 9 (2019). URL: https://api.semanticscholar.org/CorpusID:195064434.

[40] H. S. J. van der Zant et al. "Vortex dynamics in two-dimensional underdamped, classical Josephson-junction arrays". In: *Phys. Rev. B* 47 (1 1993), pp. 295–304. DOI: 10.1103/PhysRevB.47.295. URL: https://link.aps.org/doi/10.1103/PhysRevB.47.295.

[41] P. Delsing et al. "Charge solitons and quantum fluctuations in two-dimensional arrays of small Josephson junctions". In: *Phys. Rev. B* 50 (6 1994), pp. 3959–3971. DOI: 10.1103/PhysRevB.50.3959. URL: https://link.aps.org/doi/10.1103/PhysRevB.50.3959.

[42] Serena Eley et al. "Dependence of global superconductivity on inter-island coupling in arrays of long SNS junctions". English (US). In: *Journal of Physics Condensed Matter* 25.44 (Nov. 2013). ISSN: 0953-8984. DOI: 10.1088/0953-8984/25/44/445701.

[43] S. Hurand et al. "Josephson-like dynamics of the superconducting $LaAlO_3/SrTiO_3$ interface". In: *Phys. Rev. B* 99 (10 2019), p. 104515. DOI: 10.1103/PhysRevB.99.104515. URL: https://link.aps.org/doi/10.1103/PhysRevB.99.104515.

[44] James A Blackburn, Matteo Cirillo, and Niels Grønbech-Jensen. "A survey of classical and quantum interpretations of experiments on Josephson junctions at very low temperatures". In: *Physics Reports* 611 (2016), pp. 1–33.

[45] Daniel S. Fisher, Matthew P. A. Fisher, and David A. Huse. "Thermal fluctuations, quenched disorder, phase transitions, and transport in type-II superconductors". In: *Phys. Rev. B* 43 (1 1991), pp. 130–159. DOI: 10.1103/PhysRevB.43.130. URL: https://link.aps.org/doi/10.1103/PhysRevB.43.130.

[46] Serena Eley, Andreas Glatz, and Roland Willa. "Challenges and transformative opportunities in superconductor vortex physics". In: *Journal of Applied Physics* 130.5 (Aug. 2021), p. 050901. ISSN: 0021-8979. DOI: 10.1063/5.0055611. eprint: https://pubs.aip.org/aip/jap/article-pdf/doi/10.1063/5.0055611/20023261/050901_1_5.0055611.pdf. URL: https://doi.org/10.1063/5.0055611.

[47] Aharon Kapitulnik, Steven A. Kivelson, and Boris Spivak. "Colloquium: Anomalous metals: Failed superconductors". In: *Rev. Mod. Phys.* 91 (1 2019), p. 011002. DOI: 10.1103/RevModPhys.91.011002. URL: https://link.aps.org/doi/10.1103/RevModPhys.91.011002.

[48] C. Carbillet et al. “Spectroscopic evidence for strong correlations between local superconducting gap and local Altshuler-Aronov density of states suppression in ultrathin NbN films”. In: *Phys. Rev. B* 102 (2 2020), p. 024504. DOI: 10.1103/PhysRevB.102.024504. URL: https://link.aps.org/doi/10.1103/PhysRevB.102.024504.

[49] Iryna Zaytseva et al. “Upper critical field and superconductor-metal transition in ultrathin niobium films”. In: *Scientific Reports* 10.1 (2020), p. 19062.

[50] Alexander Weitzel et al. “Sharpness of the Berezinskii-Kosterlitz-Thouless transition in disordered NbN films”. In: *Physical Review Letters* 131.18 (2023), p. 186002.

[51] Serena Eley et al. “Accelerated vortex dynamics across the magnetic 3D-to-2D crossover in disordered superconductors”. In: *npj Quantum Materials* 3 (2018). URL: https://api.semanticscholar.org/CorpusID:256707280.

[52] J. E. Villegas and J. L. Vicent. “Vortex-glass transitions in low-T_c superconducting Nb thin films and NbCu superlattices”. In: *Phys. Rev. B* 71 (14 2005), p. 144522. DOI: 10.1103/PhysRevB.71.144522. URL: https://link.aps.org/doi/10.1103/PhysRevB.71.144522.

[53] Yi Sun et al. “Voltage-current properties of superconducting amorphous tungsten nanostrips”. In: *Scientific reports* 3.1 (2013), p. 2307.

[54] Chao Zhang et al. “Quasi-two-dimensional vortex–glass transition and the critical current density in TiO epitaxial thin films”. In: *Superconductor Science and Technology* 31.1 (2017), p. 015016.

[55] Zhi-Yong Song et al. “InN superconducting phase transition”. In: *Scientific reports* 9.1 (2019), p. 12309.

[56] Indranil Roy et al. “Melting of the vortex lattice through intermediate hexatic fluid in an a-MoGe thin film”. In: *Physical review letters* 122.4 (2019), p. 047001.

[57] G. Blatter et al. “Vortices in high-temperature superconductors”. In: *Rev. Mod. Phys.* 66 (4 1994), pp. 1125–1388. DOI: 10.1103/RevModPhys.66.1125. URL: https://link.aps.org/doi/10.1103/RevModPhys.66.1125.

[58] Yu N Ovchinnikov and BI Ivlev. “Pinning in layered inhomogeneous superconductors”. In: *Physical Review B* 43.10 (1991), p. 8024.

[59] CJ Van der Beek et al. “Strong pinning in high-temperature superconducting films”. In: *Physical Review B* 66.2 (2002), p. 024523.

[60] AU Thomann, VB Geshkenbein, and G Blatter. “Dynamical aspects of strong pinning of magnetic vortices in type-II superconductors”. In: *Physical review letters* 108.21 (2012), p. 217001.

[61] Alexander Urs Thomann, Vadim B Geshkenbein, and Gianni Blatter. “Vortex dynamics in type-II superconductors under strong pinning conditions”. In: *Physical Review B* 96.14 (2017), p. 144516.

[62] AR Strnad, CF Hempstead, and YB Kim. “Dissipative mechanism in type-II superconductors”. In: *Physical Review Letters* 13.26 (1964), p. 794.

[63] YB Kim, CF Hempstead, and AR Strnad. “Flux-flow resistance in type-II superconductors”. In: *Physical Review* 139.4A (1965), A1163.

[64] P Berghuis and PH Kes. “Two-dimensional collective pinning and vortex-lattice melting in a-Nb 1- x Ge x films”. In: *Physical Review B* 47.1 (1993), p. 262.

[65] ZL Xiao et al. "Edge and bulk transport in the mixed state of a type-II superconductor". In: *Physical Review B* 65.9 (2002), p. 094511.

[66] Sandro Pace et al. "Irreversible dynamics of Abrikosov vortices in type-two superconductors". In: *Physics Letters A* 329.4-5 (2004), pp. 379–384.

[67] R Griessen et al. "Evidence for mean free path fluctuation induced pinning in $YBa_2Cu_3O_7$ and $YBa_2Cu_4O_8$ films". In: *Physical review letters* 72.12 (1994), p. 1910.

[68] Roland Willa, Vadim B Geshkenbein, and Gianni Blatter. "Probing the pinning landscape in type-II superconductors via Campbell penetration depth". In: *Physical review B* 93.6 (2016), p. 064515.

[69] Martin Buchacek et al. "Persistence of pinning and creep beyond critical drive within the strong pinning paradigm". In: *Physical Review B* 98.9 (2018), p. 094510.

[70] Martin Buchacek et al. "Strong pinning theory of thermal vortex creep in type-II superconductors". In: *Physical Review B* 100.1 (2019), p. 014501.

[71] Martin Buchacek et al. "Experimental test of strong pinning and creep in current-voltage characteristics of type-II superconductors". In: *Physical Review B* 100.22 (2019), p. 224502.

[72] Lucas Backmeister et al. "Ordered Bose glass of vortices in superconducting $YBa_2Cu_3O_{7-\delta}$ thin films with a periodic pin lattice created by focused helium ion irradiation". In: *Nanomaterials* 12.19 (2022), p. 3491.

[73] RH Koch et al. "Experimental evidence for vortex-glass superconductivity in Y-Ba-Cu-O". In: *Physical review letters* 63.14 (1989), p. 1511.

[74] Zouhair Sefrioui et al. "Crossover from a three-dimensional to purely two-dimensional vortex-glass transition in deoxygenated $YBa_2Cu_3O_{7-\delta}$ thin films". In: *Physical Review B* 60.22 (1999), p. 15423.

[75] J Hänisch et al. "Vortex glass-liquid transition and activated flux motion in an epitaxial, superconducting NdFeAs (O, F) thin film". In: *MRS Communications* 8.4 (2018), pp. 1433–1438.

[76] Chao Zhang et al. "Quasi-two-dimensional vortex–glass transition and the critical current density in TiO epitaxial thin films". In: *Superconductor Science and Technology* 31.1 (2017), p. 015016.

[77] H Safar et al. "SQUID picovoltometry of single crystal $Bi_2Sr_2CaCu_2O_{8+\delta}$: Observation of the crossover from high-temperature Arrhenius to low-temperature vortex-glass behavior". In: *Physical review letters* 68.17 (1992), p. 2672.

[78] Douglas R Strachan, Matthew C Sullivan, and Christopher J Lobb. "Probing the limits of superconductivity". In: *Superconducting and Related Oxides: Physics and Nanoengineering V*. Vol. 4811. SPIE. 2002, pp. 65–77.

[79] YQ Zhang et al. "Effect of stripe order on the vortex phase transition inLa1. 44Nd0. 4Sr0. 16CuO4 films". In: *Superconductor Science and Technology* 22.8 (2009), p. 085010.

[80] DR Strachan et al. "Do superconductors have zero resistance in a magnetic field?" In: *Physical Review Letters* 87.6 (2001), p. 067007.

[81] I Zaytseva et al. "Negative Hall coefficient of ultrathin niobium in Si/Nb/Si trilayers". In: *Physical Review B* 90.6 (2014), p. 060505.

[82] *Introduction to Solid State Physics, 7th Ed*. Wiley India Pvt. Limited, 2007. ISBN: 9788126510450. URL: https://books.google.pl/books?id=F9Qu5c_hUaUC.

[83] S Dzhumanov. "Bosonization of Cooper pairs and novel Bose-liquid superconductivity and superfluidity in high-T_c cuprates and other exotic systems". In: *Physica A: Statistical Mechanics and its Applications* 517 (2019), pp. 197–209.

[84] Ekkehard Krüger. "Modified BCS mechanism of Cooper pair formation in narrow energy bands of special symmetry II. Matthias rule reconsidered". In: *Journal of superconductivity* 14 (2001), pp. 551–561.

[85] Edgar J Patiño and Daniel Lozano-Gómez. "Quantum tunneling theory of Cooper pairs as bosonic particles". In: *Scientific reports* 11.1 (2021), p. 9050.

[86] TA Mamedov and M De Llano. "Depairing and Bose–Einstein condensation temperatures in a boson–fermion superconductor model with Coulomb effects". In: *Philosophical Magazine* 93.21 (2013), pp. 2896–2912.

[87] Fritz London and Heinz London. "The electromagnetic equations of the supraconductor". In: *Proceedings of the Royal Society of London. Series A-Mathematical and Physical Sciences* 149.866 (1935), pp. 71–88.

[88] M. Tinkham. *Introduction to Superconductivity*. Dover Books on Physics Series. Dover Publications, 2004. ISBN: 9780486134727. URL: https://books.google.pl/books?id=VpUk3NfwDIkC.

[89] Alex Gurevich. "Superconducting radio-frequency fundamentals for particle accelerators". In: *Reviews of Accelerator Science and Technology* 5 (2012), pp. 119–146.

[90] J. Clarke and A.I. Braginski. *The SQUID Handbook: Fundamentals and Technology of SQUIDs and SQUID Systems*. Wiley, 2006. ISBN: 9783527604586. URL: https://books.google.pl/books?id=BsTTM-nU-JkC.

[91] Matthew Reagor et al. "Quantum memory with millisecond coherence in circuit QED". In: *Physical Review B* 94.1 (2016), p. 014506.

[92] DK Finnemore, TF Stromberg, and CA Swenson. "Superconducting properties of high-purity niobium". In: *Physical Review* 149.1 (1966), p. 231.

[93] RW Rollins and Y Anjaneyulu. "Position-dependent flux pinning by proton-irradiation damage in thick niobium samples". In: *Journal of Applied Physics* 48.3 (1977), pp. 1296–1300.

[94] Brian Rusnak et al. "In-situ proton irradiation and measurement of superconducting RF cavities under cryogenic conditions". In: *Proceedings of the 1997 Particle Accelerator Conference (Cat. No. 97CH36167)*. Vol. 3. IEEE. 1997, pp. 3096–3098.

[95] Alfred Koethe and Jens Ingolf Moench. "Preparation of ultra high purity niobium". In: *materials Transactions, JIM* 41.1 (2000), pp. 7–16.

[96] M Bahte, LN Lipatov, and F Herrmann. "Magnetization and susceptibility measurements on niobium samples for cavity production". In: *Part. Accel.* 60 (1998), pp. 121–134.

[97] V Kozhevnikov et al. "Equilibrium properties of superconducting niobium at high magnetic fields: A possible existence of a filamentary state in type-II superconductors". In: *Physical Review B* 95.17 (2017), p. 174509.

[98] Jaeyel Lee et al. "Discovery of Nb hydride precipitates in superconducting qubits". In: *arXiv preprint arXiv:2108.10385* (2021).

[99] S Ooi et al. "Observation of intermediate mixed state in high-purity cavity-grade Nb by magneto-optical imaging". In: *Physical Review B* 104.6 (2021), p. 064504.

[100] JWP Hsu and A Kapitulnik. "Superconducting transition, fluctuation, and vortex motion in a two-dimensional single-crystal Nb film". In: *Physical Review B* 45.9 (1992), p. 4819.

[101] Vladimir G Kogan and Ruslan Prozorov. "Anisotropic criteria for the type of superconductivity". In: *Physical Review B* 90.5 (2014), p. 054516.

[102] Vladimir G Kogan and Ruslan Prozorov. "Changing the type of superconductivity by magnetic and potential scattering". In: *Physical Review B* 90.18 (2014), p. 180502.

[103] Ruslan Prozorov, Mehdi Zarea, and James A Sauls. "Niobium in the clean limit: An intrinsic type-I superconductor". In: *Physical Review B* 106.18 (2022), p. L180505.

[104] Leon N. Cooper. "Bound Electron Pairs in a Degenerate Fermi Gas". In: *Phys. Rev.* 104 (4 1956), pp. 1189–1190. DOI: 10.1103/PhysRev.104.1189. URL: https://link.aps.org/doi/10.1103/PhysRev.104.1189.

[105] Herbert Fröhlich. "Theory of the superconducting state. I. The ground state at the absolute zero of temperature". In: *Physical Review* 79.5 (1950), p. 845.

[106] Emanuel Maxwell. "Isotope effect in the superconductivity of mercury". In: *Physical Review* 78.4 (1950), p. 477.

[107] CA Reynolds et al. "Superconductivity of isotopes of mercury". In: *Physical Review* 78.4 (1950), p. 487.

[108] G Gladstone, MA Jensen, and JR Schrieffer. *Superconductivity, ed. RD Parks*. 1969.

[109] D Lenk et al. "Influence of the FFLO-like State on the Upper Critical Field of a S/F Bilayer: Angular and Temperature Dependence". In: *arXiv preprint arXiv:1604.03361* (2016).

[110] Thomas R Lemberger et al. "Penetration depth study of very thin superconducting Nb films". In: *Physical Review B—Condensed Matter and Materials Physics* 76.9 (2007), p. 094515.

[111] Sung I Park and TH Geballe. "Superconducting tunneling in ultrathin Nb films". In: *Physical review letters* 57.7 (1986), p. 901.

[112] DJ Scalapino, JR Schrieffer, and JW Wilkins. "Strong-coupling superconductivity. I". In: *Physical Review* 148.1 (1966), p. 263.

[113] GM Eliashberg. "Interactions between electrons and lattice vibrations in a superconductor". In: *Sov. Phys. JETP* 11.3 (1960), pp. 696–702.

[114] KK Likharev. "Superconducting weak links". In: *Reviews of Modern Physics* 51.1 (1979), p. 101.

[115] VP Andratskii et al. "Current dependence of the microwave admittance of thin superconducting films". In: *Sov. Phys. JETP* 43.1 (1976), pp. 151–155.

[116] T Dan Bracken and WO Hamilton. "Comparison of microwave-induced constant-voltage steps in Pb and Sn Josephson junctions". In: *Physical Review B* 6.7 (1972), p. 2603.

[117] JJ Macfarlane. "Pre-rigor pressurization of muscle: Effects on pH, shear value and taste panel assessment". In: *Journal of Food Science* 38.2 (1973), pp. 294–298.

[118] Vinay Ambegaokar and Alexis Baratoff. "Tunneling Between Superconductors". In: *Physical Review Letters* 11.2 (1963), p. 104.

[119] A Verma et al. “BKT phase transition in nanoporous films of superconducting NbN”. In: *arXiv preprint arXiv:2410.22704* (2024).

[120] Vinay Ambegaokar and Alexis Baratoff. “Tunneling between superconductors”. In: *Physical review letters* 10.11 (1963), p. 486.

[121] NR Werthamer. “Nonlinear self-coupling of Josephson radiation in superconducting tunnel junctions”. In: *Physical Review* 147.1 (1966), p. 255.

[122] AI Larkin and Yu N Ovchinnikov. “Tunnel effect between superconductors in an alternating field”. In: *Sov. Phys. JETP* 24.11 (1967), pp. 1035–1040.

[123] IO Kulik. “Current flow in long superconducting junctions”. In: *Zh. Eksp. Teor. Fiz* 68 (1975), p. 2139.

[124] IO Kulik and AN Omel’Yanchuk. “Properties of superconducting microbridges in the pure limit”. In: *Soviet Journal of Low Temperature Physics* 3.7 (1977), pp. 459–461.

[125] P Dubos et al. “Josephson critical current in a long mesoscopic SNS junction”. In: *Physical Review B* 63.6 (2001), p. 064502.

[126] VM Krasnov et al. “Collapse of thermal activation in moderately damped Josephson junctions”. In: *Physical review letters* 95.15 (2005), p. 157002.

[127] VL Berezinskii et al. “Destruction of long-range order in one-dimensional and two-dimensional systems possessing a continuous symmetry group. II. Quantum systems”. In: *Zh. Eksp. Teor. Fiz* 61 (1971), p. 1144.

[128] Eric Jacob. “Topological phase transitions (BKT)”. In: ().

[129] Isadore Rudnick. “Critical Surface Density of the Superfluid Component in He 4 Films”. In: *Physical Review Letters* 40.22 (1978), p. 1454.

[130] J Pearl. *Low Temperature Physics-Lt 9, ed. by JG Daunt, DV Edwards, FJ Milford, M. Yaqub*. 1965.

[131] BI Halperin and David R Nelson. “Resistive transition in superconducting films”. In: *Journal of low temperature physics* 36 (1979), pp. 599–616.

[132] N David Mermin and Herbert Wagner. “Absence of ferromagnetism or antiferromagnetism in one-or two-dimensional isotropic Heisenberg models”. In: *Physical Review Letters* 17.22 (1966), p. 1133.

[133] Franz Wegner. “Spin-ordering in a planar classical Heisenberg model”. In: *Zeitschrift für Physik* 206.5 (1967), pp. 465–470.

[134] Paul M Chaikin, Tom C Lubensky, and Thomas A Witten. *Principles of condensed matter physics*. Vol. 10. Cambridge university press Cambridge, 1995.

[135] L Benfatto et al. “Kosterlitz-Thouless vs. Ginzburg-Landau description of 2D superconducting fluctuations”. In: *The European Physical Journal B-Condensed Matter and Complex Systems* 13 (2000), pp. 609–612.

[136] GM Bruun and L Viverit. “Vortex state in superfluid trapped Fermi gases at zero temperature”. In: *Physical Review A* 64.6 (2001), p. 063606.

[137] Naoto Nagaosa. *Quantum field theory in strongly correlated electronic systems*. Springer Science & Business Media, 1999.

[138] Jian-Huang She and Alexander V Balatsky. “Berezinskii-Kosterlitz-Thouless Transition to the Superconducting<? format?> State of Heavy-Fermion Superlattices”. In: *Physical Review Letters* 109.7 (2012), p. 077002.

[139] Sheng-Zong Chen et al. "Disorder-induced 2D superconductivity in a NbTiN film grown on Si by ultrahigh-vacuum magneton sputtering". In: *Superconductor Science and Technology* 35.6 (2022), p. 064003.

[140] David R Nelson and John Michael Kosterlitz. "Universal jump in the superfluid density of two-dimensional superfluids". In: *Physical Review Letters* 39.19 (1977), p. 1201.

[141] Sheng-Zong Chen et al. "Disorder-induced 2D superconductivity in a NbTiN film grown on Si by ultrahigh-vacuum magneton sputtering". In: *Superconductor Science and Technology* 35.6 (2022), p. 064003.

[142] R. W. Crane et al. "Fluctuations, dissipation, and nonuniversal superfluid jumps in two-dimensional superconductors". In: *Phys. Rev. B* 75 (9 2007), p. 094506. DOI: 10.1103/PhysRevB.75.094506. URL: https://link.aps.org/doi/10.1103/PhysRevB.75.094506.

[143] CGL Bøttcher et al. "Berezinskii-Kosterlitz-Thouless transition and anomalous metallic phase in a hybrid Josephson junction array". In: *Physical Review B* 110.18 (2024), p. L180502.

[144] HF Hess et al. "Scanning-tunneling-microscope observation of the Abrikosov flux lattice and the density of states near and inside a fluxoid". In: *Physical review letters* 62.2 (1989), p. 214.

[145] YB Kim and MJ Stephen. "Flux flow and irreversible effects". In: *Superconductivity*. Routledge, 2018, pp. 1107–1165.

[146] AI Larkin and Yu N Ovchinnikov. "Pinning in type II superconductors". In: *Journal of Low Temperature Physics* 34 (1979), pp. 409–428.

[147] "Absence of a finite-temperature vortex-glass phase transition in two-dimensional $YBa_2Cu_3O_{7-\delta}$ films, author=Dekker, C and Wöltgens, PJM and Koch, RH and Hussey, BW and Gupta, A, journal=Physical review letters, volume=69, number=18, pages=2717, year=1992, publisher=APS". In: ().

[148] Z Sefrioui et al. "Pure 2D vortex-glass phase transition with T_g= 0 Kin deoxygenated $YBa_2Cu_3O_{6.4}$ thin films". In: *Europhysics Letters* 48.6 (1999), p. 679.

[149] Hai-hu Wen et al. "2D Vortex-Glass Transition with T g= 0 K in Tl 2 Ba 2 CaCu 2 O 8 Thin Films due to High Magnetic Fields". In: *Physical review letters* 80.17 (1998), p. 3859.

[150] David R Nelson. "Vortex entanglement in high-T_c superconductors". In: *Physical Review Letters* 60.19 (1988), p. 1973.

[151] David R Nelson. "Statistical mechanics of flux lines in high-T c superconductors". In: *Journal of statistical physics* 57 (1989), pp. 511–530.

[152] David R Nelson and H Sebastian Seung. "Theory of melted flux liquids". In: *Physical Review B* 39.13 (1989), p. 9153.

[153] Matthew P. A. Fisher and D. H. Lee. "Correspondence between two-dimensional bosons and a bulk superconductor in a magnetic field". In: *Phys. Rev. B* 39 (4 1989), pp. 2756–2759. DOI: 10.1103/PhysRevB.39.2756. URL: https://link.aps.org/doi/10.1103/PhysRevB.39.2756.

[154] A. Houghton, R. A. Pelcovits, and A. Sudbø. "Flux lattice melting in high-T_c superconductors". In: *Phys. Rev. B* 40 (10 1989), pp. 6763–6770. DOI: 10.1103/PhysRevB.40.6763. URL: https://link.aps.org/doi/10.1103/PhysRevB.40.6763.

[155] E. H. Brandt. "Thermal fluctuation and melting of the vortex lattice in oxide superconductors". In: *Phys. Rev. Lett.* 63 (10 1989), pp. 1106–1109. DOI: 10.1103/PhysRevLett.63.1106. URL: https://link.aps.org/doi/10.1103/PhysRevLett.63.1106.

[156] "Evidence for a vortex-liquid–vortex-glass transition in epitaxial $Bi_2Sr_2Ca_2Cu_3O_{10+\delta}$ thin films, author=Wagner, P and Frey, U and Hillmer, F and Adrian, H, journal=Physical Review B, volume=51, number=2, pages=1206, year=1995, publisher=APS". In: ().

[157] Zhi-Yong Song et al. "InN superconducting phase transition". In: *Scientific reports* 9.1 (2019), p. 12309.

[158] Hyun-Sook Lee et al. "Magnetic-field-induced crossover of vortex-line coupling in $SmFeAsO_{0.85}$ single crystal". In: *Physical Review B—Condensed Matter and Materials Physics* 82.10 (2010), p. 104523.

[159] H Yamasaki et al. "Quasi-two-dimensional vortex-glass transition observed in epitaxial $\mathrm{Bi_2Sr_2Ca_2Cu_3O}_x$ thin films". In: *Physical Review B* 50.17 (1994), p. 12959.

[160] Hua Xu et al. "Dynamical scaling of $YBa_2Cu_3O_{7-\delta}$ thin film conductivity in zero field". In: *arXiv e-prints* (2008), arXiv–0803.

[161] Thomas Nattermann and Stefan Scheidl. "Vortex-glass phases in type-II superconductors". In: *Advances in Physics* 49.5 (2000), pp. 607–704.

[162] MV Feigel'Man et al. "Theory of collective flux creep". In: *Physical review letters* 63.20 (1989), p. 2303.

[163] AI Larkin and Yu N Ovchinnikov. "Pinning in type II superconductors". In: *Journal of Low Temperature Physics* 34 (1979), pp. 409–428.

[164] M. Tinkham. *Introduction to Superconductivity*. International series in pure and applied physics. McGraw-Hill, 1975. ISBN: 9780070648777. URL: https://books.google.pl/books?id=L0brob3Q9W4C.

[165] Andreas Schönenberger et al. "Strong pinning and plastic deformations of the vortex lattice". In: *Physical review letters* 77.22 (1996), p. 4636.

[166] Ernst Helmut Brandt. "The flux-line lattice in superconductors". In: *Reports on Progress in Physics* 58.11 (1995), p. 1465.

[167] S Brazovski and A Larkin. "Nonlinear conduction of sliding electronic crystals: Charge and spin density waves". In: *Le Journal de Physique IV* 9.PR10 (1999), Pr10–77.

[168] Serguei Brazovskii and Thomas Nattermann. "Pinning and sliding of driven elastic systems: from domain walls to charge density waves". In: *Advances in Physics* 53.2 (2004), pp. 177–252.

[169] Daniel S Fisher. "Threshold behavior of charge-density waves pinned by impurities". In: *Physical Review Letters* 50.19 (1983), p. 1486.

[170] Daniel S Fisher. "Sliding charge-density waves as a dynamic critical phenomenon". In: *Physical Review B* 31.3 (1985), p. 1396.

[171] G Blatter, VB Geshkenbein, and JAG Koopmann. "Weak to strong pinning crossover". In: *Physical review letters* 92.6 (2004), p. 067009.

[172] Ryoya Nakamura et al. "Thickness-induced crossover from strong to weak collective pinning in exfoliated $FeTe_{0.6}Se_{0.4}$ thin films at 1 T". In: *Physical Review B* 104.16 (2021), p. 165412.

[173] Y. B. Kim, C. F. Hempstead, and A. R. Strnad. “Flux-Flow Resistance in Type-II Superconductors”. In: *Phys. Rev.* 139 (4A 1965), A1163–A1172. DOI: 10.1103/PhysRev.139.A1163. URL: https://link.aps.org/doi/10.1103/PhysRev.139.A1163.

[174] ZL Xiao et al. “Edge and bulk transport in the mixed state of a type-II superconductor”. In: *Physical Review B* 65.9 (2002), p. 094511.

[175] MT Li et al. “Evidence for weak collective pinning and δl pinning in topological superconductor $Cu_xBi_2Se_3$”. In: *Journal of Physics: Condensed Matter* 30.31 (2018), 31LT01.

[176] Benjamin Sacépé et al. “Low-temperature anomaly in disordered superconductors near B_{c2} as a vortex-glass property”. In: *Nature physics* 15.1 (2019), pp. 48–53.

[177] R Schneider et al. “Anisotropic field dependence of the electronic transport in superconducting FeSe thin films”. In: *Superconductor Science and Technology* 33.7 (2020), p. 075011.

[178] M. J. Qin et al. “Evidence for vortex pinning induced by fluctuations in the transition temperature of MgB_2 superconductors”. In: *Phys. Rev. B* 65 (13 2002), p. 132508. DOI: 10.1103/PhysRevB.65.132508. URL: https://link.aps.org/doi/10.1103/PhysRevB.65.132508.

[179] Guy Deutscher. “Superfluid Condensation in Short Coherence Length Superconductors: The Case of the High T_c Cuprates”. In: *Journal of superconductivity* 12 (1999), pp. 15–17.

[180] Hendrik Anthony Kramers. “Brownian motion in a field of force and the diffusion model of chemical reactions”. In: *physica* 7.4 (1940), pp. 284–304.

[181] Peter Hänggi, Peter Talkner, and Michal Borkovec. “Reaction-rate theory: fifty years after Kramers”. In: *Reviews of modern physics* 62.2 (1990), p. 251.

[182] David L Gil and Donald Windover. “Limitations of x-ray reflectometry in the presence of surface contamination”. In: *Journal of Physics D: Applied Physics* 45.23 (2012), p. 235301.

[183] Xu Ming et al. “Accurate determination of film thickness by low-angle X-ray reflection”. In: *Chinese Physics* 9.11 (2000), p. 833.

[184] Sjoerd A Veldhuis et al. “A facile method for the density determination of ceramic thin films using X-ray reflectivity”. In: *Journal of sol-gel science and technology* 71 (2014), pp. 118–128.

[185] Olli V Lounasmaa. “Experimental principles and methods below 1K”. In: (1974).

[186] B Oh et al. “Upper critical field, fluctuation conductivity, and dimensionality of $YBa_2Cu_3O_{7-x}$”. In: *Physical Review B* 37.13 (1988), p. 7861.

[187] Heon-Jung Kim et al. “Fluctuation of superconductivity in MgB2 thin films”. In: *Physica C: Superconductivity* 408 (2004), pp. 72–74.

[188] SH Han and Ö Rapp. “Superconducting fluctuations in the resistivity of Bi-based 2: 2: 2: 3”. In: *Solid state communications* 94.8 (1995), pp. 661–666.

[189] UC Upreti and AV Narlikar. “Excess conductivity, critical region and anisotropy in YBa2Cu4O8”. In: *Solid state communications* 100.9 (1996), pp. 615–620.

[190] L G Aslamazov and A I Larkin. "Effect of fluctuations on the properties of a superconductor above the critical temperature". In: *Sov. Phys. - Solid State (Engl. Transl.)* 10 (Oct. 1968). URL: https://www.osti.gov/biblio/7298727.

[191] LG Aslamasov and AI Larkin. "The influence of fluctuation pairing of electrons on the conductivity of normal metal". In: *Physics Letters A* 26.6 (1968), pp. 238–239.

[192] Benjamin Sacépé et al. "Localization of preformed Cooper pairs in disordered superconductors". In: *Nature Physics* 7.3 (2011), pp. 239–244.

[193] Gufei Zhang et al. "Global and local superconductivity in boron-doped granular diamond". In: *Adv. Mater* 26.13 (2014), pp. 2034–2040.

[194] Zhuoyu Chen et al. "Carrier density and disorder tuned superconductor-metal transition in a two-dimensional electron system". In: *Nature communications* 9.1 (2018), p. 4008.

[195] Gufei Zhang et al. "Superconductor-insulator transition driven by pressure-tuned intergrain coupling in nanodiamond films". In: *Physical Review Materials* 3.3 (2019), p. 034801.

[196] Sergio Caprara et al. "Multiband superconductivity and nanoscale inhomogeneity at oxide interfaces". In: *Physical Review B—Condensed Matter and Materials Physics* 88.2 (2013), p. 020504.

[197] Giulia Venditti et al. "Superfluid properties of superconductors with disorder at the nanoscale: A random impedance model". In: *Condensed Matter* 5.2 (2020), p. 36.

[198] SERGIO Caprara et al. "Inhomogeneous multi carrier superconductivity at $LaXO_3/SrTiO_3$ (X= Al or Ti) oxide interfaces". In: *Superconductor Science and Technology* 28.1 (2014), p. 014002.

[199] VG Volotskaya, IM Dmitrenko, and AG Sivakov. "New resistive state of wide superconducting films". In: *Soviet Journal of Low Temperature Physics* 10.4 (1984), pp. 179–184.

[200] AG Sivakov et al. "Josephson behavior of phase-slip lines in wide superconducting strips". In: *Physical review letters* 91.26 (2003), p. 267001.

[201] Jun Li et al. "Local destruction of superconductivity by non-magnetic impurities in mesoscopic iron-based superconductors". In: *Nature communications* 6.1 (2015), p. 7614.

[202] VM Dmitriev et al. "Critical currents, phase slip centers, and phase slip lines in superconducting films in the absence of external magnetic field". In: *Low temperature physics* 31.2 (2005), pp. 127–136.

[203] Ambika Bawa, Rajveer Jha, and Sangeeta Sahoo. "Tailoring phase slip events through magnetic doping in superconductor-ferromagnet composite films". In: *Scientific Reports* 5.1 (2015), p. 13459.

[204] G. Berdiyorov et al. "Dynamics of current-driven phase-slip centers in superconducting strips". In: *Phys. Rev. B* 90 (5 2014), p. 054506. DOI: 10.1103/PhysRevB.90.054506. URL: https://link.aps.org/doi/10.1103/PhysRevB.90.054506.

[205] Meenakshi Sharma et al. "Complex phase-fluctuation effects correlated with granularity in superconducting NbN nanofilms". In: *Nanomaterials* 12.23 (2022), p. 4109.

[206] Shashank Kumar Ojha et al. “Flux-flow instability across Berezinskii Kosterlitz Thouless phase transition in $KTaO_3$ (111) based superconductor”. In: *Communications Physics* 6.1 (2023), p. 126.

[207] Nicola Paradiso et al. “Phase slip lines in superconducting few-layer $NbSe_2$ crystals”. In: *2D Materials* 6.2 (2019), p. 025039.

[208] VV Shmidt and AA Balkov. “Critical current in superconducting films”. In: *SOV PHYS JETP* 30.6 (1970), pp. 1137–1142.

[209] IM Dmitrenko. “Resistive state of broad superconducting films and phase-slip lines (a review)”. In: *Low Temperature Physics* 22.8 (1996), pp. 648–664.

[210] B Spivak, P Oreto, and SA Kivelson. “Theory of quantum metal to superconductor transitions in highly conducting systems”. In: *Physical Review B—Condensed Matter and Materials Physics* 77.21 (2008), p. 214523.

[211] Iraida N Demchenko et al. “Use of XPS to clarify the Hall coefficient sign variation in thin niobium layers buried in silicon”. In: *Applied Surface Science* 399 (2017), pp. 32–40.

[212] David W. Abraham et al. “Resistive transition in two-dimensional arrays of superconducting weak links”. In: *Phys. Rev. B* 26 (9 1982), pp. 5268–5271. DOI: 10.1103/PhysRevB.26.5268. URL: https://link.aps.org/doi/10.1103/PhysRevB.26.5268.

[213] CJ Lobb, David W Abraham, and M Tinkham. “Theoretical interpretation of resistive transition data from arrays of superconducting weak links”. In: *Physical Review B* 27.1 (1983), p. 150.

[214] D. J. Resnick et al. “Kosterlitz-Thouless Transition in Proximity-Coupled Superconducting Arrays”. In: *Phys. Rev. Lett.* 47 (21 1981), pp. 1542–1545. DOI: 10.1103/PhysRevLett.47.1542. URL: https://link.aps.org/doi/10.1103/PhysRevLett.47.1542.

[215] Taejoon Kouh and JM Valles Jr. “Deviations from mean-field behavior in disordered nanoscale superconductor–normal-metal–superconductor arrays”. In: *Physical Review B* 67.14 (2003), p. 140506.

[216] Rafael Taboryski et al. “Multiple Andreev reflections in diffusive SNS structures”. In: *Superlattices and microstructures* 25.5-6 (1999), pp. 829–837.

[217] Swati S Soman, K Das Gupta, and N Chandrasekhar. “Critical currents of strongly disordered ultra-thin superconducting films”. In: *Physica B: Condensed Matter* 329 (2003), pp. 1386–1388.

[218] Thomas P. Sheahen. “Rules for the Energy Gap and Critical Field of Superconductors”. In: *Phys. Rev.* 149 (1 1966), pp. 368–370. DOI: 10.1103/PhysRev.149.368. URL: https://link.aps.org/doi/10.1103/PhysRev.149.368.

[219] Chuan Li et al. “Full range of proximity effect probed with superconductor/graphene/superconductor junctions”. In: *Physical Review B* 94.11 (2016), p. 115405.

[220] Muhammad Nadeem, Michael S Fuhrer, and Xiaolin Wang. “The superconducting diode effect”. In: *Nature Reviews Physics* 5.10 (2023), pp. 558–577.

[221] Heng Wu et al. “The field-free Josephson diode in a van der Waals heterostructure”. In: *Nature* 604.7907 (2022), pp. 653–656.

[222] Kou Misaki and Naoto Nagaosa. “Theory of the nonreciprocal Josephson effect”. In: *Physical Review B* 103.24 (2021), p. 245302.

[223] Margarita Davydova, Saranesh Prembabu, and Liang Fu. “Universal Josephson diode effect”. In: *Science advances* 8.23 (2022), eabo0309.

[224] Toshiya Ideue and Yoshihiro Iwasa. *One-way supercurrent achieved in an electrically polar film*. 2020.

[225] Kun Jiang and Jiangping Hu. “Superconducting diode effects”. In: *Nature Physics* 18.10 (2022), pp. 1145–1146.

[226] Xiaolong Liu and Mark C Hersam. “2D materials for quantum information science”. In: *Nature Reviews Materials* 4.10 (2019), pp. 669–684.

[227] Ananthesh Sundaresh et al. “Diamagnetic mechanism of critical current nonreciprocity in multilayered superconductors”. In: *Nature Communications* 14.1 (2023), p. 1628.

[228] IO Kulik and AN Omel’Yanchuk. “Contribution to the microscopic theory of the Josephson effect in superconducting bridges”. In: *Soviet Journal of Experimental and Theoretical Physics Letters* 21 (1975), p. 96.

[229] AF Mayadas, RB Laibowitz, and JJ Cuomo. “Electrical characteristics of rf-sputtered single-crystal niobium Films”. In: *Journal of Applied Physics* 43.3 (1972), pp. 1287–1289.

[230] M Gurvitch. “Resistivities and mean free paths in individual layers of a metallic multilayered structure”. In: *Physical Review B* 34.2 (1986), p. 540.

[231] Morten Kjærgaard et al. “Transparent semiconductor-superconductor interface and induced gap in an epitaxial heterostructure Josephson junction”. In: *Physical Review Applied* 7.3 (2017), p. 034029.

[232] TM Klapwijk, GE Blonder, and M Tinkham. “Explanation of subharmonic energy gap structure in superconducting contacts”. In: *Physica B+ C* 109 (1982), pp. 1657–1664.

[233] M Octavio et al. “Subharmonic energy-gap structure in superconducting constrictions”. In: *Physical Review B* 27.11 (1983), p. 6739.

[234] A Chrestin, T Matsuyama, and U Merkt. “Evidence for a proximity-induced energy gap in Nb/InAs/Nb junctions”. In: *Physical Review B* 55.13 (1997), p. 8457.

[235] JC Cuevas et al. “Proximity effect and multiple Andreev reflections in diffusive superconductor–normal-metal–superconductor junctions”. In: *Physical Review B—Condensed Matter and Materials Physics* 73.18 (2006), p. 184505.

[236] Sameh M Altanany et al. “Vortex dynamics in disordered niobium thin films”. In: *Physical Review B* 109.21 (2024), p. 214504.

[237] Thomas Baumgartner et al. “Effects of neutron irradiation on pinning force scaling in state-of-the-art Nb_3Sn wires”. In: *Superconductor Science and Technology* 27.1 (2013), p. 015005.

[238] Evgueni F Talantsev, Ratu C Mataira, and Wayne P Crump. “Classifying superconductivity in Moiré graphene superlattices”. In: *Scientific reports* 10.1 (2020), p. 212.

[239] E Helfand and NR Werthamer. “Temperature and purity dependence of the superconducting critical field, H_{c2}.” In: *Physical Review* 147.1 (1966), p. 288.

[240] Matthew PA Fisher. “Vortex-glass superconductivity: a possible new phase in bulk high-T c oxides”. In: *Physical review letters* 62.12 (1989), p. 1415.

[241] MC Sullivan et al. “Zero-field superconducting phase transition obscured by finite-size effects in thick $YBa_2Cu_3O_{7-\delta}$ films”. In: *Physical Review B—Condensed Matter and Materials Physics* 69.21 (2004), p. 214524.

[242] Hua Xu et al. “Publisher’s Note: Universal critical behavior in single crystals and films of $YBa_2Cu_3O_{7-\delta}$ [Phys. Rev. B 80, 104518 (2009)]”. In: *Phys. Rev. B* 80 (13 2009), p. 139904. DOI: 10.1103/PhysRevB.80.139904. URL: https://link.aps.org/doi/10.1103/PhysRevB.80.139904.

[243] G Grimaldi et al. “Dynamic ordering and instability of the vortex lattice in Nb films exhibiting moderately strong pinning”. In: *Physical Review B—Condensed Matter and Materials Physics* 80.14 (2009), p. 144521.

[244] G Grimaldi et al. “Non-linear flux flow resistance of type-ii superconducting films”. In: *Journal of superconductivity and novel magnetism* 24 (2011), pp. 81–87.

[245] Anota O Ijaduola et al. “Critical currents of ex situ $YBa_2Cu_3O_{7-\delta}$ thin films on rolling assisted biaxially textured substrates: Thickness, field, and temperature dependencies”. In: *Physical Review B—Condensed Matter and Materials Physics* 73.13 (2006), p. 134502.

[246] M Miura et al. “Mixed pinning landscape in nanoparticle-introduced $YGdBa_2Cu_3O_y$ films grown by metal organic deposition”. In: *Physical Review B—Condensed Matter and Materials Physics* 83.18 (2011), p. 184519.

[247] B Maiorov et al. “Competition and cooperation of pinning by extrinsic point-like defects and intrinsic strong columnar defects in $BaFe_2As_2$ thin films”. In: *Physical Review B—Condensed Matter and Materials Physics* 86.9 (2012), p. 094513.

[248] Yue Sun et al. “Effects of heavy-ion irradiation on FeSe”. In: *Physical Review B* 95.10 (2017), p. 104514.

[249] A Volodin et al. “Magnetic-force microscopy of vortices in thin niobium films: Correlation between the vortex distribution and the thickness-dependent film morphology”. In: *Europhysics Letters* 58.4 (2002), p. 582.